DEVELOPMENT AND ANALYSIS OF A COMPUTER MODEL OF ENDOMETRIAL THERMAL ABLATION FOR THE TREATMENT OF MENORRHAGIA

by

DANIEL MARTIN REINDERS

B.Sc. Honours, The University of British Columbia, 1996

A THESIS SUBMITTED IN PARTIAL FULFILMENT OF THE REQUIREMENTS FOR

THE DEGREE OF

MASTER OF SCIENCE

in

THE FACULTY OF GRADUATE STUDIES

(Department of Bio-resource Engineering)

We accept this thesis as conforming
to the required standard

THE UNIVERSITY OF BRITISH COLUMBIA

APRIL 2002

In presenting this thesis in partial fulfilment of the requirements for an advanced degree at the University of British Columbia, I agree that the Library shall make it freely available for reference and study. I further agree that permission for extensive copying of this thesis for scholarly purposes may be granted by the head of my department or by his or her representatives. It is understood that copying or publication of this thesis for financial gain shall not be allowed without my written permission.

Department of Bioresource Engineering

The University of British Columbia
Vancouver, Canada

April 25, 2002

ABSTRACT

Menorrhagia, the condition of excessive menstrual flow, affects up to 20% of women at some point in their lives. In the past decade a new treatment, endometrial thermal ablation, has been developed. Rather than removing the whole uterus, as in a hysterectomy, only the inner lining responsible for menstrual flow is eliminated. A computer model of the heat transfer and tissue burning process was created to analyse two different approaches that utilize heated liquid contained in a flexible balloon to cauterise the endometrium. One approach maintains a constant fluid temperature throughout the treatment protocol. The other approach, referred to in this thesis as the Thermal Reservoir System (TRS), oscillates preheated fluid between the balloon and a reservoir via an insulated tube. Validation of the model predictions was performed using data from the literature, meat analogues of the uterus with thermometry data, and the results of clinical trials of the TRS. The model accurately predicts burn depth within the limits of the inter-individual variation.

The results indicate that both devices provide an adequate degree of endometrial destruction with minimal risk of thermal damage to organs in the peritoneal cavity. In general, the TRS is predicted to be less affected by variation in individual treatment parameters (such as the uterus cavity volume and the blood perfusion rate). The model also indicates that the use of higher temperatures improves the specificity of the burn injury, reducing damage to the non-targeted tissue while adequately cauterising the targeted tissue.

The use of computer modelling in the study of endometrial thermal ablation has been very fruitful. As a result of this study, many useful insights have been obtained regarding both the physics of the TRS device and the general process of endometrial thermal ablation.

Key Words

endometrial thermal ablation, menorrhagia, burn, hyperthermia, coagulation

Table of Contents

List of Tables

List of Figures

Nomenclature

D&C	Dilation and Curettage
H&E	Hematoxylin and Eosin
NADH	Nicotinamide Adenine Dinucleotide Reduced
NBT	Nitroblue Tetrazolium
Nd:Yag	Neodymium:Yttrium Aluminum Garnet
TCRE	Trans-cervical Resection
TRS	Thermal Reservoir System

SYMBOLS

k_t	thermal conductivity - tissue	$W \cdot m^{-1} \cdot {}^{o}C^{-1}$
k_L	thermal conductivity – balloon liquid	$W \cdot m^{-1} \cdot {}^{o}C^{-1}$
ρ_t	density – tissue	$kg \cdot m^{-3}$
ρ_b	density – blood	$kg \cdot m^{-3}$
ρ_L	density – balloon liquid	$kg \cdot m^{-3}$
c_t	heat capacity - tissue	$J \cdot kg^{-1} \cdot {}^{o}C^{-1}$
c_b	heat capacity - blood	$J \cdot kg^{-1} \cdot {}^{o}C^{-1}$
c_L	heat capacity – balloon liquid	$J \cdot kg^{-1} \cdot {}^{o}C^{-1}$
ω	blood perfusion rate	$mL_{blood} \cdot mL_{tissue}^{-1} \cdot s^{-1}$
q_m	metabolic rate	$W \cdot m^{-3}$
W	water concentration	$kg \cdot m^{-3}$
D_W	water diffusivity	$cm^2 \cdot s^{-1}$
H_{vap}	heat of vaporization of water	$J \cdot kg^{-1}$
W_{vap}	amount of water vaporized	$kg \cdot m^{-3}$
T	temperature	^{o}C
t	time	s
h	heat transfer coefficient	$W \cdot m^{-2} \cdot {}^{o}C^{-1}$
E	elastic modulus	kPa
ν	Poisson's constant	dimensionless
θ	Blood perfusion temperature sensitivity	$^{o}C^{-1}$
ϕ	Blood perfusion temperature response rate	s^{-1}
Ea	activation energy	$KJ \cdot mole^{-1}$
A	time scaling term	s^{-1}

Acknowledgments

I would like to acknowledge the help and support of my academic advisors, Dr. Susan Baldwin and Dr. Joel Bert. Without their help and guidance this thesis would not have been possible, and their efforts are sincerely appreciated. I would also like to thank the chief engineer of my sponsoring company, Monty Bruce, for his technical and practical support regarding endometrial thermal ablation, the TRS, and the experimental apparatus used in the meat experiments. I would also like to thank my sponsoring company and the National Science and Engineering Research Council of Canada for funding my Industrial Post-graduate Scholarship that allowed this work to be performed. Finally I would like to thank my wife, Deborah Ling, for her support and her outstanding illustrations.

Chapter 1: Introduction

1.1 Background

Menorrhagia is the condition of excessive menstrual bleeding, usually defined as more than 80mL per month. It affects approximately 20% of women at some point in their lives, primarily in the years just before menopause. In approximately half of cases there is no sign of pathological disease. When hormonal therapy and dilation and curettage fail, a hysterectomy was usually performed. Within the last decade however new alternatives have appeared that prevent bleeding by removing the endometrium while leaving the healthy portions of the uterus intact. Thermal ablation techniques to cauterise the endometrium predominate, although cryoablation has also been used. Different heat delivery mechanisms have been used, including: Nd:Yag laser, microwave, rollerball electrocoagulation, and hot liquid either freely instilled or contained in a balloon. The balloon ablation devices available currently maintain a constant fluid temperature, either by heating the balloon liquid directly or by continuous replacement of the cooled liquid with fluid at the desired temperature. A new approach oscillates glycerine between the balloon and a pre-heated reservoir, with mixing occuring during each exchange. This device does not maintain a constant balloon temperature, and the advantages and disadvantages of this approach were unknown prior to this investigation.

1.2 Objectives

The objectives of this research were to develop, validate and evaluate a theoretical model of endometrial thermal ablation, including the new, pulsed glycerine reservoir device and the constant temperature devices. The research had several individual objectives:

- Develop a mathematical model of heat transfer in living tissue. A literature review was conducted to either select or develop a model, and determine parameter values.
- Develop a mathematical model of thermal damage to tissue. A model of the response of tissue to hyperthermic exposure was selected from the literature. Re-calibration of the model for thermal damage appropriate to internal tissues was performed where required.
- Develop a mathematical model of the glycerine reservoir device, for predicting the balloon fluid temperature.
- Develop experimental protocols for calibrating model parameters and validating the temperature profiles predicted.
- Validate model predictions with published literature and clinical trial results.
- Perform a sensitivity analysis of model parameters.
- Analyse the model for implications and improvements, and compare predictions for the thermal reservoir and the constant temperature devices.

1.3 Motivation

The initial motivation for this project was to assess the effect of the higher temperatures used in this device on treatment efficacy and safety. The initial reservoir temperature is 173°C, and it was known prior to this research that the maximum balloon bulk fluid temperature was approximately 155°C. These temperatures are much greater than the currently available devices (which treat at 75-87°C), and the implications of using higher temperatures were not really known. Intuitively it was expected that a brief treatment at high temperature would cause less damage to the desirable tissue than a longer treatment at low temperature; it was hoped that a computer model of the thermal ablation process would be useful for assessing the validity of this expectation.

An additional motivation was to increase the understanding of the thermal characteristics of the device, in particular to determine the temperature of the cavity surface that occurs during treatment. Previous research had established the balloon temperature, and the temperature in the exterior of the meat models of the uterus. However the behaviour of the surface temperature was not really known prior to this research.

1.4 Layout

This thesis is organized as nine chapters. Chapter 2 provides background on menorrhagia, its treatment, and balloon thermal ablation (including the glycerin reservoir device). Chapter 3 reviews the pathophysiology of tissue burns, and a mathematical model of tissue damage that is appropriate for the uterus is

presented. In Chapter 4 the heat transfer model is presented. This includes heat transfer within the tissue (including modifications to the blood perfusion rate), the balloon temperature calculation algorithm, and parameter selection. In Chapter 5 the protocol used for the uterus-analogue meat trials is presented, and the use of data from this protocol in the calibration of model parameters is discussed. Chapter 6 validates the model predictions using data from the literature, the meat experiments and recently performed clinical trials. Chapter 7 discusses the findings of the model with regard to safety and efficacy of the endometrial ablation device. In Chapter 8 recommendations for future research are discussed. Finally the thesis conclusions are discussed in Chapter 9.

Chapter 2: Background

2.1 Introduction to Menorrhagia

Menstrual problems are a significant concern for gynaecologists; it is estimated that 21% of gynaecology referrals are for menstrual dysfunction (1). Menorrhagia is the condition of excessively heavy menstrual flow, defined as the loss of 80 mL of blood or more per menstrual cycle (2), and may also refer to prolonged menstrual bleeding (>8 days). Dysfunctional uterine bleeding is defined as "excessive bleeding of uterine origin, which is not due to organic pelvic disease, systemic diseases or complications of pregnancy" (3). Ovulation may not occur, in which case the hypothalamus is likely to be the problem; alternatively the woman may be ovulatory, suggesting a complicated problem within the endometrium. The goal of the treatment in all of these conditions is to reduce or eliminate the magnitude of the menstrual flow.

Dysfunctional uterine bleeding is commonplace, the probability of a women suffering from menorrhagia has been estimated to be 20-30% (4). 42% of hysterectomies in the United Kingdom were found to be for dysfunctional uterine bleeding (5). It has been found that between 228,000 and 292,000 of the 600,000 hysterectomies performed annually in the United States are for refractory uterine bleeding, and in 100,000 of these cases there was no anatomical pathology observed (6),(7). The economic cost of this disorder is significant; a hysterectomy may cost

approximately $8,000 to $15,000 US per procedure (7), and this represents a sizeable national expense considering how often this procedure is requested.

There are many possible causes of menorrhagia (3). The problem may be structural. Fibroids, also known as leimyomata, are overgrowths of the normal uterine muscle and fibrous tissue. Approximately 30% of women with fibroids will report menstrual disorders (8). Adenomyosis is a benign condition where the lining of the womb penetrates deeper into the myometrium than normal. Infections may result in menorrhagia, as can pre-cancerous tissue growth. Non-structural causes include endocrinologic, hematologic and iatrogenic problems. An example of an endocrinologic cause is typically found in premenopausal women, where an increase in estrogen production and/or a decrease in progesterone production may lead to endometrial over-stimulation. Clotting diseases may be a hematologic cause of menorrhagia, while the use of anti-coagulants may be an iatrogenic source. It is important to rule out underlying causes that may present a danger to the patient prior to determining the treatment approach. There are many pathological causes of menorrhagia, but approximately 50% of uteri obtained by hysterectomy for menorrhagia show no visible signs of disease upon pathological examination (9). The diagnosis of 1000 women with menorrhagia who were examined in a private clinic is presented in Table 1.

Table 1 – Final diagnosis of 1000 women with menorrhagia diagnosed in a private clinic, showing the number of women (N) in each category (9).

Diagnosis	N
Adenomyosis	440
Fibroids	251
Dysfunctional uterine bleeding	138
Endometriosis-ovarian +	76
Tubovarian mass	25
Polyp (uterine/cervical)	18
Hypothyroidism	12
Cervical cancer	10
Endometrial cancer	10
Thrombocytopenic purpura	7
Estrogen-secreting tumour	4
Tuberculosis	8
von Willebrand's disease	1

2.2 General Anatomy of the Uterus

Prior to discussing treatment methods for menorrhagia, some basic facts about the uterus and the menstrual cycle will be presented. The following is an anatomical summary of information presented in Gray's anatomy (10). The uterus is a hollow, thick-walled organ that encases the foetus during pregnancy. It is situated in the pelvic cavity between the bladder and rectum (see Figure 1). It generally is oriented at an angle forward relative to the axis of the vagina, unless displaced by a full bladder. The uterus generally measures about 7.5 cm in length, 5cm in width, and weighs 30 to 40 grams. On the exterior of the uterus there is a slight constriction midway up the body known as the isthmus. Above this is the body of the uterus; the Fallopian, or uterine tubes enter at the superior-lateral portion of this feature (see Figure 2). During

ovulation the ova is released from the ovaries and carried into the uterine cavity by these tubes. If fertilization occurs the ovum will implant in the wall of the uterine cavity. Anterior to the Fallopian tubes is a convex structure known as the fundus. Most of the exterior of the uterus is covered by a thin peritoneum known as the serosa. This layer covers all of the intestinal surface, the fundus and the vesicle surface as far as the cervical area.

The cervix is the posterior entrance to the uterine cavity, anterior to this is the cervical canal. This connects the vaginal cavity to the uterine body cavity (Figure 3). The body cavity is a slit, flattened dorsal-ventrally. It is shaped as an inverted triangle, with vertices at the fallopian tubes and cervical canal. Inside the cavity is the endometrium layer, approximately 4mm thick; this is the layer that is shed during menstruation. The interior lining of this layer consists of a columnar, ciliated epithelium. The functional layer of the endometrium, in contact with the uterine cavity, contains the tube-like uterine glands. This layer is supplied by what are known as spiral arteries (see Figure 4). Below the functional layer is the Stratum Basalis; this is the portion of the endometrium that is not sloughed off during each cycle and is also the source of regeneration for the functional layer. This layer is supplied with blood by the basal arteries; these vessels do not undergo cyclical changes.

In between the endometrium and the serosa is the myometrium, which accounts for the majority of the volume of the uterus. It is a dense, collagenous tissue, with irregular bundles of smooth muscle fibres. The uterine artery penetrates this layer and branches enter a structure known as the arcuate wreath (see Figure 4); the

vessels of this structure extend parallel to the cavity surface. From this structure the radial arteries extend towards the cavity surface, joining with the basal arteries at the boundary of the myometrium and endometrium (11).

2.3 The Menstrual Cycle

The thickness of the endometrium changes significantly throughout the menstrual cycle (see Figure 5). The usual cycle lasts 28 days with the first day of the cycle being the first day of menstruation (12). The menstrual stage is the first 3-5 days of the cycle, during which time there is an external menstrual discharge. The functional layer of the endometrium undergoes necrosis and sloughs off. In addition the walls of blood vessels near the surface rupture and contribute to the menstrual flow.

In the follicular, or proliferative stage, menstrual flow ceases and the endometrium layer increases in thickness. Epithelial cells from the uterine glands resurface the epithelium and add to the thickness of the endometrium. Meanwhile spiral arteries begin to grow into the regenerating tissue, and the ovarian follicles mature and secrete estrogen. Ovulation, the release of the ova and its transport into the reproductive tract, occurs on the fourteenth day of the idealized cycle; this period is known as the ovulatory phase. After the ovulation phase ends, the luteal (or secretory) phase begins and extends until menstrual flow resumes. Endometrial thickness increases to its maximum of approximately 4 to 5 mm, due to cell hypertrophy, edema and increased vascularity. In the last day or two the spiral

arteries undergo sporadic contractions, and the functional layer shrinks due to anaemia. As the spiral arteries continue to contract, episodes of vascular engorgement cause the overlying tissue to lose integrity and slough into the uterine cavity, thus initiating menstruation.

2.4 Treatments for Menorrhagia

In general a non-invasive treatment is preferred to a surgical intervention. Counselling may be an important option; it has been shown that only 40% of women complaining of menorrhagia actually have objective menorrhagia (13). Where appropriate, in the absence of pre-cancerous tissue for example, hormonal intervention is sometimes effective at controlling menorrhagia. Oral contraceptives are up to 50% effective, but may be accompanied by undesirable side effects. If taken continuously the woman may be made amenorrheic, in the absence of breakthrough bleeding (13). Non-steroidal anti-inflammatory medications are only 30% effective and can lead to gastrointestinal problems (2). Anti-fibrinolytics are up to 50% effective but may cause headaches, gastro-intestinal side effects, vertigo and possibly an increased thrombotic tendency (2). Danazol, a chemically modified androgenic steroid, is frequently used to thin the endometrium and is very effective, but may cause androgenic side effects such as weight gain and skin rashes (13). Gonadotropin-releasing hormone agonists are also very effective but may cause side effects consistent with an insufficient level of estrogen (2). Although these treatments may bring relief from menorrhagia, they represent an ongoing cost and may result in unacceptable side effects. The statistics reveal that chemical treatment yields

unacceptable results more often than acceptable; sixty percent of patients with menorrhagia undergo hysterectomy within five years of referral to a gynaecology outpatient clinic (1).

Typically if hormone therapy is ineffective then dilation and curettage (D&C) will be attempted. This is a very unpleasant scraping of the inside of the uterus. In addition, this procedure is rarely effective (14), and decreased flow usually only lasts for a few cycles (2). Until recently the primary alternative was a hysterectomy, the surgical removal of the entire uterus. This is a major surgical procedure, one that requires the use of general anaesthetic with the associated risks. The procedure has an estimated mortality rate of one to two per thousand, due to cardiac arrest, pulmonary emboli and/or respiratory arrest (7). In women under the age of 50 the mortality risk is lower, 4.2 per 10,000 (13). Complications are not infrequent; there is a 25% risk for a vaginal hysterectomy and a 43% risk for an abdominal hysterectomy (13). These complications can include bowel injury, ureter injury, bleeding, infectious morbidity, paralytic ileus, vault granulation, nerve injury, thrombophlebitis and pulmonary emboli (7). Physical side effects include possible incontinence, pelvic pain, genital prolapse, constipation, fatigue and sexual dysfunction. Recovery typically takes two to three weeks. Six to twelve months after the procedure the most common side effects are weight gain, hot flashes, depression and diminished sexual interest (2).

In the early 1980's transcervical resection (TCRE) became available as an alternative treatment for menorrhagia. An electrical cutting loop is used to remove the endometrium while the uterus is distended with an electrolyte-free fluid. Possible complications include uterine perforation, air emboli, reactions to the distension media, like fluid overload, pulmonary and cerebral edema (15). This procedure has been shown to be effective; it was found in a population of 399 subjects that the probability of receiving a hysterectomy in the first year after TCRE was 12.1%, and that there was an additional 12.8% chance of having a hysterectomy in the following four years (16). Another study of 525 patients indicated that after five years there was a 9% probability of requiring a subsequent hysterectomy (17).

An alternative to TCRE is "roller ball" electro coagulation, in which the tissue is thermally coagulated without cutting; this procedure is easier and is less likely to penetrate the myometrium than the use of an electrical cutting loop (6). A five-year follow-up study of 42 patients indicated that there was a 35% probability that a hysterectomy would be required after rollerball ablation (18). Another study of 40 patients indicated that menorrhagia was not alleviated in 17.5% of patients treated (19). A study of 114 women found that 86.7% were very satisfied with the results of the rollerball ablation (20). Potential adverse side effects associated with the distension medium remain. The instrument itself is also complicated and expensive, and a general anaesthetic is required.

The Nd:YAG laser, delivered by optical fibres, also uses heat to locally coagulate the endometrium. Unlike the CO_2 and argon laser, the Nd:YAG laser penetrates up to 4 mm beneath the tissue surface (6). Unfortunately the cost of the laser is significant (~£80,000-100,000), and health authorities have limited the laser fibre itself to single use only, further increasing the cost (21). The success rate for laser ablation has been reported as high as 90%, although in that initial study only 22 patients were used (14). A study of a far larger population (407 women) by the same author supported this value; it also indicated only an 11% failure rate, evaluated up to six months after treatment (6). Complications from laser ablation occurred in 40 of these patients, the primary problems being fluid overload (which led to pulmonary edema in two women), profuse bleeding and hematometra.

Both rollerball and laser ablation utilize hysteroscopy to guide the small scale coagulation process. This has the advantage of allowing inspection of any physical anomalies but requires the attention of an experienced surgeon; thus the cost of the procedure is greatly increased over one which requires only the attention of nursing staff. As with all types of hysteroscopic surgery, uterine perforation is a risk, particularly with inexperienced operators (6). A risk that is present in both treatments is fluid absorption resulting in hyponatremia, a reduced sodium concentration in the blood; fluid absorption should be particularly avoided during TCRE and rollerball ablation because the distension media is electrolyte free (6). Endometrial thinning prior to treatment is common for these treatments, typically using leuprolide, danazol or medroxyprogesterone acetate (19), (6).

Total cavity ablation techniques, like thermal ablation, were introduced in the 1990's, and are a new alternative to the localized, hysteroscopic techniques presented previously. These techniques coagulate the majority of the endometrium surface at once, without hysteroscopic examination. There have been several approaches to total cavity ablation. Vilos (22) tabulated a list that included three hot water intrauterine balloons, two intrauterine free saline solutions, a multielectrode electrocoagulating balloon, a 3-D bipolar electro coagulation probe, a microwave probe, a diode fibre laser and three cryoprobes. Because these devices do not require the attention of a highly trained surgeon, there is the potential for a significant cost savings over hysteroscopic ablation techniques.

2.5 Endometrial Thermal Ablation With Heated Liquid

A recent innovation in the field of endometrial ablation is the use of liquid as a heat delivery mechanism, as compared to other sources such as laser, microwave, electrical or radio frequency based devices.

Saline applied directly inside the uterine cavity without a balloon, can be used (22); for example the Hydrothermablator™ device infuses preheated saline under hysteroscopic observation. The treatment temperature of this device is 90°C, this temperature is maintained for 10 minutes. The preliminary result of a study of fifty women indicated that six months after treatment only 15% were neither amenorrheic nor hypomenorrheic. The balloon pressure of this system is below 45 mmHg. If the balloon pressure were to rise higher than approximately 70 mmHg there would be a

risk of fluid spill into the peritoneal cavity through the Fallopian tubes (23). In the EnAbl™ system, free saline is infused at a temperature of 70-85°C for 15 minutes, using a computer-controlled circulation system (24).

The Cavaterm™ device consists of a disposable silicone balloon catheter with a heating element within the balloon and an integrated controller. A 1.5% glycine solution is used, and an oscillating pump agitates the liquid; this ensures adequate mixing of the fluid. A temperature difference between different points on the balloon surface of up to 18°C has been observed in the absence of mixing (25). Before treatment, curettage is performed to thin the endometrium; therefore this treatment may be performed at any phase of the menstrual cycle. The balloon is inflated until a pressure of 180-200 mmHg is obtained. The fluid temperature is maintained at a temperature of 75°C for 15 minutes, although in the initial clinical trial the treatment involved 30 minutes of hyperthermia (25). Patients have generally been satisfied by treatment with this device; a study of 136 patients indicated a satisfaction probability of 95%.

The Thermachoice™ system also utilizes a balloon to contain the liquid (a 5% dextrose solution). This system is designed to operate at a higher temperature than Cavaterm™; the current treatment protocol is to maintain a temperature of 87°C for 8 minutes. This temperature ensures that water vaporization does not occur when treating at high altitude. Treatment balloon pressure is 160-180 mmHg. The Thermachoice™ 1 device utilizes a latex balloon to house a heating element and two temperature sensors. A trial of 121 women treated with this device found that only

10% required a second surgical procedure due to continued menorrhagia (26). No complications occurred during these procedures, although three patients developed what was assumed to be mild endometritis, and two patients had hematometra. A larger study of 296 women found that 12% were still experiencing menorrhagia one year after treatment (5). Another study of 125 patients found that only 9% were unsatisfied or felt that the procedure had not been effective (27).

The Thermachoice™ 2 device is similar to its predecessor, but it also contains an impeller to agitate the fluid, and replaces the latex balloon with a silicone one (22). An unpublished study of 102 patients compared the results of the two versions of the Thermachoice™ device. Quantitative results were not reported, however it was indicated that there was a greater reduction in post-treatment menstrual bleeding when the device with the fluid agitating impeller was used compared to a previous study using the passive circulation device (22).

MenoTreat™ is another device that uses heated liquid encased in a silicone balloon to treat menorrhagia. Heated saline from the system controller was circulated through the balloon by a variable speed peristaltic pump, set to maintain an operational pressure of 200 mmHg. The liquid temperature is maintained at 85°C for 11 minutes. A clinical trial tested 51 patients using the prototype of this device. The success rate of this trial, defined as a reduction in a validated pictogram bleeding score of 50% for at least 80% of patients, was 74-95% (95% confidence interval) (28). It is apparent from the reviewed literature that the success rates of total cavity ablation techniques are at least as good as hysteroscopic methods. It is likely that the

hysteroscopic methods will therefore fall out of clinical favour, due to the less invasive and less expensive nature of the total cavity techniques.

2.6 Safety Concerns of Endometrial Balloon Ablation

There are several safety concerns that need to be addressed before there can be widespread acceptance of balloon endometrial ablation. These concerns include: uterine perforation, genital tract burns, balloon bursting, and heat conduction into the peritoneal cavity.

The risk of perforation in a normal uterus appears to be quite small. Attempts to perforate uterine specimens with the Thermachoice™ catheter were reported to be unsuccessful unless a forceful stab was used (29). One advantage of balloon devices is the possibility of detecting uterine perforation during treatment. For example the Thermachoice™ device automatically deactivates when pressure falls below 45 mmHg or rises above 210 mmHg. This mechanism also minimizes any extraneous damage that may occur should balloon bursting occur. Only the heat stored in the liquid at the time of rupture is available to cause injury. Free fluid could flow out of the cervix and cause injury to the cervical canal and vaginal mucosa, causing damage in proportion to the speed of fluid leakage and inversely related to the surface area affected since there is a finite amount of heat available in the liquid (29). The absorption of fluid is also a concern; however the intrauterine pressure will be low and the vessels of the superficial endometrium will be coagulated, limiting the amount of fluid that could be absorbed. Although the risk is real, it appears to be very small. Fernandez et al. (30)

report that there have been no cases of balloon rupture in ~1,800 Thermachoice™ procedures performed worldwide. The risk of genital tract burns is minimized by either placing the heater within the balloon itself, or by thermally insulating the shaft that is used to transport the heated liquid to the balloon.

The risk of ancillary damage to the outer myometrium and the peritoneal organs surrounding the uterus has been assessed for different ablation devices by experimental measurements and/or numerical simulation. Neuwirth et al. (29) reported results from clinical trials in 109 patients where thermocouples were surgically implanted in the serosa of patients. The maximum temperature on the exterior of the uterus, during treatment with the Thermachoice™ 1 device and protocol, ranged from 31.7 to 37.7°C (mean 35.2°C). It should be noted that the normal temperature of the body core is 37°C; the core temperature may have been depressed due to the effect of general anaesthesia. Another study examined the effect of increasing the treatment time of the Thermachoice™ device (31); serosal temperatures were investigated in 8 patients treated for times ranging from 8 to 16 minutes. It was found that the maximum temperature observed was 39.1°C, as compared to the control temperature of approximately 35°C. Interestingly the maximum temperature was observed at approximately 13 minutes; afterwards the temperature fell, probably due to a delayed increase in blood perfusion. A study done for the Cavaterm™ device (32) found that the increases in temperature of the surrounding tissues were too small to measure accurately (<1 degree difference).

Shah et al. (33) implanted thermocouples in the serosa, among other areas, of 39 patients treated with the Thermachoice™ device. Control measurements were obtained for ten minutes prior to treatment; the average temperature for the uterus during this period was 23.5°C (range 23.7-24.9°C). No reason was given for this sub-physiologic temperature, but it is likely to be a result of both open surgery and anaesthesia. The average serosal temperature was 29.2°C, with minimum temperature of 20.6 and a maximum of 46.7°C. This raises some concern if a local anaesthetic were to be used in place of general anaesthesia. If the maximum observed serosal temperature was 46.7°C, this translates into a temperature rise of 23.2°C over the baseline temperature. If this temperature rise were to occur at the normal physiologic temperature then the serosa would have experienced a maximum temperature of 60.2°C. If this result were correct, then this serosal temperature would be sufficient to immediately cause irreversible damage to the adjacent tissue, although it should be emphasized that the effect of blood perfusion means that the temperature rise would not be identical at the normal core temperature.

A numerical model of the original Cavaterm™ treatment protocol (75°C for 30 minutes) was created and analysed by Persson et al. (34). A finite element model was used to estimate the temperature distribution in an axially symmetric model of the uterus, assuming an approximately ellipsoidal balloon shape after inflation. The model included terms to account for the effect on blood perfusion rate of balloon pressure, vasodilation due to thermal stimulation and vascular stasis due to thermal damage. The model indicated that tissue that was 9.2 mm from the cavity surface could expect

to experience a maximum temperature of 45°C, although this distance would increase to 18.4 mm in the absence of blood perfusion. These results suggest that a dangerous serosal damage would not be expected for the average uterine wall thickness expected, although this situation could conceivably occur in a uterus with a compromised blood perfusion system.

2.7 The Thermal Reservoir System

A new endometrial balloon thermal ablation device that is significantly different from devices such as Thermachoice™ and Cavaterm™ has been developed. This device is referred to here as the Thermal Reservoir System (TRS), and consists of a handheld device in lieu of a desktop controller (Figure 6). The heat-delivery liquid is glycerine, rather than a saline or dextrose solution. The boiling temperature of glycerine is much higher than water, allowing higher fluid temperatures to be used without risk of vaporization occurring within the balloon. During treatment the liquid is agitated by pulsing it back and forth between a reservoir in the hand-held unit and the balloon. The oscillation of the liquid takes approximately 1 second, the liquid is stagnant within the balloon for approximately 8 seconds resulting in a 9 second cycle period. The balloon pressure is maintained at 180 mmHg, and the deflation process is a passive one, with the exception of the first two pump cycles in which the glycerine is actively pumped out. The total treatment time is 2.1 minutes, and the current cycle regime is listed in Table 2.

Table 2 – The Fluid transfer protocol for the TRS device. Residence time refers to the period where the fluid remains held in the balloon, while oscillation time refers to the deflation and inflation period. In passive deflation the elastic pressure of the uterus causes partial fluid exchange, while in active fluid exchange the fluid is completely exchanged utilizing the pump.

Cycle Number	Residence Time (s)	Oscillation Time (s)	Deflation Method
1	7	1	Passive
2	4	1	Active
3	4	1	Active
4 - 12	8	1	Passive

Other thermal ablation devices maintain the balloon-fluid temperature close to a set point, either using a heater within the balloon or by infusion of fresh, heated liquid. In the TRS device, the balloon-fluid is only heated initially outside of the balloon in a reservoir. A reservoir containing 32.5 grams of glycerine (25.8 mL) is heated to 173°C and then fluid is injected into the balloon for 8 seconds after which the fluid is drawn back into the reservoir where it mixes with the warm glycerine for 1 second before being re-injected into the balloon for another 8 seconds and so on. There is a maximum of 10.7 kJ available in the glycerine to heat the uterus above the normal body temperature, although in practice complete thermal equilibration does not occur.

Although the glycerine in the reservoir starts at 173°C, the temperature of the liquid first entering the balloon is approximately 155°C. This temperature drop is believed to be due to heat transfer between the fluid and the insulated shaft (initially at room temperature). The balloon-fluid temperature drops throughout treatment as a result of heat transfer to the uterine tissue. For a typical treatment the final balloon-fluid temperature is between 110 and 125°C. Thus, the balloon-fluid temperature in the TRS device is not constant for the duration of treatment and will be affected by

variables such as the uterus thermal properties, uterus cavity volume and blood perfusion rate, which can vary between patients. This reservoir arrangement avoids the need for a heater to be mounted within the balloon.

Chapter 3: Burn Pathophysiology and Modelling

In this next section, a literature review is presented on the cellular and physiological changes that take place in tissues heated above 42 °C. The goal was to identify the histological criteria for permanent tissue destruction and the times at which tissue destruction was observed when temperatures greater than 42 °C were applied. This review was done so as to obtain an accurate mathematical representation for the progression of tissue burns. However, before this could be modelled the events that occur during and after thermal injury had to be characterized. The thermal susceptibility of uterus tissue has not yet been quantified for any damage endpoint; therefore, the burn and healing process is identified for a variety of tissues in the hopes of establishing a range of possible susceptibilities.

3.1 Types of Thermal Damage

Thermal damage effects are grouped here into three categories, mild, moderate, and severe damage. Mild effects are those where complete healing is likely, moderate effects are those where healing is possible but permanent damage may result and severe damage is where total tissue necrosis is expected to occur immediately.

3.1.1 Mild Damage

ERYTHEMA (reddening of the tissue resulting from a variety of causes)

One of the most obvious differences between tissue burned *in vitro* and *in vivo* is the presence, in living tissue, of a red ring surrounding the coagulated tissue (the "red zone"). Microscopic examination reveals that the vascular system in this zone is engorged with red blood cells, a condition known as erythema. This redness is a result of hemostasis (cessation of blood flow), hemorrhage (internal bleeding) or hyperemia (vasodilation and increased blood perfusion) (35). Erythema is considered mild if it is due to vasodilation, otherwise it is a sign of moderate or severe damage. In burns, a red zone can develop within thirty seconds, and can persist for many days. Thomsen (35) describes an unpublished experiment where a red rim in burned goat breast lasted 13 days, at which point the necrotic tissue was replaced with scar tissue.

Many investigators have reported the hemorrhagic ring around coagulated tissue. Morrison (36) described a gradation of erythema around burned liver tissue. In the highly damaged liver tissue, it was caused by ghost red blood cells, cells void of heme due to loss of membrane integrity; in less damaged tissue the redness was caused by normal, intact red blood cells. Another author's observations corroborated these findings in liver following hyperthermia (37). In prostate tissue, a ring of hemorrhage and tissue disruption has been observed separating the central coagulated tissue from undamaged prostate tissue (38),(39),(40). The hemorrhagic

ring has also been observed in myocardial tissue. The pale tan zone of acute necrosis was observed to be surrounded by the red rim which sharply demarcated the injured from uninjured myocardium (41). A reddened marginal area around the necrotic zone has been reported in the prostate following laser ablation. This area was found upon microscopic inspection to consist of dilated, thrombotic vessels (filled with blood clots) and areas of hemorrhage (42).

The hemorrhagic ring observed around internal burns may be analogous to the redness observed in a first-degree skin burn. An exposure of low intensity may result in disturbances of dermal blood vessels without causing irreversible damage to overlying epithelial cells. The escape and extravascular deterioration of red blood cells could result in the brown discoloration that has been observed to persist for up to one-week (43).

EDEMA (presence of abnormally large amounts of fluid in the intracellular tissue spaces)

Tissue that is thermally damaged but continues to be supplied with blood is frequently observed to swell and accumulate fluid. Water, in the presence of a semi-permeable membrane, tends to move from regions of higher to lower concentration and from high pressure to low pressure. Thus if pure water is placed on one side of a membrane permeable only to water, and a salt-water solution is placed on the other side; there will be a flux of water into the salt-water side. This phenomenon is known as osmosis. If a sufficiently large hydrostatic pressure is applied to the salt-water

solutio;n the net flux of water can be reversed and water will flow into the pure water solution, a process known as reverse osmosis. This relationship is readily apparent in the model for transcapillary fluid flow, also known as Starling's hypothesis. In the Starling equation the net flux of fluid is determined by the interaction of the hydrostatic pressure difference driving fluid into the tissue with the colloid osmotic pressure difference that favours fluid retention in the capillaries, i.e.,

$$J = L_p A\left[P_c - P_{IF} - \sigma\left(\pi_{PL} - \pi_{IF}\right)\right] \quad (1)$$

where:

J is the net flux of fluid into the tissue from the capillaries
L_p is the hydraulic conductivity of the capillaries
A is the capillary surface area available for exchange
P_c is the capillary hydrostatic pressure
P_{IF} is the interstitial fluid hydrostatic pressure
σ is the capillary reflection coefficient for proteins
π_{PL} is the plasma colloid osmotic pressure
π_{IF} is the interstitial colloid osmotic pressure

In the Starling hypothesis, the reflection coefficient relates to the permeability of the capillary barrier to proteins: if it is impermeable the value is one and if it is completely permeable the value is zero. In burned tissue, capillary walls have a reduced capacity to act as a molecular sieve; thermally damaged endothelial cells that line the capillary lumen tend to become more spherical and consequently spaces may open up between contacting cells, resulting in a reduced reflection coefficient (44). The increase in pore size allows additional proteins to enter the interstitial spaces that would normally remain in the vascular system (45). The transfer of these proteins will contribute to the osmotic gradient, favouring further movement of water to the

interstitial spaces (46). The increase in capillary permeability (allowing passage for molecules up to 125 kD in size) is due both to direct thermal injury (47) and chemical mediators (48). Thermally damaged proteins in the tissue may degrade into smaller molecules, also contributing to the osmotic gradient (49). The lymphatic system, which normally helps remove excess water, may be damaged by thermal injury and thus contribute further to the swelling already caused by vascular damage (50),(51). In the bat wing, edema was observed two hours post burn and persisted for two weeks. The author suggests that the loss of lymphatic contractile activity, due to thermal damage, enhanced fluid accumulation by reducing the removal rate of excess fluid (51).

3.1.2 Moderate Injury

VASCULAR STASIS (Decreased blood perfusion due to thermal damage to blood cells and vessels)

During thermal damage, the capillary system can become clogged with red blood cells and tissue blood perfusion will decrease, and possibly may cease altogether. Causes of vascular stasis may include a combination water loss due to increased vessel permeability and tissue edema, damage to the endothelial cells that make up the capillary network and the direct thermal coagulation of red blood cells. The time required for complete stasis tends to decrease with increasing burn severity. Canine myocardium perfusion was significantly reduced up to 6 mm beyond the acute lesion, following sixty seconds of radio frequency catheter ablation producing an interface temperature of 85°C (52). The perfusion rate was 48% of normal within the first three millimeters outside the lesion, and was 82% of normal between three

and six millimeters away from the lesion. Following a 43°C burn for 20 minutes in rat skeletal muscle, vascular congestion appeared in 30% of the vessels at 5 minutes, 78% at 6 hours, 71% at 48 hrs and 14% of vessels at 7 days (53). Thus, vascular stasis peaks some time after the burn and then blood perfusion resumes as the tissue heals. In the mouse ear a burn for twenty seconds at 53°C resulted in complete stasis within two hours; in some cases stasis occurred as early as five minutes post-burn for the same temperature. The occurrence of vascular stasis was strongly temperature dependent; no stasis was observed to occur when the exposure temperature was decreased by just 2 °C (54).

Ross and Diller directly visualized the perfusion of individual blood vessels in the hamster cheek pouch during hyperthermia. They developed an exponential function analogous to the Arrhenius function (see Appendix B) for predicting the onset of vascular stasis, using the appearance of instantaneous stasis in 95% of blood vessels within 20 seconds after the burn as the definition of vascular stasis (55).

Another investigator observed the vascular system of the guinea pig following a partial thickness skin burn and described vascular stasis due to the swelling of the endothelial cells resulting in the occlusion of the capillary vessel. Although the morphological appearance of thermal damage only extended through part of the skin thickness, eventual ischemia was observed throughout the whole dermis and epidermis. Two hours post-burn the dermal capillary endothelial cells appeared swollen, in some cases obliterating the capillary lumen and blocking blood flow. Eight hours post-burn vacuolisation of the shallow endothelial cells was apparent, with

sloughing of cell contents into the capillary lumen. Red blood cells had escaped the vascular system into the surrounding matrix. Within four days the capillary plexus had become completely obliterated, the tissue had necrotized (56).

In the bat wing, vascular stasis was microscopically observed to occur within thirty minutes following a contact burn of 55°C for 30 seconds (51). Leukocytes adhered to the vessel walls, in some cases completely lining the veins. Later these leukocytes were observed to migrate into the interstitial spaces. Platelets lined the inner walls of arterial vessels, and platelet aggregates were seen moving in the blood stream of arterial and venous vessels. Within one to two hours, haemorrhaging was observed at some venous confluences and along arterial vessels. In this case platelet aggregation was a key contributor to vascular stasis.

3.1.3 Severe Injury

COAGULATION

Thermal coagulation refers to the irreversible alteration of cell and tissue contents that are visible to the naked eye (57). Most coagulated tissues become whiter and more opaque, although collagenous tissues may become translucent. Unfortunately the term coagulation is often used without definition in the literature. Thermal coagulation should not be confused with the coagulation of blood that occurs upon exposure to air. In burn terminology, coagulation is the visible manifestation of the protein denaturation.

The visible whitening of coagulated tissue is not believed to be due to the denaturation of a single protein. The rate kinetics of coagulation are best described by a distribution of rates constants (58); thermal coagulation was found in this study to be better modelled as the additive effect of many individual reactions, each with its own rate constant. Coagulation occurs at higher temperatures and after longer burn times than the milder effects. For example, Jacques et al. fit first-order rate kinetics to the optical whitening of liver and found coagulation half times of 17, 173 and 9010 seconds at 70, 62.5 and 50°C respectively (58). In contrast, the eventual production of skin blisters is predicted to occur at 2.7×10^{-4}, 0.04 and 201 seconds for the same temperature set (59).

Cells in coagulated tissue may or may not be physically intact. In severely coagulated tissues the proteolytic and lipolytic enzymes that degrade dead cells are denatured and the cells, although dead, appear normal. In fact, 19th century anatomists would "fix" tissues by boiling them (35). These dead cells will persist until new blood vessels bring inflammatory cells to invade and digest the necrotic tissue (60).

In less severely coagulated tissue (tissue burned for less time or at a lower temperature), necrosis occurs because of the rupture of lysozomes that release the proteases and lipases that digest the cells and the surrounding matrix (35). The microscopic appearance of these dead cells is variable; for example, muscle cells tend to assume a "herringbone appearance" (51) while nerve cells become shrunken with

condensed nuclei (61).

COLLAGEN DENATURATION

The denaturation of collagen fibers may serve as a marker of severe thermal damage (43). The normally striated collagen fibers become unravelled, shrink along their axes, swell radially, and lose their striations (see Figure 7) (57),(62). Thermal treatment of the colon wall, where a maximum temperature of 66°C was reached, reduced the bursting strength of the colon due to hugely swollen collagen bundles and fibres (63).

Denaturation of collagen can be indirectly measured through the macroscopic shrinkage of the tissue. For example, the exposure of bovine chordae tendineae, a highly collagenous tissue, to a temperature of 65°C for 100 seconds resulted in lengthwise shrinkage of 20% (64). This shrinkage occurs because the collagen molecule axes are orientated parallel to the tendon axes, thus when the collagen shrinks axially the tendon does too.

The degree of collagen denaturation can be measured using changes in birefringence (62). This involves illuminating the tissue with incident light polarized 90° to an optical analyser located above the section. Birefringent tissue will rotate the polarized light, resulting in tissue that appears bright within the dark field. Collagen and elastin exhibit birefringence and will lose this capacity when thermal denaturation occurs; in collagen this loss is associated with the conformational change of the

collagen molecule from a rod-like α-helix form to a random coil organization (62).

Because collagen denaturation can be readily quantified, it may serve as a useful marker of severe thermal damage. Although the viability of the tissue is usually the variable of interest, collagen shrinkage and birefringence loss require the large temperatures or long exposure times that are associated with tissue that is killed immediately; suggesting that these collagen-descriptive variables may be substituted.

3.2 Burn Depth Progression and Healing

Quantification of the depth of injury during uterine thermal ablation is usually done immediately after the hysterectomy, which is carried out following some thermal ablation clinical trials. However, the volume of damaged tissue in most burns, both external and internal, increases for several days following the initial trauma; after which healing begins. A general summary of the events that occur following thermal injury of internal tissues is proposed in Figure 8. The conceptual framework developed will then be applied to endometrial thermal ablation, with the aim of selecting the appropriate damage description that will predict a successful treatment. There are several key features of this diagram that will be discussed in this section: the increase in necrotic depth within the first week, the regeneration of destroyed tissue and removal of necrotic debris, and the possible replacement of necrotic tissue with scar tissue.

In sufficiently thermally damaged tissue, there is a boundary between tissue that is immediately killed, and that which is mortally wounded and will die later (usually over the course of several days to one week). In one study the prostate lesion was at maximum size on the eighth day, with most of the necrotic area increase occurring between the first and the third day post-burn (see Figure 9) (40). The coalesced area of eventual necrosis appeared to fall within a red zone, providing an obvious maximum limit for cavity formation (38). In burned rabbit muscle the necrotic debris cavity and coagulation zone was at its maximum size seven days following burning (65). Lesions induced in liver were also largest on the seventh day, again most of the degeneration occurred on the second and third day (66). An exception to this trend was found in burned prostate tissue, where the eventual cavity size corresponded to the zone of immediate coagulation (67); the reason for this discrepancy is not known.

Healing of the burned tissue cannot start until the dead cells are removed. Initially, inflammatory cells, particularly polymorphonuclear white blood cells (also called neutrophils) infiltrate the damaged tissue. These cells break down necrotic debris, which is released into the circulation and removed or recycled in various organs. Large components of the necrotic tissue are enveloped by the neutrophils and digested whole in a process called phagocytosis. This cleaning process typically begins three to five days post-burn in the viable tissue adjacent to the necrotic region.

The infiltration of inflammatory cells after burn injury is the most commonly reported microscopic aspect of burn wound healing. Neutrophils are usually the

earliest white blood cells to arrive at the wound (68) and are commonly reported in healing dermis (56),(69). One author noted neutrophil infiltration within seven hours in burned mouse legs (70). Ngim (71) described the infiltration of lymphocytes, plasma cells and eosinophils (types of white blood cells) into damaged dermis. The neutrophil infiltration tends to occur prior to the macrophage infiltration. In one study maximum neutrophil concentrations occurred at six hours post-burn while mononuclear macrophages were at maximum concentration 48 hours post-burn (53). In a muscle burn leukocyte infiltration was observed to begin two hours post-burn, the magnitude of this infiltration increased significantly over time (72).

In internal injuries adjacent to cavities the necrotic material tends to slough off during wound healing. Canine prostate has been observed to slough off regularly over a period of several weeks. Johnson (38) reported cavity formation was complete within seven weeks, while Suzuki (73) described sloughing over a period of three to four weeks. In humans the sloughing process of the prostate is observed to occur less regularly over a period of twelve weeks (74), (40).

After the necrotic tissue is removed the process of regeneration can occur. New blood vessels start to enter the damaged tissue in a process known as angiogenesis. Fibroblasts, the stem cells for fibrocyte connective tissue cells, are essentially repair cells and they proliferate and form collagen to support the new tissue. Anzai et al. (65) found a zone of ongoing coagulative necrosis outside of a cavity of necrotic debris in burned rabbit muscle. The nuclei in this zone became condensed six days after burning and disappeared. On the third to seventh day post-

burn a rim consisting of neutrophils and lymphocytes surrounded the necrotized zone. Gradually the population of cells in this rim became dominated by macrophages. Thirty days later fibroblasts, histocytes, and lymphocytes had replaced the necrotic tissue (75).

In some tissues the vascular and fibrotic proliferation overcomes the growth of normal tissue. In such tissues the blood vessels are resorbed and the collagen fibers become larger and more densely packed, forming scar tissue in a process that takes weeks or months to complete. Scar tissue formation is regularly observed in internal burns. In thermally damaged liver, a fibrous capsule was observed to be well-formed thirty days after the initial injury. This capsule still contained necrotic tissue with aggregated nuclear DNA. The boundary of this cavity was well correlated with the outer zone of vascular stasis (37). Another study on the liver found that local fibrosis, along with hepatocyte loss and lobular architecture change, was one of the best correlates of thermal dose (76). Mathewson (66) found that after peaking on the seventh day a lesion induced in liver would shrink over the next ten weeks; eventually healing was complete and only a small fibrous nodule remained sixty days later.

In burned muscle tissue the outer rim of white blood cells was also a zone of fibrovascular restoration. The necrotic debris cavity was observed to shrink over the following weeks and became surrounded by fibrous scar tissue. For lower intensity burns the necrotic debris cavity became completely replaced by scar tissue (65). In the rabbit Fallopian tubes thermally injured by an endoluminal coagulation procedure, blockage with scar tissue was observed within only three days (77). The blockage did

not occur immediately, but rather was a continuously developing phenomenon. The length of scar tissue was much smaller than the length of burned tissue; the authors propose that the scar tissue caused the tube to shrink longitudinally. The extent of regeneration is very tissue specific. For example, liver tissue will partially regenerate and partially be replaced with scar tissue (66), while burned heart tissue never regenerates (35).

3.3 Special Considerations for Skin Burns

In skin burns, the extent of tissue damage also increases long after the burn injury. For example, maximum damage was observed after four days in three separate burn-injury studies (68),(69),(70). There is strong evidence that the progression of burn depth in skin wounds is due primarily to desiccation. Covering a partial thickness burn wound with an osmotically neutral solution greatly reduces the eventual depth of damage (78). In both covered and uncovered wounds, injured by a ten-second exposure to 75°C, oxygen consumption and sensation ceased immediately. The depth of ischemia gradually increased, blood flow throughout the depth of the tissue had ceased within sixteen hours. In the covered wound blood flow returned within one week, beginning in the deeper layers and progressing outwards. Sensation resumed when blood perfusion was returned, but oxygen consumption took one to two weeks to return. Edema was maximal at four hours, and subsided more quickly than the ischemia. Healing in the covered wound progressed by migration of living epithelial cells from the viable roots of the dead hair follicles. In uncovered wounds these migrating epithelial cells would fail to survive.

Another author compared moist, impermeable dressings to dry (gauze) dressings in the healing of partial thickness wounds (68). At the third day the moist covering was in a more advanced state of healing, as indicated by the greater number of macrophages and reduced neutrophil number (neutrophils tend to leave the wound bed before macrophages arrive). By seven days there were many blood capillaries in the regenerative tissue of the moist wound and it had completely re-epithelialized. In comparison, the dry wounds were less vascular with irregularly arranged fibroblasts and fewer capillaries. By two weeks the moist wound was in better condition, being completely covered by a differentiated keratinized epithelium. The dry wounds at this time had incomplete epithelialization with scab formation. In the uterus, tissue would not dry out and thus we would not expect to see the same extent of damage as observed in unprotected skin.

3.4 Burn Pathophysiology and Endometrial Thermal Ablation

The goal of endometrial thermal ablation is to reduce or eliminate menstrual bleeding by thermally damaging the endometrium while minimizing damage to the myometrium. Because of the excellent regenerative properties of the endometrium (79), it is believed that the entire layer must be destroyed to prevent the further contribution to menstrual bleeding of any particular point. However the previous review of thermal damage forms raises the question of what one means by the term 'destroyed'. Should the endometrial thickness be the target for immediate necrosis or for eventual necrosis? In principle, eventual necrosis should result in the death of the

endometrial layer and a successful treatment; however one could hypothesize that pockets of surviving endometrial cells could regenerate the layer. Certainly *in vitro* experiments indicate that a small fraction of cells subjected to hyperthermia will remain viable after being subjected to many times the dose required to kill the majority of the cells (80). The question of what is the required burn depth for endometrial thermal ablation is an empirical one that cannot be answered conclusively by theoretical arguments alone.

Based on the burn literature of other tissues, there are two possible mechanisms by which hyperthermia may cure menorrhagia. For the treatment to be successful, the necrotic tissue may either be replaced by scar tissue, or it may slough off into the uterine cavity. There is evidence that both effects occur. Buckshee et al. (81) found that six months following a treatment of 87°C for approximately 8 minutes that the majority of the endometrium had become scarred, as determined by hysteroscopy. Particularly noteworthy was that in patients who had amenorrhea the whole cavity had become fibrotic and scarred. If patches of the endometrium were visible they were atrophic.

The idea that there is sloughing of the damaged tissue is supported by the study of Goldrath et al. (14). After five months, a curettage procedure could not find muscle or scar tissue, and only limited endometrial fragments could be obtained. A hysterectomy of one amenorrheic patient 10 months after treatment revealed that the cavity was lined by a simple epithelium that was directly attached to normal appearing myometrium, with only an occasional small endometrial gland present. Hysteroscopy

was performed on another successfully treated patient in this study six months after treatment. No areas of normal endometrium were seen, and there was evidence of collagen deposition on apparently normal endometrium without any surface epithelium. The lack of normal endometrial tissue in either of these cases suggests that the necrotized endometrial tissue had either sloughed off or been absorbed into the blood stream.

Magnetic resonance imaging was used in one empirical study of laser thermal ablation to correlate post-treatment changes with treatment outcome (82). It was found that immediately after treatment the volume of the uterus body increased by an average of 21%. This swelling was accompanied by a loss of definition of the zonal architecture of the uterus. In five of the eight patients tested there was an immediate thickening of the endometrium; this event appeared to be the best indicator of a positive clinical outcome. An increase in the junctional zone/outer myometrium width ratio, thought to be associated with myometrial edema, was also noted but was not statistically related to patient satisfaction. Unfortunately a concurrent histopathological analysis was not performed, and therefore the utility of this study in determining the desired burn depth is limited.

Additional qualitative observations were obtained in a study of the healing process following laser ablation of the endometrium (83). Three histological samples were obtained at four weeks by curettage, and additional patients were sampled at six and fifteen weeks after the ablation. Additional histological samples were obtained no earlier than three months after treatment from women who had hysterectomies due to

dissatisfaction with the ablation treatment result. The samples taken before three months consisted primarily of blood, mucus and fibrin. Necrotic tissue fragments and granulation tissue were present with viable endometrial tissue, which showed evidence of proliferative activity. The curettings obtained after three months were composed of fibroconnective tissue with variable amounts of cyclical endometrial tissue. Re-epithelization appeared to be complete three months after treatment. The authors note that re-epithelization requires only several days following menstruation, compared to three to six months required for thermal ablation. However following menstruation the re-epithelialization occurs from the denuded edges of the endometrial glands. However these glands are destroyed in thermal ablation and therefore re-epithelialization must occur from the tubal ostia and isthmus, a significantly slower process.

These results suggest that the appropriate damage end-point would be a burn inducing scar tissue that slightly penetrates the myometrium. Unfortunately no information is available to calibrate the model this outcome, nor is it even known whether an Arrhenius model would be appropriate. The clinical results of hyperthermia in the porcine liver suggest that, if the liver may be considered an analogue for the healing pattern of the uterus, sloughing of damaged tissue or its replacement with scar tissue will be bounded by the depth of coagulation and by the depth of erythema and vascular stasis (37). The boundary of the fibrous capsule that was formed in the liver was found to be correlated with the dark red tissue that was congested with erythrocytes. Because the depth of hyperemia appears to be correlated with the depth of eventual necrosis in at least one tissue (84), the latter will

be assumed as an outer boundary for possible sloughing and scar tissue formation. Information in a separate paper supports this assumption; Thomsen (35) alludes to observing that the outer boundary of the red zone corresponds to the boundary of eventual necrosis in the human endometrium and myometrium. However the experimental data supporting this assertion were not found in the stated reference (84); since this paper was from a conference proceeding it is possible that the information was only presented orally.

Although there is some evidence that supports the contention that the depth of sloughing is bounded by the depth of coagulation and eventual necrosis, it will not be proven until the hypothesis is properly investigated. The Thermachoice^{TM} device procedure utilizes 87°C water for 8 minutes to induce endometrial thermal damage. The probability of a patient being 'very satisfied' with this procedure was reported to be 85.6% (n = 129) (20). Based on this information and the previously described results of histochemical analysis it is suggested that the inner (least thermotolerant) boundary of predicted eventual necrosis should at least include the full thickness of the endometrium.

3.5 Algorithm for Calculating Thermal Damage to Tissue

It is common knowledge that burns take less time to develop at higher applied temperatures. However it was just over fifty years ago that this relationship was quantified and mathematically analysed (59). The time required for the formation of skin blisters (vesicles) varies greatly with temperature; over six hours are required at

44°C, while only seconds are required at temperatures greater than 55°C (85). The Arrhenius relationship, an expression borrowed from the description of chemical reaction rates in physical chemistry, was found to yield a good fit to the data over the temperature range (44-100°C) investigated; although at temperatures greater than approximately 55°C the agreement is poorer. The following equation was derived by Henriques (59) to quantify the extent of thermal injury in skin:

$$\Omega = A\int_{t_0}^{t_1} e^{\frac{-E_a}{RT}}\,dt \quad (2)$$

Ω = dimensionless measure of tissue damage
E_a = activation energy (6.23×10^5 J/mole)
R = ideal gas constant (8.3145 J/mole.K)
A = scaling factor (3.1×10^{98} 1/s)
t = time (s)

Henriques defined irreversible damage to the epidermal layer to occur when Ω was greater than a value of one, as per equation 2 and the temperature-time history of the dermal/epidermal boundary (59). The correspondence between the predictions of equation 2 (using the parameter values listed above) and the data is excellent (86). Unfortunately the details of the fitting process were not presented in Henriques' study; however it is clear from visual inspection of the data and the fitted function that the correspondence is very good (see Figure 10). Although the Arrhenius expression appears to lose validity above approximately 55°C, it should be noted that the temperature refers to the applied water temperature; the actual temperature at the epidermis/dermis interface will be lower for short exposures.

The success of this equation for describing thermal damage to tissue is in some respects surprising. The Arrhenius equation is derived to model the single step denaturation of a solitary molecule, yet in living tissue a staggering array of biochemical changes occurs when tissue burning occurs. Henriques (59) states:

"As to the number and the kinds of proteins involved, the specific nature of thermally induced reactions and the individual rate of each protein alteration, nothing can be stated. Further, it is probable that at any given hyperthermic level any one of these numerous protein alterations is potentially capable of producing cell death.

With no intention whatsoever of inferring that the thermal effects on living protoplasm can be ascribed to the alteration of any single protein, it is of value to make for the moment this extreme oversimplification..."

Despite its acknowledged simplifications; many scientists have utilized the Arrhenius model over the intervening years as a convenient approximation. The Henrique Arrhenius parameter values were derived for predicting skin blister formation due to irreversible damage to the dermis-epidermis interface. However the parameters have also been applied for predicting everything from full thickness skin burns (87), (49), to lesion formation in internal tissues (88). It is not clear whether such a broad application of these parameter values is appropriate, and the Arrhenius expression has been inconsistently applied. For example, one study assumes that a third-degree burn occurs if the damage integral at the base of the dermis exceeds a value of one (87); another study assumes that a third-degree burn occurs if the damage integral exceeds 10,000 at the epidermis/dermis interface (89).

There are several reasons for the confusion in the literature regarding the appropriate use of both the Arrhenius model and of specific parameter sets. These issues are introduced below, and will be discussed in detail later:

1. Different definitions of tissue burning have been used in model calibrations. Some studies use eventual tissue necrosis; others use such measures as optical property changes (coagulation), collagen denaturation, and vascular stasis. The eventual necrosis of the tissue is induced before the other, more severe, endpoints.

2. Different tissues have different responses to hyperthermia. For example, it has been shown that the bladder neck has a higher resistance to heat damage than the urethral mucosa (73). Tissues are capable of biological and physiological adaptations to repeated thermal stress (90).

3. The fate of burned tissue is not always immediately obvious. The zone of necrosis frequently grows to its maximum size three to seven days post-burn for a sufficiently damaging hyperthermic treatment (66),(40). Model calibrations based on immediate damage will result in underestimates of the final extent of tissue destruction. This observation limits the utility of *in vitro* experiments in assigning values to the thermal susceptibility of tissue.

4. Local tissue damage may not be independent of neighbouring tissue damage. An implicit assumption used in all Arrhenius analysis of deep tissue burns is that the extent of damage can be determined solely from the point temperature history of the tissue. This assumption has neither been experimentally verified nor rejected; this issue simply has not been addressed in the literature.

5. The extent of eventual tissue damage depends on the conditions during healing. An example of this issue is the difference in necrosis of dried partial thickness skin burns versus ones hydrated during the healing process (91). Necrosis deepened to 0.49 mm in dry tissues, while essentially no necrosis occurred in liquid covered burns. The use of anticoagulants, steroids and other pharmacological agents has been shown to affect the burn healing process (92),(46), (93). Post-burn cooling reduces edema and helps minimize progressive tissue damage (94), (95). Clearly the time-temperature threshold for "reversible" and "irreversible" damage is conditional; it must take into account the physical and biological environment of the tissue.

6. The extent of tissue regeneration may be important. In some medical procedures it may not be the depth of immediate or eventual necrosis, but the depth of eventual replacement with scar tissue that is important. Tissues vary in their regenerative capacity; heart muscle never regenerates naturally while skin readily regenerates (35). Therefore knowledge of the depth of either immediate or eventual necrosis may not be sufficient by itself to predict the treatment outcome.

Many of the above factors have not been explicitly considered during derivation of published Arrhenius function parameter values. The resulting confusion makes selection of the appropriate values for a given tissue and burn severity difficult, particularly for internal tissues where less data are available. The reasoned selection of parameter values and burn definitions requires a more detailed understanding of what happens when tissue is thermally damaged. In the following section several manifestations of thermal damage are discussed and are later utilized to develop a general technique for the prediction of thermal injury in tissues with unknown thermal response characteristics.

3.6 Modelling Skin Burns

Skin burn analysis dominates the burn prediction literature; a discussion of the science of thermal injury would be incomplete without introducing the topic of thermal injury to the skin. Skin burns have traditionally been classified as first, second or third degree (48). Henriques and Moritz damage integral values of 0.53, 1.0 and 10,000 at the epidermis/dermis interface have been associated with each respective degree of damage (96). In the first-degree burn the damage is reversible, the tissue is not permanently damaged. The only macroscopic sign of injury is an inflammatory response known as hyperemia. The blood supply of the dermis is increased, resulting in a reddish appearance to the skin. Some mild edema, a fluid build-up in the tissue, may also occur which results in a swelling of the affected tissue.

The second-degree burn is defined by the formation of skin blisters. The attachment of the epidermis to the dermis becomes weakened. Damage to the vascular system increases the permeability of blood vessels, resulting in a fluid build-up in the tissues. This edema then exerts a pressure that forces the epidermis apart from the dermis – resulting in blistering. Removal of the blister epidermis results in significantly greater tissue destruction due to desiccation of the underlying dermis.

The third-degree burn is defined as complete destruction of the epidermis and dermis. This includes the vascular system, the loss of which prevents edema since dermal blood supply ceases. Surprisingly third-degree burns are not very painful as the dermal nerves are also destroyed; though the healing process is apparently excruciating. In the third-degree burn, because the dermis base is destroyed healing must progress from the edge of the burn. The fourth degree burn, where destruction proceeds into the underlying body tissues, is also possible although the term is rarely used in the literature (48).

It is common to see the second and third degree burn redefined as partial and full thickness burns. The original 'degree' classification system lacks the ability to differentiate between moderate and severe burns (97). A second-degree burn would include everything from burns that produce mild blistering to burns that almost destroy the base of the dermis. The partial thickness burn, by including a measurement of the depth of tissue necrosis, allows for a more graded description of moderate burns. The technical difference between a partial thickness and a full thickness burn is that a partial thickness burn heals from underlying layers, while a

full thickness burn heals from the burn edge.

The threshold for thermal damage established by Henriques (59) has acquired legendary status. Although the Henriques damage integral is not directly relevant to predicting internal burns, it has a pre-eminent place in the literature that warrants a discussion of a number of issues that surround this Arrhenius expression. The activation energy was reported to be 150 kilocalories per mole, based on an assumed ideal gas constant of exactly two calories per degree per mole. Based on these values the formula for the rate of damage accumulation is presented as:

$$\frac{d\Omega}{dt} = 3.1x10^{98} e^{\frac{-75000}{T(K)}} \quad (3)$$

Unfortunately the value of 2.0 for the ideal gas constant is not accurate; a value of 1.98 is better. Although the difference is small the effect on the burn threshold time is quite large. If the R value of 2.0 is used, as was done by Henriques, the activation energy is calculated to be 150,000 calories per mole, which if converted to SI units is 627.6 kJ/mole. However if the combined activation energy and ideal gas constant ratio of 75,000 is multiplied directly by the R value of 8.3145 J/(K·mole), the activation energy is calculated to be 623.6 kJ/mole. At 45°C the former yields a second-degree burn in 587 minutes while the later causes irreversible damage in 129 minutes. In comparison, their data found that a second-degree burn occurred after 180 minutes. Clearly the Arrhenius expression is highly affected by the number of significant figures used for the activation energy.

A case can be made that the correct value is 623.6 kJ/mole, both because it agrees better with their experimental data and because it is likely that the value of 75,000 was derived during the fitting process and was later converted to the activation energy by multiplication with the utilized ideal gas constant value of exactly two. Unfortunately a value of 627 kJ/mole has become widely repeated in the literature (98),(99),(100) and has become a self-propagating error as new studies repeat parameter values without examining the original study of Henriques.

Henriques did not provide details about the linear regression performed on the Moritz data, only mentioning that calibration was performed using "standard graphical procedures". A new analysis of the Moritz data was recently performed which found different optimal values for the Arrhenius parameters (86). It is interesting that the new values predict thermal damage thresholds that are similar to those obtained using the activation energy of 623.6 kJ/mole. For example the new values predict thermal damage at 45°C after 184 and 135 minutes respectively (two sets of Arrhenius parameters were obtained over the tmperature ranges of 44-53°C and 44-55°C), closer to 129 minutes for 623.6 kJ/mole than to 468 minutes for 627 kJ/mole.

This recent re-analysis of the Moritz data used the least squares method for parameter estimation. For Arrhenius-style functions this method over-emphasizes the high temperature data points where the proportional error is largest. At high temperatures deviations from the transient expected temperature profile will have a significant effect on the depth of tissue burned. An improved method would use weighted residuals to emphasize the data points with the greatest certainty.

The Arrhenius function derived is deterministic in nature, i.e., predicted irreversible damage is certain to either occur or not occur. A better model might use a probabilistic approach to account for the effect of variation among and within subjects. For example, consider the Moritz data at 49°C for eight minutes: four pigs showed only scaling, one had small ulcers form and two had complete epidermal necrosis. The variation in burn depth can be quite large. Takata notes that "it was found that the large variations in the depths of irreversible damage pre-empted the establishment of well-defined constant depth-of-damage curves", and chose instead to simply utilize the mean depth of damage (101). The variability in hyperaemic reaction in humans was found to be so great that little could be inferred as to the applicability of porcine data to human reactions (43).

We performed an analysis of variance for the burn depth in rabbits, utilizing data from 27 burns in eight rabbits treated at 80°C for 14 seconds (102). With one exception each rabbit received multiple burns, allowing the estimation of inter-animal and intra-animal variability. The burn depth was 1.96 ± 0.84 mm; no difference in inter-animal susceptibility was detected ($P>0.25$). Depth of tissue necrosis was determined three days post-treatment. Interestingly there is almost four orders of magnitude difference for the estimated Henriques damage integral across the range of the confidence interval for the burn depth. It is not clear whether the variation in burn depth is due to an intrinsic difference in thermal susceptibility and healing rate, or if physical factors such as perfusion rate, stamp pressure or stamp temperature-drop rate are responsible. Additional experiments with improved control of physical factors

would be required to determine the variation of thermal susceptibility; one approach could establish a probabilistic model utilizing the damage integral in the probability density function. Although skin burn data are not directly relevant to predicting thermal injury in internal tissue, these results suggest that significant variation may be encountered in clinical hyperthermia and that published experimental results should be accepted cautiously as small discrepancies in reported burn depth can have major effects on the calibrated Arrhenius values.

3.7 Modelling Internal Burns

The traditional three-degree classification system has little relevance to internal burns. Since the categorization depends on anatomical structures specific to the skin, its use for internal burns is nonsensical. Although a third degree burn includes vascular stasis in the definition, the stasis occurs because the depth of necrosis has become sufficiently large to destroy the dermal capillary plexus. In other words, the classification system is a measurement of necrosis depth and is not directly relevant to the degree of damage at a single point. This inapplicability is also true for the partial and full thickness classification system. Despite these limitations it is true that increasing values of the damage integral at a given point are associated with increasing severity of injury expression. For example Sevitt (103) describes how the time delay until vascular stasis in guinea pig skin decreases as the hyperthermic exposure time increases at the temperatures used.

Many different coefficients for the Arrhenius function have been reported in the literature. Selecting the appropriate parameter combination requires an understanding of the merits and demerits of the reported values, as well as an understanding of the temperature range of applicability. The range of validity is particularly important for severe tissue damage thresholds calibrated at high temperatures.

One of the key concepts presented in this literature review is that it is important to make a distinction between damage integrals reflecting immediate necrosis and those calibrated for eventual necrosis. For example, describing the loss of collagen birefringence with an Arrhenius function is conceptually appropriate, although the use of first order kinetics may not be valid – multiple exponential functions have been proposed (104).

The use of the Arrhenius function for eventual tissue damage is conceptually more problematic. Certainly it is reasonable to assume that eventual cell death is precipitated by chemical changes that occur at the time of tissue burning. But the temporal separation of cause and effect allow other factors to influence the extent of tissue destruction. The best example of this concept is the tremendous difference a fluid environment makes in the eventual depth of necrosis of the partial-thickness skin burn (91). In such a scenario the conditions at one point, the skin surface, influence the outcome at a different point inside the tissue. The depth of eventual necrosis is not determined by passive factors such as biochemical or mechanical factors, rather physiological factors actively affect the burn outcome.

It may be possible to calibrate an Arrhenius function that predicts the depth of necrosis under the two conditions; this could be done by recording and analysing the time-temperature series at the lesion boundaries under a variety of applied skin surface temperatures. Conceptually the use of two different damage integrals depending on the healing conditions is incompatible with burn depth being determined solely by a simplistic set of chemical reactions that only occur at the time of burning. An improved model would take into account the initial depth of critically damaged tissue, the transport of water within the tissue, the initiation and later cessation of vascular stasis, and the migration and function of repair cells such as leukocytes and fibroblasts. Such a comprehensive model would be very complicated and would require a great deal of experimentation in order to calibrate the model parameters. Given the problems inherent in directly modelling the healing process, it is sensible to resort to Arrhenius function correlations for burn depth prediction – with the understanding that the values obtained do not represent a specific physical quantity.

3.8 Burn Classification Scheme and Parameter Selection for a Tissue with Unknown Thermal Damage Susceptibility

The response of tissue to thermal stress cannot be accurately predicted *a priori*; it must be determined experimentally. Susceptibility depends on the specific biochemistry of the tissue, a fact that is evident by the capacity of tissues to develop tolerance to mild hyperthermia (105), (106). It also depends on the physiology of the tissue and the healing capacity of the animal. If one wishes to model a tissue for

which the experiments have not been performed, such as for the thermal susceptibility of the uterus, then damage integral calibration presents a real problem. This section aims to develop a rational strategy for predicting the depth of tissue damage in a novel tissue.

The Arrhenius parameters chosen depend on the damage marker of interest. Based on concepts developed in this review of Arrhenius parameters and the pathophysiology of burning, three categories of damage thresholds are proposed for an arbitrary tissue. Each category will be associated with its own Arrhenius parameters. It should be emphasized that empirical evidence of adequate fit is required before the Arrhenius expression can be used with complete confidence (regardless of the choice of parameters).

3.8.1 Proposed Burn Classification Scheme

1) TYPE ALPHA – Guaranteed Immediate Necrosis

This category indicates the depth to which the tissue is certain to be destroyed immediately. Cells at the boundary of this zone die when the hyperthermic treatment is over. Cells outside of this area may die later, however cells within this zone are guaranteed to have been killed at some point during the treatment. Ideally it would be possible to calibrate the Arrhenius parameter with the boundary between immediate and delayed necrosis. Unfortunately the experimental work to establish this boundary has not been performed; the vitality of tissue immediately after hyperthermic treatment

has not been used to calibrate a damage integral. Although the desired function is not available, one may utilize data from other end-points that are associated with immediate cell death to estimate the time-temperature relationship that will guarantee the immediate death of the tissue. For example, optical coagulation or denaturation of the collagen of a tissue is almost certainly associated with other reactions that are immediately lethal.

In this classification scheme the depth of coagulation will, in practice, usually be the functional demarcation of the alpha burn depth. The use of optical coagulation as an indicator of guaranteed immediate necrosis is an approximation that is expected to prove convenient in the clinical setting. Although useful, the concept of guaranteed immediate necrosis is subtler than just the depth of visible colour change. Specifically all tissue that is coagulated is guaranteed to be immediately killed, but not all immediately killed tissue is guaranteed to be coagulated. Because of the absence of data on the depth of immediate necrosis, coagulation may be used as an imperfect alternative measure.

2) TYPE BETA - Eventual Necrosis

There is often a time delay between the initial insult and the cell death, as evidenced above where burn depths were found to be maximal 5 to 7 days following the initial injury. This proposed threshold represents the zone of "irreversible damage"; the tissue has been mortally wounded and though alive immediately after the burn, will die within several days. In the following weeks and months the living tissue will return, however this will be due to the infiltration and growth of new tissue,

the original tissue itself has died.

It should be stressed that whether the thermal injury is irreversible or not depends on the healing conditions of the wound. For example the use of anti-inflammatory measures may change the values of the Arrhenius parameters. This is the mildest form of thermal injury in this classification system. No tissue death will occur deeper than this boundary, although further from the heat source the tissue may have been sub-lethally damaged.

The results of this literature review suggest that the maximum depth of necrosis will not extend beyond the hyperemic 'red zone', and in at least one tissue the depths of the red zone and eventual necrosis were equal. Thomsen investigated this quantitatively for the rat liver subjected to a 10 second pulse from a 9 watt Nd:YAG laser (84). The red zone diameter was strongly correlated with the diameter of the necrotic region as measured three days later, although data from only four experiments was presented (see Figure 11).

3) TYPE CHI – Scar Tissue Formation

In some cases the parameter of interest is the depth of formation of scar tissue. For example, in a cauterisation treatment the procedure is a failure if the target tissue regenerates following necrosis. The success of the procedure is neither determined by the depth of the eventual necrosis, nor by the depth of immediate necrosis. Success depends on the depth to which scar tissue has replaced normal tissue.

Unfortunately no attempt to correlate the depth of scar tissue formation with burn severity has been observed in the literature. It is not known if it is even possible to correlate this definition with an Arrhenius function, given the large temporal separation between cause and effect and the possible influence of neighbouring tissue in the healing process. It is likely that the appropriate parameter value would be specific to individuals and their propensity toward scar tissue formation. It is known that some tissues are more prone to scar tissue formation than others. In the myocardium the depth of the chi-burn threshold is likely to be very close to the depth of alpha burns where tissue regeneration is negligible, all tissue that is thermally damaged is replaced with scar tissue. In other tissues the volume of scar tissue will be much smaller than the volume of injured tissue, for example in damaged liver only a small nodule of scar tissue remained inside the original zone of immediate necrosis (66).

3.8.2 Burn Classification Scheme Parameter Values

A review of the literature concerning the thermal damage susceptibility of internal tissue suggested that no single damage integral would predict a given end-point in all tissues. There is simply too much variability, both in the immediate damage caused by hyperthermia and the physiological response and healing process that follows. In the absence of experimental data the most rational approach for an unstudied tissue is to utilize a range of parameters that are likely to incorporate the actual damage integral. Therefore we propose to utilize three Arrhenius functions for each burn classification, a function to represent the least and most severe extent of tissue damage that might cause the outcome of interest, as well as an intermediate

"best guess" Arrhenius function.

Three graphs have been prepared that collate information from many studies regarding the thermal dose required to induce various damage end-points in many different tissues. The first graph (Figure 12) compares the chosen alpha burn parameters to known data points and equations describing severe forms of thermal damage indicative of immediate cell death. The second graph (Figure 13) performs the same task for the beta burn and indicators of eventual necrosis and mild damage. Figure 14 combines the proposed alpha and beta burn thresholds onto a single graph. Data were obtained from two sources, from published individual time-temperature combinations and published equations for thermal damage prediction (described in Appendices A and B). The individual data points are from experiments where the time-temperature series at the location of interest was known with confidence. In many studies this condition of temperature certainty was not met, for example there were studies that elevated the temperature some distance from the location of interest, fixing the thermal boundary condition for a set temperature and time. In principle the internal temperatures could be derived mathematically, however this introduces additional uncertainty (due to variability of the tissue perfusion rate, thermal conductivity and tissue geometry) and so data from these studies were not incorporated. The damage prediction equations obtained from the literature have only been presented over their individual range of validity.

Table 3 – Proposed Arrhenius values for determining the plausible thermal insult thresholds for eventual necrosis and guaranteed immediate necrosis. Lower limit refers to the least thermotolerant boundary, and the upper limit reflects the boundary most resistant to high temperature.

Threshold	Alpha Burns – Guaranteed Immediate Necrosis		Beta Burns – Eventual Necrosis	
	Pre-Exponential (1/s)	Activation Energy (kJ/mole)	Pre-Exponential (1/s)	Activation Energy (kJ/mole)
Lower limit	1.5×10^{66}	430	1.0×10^{100}	623
Median	5.0×10^{50}	340	1.0×10^{99}	623
Upper limit	1.5×10^{43}	300	1.0×10^{98}	623

Table 3 lists the proposed Arrhenius values for predicting the depth of alpha and beta burns. Unfortunately there is neither a sufficient amount nor a sufficient quality of data for a statistical analysis; the proposed burn thresholds have been fit by hand. A rigorous approach would be difficult, since many different tissue types would have to be analysed for a consistent end-point; additionally a statistical parameter selection procedure would optimise for the most commonly reported tissues at the expense of rarely investigated tissues. Additionally each data point or damage function may represent results obtained from different numbers of replications, a factor that would have to be included in any data fitting performed.

The selection of parameters for the alpha and beta burn functions was performed by hand, and was conducted with the aim of including all data points and Arrhenius functions within the boundaries for the burn type. In the case of the beta burn it was found that the activation energy used by Henriques was in excellent agreement with the data points and damage integrals associated with eventual necrosis. The damage prediction functions obtained in the literature for internal tissues generally assume that the time required for eventual necrosis approximately

halves for every degree of temperature increase. This relationship holds approximately true for the Henriques parameter values, and in the absence of contrary data it was decided to retain this temperature relationship. The thresholds for eventual necrosis were obtained by adjusting the frequency factor but not the activation energy of the Henriques damage integral. However we acknowledge that there are limited data available at temperatures greater than 50°C, and that these functions should be considered tentative at temperatures greater than this.

Estimating the range of thermal conditions that induce alpha burns is more difficult than for beta burns. Unfortunately few investigators have examined the rate of optical coagulation or birefringence loss over the complete range of supra-physiological temperatures. The presence of critical temperatures, where there is a change of values for the Arrhenius parameters or function form, is probable. Indeed for some alpha burn indicators with low activation energies a critical temperature is necessary for extrapolation to low temperatures; otherwise these functions will predict thermal damage within hours at the normal physiological temperature of the organism. Estimates for alpha burn thresholds should be considered preliminary until more data is obtained over a wider range of temperatures.

3.9 Relation of Burn Severity Categories to Histochemical Staining Depth

The most frequently reported expression of thermal damage in endometrial thermal ablation is not coagulation, collagen denaturation or eventual tissue necrosis; it is the depth of histochemical staining. Hematoxylin and eosin will stain tissue

components such as myelin, elastic and collagenic fibres, muscle striations and mitochondria, but its most common application is as a nuclear dye, and is used to detect disrupted cells (24). The diaphorases are dehydrogenase enzymes which catalyze the dehydogenation of nicotinamide adenine dinucleotide reduced (NADH) and phosphate reduced (NADPH). Dehydrogenase activity is demonstrated using tetrazolium salts, which accept the hydrogen released from the substrate (107). The reduced tetrazolium salt then forms insoluble and highly visible microcrystalline deposits. In the review of endometrial thermal ablation it was nitroblue tetrazolium (NBT) that was used. Tissue without functional diaphorases will not stain and are considered nonviable (24); it is a marker of irreversible cell damage (29).

Comparison of the depth of vital staining to the depth of alpha or beta thermal damage is complicated by the lack of published Arrhenius values for the thermal boundary of histochemical stains. The detection of disrupted cells by Hematoxylin and eosin staining suggests that this method detects the depth of thermal coagulation, although this hypothesis has not been confirmed experimentally. It is mentioned by Neuwirth et al. that the oxidative enzymes, those stained by NBT, are destroyed after exposure to 55°C for 60 seconds (29). However the source of this information could not be found in the literature cited (107). In comparison, at this temperature, the lower time threshold for an alpha burn is 186 seconds and the upper time threshold for a beta burn is 18 seconds. It is suggested therefore that the boundary for NBT staining lies between the lower alpha and upper beta burn threshold. This contention is supported by the results of the TRS clinical trials. It was observed that diaphorase negative depth was slightly outside the depth of visible coagulation observed prior to

staining, and well inside the depth of the red zone (suggesting that the loss of diaphorase enzymes are not the cause of eventual necrosis in tissue).

Quantitative experiments are recommended to determine whether the depth of vital staining may be determined by an Arrhenius expression, and if so what activation energy and rate constant would be appropriate. It is also recommended that damage thresholds in addition to the depth of vital staining should be reported. Specifically the depth of coagulation prior to staining should be noted, and the depth of the red zone should also be reported as this may indicate the depth of eventual necrosis.

3.10 Burn Depth Algorithm Implementation

The Arrhenius damage integral was integrated utilizing a trapezoidal method, where the rate of damage accumulation used is an average of the rate at the start and end of the time step. A linear interpolation method is used to estimate the burn depth (where $\Omega = 1$). The bordering cells of the burn threshold are determined, where the damage integral is less than or greater than one. The burn depth is then estimated using the following formula:

$$x_{thr} = x_i + (x_{i+1} - x_i)\left(\frac{1-\Omega_i}{\Omega_{i+1} - \Omega_i}\right) \quad (4)$$

Where:

x_{thr} is the burn depth
x_i is the last cell from the interior that is supra-threshold
x_{i+1} is the first cell from the interior that is sub-threshold
Ω_i is the damage integral

Burn depths were reported in the initial, undistended coordinates. As the uterus expands around the inflating balloon, the tissue become thinner due to conservation of volume considerations. This effect is most pronounced at the cavity surface. Therefore a burn to a certain depth in a distended cavity will appear deeper when the uterus returns to its undistended form.

Chapter 4: Model of Endometrial Thermal Ablation

So as to address the objectives of the project, a mathematical model was developed of endometrial thermal ablation that includes heat transfer from the balloon fluid to the endometrium and through the uterine wall.

This chapter describes the mathematical model that was developed. The following two algorithms will be described first: (1) Calculation of the temperature profile through the uterine wall, and (2) Estimation of the balloon fluid temperature. Next the numerical techniques used to solve the equations will be described and finally the actual computer program will be presented (computer code can be found in Appendix E).

4.1 Algorithm for Calculating Temperature Distribution in the Uterus

Basic Heat Transport Equation

The calculation of heat transfer in inanimate objects is well understood using the Fourier heat conduction equation for an isotropic body:

$$\frac{\partial T}{\partial t} = \frac{k_t}{\rho_t c_t} \nabla^2 T \quad (5)$$

This equation cannot readily be applied to living tissue because of the convective

effect of blood flow. In the hyperthermic situation blood flow will tend to normalize the tissue temperature towards the core temperature, since the incoming blood will have been thermally equilibrated during passage through the arterial system. In principle one could solve the temperature distribution directly through a combination of conduction and convection terms in the heat equation in the blood vessels, and only conduction terms in the interstitial spaces. The computational demands of such a model would be enormous for even a small volume of tissue; however an even larger problem is the lack of detailed, quantitative information regarding the fine structure of blood vessels in the majority of tissues – including the uterus.

Given the tremendous difficulties inherent in a direct solution, attempts have been made to derive approximations. The first of these is Pennes' bio-heat equation (108). This model treats the blood supply as a distributed heat sink. At any given point in the tissue, blood appears, exchanges heat with the tissue, and then is removed. Note that in this model blood flow is a scalar quantity, it does not have a direction. Although this model may seem very simplistic, it has been fairly successful in describing tissue temperature profiles. A diagram representing the application of the Pennes heat equation to a control volume is presented in Figure 15. Essentially the equation states that the rate of heat accumulation is equal to the difference between the heat flux entering and leaving the control volume, plus the heat exchanged with the blood and added through metabolic activity, i.e.,

$$\frac{\partial T}{\partial t} = \frac{k_t}{\rho_t c_t}\nabla^2 T + \frac{\omega_b \rho_b c_b}{\rho_t c_t}(T_b - T) + \frac{q_m}{\rho_t c_t} \quad (6)$$

where:

c_b is the blood heat capacity
c_t is the tissue heat capacity
k_t is the thermal conductivity
q_m is the metabolic heat generation rate
T is the local temperature
T_b is the blood temperature
t is time
ρ_t is the tissue density
ρ_b is the blood density
ω_b is the rate of blood perfusion

The Pennes equation has been used many times throughout the literature(99),(109),(110), (111), (112). The ubiquitous nature of the Pennes equation is an indication of the lack of viable alternatives; it is the most popular even though the Pennes equation has a number of limitations. It cannot accommodate the effect of counter-current heat transfer between small arteries and veins, major vessels or possible pre-equilibration of the incoming blood. The assumption that the majority of heat exchange occurs at the level of the capillaries has been shown to be incorrect, it has been demonstrated that thermal equilibration occurred prior to the blood reaching the capillary beds (113). There have been several alternative models proposed (114); however models that could yield an improved temperature distribution estimate would require detailed knowledge of the microvascular anatomy and physiology of the uterus. For example, the Weinbaum-Jiji model can only be applied in situations where the vascular anatomy and the blood velocities are known, and the modelling volume includes many vessels, and the vessel equilibration length is small compared to the

actual length of the vessel (115). In the absence of the required information for the human uterus, the Pennes equation is the best option for the analysis of endometrial thermal ablation.

Geometry

A hollow sphere was used as the conceptual model for the uterus. Although the deflated uterus cavity takes the shape of a flattened "V", it was observed with specimens obtained by hysterectomy that the inflated balloon would cause the cavity to conform approximately to the approximately spherical shape of the balloon. The assumed geometry of the model is presented in Figure 16. The thickness of the uterus was selected such that the model could be considered semi-infinite. The thickness was incrementally increased until further increases did not result in any predicted significant temperature elevation. During the treatment period, the balloon was assumed to be in complete contact with the tissue. Following treatment the balloon would be removed and the cavity in reality would reassume a flattened "V" shape, resulting in an effectively symmetrical temperature distribution through both uterus sides; therefore each section of endometrium and myometrium may be assumed to be insulated on the cavity boundary. In the model the cavity was assumed to return to its original radius and an insulated boundary condition was implemented.

Boundary Conditions

In principle one would have to model thermal conduction from the uterus cavity to the epidermis to obtain the theoretically perfect temperature time-series. However this approach is unnecessary and computationally wasteful; in practice there is minimal temperature elevation within a centimeter of the outside of the myometrium (see Figure 17). It is assumed that the fluid of the peritoneum is maintained at body core temperature (37°C).

$$T_{\infty} = 37^{\circ}\mathrm{C} \quad (7)$$

Either of two boundary conditions was used for the balloon cavity surface, the interior boundary condition, depending on the nature of the thermal ablation device. In modelling of the Thermachoice™2 device the heat transfer coefficient was considered effectively infinite, and a constant balloon-fluid temperature was used as the inside boundary condition.

$$T_{\text{interior}} = T_{\text{balloon}} \quad (8)$$

If the balloon fluid is not well mixed, then the full equations of continuity, momentum and energy inside the balloon would have to be solved simultaneously, which would be effectively intractable. A more tractable method was used that assumes well-mixed fluid in the central bulk of the balloon and a stagnant boundary layer at the inside balloon wall. The concept of a stagnant boundary layer is a simplification, there is not actually a sharp zone of fully-mixed and unmixed fluid;

rather the magnitude of mixing will continuously decrease from the fully mixed interior to the no-slip boundary condition at the balloon boundary. This complicated convection process are lumped into a single parameter, the heat transfer coefficient:

$$\left.\frac{\partial T}{\partial x}\right|_{\text{interior}} = -\frac{h}{k_t}\left(T_{\text{balloon}} - T_{\text{interior}}\right) \quad (9)$$

The heat transfer coefficient can be used to estimate the thickness of the hypothetical boundary layer, using the following formula (neglecting differences between the thermal conductivity of the balloon fluid and the balloon material).

$$\Delta x_{boundary} = \frac{k_L}{HTC} \quad (10)$$

4.2 Modifications to the Perfusion Rate

Most solutions of the Pennes equation (Equation 6) assumed a constant blood perfusion rate, which is not expected to be the case in endometrial thermal ablation. There are a number of important phenomena that can affect the perfusion rate, and appropriate mathematical approximations were developed. Factors that effect blood perfusion during endometrial thermal ablation include balloon pressure, thermally induced perfusion rate increases and the loss of circulation due to thermal damage to the vascular network.

4.2.1 Balloon Pressure and the Stress Distribution in the Uterus

The balloon pressure affects not only the blood perfusion rate, but also the temperature at which tissue water boils (dealt with later). The need for its inclusion in the model is apparent from the results of Vilos et al. (116). They found that there was only 44% satisfaction when patients were treated at a balloon pressure of 80 – 150 mmHg, while patients treated at 151 to 180 mmHg had an 80% probability of satisfaction. The increase in patient satisfaction with greater treatment pressure can probably be attributed primarily to an associated decrease in blood perfusion and hence higher uterine temperatures (and also better balloon-uterine wall contact).

A solution for the stress distribution in a thick-walled hollow sphere (117) was found that was appropriate for the geometry of the computer model, and this was used to approximate the stress distribution in the wall. This is an equilibrium model that assumes spherical symmetry in a homogenous material; therefore it will be assumed that the uterus reacts to pressure changes instantly. Although the model may calculate the tangential stress (tension for higher internal pressure); this feature is not relevant to the thermal model and is not included below in the model description. Thus, the normal stress is given by:

$$p_{rr} = -\sigma_{rr} = -\left(\frac{1}{1-\psi^3}\right)\left[\psi^3\left(1-\frac{R_o^3}{r^3}\right)p_i - \left(1-\frac{\psi^3 R_o^3}{r^3}\right)p_o\right] \quad (11)$$

$$r' = r + ar + \frac{b}{r^2} \quad (12)$$

$$a = \frac{p_i R_i^3 - p_o R_o^3}{(3\lambda + 2\mu)(R_o^3 - R_i^3)} \quad (13)$$

$$b = \frac{R_i^3 R_o^3 (p_i - p_o)}{4\mu(R_o^3 - R_i^3)} \quad (14)$$

$$\lambda = \frac{E\nu}{(1+\nu)(1-2\nu)} \quad (15)$$

$$\mu = \frac{E}{2(1+\nu)} \quad (16)$$

Where:

p_{rr}=local pressure (kPa)
σ_{rr}=radial stress (kPa)
R_i=pre-deformation internal radius (mm)
R_o=pre-deformation external radius (mm)
P_i=interior pressure (kPa)
P_o=exterior pressure (kPa)
ψ=Ri/Ro
r =undisplaced position (mm)
r'=displaced position (mm)
E=elastic modulus (kPa)
ν=Poisson's constant

It should be emphasized that in this model the elastic parameters (E and ν) do not affect the radial stress felt at the initial position. These parameters do have an effect of course; they determine the displacement in response to applied pressure. For example a steel sphere would expand less than a rubber sphere for the same internal pressure, but the stress distribution at any original, undistended location would be the same. From a treatment modelling perspective, it is the displaced uterus volume that we are interested in, therefore the initial cavity radius is selected to yield the desired displaced volume.

Figure 18 illustrates the typical pressure distribution expected for an average uterus cavity (11 mL), expressed both in terms of the initial and displaced position. Points closer to the cavity surface become compressed, while points on the outside of the uterus are less affected by the internal pressure. Figure 19 illustrates the effect of using increased balloon pressure on displacement and pressure distribution; note the compression of the interior shells. The effect of compression is important for calculating the burn depth in the undistended uterus cavity. Given the same temperature profile and exposure time, a compressed tissue will have experienced a greater burn depth upon relaxation (decompressing the tissue to its initial state) than if that tissue was not compressed at all.

4.2.2 Estimating the Effect of Pressure on Blood Perfusion

It is assumed that it is the radial compression stress that determines blood perfusion changes. A blood vessel that runs tangentially to the cavity surface would tend towards collapse if the compression force exceeded the blood pressure (see Figure 20), neglecting additional structural support of the vessel wall. Both the radial compressive force and the tangential tension force would contribute to vessel collapse. A vessel running radially (outwards or inwards) would tend to be held open; however such a vessel must either lead to or come from a vessel running tangentially. Therefore it is assumed that it is the tangential vessels that determine the extent of vascular stasis. A similar argument may be applied to gas bubbles in the uterus wall, the elevation of boiling temperature is determined by the sum of the ambient atmospheric pressure and the local force of compression.

As blood travels through the vascular system the pressure is reduced, a process known as head loss. Mean arterial pressure is approximately 100 mmHg, while in capillaries it is only 25 mmHg (118), both of which are low enough to be affected by a balloon pressure of 180 mmHg. An experiment examining blood flow in compressed spinal nerve roots found that a pressure applied to the capillaries of 40 mmHg would stop blood flow, while 127 mmHg of pressure was required to stop blood flow in arterioles(119). Note that in this experiment the mean arterial pressure was 150 mmHg. In contrast Vollmar et al. (120) found that arteriolar flow in striated hamster muscle tissue ceased at 25.6, 28.3, 34.5 and 44.4 mmHg of applied pressure in vessels of 20, 20 to 40, 40 to 60 and greater than 60 μm in diameter respectively. They also found that blood flow ceased in 50% of muscle capillaries with an applied pressure of 12 mmHg.

The Pennes approach to modelling blood flow treats the vascular system as a uniform "sink" term. This approach greatly simplifies calculation, and is very useful for tissues where the vascular structure is poorly understood. However the simplicity of this model is a liability for creating a pressure-induced perfusion reduction term. It is not clear from the Pennes equation which vessels dominate the heat transfer process, and therefore it is not clear what calibre of vessel should be used to generate the stasis threshold. Chen and Holmes (113) found that thermal equilibration in muscle occurred prior to the blood reaching the capillary beds. Another mathematical model of heat transfer in tissue predicted that all thermally significant vessels in muscle are larger than 50 μm in diameter (121). Based on this information, we selected a

pressure of 45 mmHg as the critical pressure for blood flow cessation, from the data of Vollmar for arterioles greater than 60 μm in diameter (120).

To determine the blood perfusion modification, a pressure factor similar to the approach used by Persson et al. (34) was used. In this model of endometrial thermal ablation the uterus was divided into many zones, and the stress distribution for each layer was calculated. This pressure factor was calculated using equation 17 and applied as a multiplier to the base perfusion rate. One significant difference is that their model utilized the arterial pressure of 140 mmHg, much higher than the pressure required to induce stasis in the arteriolar or capillary system. The pressure factor is given by:

$$PF = \begin{cases} \dfrac{45\ \text{mmHg} - P_{tr}}{45\ \text{mmHg}} & \text{if } P_{tr} < 45\text{mmHg} \\ 0 & \text{if } P_{tr} > 45\text{mmHg} \end{cases} \quad (17)$$

Figure 21 illustrates calculated perfusion pressure factor with distance using Equations 11 and 17. Perfusion is predicted to cease over approximately the first 5 mm from the cavity surface in the displaced uterus; the perfusion rate is also significantly reduced in tissue beyond this point. Since the endometrium is rarely thicker than 5 mm, it is suggested that only myometrial blood perfusion is able to affect treatment outcome during thermal ablation treatment at standard balloon pressures, and therefore the endometrium blood perfusion term was assumed to have no effect.

4.2.3 Estimating the Effect of Temperature on Blood Perfusion

It is well known that the perfusion rate rises during exposure to hyperthermia; the organism automatically flushes the affected area with blood in an attempt to cool the tissue and minimize thermal injury. Although some general information is available, no equation of state was found in the literature that would predict how local temperature effects blood perfusion to the uterus. A simple algorithm for estimating the perfusion increase was developed, based on information gleaned from several papers. This algorithm is considered an approximation; it is certain that the full complexity of temperature induced perfusion changes is not included. However it is felt that the failure to include this perfusion modification factor (i.e. constant blood flow rate) would cause even greater inaccuracy than imperfections in the model.

Prior to presenting the perfusion modification equation, the studies used in its derivation will be reviewed to provide a sense of the difficulties involved in successful modelling of the perfusion response. Xu et al. (122) measured the perfusion rate in the canine prostate during radiofrequency heating (see Figure 22). Several interesting phenomena should be noted. First there appeared to be a time lag between the increase in temperature and the perfusion response. Unfortunately data was available only in five-minute increments. Therefore it is not possible to say what the actual time lag is, only that the delay was between five and ten minutes at 10 W treatment power and was less than five minutes at 15 W. At constant power, blood perfusion rate to the area was observed to oscillate resulting in oscillation of tissue temperature. The authors suggest that the blood perfusion control system might be modelled

utilizing both the temperature and the rate of change of temperature with respect to time.

In the field of microwave-induced thermal therapy, the qualitative response of the tissue has been found to depend on the magnitude of the heating power applied. Roemer et al. (123) identified four different temperature responses to different levels of applied microwave energy. Figure 23 provides examples of each response, where the effects of changes in the perfusion rate are detectable as oscillations in the temperature. The first response at low power is a simple monotonic approach to the steady-state temperature. The second response occurs if the tissue temperature rises above a "critical temperature" which invokes an increase in perfusion rate that decreases the temperature. In this response form, the temperature overshoots the eventual steady-state value. As the applied power is increased further large oscillations of the temperature occur. One of the responses involves decaying oscillations around the steady-state temperature, while the other response never converges to an equilibrium temperature.

Very large increases in the perfusion rate have been observed in rat skin and muscle when heated at temperatures greater than 44°C, up to nine-fold over the original perfusion rate in muscle (124) (see Figure 24). The data from this experiment suggest that the perfusion rate responds more quickly at higher temperatures, in skin the perfusion rate had already peaked by thirty minutes and was decreasing after two hours of exposure to either 44 or 45°C, while at lower temperatures the perfusion rate was continuing to increase. The cause of this time-response effect is unknown; it may

be a reaction to the greater stimulus, or due to the superimposition of vascular stasis effects on a common response rate. Unfortunately data were obtained at fifteen-minute intervals, and so the speed of response at 45°C in skin cannot be quantified in greater detail.

Dudar and Jain (125) examined the microcirculatory response to hyperthermia in New Zealand white rabbits that were surgically implanted with small observation chambers. This chamber became surrounded by fully repaired tissue within six weeks, after which the tissue was scheduled to be subjected to contact hyperthermia and the blood flow in individual vessels was quantified with an optical photometer. The time required to reach the maximum perfusion rate increased from 40 to 46°C, and decreased once the temperature exceeded this range (see Figure 25). This finding is not in agreement with other studies, and the authors acknowledge that in their literature review this was the only case where an inverse relationship between temperature and perfusion response time had been found. It should be mentioned that a positive correlation between temperature and response time was only observed below 46°C. The maximum perfusion multiplier was also bimodal, increasing to the maximum observed perfusion multiplier of 6.8 at 45.7°C and decreasing at greater temperatures. One consideration is that the normal physiological temperature is approximately 30°C for the rabbit ear, the quantitative relationship for elevated perfusion may not apply to internal tissues maintained at 37°C.

The studies presented thus far have utilized temperatures that are within a few degrees of normal physiological temperatures. Unfortunately data at higher temperatures (>50°C) are scarce; this lack of data is problematical for modelling endometrial thermal ablation where the applied temperature is very high. Taheri et al. looked at the effect of scalding on the blood flow rate of the femoral artery in the canine hind paw (126), (127). In one study the blood flow had increased 3.5 times over the perfusion in the uninjured limb (where the perfusion rate remained essentially unchanged) following immersion of the limb in boiling water for five seconds (126). The increase in perfusion rate was complete within five minutes, the minimum time interval used for data acquisition. The perfusion rate remained elevated throughout the three-hour post-trauma observation period.

This experiment was repeated later with more temporal detail recorded in the immediate post-burn period (127). There was an immediate three-fold increase in femoral artery blood flow to the injured hind limb. The perfusion rate was increased further to five-fold by five minutes following scalding. The perfusion rate plateaued at a slightly smaller level in the following two-hour observation period. It should be noted that the perfusion increase recorded refers to the whole limb; local deviations from the mean blood flow are anticipated.

Based upon the reviewed literature, one may speculate on the form of the equations that may be used to approximate the perfusion response to hyperthermia. Several important guidelines are presented below:

- There appears to be a time delay between the stimulus (increase in temperature) and the response (increase in blood flow).
- There is a maximum perfusion rate, occurring when vasodilation is complete. The maximum perfusion multiplier of the uterus is unknown.
- The magnitude of the perfusion increase is very complicated and the correct form of the function is not known. However it is generally accepted that higher temperatures induce a greater perfusion response.

These guidelines suggest that the perfusion response may be modelled, as a gross approximation, using two exponential functions. The first function describes the relationship between the temperature and the steady-state perfusion multiplier; in such a formulation the perfusion multiplier asymptotically approaches the physiological limit. An exponential function will result in an approximately linear relationship between the perfusion rate increase and the temperature near physiologic levels; therefore in the lower temperature limit this model is consistent with the published linear relationship between perfusion and temperature (128).

The second exponential function accounts for the time delay between stimulus and response; in this formulation the actual perfusion multiplier is assumed to monotonically approach the steady-state limit. Where the temperature is not constant

these equations are evaluated over each time step.

The equations are presented below:

$$\omega_{\infty} = \omega_{\max} - (\omega_{\max} - \omega_0)\exp[-\theta(T(t) - T_b)] \quad (18)$$

$$\omega(t) = \omega_{\infty} - (\omega_{\infty} - \omega_0)\exp[-\phi t] \quad (19)$$

where:

$\omega(t)$ is the blood perfusion rate at time = t
ω_0 is the normal blood perfusion rate
ω_{∞} is the steady-state blood perfusion rate
ω_{max} is the maximum possible blood perfusion rate
T(t) is the temperature at time = t
T_b is the blood temperature (the normal physiological temperature)
θ is the temperature sensitivity factor ($°C^{-1}$)
ϕ is the time response factor (s^{-1})

The above formulation implicitly assumes that the perfusion rate adjustment is determined locally. Although fine-scale perfusion changes have not been investigated, Roemer et al. (123) found that perfusion induced temperature oscillations induced by hyperthermia at 1.5 cm depth did not affect the perfusion rate at 4.5 cm depth in canine muscle. However that is still a depth difference of 30 mm, which is far greater than the depth of temperature elevation observed during endometrial thermal ablation. Certainly the concept of local perfusion adjustment is consistent with the observation that a burn generally consists of a central coagulated area surrounded by a hyperemic ring, itself surrounded by unaffected tissue (35). Steep blood flow gradients have been observed within hyperthermically treated muscle; this finding is suggestive that the perfusion response is indeed highly localized (129).

Several features that have been observed in tissue have not been included due to a lack of replication and the unavailability of calibration data. Sekins et al. (129) suggest that the blood perfusion below a critical temperature increases only in accord with the increase in tissue metabolism and hence tissue oxygen requirement. Once the critical temperature (~41.5°C) is exceeded it is proposed that the blood flow then increases rapidly, as was demonstrated in their experiment with microwave induced hyperthermia in human thigh muscle (see Figure 26). The concept of a critical temperature for perfusion enhancement is consistent with data obtained from rat skin (Figure 27) following thirty minutes of hyperthermia (124). Dudar and Jain however did not find a critical temperature effect, although the data set was too small to be conclusive. Specifically of the five treatments below the critical temperature, three showed an elevated perfusion rate and two did not.

This formulation does not include the additional perfusion response that may occur due to the rate of temperature change. Although this effect is suspected to be important, there simply isn't an experimental basis available for parameter estimation. The temperature dependence of the speed of perfusion response has also not been included. Any of these effects on the perfusion rate could significantly impact the results of simulated hyperthermia; however their inclusion cannot be justified based on existing information.

The maximum perfusion multiplier will be assumed in this model to be nine times the nominal value, based on the maximum perfusion multiplier observed in rat

muscle subjected to hyperthermia (124). Little data are available to quantify the θ-factor for temperature sensitivity, and what is available is not in quantitative agreement. Xu et al. (122) had observed in the canine prostate a perfusion increase of 3.5 and 4.0 times at 41.5 and 43.1 °C respectively, although it should be mentioned that these data conflict with the unproven concept of a critical temperature at 41.5°C. Based on the information provided by the canine prostate (122) the best-fit θ-factor value is tentatively assumed to be 0.078 $^{\circ}C^{-1}$ (determined by a transformed least-squares method). The relationship of the steady-state perfusion rate multiplier to the applied temperature is presented graphically in Figure 28.

Controlled calibration data for the ϕ-factor for time response are not available; what data are available are not in quantitative agreement. In general the reviewed literature indicates that the perfusion rate will stabilize within ten minutes at high temperatures and within tens of minutes at temperatures close to physiological levels. In some cases the perfusion response was fast at near-physiologic temperatures, including the data of Xu et al. (122) used to calibrate the θ term. Because the endometrial ablation process takes less than ten minutes, the assumption was made that the short time-scale response is important to include. Additionally in the data of Dudar and Jain (125) the time until maximum perfusion was typically ten minutes, consistent with a general fast response, with the exception of the temperature range of 44 to 46°C.

Significantly Andersen et al. (31) found that the serosal temperature during endometrial thermal ablation tended to reach a maximum after ten to twelve minutes of treatment, decreasing 1-2°C afterwards. It would be tempting to use this time directly to calibrate the ϕ-factor; however the serosa is separated from the thermal balloon by approximately twenty millimeters of perfused tissue, and the cumulative effect of a delayed perfusion response progressing through the tissue and affecting the temperature distribution needs to be considered. It was found in the same experiment that the serosal temperature of a patient treated for eight minutes did not change; therefore the outer tissue layers where the perfusion response occurred would have had only several minutes of exposure to elevated tissue temperatures. In light of the Andersen data (31), and the other reviewed studies (126),(127), a tentative ϕ-factor value of 0.0046 seconds (equivalent to a response half-time of 2.5 minutes) was selected.

4.2.4 Vascular Stasis due to Thermal Injury

Thermal damage to the vascular network will result in vascular stasis, the cessation of blood flow. Thus, burn-induced reduction of the blood perfusion rate was included in the Pennes bioheat equation for the model predictions to improve accuracy. Although a significant amount of information is available for the occurrence of stasis in tumors, it is known that tumors have a significantly lower thermotolerance than normal tissue and cannot be properly used for calibration (125). Quantitative information was found in two studies using normal (non-cancerous) tissues that

microscopically examined the patency of the microcirculation during hyperthermia. Ross and Diller (55) examined the vessels in the hamster cheek pouch at temperatures ranging from 60 to 85°C. They found the following temperature-time relationship would result in permanent stasis in 95% of vessels within twenty seconds after a burn:

$$t = \exp[0.153(85 - T)] \quad (20)$$

Where:

t is the contact time (s)
T is the contact temperature (°C)

Dudar and Jain (125) conducted a similar study in the rabbit ear at temperatures closer to physiological levels. Individual blood vessels were visualized and the time until vascular stasis was recorded (see Figure 25). The target temperature was maintained for one hour and it was found that stasis would not occur within this period if the temperature were lower than 47.1°C. Utilizing their data, we found that the following Arrhenius function could adequately describe the time until stasis occurs :

$$t(s) = \left(8.3x10^{29} \exp\left[\frac{-204{,}054}{RT(K)}\right]\right) \quad (21)$$

Although this function was evaluated over a small temperature range (47.1 to 52.4°C), it extrapolates to approximately the same time-temperature combinations Ross and Diller found at temperatures between 60 and 85°C (55). This correspondence is presented in Figure 29; because of the approximate

agreement of these functions the Arrhenius function derived for the Dudar and Jain data (125) will be used in the endometrial thermal ablation model to predict stasis. The stasis function parameter values used are considered tentative until data can be obtained across a broader range of temperatures using an identical experimental protocol. For example, the present function predicts stasis occurring before eventual necrosis at temperatures below 47°C. This could present a problem for low temperature exposures, however the treatment time of endometrial thermal ablation is much shorter than required for stasis at this temperature and therefore the low temperature validity problem may be ignored. Certainly one would expect the occurrence of vascular stasis to occur at a higher temperature than general thermal injury; hyperaemia, the hemorrhagic ring characteristic of internal burns, would not be possible if vascular stasis was the first effect to occur.

4.3 Post-treatment Model Conditions

Burn depth continues to increase after treatment ends, as the heat stored in the uterus tissue dissipates through either conduction or perfusion. Modelling of heat transfer through the tissue continued for times greater than the burn time until burn depth ceased increasing significantly (<0.1 mm/min). There are several differences between the treatment and post-treatment uterus that must be included in the model. The first is the cavity boundary condition changes. Once the balloon is removed the two faces of the endometrium come together, resulting in a reflection boundary condition. Although the exact change in geometry cannot be modelled under the assumption of spherical symmetry, the reflection boundary condition is implemented

by assuming that the cavity surface becomes insulated after treatment (zero heat flux). Once the balloon is deflated the intracavity pressure returns to normal. This has two effects: the uterus returns to it's undistended size and the blood perfusion is no longer reduced by compression of the blood vessels. The first effect is implemented by substituting the undistended cell coordinates into the program; the second effect must be implemented while considering the elevation of the blood perfusion due to temperature and the loss of blood flow due to thermal damage. If thermal damage has not caused blood flow to cease, the steady-state blood flow rate (ω_∞ from Equation 18) is adjusted to take into account the base perfusion rate in the absence of cavity pressure. Furthermore if the current blood flow rate is less than the undistended base perfusion rate, then the current rate is set to the normal perfusion value for the uterus.

4.4 Modifying the Heat Equation for Tissue-Water Vaporization

The solution of the bio-heat transfer PDE is a complicated task if the vaporization of water must be included. The tissue becomes an "open" system where heat is not conserved, as water vapour is assumed to be driven into the Fallopian tubes or the cervix. In the modified Pennes equation, there are now two unknown terms – the rate of change of temperature and rate of heat loss due to vaporization. Vapourization most likely results in transport of water through the tissue, which will affect the heat transfer properties of the tissue.

The bioheat equation is given below, as modified for vaporization and water transport:

$$\rho_c c_t \frac{\partial T}{\partial t} + H_{vap} \frac{\partial W_{vap}}{\partial t} = k_t \nabla^2 T + \omega_b \rho_b c_b (T_b - T) + q_m + c_{H2O} \nabla T \cdot \dot{W} \quad (22)$$

This differs from the previous Pennes equation (6) by the addition of two terms. The second term on the LHS represents the latent heat of vapourization, and the last term on the RHS represents the enthalpy of water flowing through the tissue. At any instant of time, only vaporization or temperature increase may occur. However the model is solved over small but discreet time intervals, and within any time step it is possible to have both temperature changes and vaporization occurring. For example, at the start of the time step the temperature may be slightly below the boiling temperature; if the heat flux is large enough the temperature will be raised sufficiently high that vaporization will occur at the end of the time step.

4.4.1 Water Transport

It is assumed that water-transfer through tissue can be modelled by Fick's law, however it is acknowledged that this approach is simplistic To be modelled correctly, the water transport would be a complicated problem involving a temperature dependent interplay between the hydraulic conductivity, hydrostatic pressure and the osmotic pressure of biological components (130). The assumption of Fickian water diffusion has been commonly used in the analysis of coupled heat and water transfer in various products of the food industry, including beef meatballs (131), tortilla

chips (132) and french fries (133). The effect of blood perfusion on water transport is neglected in this formulation, although it is readily included with a source/sink term analogous to that used for temperature. The following formulation expresses water content in terms of partial density (mass water/unit volume):

$$\frac{\partial W}{\partial t} + \frac{\partial W_{vap}}{\partial t} = D_W \nabla^2 W \quad (23)$$

$$\left.\frac{\partial \mathrm{W}}{\partial \mathrm{r}}\right|_{R_l} = 0 \quad (24)$$

$$W\big|_{r=\infty} = 850 \ kg \cdot m^{-3} \quad (25)$$

$$W\big|_{t=0} = 850 \ kg \cdot m^{-3} \quad (26)$$

where:

W is the water concentration
W_{vap} is the mass of water vaporized
D_w is the diffusivity of water in the tissue

The flux of water is a time-derivative vector, and is calculated as below:

$$\dot{\vec{W}} = D_W \nabla W \quad (27)$$

4.4.2 Heat Transport With Vapourization

This formulation for coupled heat and mass transfer includes three unknowns (the time derivatives of temperature, water concentration and water vaporized) and just two equations (22 and 23); therefore additional information is required for a solution. In this program, phase equilibrium is assumed – vaporization is assumed to occur whenever water is present and there is a net deposition of heat in tissue already at its boiling point. Therefore if the net flux of heat into a control volume is predicted to

raise the temperature above the boiling point, the rate of vaporization is increased in order to result in a tissue temperature at the boiling point.

The heat transported by water vapour as it exits through the tissue is also not accounted for. This consideration becomes important if the rate of water transport to the cavity surface should become less than the rate of water vaporization, leading to desiccation. Steam transport through the crust would have an effect on the temperature profile of this region, which in turn would affect the temperature in the hydrated tissue (133). No desiccated crusts have been observed in clinical trials, indicating that the neglect of this term representing the heat transported by water vapour is reasonable.

In principle, if only surface vaporization occurs then the water concentration profile need not be estimated. If it is assumed that water is transferred quickly from surrounding tissue to maintain the water content of the tissue where vapourization is occurring, then the temperature can be assumed to be constant at the boiling point of water regardless of the rate of vaporization. However the inclusion of tissue-water concentration information provides a crude indication of the likelihood of crust formation, and was therefore included in the model. However unless desiccation were to occur the water concentration profile would have no effect on the temperature time-series, and therefore improving the accuracy of the water diffusion equations was not considered a worthwhile pursuit. The water concentration profile will also serve as a warning as to whether the assumption that thermal properties of fully hydrated tissue are acceptable is valid for a particular thermal treatment.

An additional reason for the more detailed vaporization model was that it was not clear *a priori* if vaporization could occur inside the tissue while not occurring at the surface of the uterine cavity. The inflation pressure of the balloon increases the boiling point at the cavity surface, and the stress, and consequently the boiling temperature, is reduced with increasing distance from the cavity. If the boiling temperature decreased more quickly than the tissue temperature with increasing distance then interior vaporization would be possible. The model results have not supported this hypothesis, however it was an issue deserving of consideration.

The complete set of equations, initial conditions and boundary conditions are listed below:

$$\rho_c c_t \frac{\partial T}{\partial t} + H_{vap} \frac{\partial W_{vap}}{\partial t} = k_t \nabla^2 T + \omega_b \rho_b c_b (T_b - T) + q_m \quad (28)$$

$$\frac{\partial W}{\partial t} + \frac{\partial W_{vap}}{\partial t} = D_W \nabla^2 W \quad (29)$$

$$T(r)\big|_{t=0} = 37^\circ C \quad (30)$$

$$T\big|_{r=\infty} = 37^\circ C \quad (31)$$

$$T\big|_{r=R_i} = T_{balloon} \quad (32)$$

or

$$k_t \frac{\partial T}{\partial r}\bigg|_{r=R_i} = HTC(T_{balloon} - T(r = r_i)) \quad (33)$$

$$\frac{\partial \mathrm{W}}{\partial r}\bigg|_{r=R_i} = 0 \quad (34)$$

$$W\big|_{r=\infty} = 850 \ \ kg \cdot m^{-3} \quad (35)$$

$$W(r)\big|_{t=0} = 850 \ \ kg \cdot m^{-3} \quad (36)$$

4.5 Parameter Selection

The following section reviews the literature that was used to calibrate the model parameters. In some cases experimentally determined values are available, in other cases the parameter values were calculated from the known properties of the uterus. A list of the values selected for the parameters is presented in Table 4, and following this is a discussion of each parameter value selected.

Table 4 – Summary of selected model parameter values.

Parameter	Value Selected	Units
k_t	0.542	$W \cdot m^{-1} \cdot K^{-1}$
$k_L(134)$	0.285	$W \cdot m^{-1} \cdot K^{-1}$
ρ_t	1062	$kg \cdot m^{-3}$
ρ_b	1060	$kg \cdot m^{-3}$
$\rho_{L(134)}$	1260	$kg \cdot m^{-3}$
c_t	3600	$J \cdot kg^{-1} \cdot K^{-1}$
c_b	3770	$J \cdot kg^{-1} \cdot K^{-1}$
$c_L(134)$	2428	$J \cdot kg^{-1} \cdot K^{-1}$
q_m	170	$W \cdot m^{-3}$
endometrium thickness	4	mm
myometrium thickness	13	mm
mean cavity volume	11	mL
water diffusion coefficient	2.5×10^{-5}	$cm^2 \cdot s^{-1}$
endometrial blood flow	0.0047	mL blood·mL tissue^{-1}·s^{-1}
myometrial blood flow	0.00375	mL blood·mL tissue^{-1}·s^{-1}
modulus of elasticity	150	kPa
Poisson's constant	0.499	dimensionless
vascular stasis pressure	45	mmHg
maximum perfusion multiplier	9	dimensionless
θ	0.078	$°C^{-1}$
ϕ	0.0046	s^{-1}
$H_{vap}(135)$	2.26×10^6	$j \cdot kg^{-1}$

Thermal Conductivity

Direct measurement of the thermal conductivity of the human uterus has been performed *in vitro* (136). There was no significant difference in thermal conductivity for samples either with or without endometrium tissue. Therefore their value of 0.542 (± 0.008) $Wm^{-1}K^{-1}$ was used in the computer model for all uterine tissue. The conductivity of coagulated uterus tissue was also measured and found to be 0.518 $Wm^{-1}K^{-1}$, following a loss of 6.5 % of it's water content by mass (from a mass water content of 81.6%). The uterine tissue was treated at 80°C in a sodium chloride solution for fifteen minutes, a thermal treatment that is much more severe than is expected for thermal ablation treatments. Therefore a constant thermal conductivity was used for all states of tissue.

Density

The density of uterine tissue was estimated from the following correlation (137).

$$\rho_t = \frac{1}{\sum_n \left(\frac{m_n}{\rho_n}\right)} \doteq \frac{1}{\left(\frac{m_{water}}{1000} + \frac{m_{protein}}{1540} + \frac{m_{fat}}{815}\right)} = 1062\,\mathrm{kg\,m^{-3}} \quad (37)$$

The mass fractions used were 0.8, 0.18 and 0.02 for water, protein and fat respectively, based on chemical analysis (138). This density of water in tissue is therefore 850 $kg{\cdot}m^{-3}$. The density of whole blood is not significantly different from the expected density of the uterus; Torvi et al. (87) used a blood density of 1060 $kg\ m^{-3}$.

Heat Capacity

No experimentally determined values for the heat capacity of uterus tissue was found in the literature review; therefore this parameter was estimated by averaging the heat capacities of its individual components(137):

$$c_t = \sum_n c_n m_n = (4.2m_{water} + 1.09m_{protein} + 2.3m_{fat})10^3 = 3{,}600\ \mathrm{J\,kg^{-1}K^{-1}} \quad (38)$$

The heat capacity of whole blood used was 3770 J $kg^{-1}K^{-1}$; this value has been used in models of skin burns (87).

Endometrium Thickness

There is a great deal of data available on the thickness of the endometrium; this information is non-invasively obtained by either ultrasonographic or magnetic resonance examination (139). The general procedure involves taking measurements in the pelvic longitudinal plane and measuring the maximum thickness of the endometrium tissue (140). The ultrasonography technique has been shown to yield reproducible results, both by the same observer and between different observers (141). Endometrial thickness is typically reported as the sum of the thicknesses of both layers, since this is the parameter that is measured during ultrasonography (142). For modelling purposes it is the thickness of a single layer that is important for burn depth calculations, therefore in this review the reported thickness has been halved if appropriate.

The thickness of the endometrium is strongly affected by the stage of the menstrual cycle. The endometrium thickness reaches a maximum following the luteal phase, decreasing to a minimum following menstruation (143). There are many other factors that can influence the thickness of the endometrium. Subject age has an effect; Fitzgerald et al. (144) found that endometrial thickness on the day of ovulation increased continually throughout the ages 21 to 45, increasing from 6.05 to 7.95 mm. In contrast, maximum luteal phase endometrial thickness occurred between the ages of 32 to 36 (6.45 mm thickness). In post-menopausal women a higher body mass index is associated with an increased endometrial thickness (145). Bornstein et al. (146) did not find such a relationship for post-menopausal women; although an unknown number of women were excluded due to obesity (body mass index>32), the effect of this exclusion is not clear. They did find a positive correlation between hypertension and endometrial thickness however.

The thickness of the endometrium may also be modified by various chemicals, a fact often used to "pre-thin" the endometrium prior to endometrial ablation. Substances used have included: danazol (a chemically modified androgenic steroid (147)), medroxyprogesterone acetate (148), nafarelin (148), and various GnRH agonists (149), (147). Pre-treatment therapy is usually conducted for several weeks prior to surgery (147).

Figure 30 presents endometrial thickness data compiled from many sources, normalized for a standard cycle with ovulation on day fourteen. Clearly the endometrium thickness increases throughout the cycle, from approximately two to five

millimeters. However there is some quantitative disagreement among the studies; for example Bakos et al.(150) found significantly thicker endometrium throughout the cycle than the other authors. These figures represent average thickness; the maximum thickness can be even larger. Endometrium up to eight millimeters thick has been reported (150), suggesting that a pre-treatment ultrasound exam may be advisable prior to thermal ablation.

The data presented in Figure 30 was derived from normal women; an important question is whether women suffering from menorrhagia have normal endometrial thickness? Hurskainen et al. (151) reports that the average endometrium thickness of 60 women with dysfunctional uterine bleeding was 5.3 mm (3.0 – 10.0), although it is not clear from the reported methods if this value refers to the single or double layer endometrial thickness. Another investigator (148) found that the endometrial thickness in affected women was 2.0 mm. It is not clear if the mean endometrial thickness is different between normal and menorrhagic women, however there is no evidence at present that there is a difference. Based on this review an endometrial thickness of 4.0 mm was selected for the untreated uterus, with the caveat that the endometrium may be significantly thicker or thinner than this value. In practice the thickness of the endometrium has little effect on the calculation of the temperature distribution; the thermal properties of the myometrium are not significantly different from the endometrium. Dilation and curettage can greatly decrease the endometrial thickness as well; this procedure will likely decrease the desired burn depth during thermal ablation.

Myometrium Thickness

The greater the thickness of the myometrium (and endometrium), the lower the risk of thermal damage to other internal organs. Therefore it is important to estimate the mean myometrial thickness, as well as the minimum thickness that is expected to be encountered. This information has been obtained in the same manner as the endometrial thickness, although less information is available.

Strohmer et al. (142) investigated in 76 nulliparous women the variation in various uterus dimensions using transvaginal ultrasound during the midfollicular and early luteal phase of a stimulated cycle. When measured at the fundus the myometrial thickness were 12.5 (± 2.5) and 11.7 (± 3.6) mm for each respective portion of the cycle. The myometrial thickness at the body of the uterus, calculated by subtraction of the endometrial thickness, was 12.35 and 13.05 mm respectively. A different study examined various uterus dimensions with both ultrasound and magnetic resonance imaging in twelve women with normal cycles (139). By ultrasound the myometrial thickness was 13.3 mm in the early portion of the cycle and 13.1 mm in the late portion of the cycle. The thickness when measured by MRI was 13.3 mm and 13.6 mm in the early and late phase. A study examining the endometrial and myometrial thickness of 109 post-menopausal women found that the average myometrium thickness was between 10 and 12 mm if measured within fifteen years of menopause, in both the presence and absence of hormone replacement therapy(152). In excised uteri that had been subjected to thermal ablation, the total thickness of the uterine wall, including the endometrium was 20 mm (range 15-25 mm) (31). The myometrial thickness would therefore by approximately 16 mm, which is larger than the previously

mentioned studies. Possibly the discrepancy is due to the small sample size (eight uteri). Based on the literature reviewed, a mean myometrium thickness of 13 mm is assumed.

Uterus Cavity Volume

The interior volume of the uterus is a function of its initial size and the inflation pressure. Vilos et al. (116) established the pressure-volume relationship for nine uteri, and found that they ranged from 2 to 20 mL; the maximum applied pressure was 250 mmHg. At approximately 170-180 mmHg the mean volume appeared to be between 8 and 10 mL. In a different study 13 uteri were examined utilizing pressure in the range of 90 to 165 mmHg (81). The mean volume (acknowledging the confounding effect of variable inflation pressure) was 9.8 mL (range 5 to 28 mL). The largest reported cavity volume was not a result of high inflation pressure; in that case the pressure was only 98 mmHg. In this study the maximum permitted utero-cervical length was 12 cm, effectively excluding extremely large cavity volumes. The results of five *in vitro* endometrial thermal ablation procedures, utilizing uteri obtained from hysterectomy for menorrhagia, included balloon volume information (32). Balloon volume was reported to range from 2 to 16 mL; the average volume was 7.1 mL based a balloon pressure of approximately 180 mmHg. Results from clinical trials in Mexico City and London were reported by Neuwirth et al. (153). At a pressure of 70-80 mmHg, the mean cavity volume among eight patients was 6 mL (range 3 to 10 mL). Most importantly, a study of 296 thermal ablation treatments reported that the mean volume of fluid required to fill the cavity at a pressure between 140 and 190 mmHg was 11.4 mL (SD 6.6), and the range was from 2 to 55 mL (5). Based on these results a mean cavity volume of

11 mL was assumed, although cavity volumes can occur within a range of a minimum of 2 mL to possibly greater than 28 mL. The effect of such a large variation in cavity volume on the outcome of thermal ablation is an important consideration.

Water Diffusion Coefficient

Data for the diffusivity of water in the myocardium were used for the water diffusion coefficient (154). It was found that the diffusion coefficient of water ranged from 1.8 to 2.5 x 10^{-5} $cm^2 \cdot s^{-1}$, depending on the orientation of the muscle fibers. This is smaller than the diffusion coefficient of free water at 37°C (3.0 x 10^{-5} $cm^2 \cdot s^{-1}$); the authors suggest that this reduction is due to interactions between water and the cellular cytoplasm. The diffusion coefficient selected was 2.5 x 10^{-5} $cm^2 \cdot s^{-1}$, although this may underpredict water flux compared to a model that incorporates hydraulic conductivity.

Metabolic Rate

The metabolic rate of heat generation in resting muscle was calculated to be 170 $W \cdot m^{-3}$, at 37°C (137).

Blood Perfusion Rate

The blood perfusion rate has a significant effect on both the transient and steady state temperature distribution; an accurate estimate of the value of this parameter is important. Data pertaining to the perfusion rate of both the endometrium

and myometrium in humans was reviewed; results from animal studies were examined but not included due to concerns about the applicability of the results to humans.

Jansson (155) examined myometrial blood flow in the myometrium of eleven non-pregnant uteri, investigated using $Xenon^{133}$ clearance during abdominal operations for ovarian cysts or sterilization. The average perfusion rate for eighteen measurements in these women was 0.00383 s^{-1}, ranging from a minimum of 0.00137 to a maximum of 0.00675 s^{-1}. The elimination rate was well fitted by a mono-exponential curve, leading the author to suggest that the myometrium is a relatively homogenous tissue, in terms of its vascularity. Importantly, measurements of blood flow taken at various locations within the uterus (fundus, body, isthmus) indicated that the blood flow rate was essentially uniform throughout the uterus. Therefore the variation that was observed can be assumed to be truly due to differences among individuals, and is not an artefact of local variations in the blood perfusion rate. It was observed that increasing parity was associated with an increased perfusion rate, although the sample size was too small to permit a statistical evaluation of this correlation.

In another study, the orientation of the subject was found to have an effect on the uterine blood flow rate (156). Women changing from a horizontal to a vertical position experienced a 44% decrease in uterine perfusion. Mean myometrial blood flow in six supine, unanaesthetized women was 0.00313 s^{-1}; this variable was correlated with the endometrial blood flow of 0.00297 s^{-1} ($r=0.90$, $p<0.05$). Five additional measurements suggested that the myometrial blood flow was 0.00375 s^{-1}.

This value was selected for the myometrial perfusion rate parameter; it is in excellent agreement with the value reported by Jansson for the myometrium.

A two-compartment model was used to evaluate blood flow in the whole uterus, as assessed by Xenon 133 clearance following tracer injection in the uterine artery (157). The average perfusion rate for these compartments was 0.00586 s^{-1} and 0.00205 s^{-1} for each respective compartment. Although these values cannot be employed in the mono-exponential formulation used in the blood perfusion term of the thermal ablation model, it is encouraging that the reported blood flow rates lie between the bounds of the fast and slow compartments recorded for the whole uterus.

The perfusion rate of the endometrium was examined for women with normal menstrual cycles and dysfunctional uterine bleeding (158). Analysis was performed using both multi-exponential and mono-exponential curves for $Xenon^{133}$ elimination. For women with normal menstrual cycles the mean blood flow rate was 0.00462 s^{-1}, and ranged from 0.00152 to 0.01135 s^{-1} over the seventeen women examined. The mean blood flow rate in the menorrhagic endometrium of twenty women was 0.0047 s^{-1}, and ranged from 0.00148 to 0.00948 s^{-1}. Peak perfusion appeared to occur in the middle follicular period (idealized cycle days 8-12). The value of 0.0047 s^{-1} was selected for the endometrium, this value is slightly higher than the value of 0.00375 s^{-1} used for the myometrium.

Elastic Parameters

The model of the stress distribution in the distended uterus requires two parameters, Young's modulus and Poisson's ratio. Biological tissue in general is essentially incompressible, and the appropriate value of Poisson's constant is the limit approaching 0.5 - the theoretical maximum value (117). In practice a value of 0.499 was used to prevent division by zero when calculating equation 15. The elastic modulus of myometrial tissue was estimated from the data of Pearsall and Roberts (159). They estimate the modulus to be 1000 kPa; however this measurement is for an applied stress of 10 psi. The stress-strain relationship for uterine muscle is highly non-linear (essentially logarithmic – see Figure 31), therefore this value would significantly underestimate the strain observed at a lower stress level. It was estimated from the author's figures that if a linear stress-strain relationship is assumed, then a 150 kPa modulus will result in the observed strain of 0.45 at a stress of 10 psi. In comparison, Persson et al. (34) estimated the elastic modulus to be 80 kPa based on their clinical observation that a balloon pressure of 22.1 kPa results in a balloon volume of 9 mL. It is not clear how they chose this value, the initial cavity volume was not given.

The non-linear elasticity of uterine tissue is consistent with a report in the literature of a "natural volume" of the uterus cavity (116). A silicone balloon was inserted into a uterus and filled with a 5% dextrose solution until the pressure stabilized. Then pressure-volume curves were obtained by the incremental infusion of

additional fluid (see Figure 32). The authors observed that at pressures greater than 170 to 180 mmHg, attempts to infuse even a small amount of fluid would induce muscular contractions which resulted in a large increase in intrauterine pressure.

Unfortunately no information is available on the effect of muscular contractions on the stress distribution in the uterus. This adds additional uncertainty to a model that is already made approximate by the use of a linear stress-strain relationship in tissue that has a non-linear response. The effect of pressure on perfusion cannot be ignored, and a solution to the elasticity problem that uses a non-linear version of Hooke's law was not found; therefore the linear version will be used as an approximation.

4.6 Numerical Solution of Coupled Heat and Mass Transfer Equations

The finite volume method was used for this analysis, although other investigators used a finite difference or finite element method to solve heat transfer in tissue. One advantage of the finite volume method is that conservation laws are automatically maintained; this is not always the case for other methods, particularly for the finite difference method. In the control volume method, computational shells are defined within the volume of the tissue. During simulation the total heat present in the shell is assessed, and from this value an average temperature for the shell can be determined. The net flux of heat into or out of the shell, when combined with source/sink heat transfer, will determine the rate of change of the shell temperature. By the divergence theorem these equations are converted to control volume form (n is

the unit vector normal to the control volume, Ω refers to the control volume and $\delta\Omega$ is the control volume surface):

$$\iiint_{\Omega}\left(\frac{\partial W}{\partial t}+\frac{\partial W_{vap}}{\partial t}\right)\ dV=\oint_{\partial\Omega}D_{W}\nabla W\cdot\vec{n}\ \ ds \quad (39)$$

$$\iiint_{\Omega}\rho_{c}c_{t}\frac{\partial T}{\partial t}dV+\iiint_{\Omega}H_{vap}\frac{\partial W_{vap}}{\partial t}dV$$
$$=\oint_{\partial\Omega}k_{t}\nabla T\cdot\vec{n}\ \ ds+\iiint_{\Omega}\left(\omega_{b}\rho_{b}c_{b}\left(T_{b}-T\right)+q_{m}\right)\ \ dV+\oint_{\partial\Omega}c_{H2O}T\cdot\dot{\vec{W}}\cdot\vec{n}\ \ ds \quad (40)$$

An explicit solution of the above system of equations is straightforward, however such a solution would require extremely small time steps to maintain stability. Therefore a trapezoidal solution (the Crank-Nicolson method, (160)) will be used, an approach that requires data at the start of the time step and data solved for at the end of the time step. However, the above set of equations is coupled, greatly complicating the solution by requiring the use of flux Jacobians to approximate the solution (161). There is an opportunity to avoid Jacobians if we assume that the rate of heat transport due to water movement is insignificant; in this case the equations become effectively uncoupled and only 'communicate' by the unknown value of the rate of water vaporization. To test the validity of this assumption, the flux of heat across a plane was compared for conduction and transport respectively. A simple calculation suggests that the effect of this term on temperature will not be significant. If a complete gradient occurs over 1 mm (100% hydration to 0% hydration, 100°C to 0°C) then the transport of water with a temperature gradient would result in a temperature

change of 13°C per minute. Although such a value appears significant, the gradients are extreme possibilities. If these same gradients occur over the space of 5 mm then the rate of temperature change is only 0.5 degrees per minute. The neglect of this factor does introduce some error; however, under normal conditions its effect is relatively minor.

It is desirable to easily switch geometrical arrangements rapidly to allow for three possible problems: planar, cylindrical and spherical geometry. The flux term uses a multiplier (represented as α) equal to the area of the shell boundary divided by the volume of the cell. Consider a shell with boundaries at cell numbers i and i+1. Alpha coefficients must be determined for both sides of the cell (signified by the symbol 'j', this refers to either cell number i or i+1).

Planar:

$$\alpha_j = \frac{1}{x_{i+1} - x_i} \quad (41)$$

Cylindrical:

$$\alpha_j = \frac{2r_j}{r_{i+1}^2 - r_i^2} \quad (42)$$

Spherical:

$$\alpha_j = \frac{3r_j^2}{r_{i+1}^3 - r_i^3} \quad (43)$$

4.7 Spatial and Temporal Discretization

The implicit trapezoidal method assumes that the rate of change of the parameter of interest is equal to the average of the flux integral at the beginning and end of the time-step (a purely implicit method only uses the flux integral at the end of the time step). The trapezoidal method is second order accurate, while a purely implicit method is only first order accurate in time; however the trapezoidal method has a maximum stable time step – consistent with its hybridisation with an explicit method. Expressing this formulation abstractly (where U is the value of interest, and FI is the flux integral around the cell):

$$\frac{\partial U}{\partial t} = \frac{FI^{n+1} + FI^{n}}{2} \quad (44)$$

Expressing this formulation more specifically for the vaporization problem:

$$\frac{\partial W_i^n}{\partial t} = \frac{1}{2}\left(\begin{array}{l}\left(D_w\alpha_{i+1/2}\left(\frac{W_{i+1}^{n+1}-W_i^{n+1}}{x_{i+1}-x_i}\right)-D_w\alpha_{i-1/2}\left(\frac{W_i^{n+1}-W_{i-1}^{n+1}}{x_i-x_{i-1}}\right)\right)\\ +\left(D_w\alpha_{i+1/2}\left(\frac{W_{i+1}^{n}-W_i^{n}}{x_{i+1}-x_i}\right)-D_w\alpha_{i-1/2}\left(\frac{W_i^{n}-W_{i-1}^{n}}{x_i-x_{i-1}}\right)\right)\end{array}\right) - \frac{1}{2}\left(\frac{\partial W_{vap}^{n+1}}{\partial t}+\frac{\partial W_{vap}^{n}}{\partial t}\right) \quad (45)$$

$$\frac{\partial T_i^n}{\partial t} = \frac{1}{2}\left(\left(\frac{k_t}{\rho_t c_t}\alpha_{i+1/2}\left(\frac{T_{i+1}^{n+1}-T_i^{n+1}}{x_{i+1}-x_i}\right)-\frac{k_t}{\rho_t c_t}\alpha_{i-1/2}\left(\frac{T_i^{n+1}-T_{i-1}^{n+1}}{x_i-x_{i-1}}\right)\right)\right.$$
$$\left.+\left(\frac{k_t}{\rho_t c_t}\alpha_{i+1/2}\left(\frac{T_{i+1}^{n}-T_i^{n}}{x_{i+1}-x_i}\right)-\frac{k_t}{\rho_t c_t}\alpha_{i-1/2}\left(\frac{T_i^{n}-T_{i-1}^{n}}{x_i-x_{i-1}}\right)\right)\right)$$
$$+\frac{1}{2}\frac{\omega_i \rho_b c_b}{\rho_t c_t}\left(\left(T_b - T_i^{n+1}\right)+\left(T_b - T_i^{n}\right)\right)+\frac{q_m}{\rho_t c_t}-\frac{H_{vap}}{2\rho_t c_t}\left(\frac{\partial W_{vap}^{n+1}}{\partial t}+\frac{\partial W_{vap}^{n}}{\partial t}\right) \quad (46)$$

It is convenient to substitute the value at the end of the time step (T^{n+1}) with the current value plus the change in that value ($T^n + \delta T^n$). Performing this operation, one obtains:

$$\frac{\delta W_i^n}{\Delta t} = \frac{1}{2}\left(\left(D_w\alpha_{i+1/2}\left(\frac{W_{i+1}^n+\delta W_{i+1}^n - W_i^n - \delta W_i^n}{x_{i+1}-x_i}\right)-D_w\alpha_{i-1/2}\left(\frac{W_i^n+\delta W_i^n - W_{i-1}^n - \delta W_{i-1}^n}{x_i-x_{i-1}}\right)\right)\right.$$
$$\left.+\left(D_w\alpha_{i+1/2}\left(\frac{W_{i+1}^n - W_i^n}{x_{i+1}-x_i}\right)-D_w\alpha_{i-1/2}\left(\frac{W_i^n - W_{i-1}^n}{x_i-x_{i-1}}\right)\right)\right)$$
$$-\frac{1}{2}\left(\frac{\partial W_{vap}^{n+1}}{\partial t}+\frac{\partial W_{vap}^{n}}{\partial t}\right) \quad (47)$$

$$\frac{\delta T_i^n}{\Delta t} = \frac{1}{2}\left(\left(\frac{k_t}{\rho_t c_t}\alpha_{i+1/2}\left(\frac{T_{i+1}^n+\delta T_{i+1}^n - T_i^n - \delta T_i^n}{x_{i+1}-x_i}\right)-\frac{k_t}{\rho_t c_t}\alpha_{i-1/2}\left(\frac{T_i^n+\delta T_i^n - T_{i-1}^n - \delta T_{i-1}^n}{x_i-x_{i-1}}\right)\right)\right.$$
$$\left.+\left(\frac{k_t}{\rho_t c_t}\alpha_{i+1/2}\left(\frac{T_{i+1}^n - T_i^n}{x_{i+1}-x_i}\right)-\frac{k_t}{\rho_t c_t}\alpha_{i-1/2}\left(\frac{T_i^n - T_{i-1}^n}{x_i-x_{i-1}}\right)\right)\right)$$
$$+\frac{1}{2}\frac{\omega_i \rho_b c_b}{\rho_t c_t}\left(\left(T_b - T_i^n - \delta T_i^n\right)+\left(T_b - T^n\right)\right)+\frac{q_m}{\rho_t c_t}-\frac{H_{vap}}{2}\left(\frac{1}{\rho_t c_t}\frac{\partial W_{vap}^{n+1}}{\partial t}+\frac{1}{\rho_t c_t}\frac{\partial W_{vap}^{n}}{\partial t}\right) \quad (48)$$

Arranging all the sigma terms on the left results in:

$$
\begin{aligned}
&-\Delta t\left(\frac{D_w\alpha_{i+1/2}}{2\left(x_{i+1}-x_i\right)}\right)\delta W_{i+1}^n \\
&+\left(1+\Delta t\left(\frac{D_w\alpha_{i+1/2}}{2\left(x_{i+1}-x_i\right)}+\frac{D_w\alpha_{i-1/2}}{2\left(x_i-x_{i-1}\right)}\right)\right)\delta W_i^n \\
&-\Delta t\left(\frac{D_w\alpha_{i-1/2}}{2\left(x_i-x_{i-1}\right)}\right)\delta W_{i-1}^n \\
&=\Delta t\left(D_w\alpha_{i+1/2}\left(\frac{W_{i+1}^n-W_i^n}{x_{i+1}-x_i}\right)-D_w\alpha_{i-1/2}\left(\frac{W_i^n-W_{i-1}^n}{x_i-x_{i-1}}\right)\right) \\
&\qquad -\frac{\Delta t}{2}\left(\frac{\partial W_{vap}^{n+1}}{\partial t}+\frac{\partial W_{vap}^n}{\partial t}\right) \qquad (49)
\end{aligned}
$$

$$
\begin{aligned}
&-\Delta t\left(\frac{k_t}{2\rho_t c_t}\frac{\alpha_{i+1/2}}{\left(x_{i+1}-x_i\right)}\right)\delta T_{i+1}^n \\
&+\left(1+\Delta t\left(\frac{k_t}{2\rho_t c_t}\frac{\alpha_{i+1/2}}{\left(x_{i+1}-x_i\right)}+\frac{k_t}{2\rho_t c_t}\frac{\alpha_{i-1/2}}{\left(x_i-x_{i-1}\right)}-\frac{\omega_i\rho_b c_b}{2\rho_t c_t}\right)\right)\delta T_i^n \\
&-\Delta t\left(\frac{k_t}{2\rho_t c_t}\frac{\alpha_{i-1/2}}{\left(x_i-x_{i-1}\right)}\right)\delta T_{i-1}^n \\
&=\Delta t\left(\frac{k_t}{\rho_t c_t}\alpha_{i+1/2}\left(\frac{T_{i+1}^n-T_i^n}{x_{i+1}-x_i}\right)-\frac{k_t}{\rho_t c_t}\alpha_{i-1/2}\left(\frac{T_i^n-T_{i-1}^n}{x_i-x_{i-1}}\right)\right) \\
&\qquad +\Delta t\left(\frac{\omega_i\rho_b c_b}{\rho_t c_t}\left(T_b-T_i^n\right)\right)+\Delta t\frac{q_m}{\rho_t c_t}-\Delta t\frac{H_{vap}}{2\rho_t c_t}\left(\frac{\partial W_{vap}^{n+1}}{\partial t}+\frac{\partial W_{vap}^n}{\partial t}\right) \qquad (50)
\end{aligned}
$$

4.8 Boundary Condition Implementation

Although it is possible to implement boundary conditions directly with the control volume method, it is often easier to use what are known as 'ghost cells'. The regular spacing of the control volumes are extended past the physical boundaries by one cell. The ghost cells are aphysical, but are solved as if they were real. The value of the cell

(temperature or water concentration) is set such that the desired boundary condition is enforced.

Fixed temperature or water concentration:

$$T_0 = 2T_{balloon} - T_1$$

$$W_{i\max+1} = 2(850 \ \ kg \cdot m^{-3}) - T_{i\max}$$

$$T_{i\max+1} = 2(37^o C) - T_{i\max} \quad (51)$$

Water boundary condition at balloon surface:

$$W_0 = W_1 \quad (52)$$

Heat Transfer Coefficient (thermal barrier):

$$T_0 = T_1 + (x_1 - x_0)\frac{h(T_{balloon} - T_1)}{k_t} \quad (53)$$

The implicit solution of the heat transfer equation also requires the solution of the rate of change of the value of the ghost cell. Note that in every case, for this order of spatial discretization accuracy, the ghost cell value is strictly a function of the actual value of the nearest cell and the specific boundary condition. By taking the derivative of the ghost cell with respect to the neighbouring cell one may determine the appropriate relationship for the implicit solution, as is shown in the following equations.

Fixed temperature or water concentration:

$$\delta T_0 + \delta T_1 = 0$$
$$\delta T_{i\max+1} + \delta T_{i\max 1} = 0$$
$$\delta W_{i\max+1} + \delta W_{i\max 1} = 0 \quad (54)$$

Water boundary condition at balloon surface:

$$\delta W_{i\max+1} - \delta W_{i\max} = 0 \quad (55)$$

Heat Transfer Coefficient

$$\delta T_0 - \left(1 - (x_1 - x_0)\frac{HTC}{k_t}\right)\delta T_1 = 0 \quad (56)$$

4.9 Matrix Solution

Having manipulated the discretized partial differential equation into the preceding form, an algorithm may be constructed which solves this system of equations for the value of the delta terms, and hence the temperature and water concentration values at the end of the time step. Equation 49 and 50 may be represented as (substitute W for T in the case of water diffusion):

$$a_i \delta T_{i-1} + b_i \delta T_i + c_i \delta T_{i+1} = r_i \quad (57)$$

This may form a matrix of i_{max}+2 terms, once the appropriate expressions for the ghost cells are included.

$$\begin{pmatrix} b_0 & c_0 & & & & & \\ a_1 & b_1 & c_1 & & & & \\ & a_2 & b_2 & c_2 & & & \\ & & \ddots & \ddots & \ddots & & \\ & & & a_{i\max} & b_{i\max} & c_{i\max} & \\ & & & & a_{i\max+1} & b_{i\max+1} & \end{pmatrix} \begin{pmatrix} \delta T_0 \\ \delta T_1 \\ \delta T_2 \\ \vdots \\ \delta T_{i\max} \\ \delta T_{i\max+1} \end{pmatrix} = \begin{pmatrix} r_0 \\ r_1 \\ r_2 \\ \vdots \\ r_{i\max} \\ r_{i\max+1} \end{pmatrix} \quad (58)$$

Terms b_0, c_0 and r_0 are for the interior ghost cell, while terms a_{imax+1}, b_{imax+1} and r_{imax+1} are for the exterior, as determined by the previous differentiation of the discretized boundary conditions. For example, if the interior boundary condition were fixed temperature, while the exterior condition were insulated, then the solution matrix would be:

$$\begin{pmatrix} 1 & 1 & & & & & \\ a_1 & b_1 & c_1 & & & & \\ & a_2 & b_2 & c_2 & & & \\ & & \ddots & \ddots & \ddots & & \\ & & & a_{i\max} & b_{i\max} & c_{i\max} & \\ & & & & 1 & -1 & \end{pmatrix} \begin{pmatrix} \delta T_0 \\ \delta T_1 \\ \delta T_2 \\ \vdots \\ \delta T_{i\max} \\ \delta T_{i\max+1} \end{pmatrix} = \begin{pmatrix} 0 \\ r_1 \\ r_2 \\ \vdots \\ r_{i\max} \\ 0 \end{pmatrix} \quad (59)$$

The direct solution of this matrix would require a number of operations of the order $(imax + 2)^3$. The Thomas algorithm (162) capitalizes on the banded, tri-diagonal nature of this matrix to arrive at a solution in a number of operations that is approximately proportional to imax+2. The solution is obtained by performing the following operations.

1) For cells 0 to imax perform the following operations:

$c_i=c_i/b_i$

$r_i=r_i/b_i$

$b_i=1$

$b_{i+1}=b_{i+1}-c_ia_{i+1}$

$r_{i+1}=r_{i+1}-r_ia_{i+1}$

$a_i=0$

2) Set $r_{imax+1}=r_{imax+1}/b_{imax+1}$, then set b_{imax+1} equal to one

3) Perform the following substitution backwards, from cell imax to cell 0

$r_i = r_i - r_{i+1} c_i$

$c_i = 0$

The right hand side vector that results is the solution of the system of equations. The temperature at the end of the time step is then simply equal to the temperature at the start of the time step plus the solved change in temperature. This process is repeated for the water concentration profile.

To account for vaporization, the matrix solution protocol is slightly modified. The rate of vaporization calculated at the end of the previous time step is used as the rate of vaporization at the start of the new time step. At the very start of treatment simulation this will be equal to zero for all cells, i.e., no vaporization has yet occurred. The assumption is made that no vaporization occurs at the end of the time step, and the Thomas algorithm is applied. If the estimated temperature at the end of the time step in any cell exceeds the local boiling temperature, and water is present in the cell, then a new rate of vaporization (LHS) is estimated that would enforce phase equilibrium based upon the old rate of vaporization (RHS):

$$\frac{\partial Wvap_i^{n+1}}{\partial t} = \frac{\partial Wvap_i^{n+1}}{\partial t} + \frac{2\rho_t c_t}{H_{vap}\Delta t}\left(T_i^{n+1} - BTemp_i\right) \quad (60)$$

The factor of '2' on the RHS of equation 60 is a result of the fact that the average rate of vaporization is being adjusted to the correct level by only varying the rate of vaporization at the end of the time-step. If vaporization occurred and the

estimated temperature at the end of the time step is less than boiling then this calculation is also performed, and will reduce the rate of vaporization to correct overshoot. If there is insufficient water available to maintain the boiling temperature, then the rate of vaporization is reduced sufficiently to evaporate the remaining water. The updated estimate of the rate of water vaporization at the end of the time step is then adopted and the system of equations is re-solved. This iterative process continues until there is sufficient agreement between the previous and current estimate of the rate of vaporization (absolute difference less than 0.0001 $kg \cdot m^{-3} \cdot min^{-1}$).

4.10 Algorithm for Calculating the Balloon-Fluid Temperature

Two different thermal ablation devices are modelled in this thesis. In one device, the balloon fluid temperature is maintained constant and because the fluid is well mixed a simple boundary condition could be used at $r=R_i$ (the surface of the endometrium), $T=T_{balloon}$, where $T_{balloon}$ is the temperature of the balloon fluid. In the second device (the TRS device) the fluid within the balloon is subject to both forced and natural convection (direct observation of the fluid when treating a silicone model uterus indicates that turbulence occurs during each balloon inflation).

The TRS device was treated as a series of three, fully mixed, compartments (see Figure 33). During each pulsation fluid is assumed to be instantaneously exchanged between the compartments; heat exchange to the uterus occurs during the period between pulsations.

Balloon compartment

The fluid in the balloon is assumed to be fully mixed, and a heat transfer coefficient is used to model the thermal resistance of the silicone balloon and the stagnant boundary layer of glycerine. There is a minimum residual volume (0.5 mL assumed) that occurs during active deflation, this represents heat stored in the balloon material and the film of glycerine that remains in the balloon. During passive deflation, where the reservoir pressure is reduced to zero (ambient), it is assumed that there is an additional residual volume of glycerine that remains in the balloon; heat exchange occurs normally. It is assumed that the balloon retains a spherical shape during partial deflation, reducing the surface area available for heat transfer and consequently reducing the rate of heat loss from the balloon. The residual volume is initially assumed to be equilibrated with the body core temperature.

Shaft Compartment

The shaft conducts glycerine between the reservoir and the balloon. The shaft is assumed to be insulated, although in reality the shaft surface may warm to a maximum of approximately 44°C during treatment (Monty Bruce, Pers. Comm.). The shaft fluid is initially assumed to be equilibrated at room temperature. The volume of glycerine within the shaft has been calculated as 1.16 mL.

Reservoir compartment

The reservoir consists of a hollow aluminum cylinder that is the external boundary of a silicone balloon that contains all glycerine that is not in the balloon or shaft. The action of pneumatic pressure on this balloon is what causes fluid pulsation

to the balloon. In addition the modelled volume of glycerine is increased to account for the additional heat stored in the warmed components of the TRS, the amount of this increase is to be determined during parameter fitting. However the external components also represent a source of heat loss. Based on the knowledge that the TRS device requires 12.6 watts of power to maintain the treatment temperature of 173°C, a combination area and heat transfer coefficient of 0.085 $W \cdot K^{-1}$ was derived to model this heat loss from the reservoir.

4.11 Program Description and Error Checking

The program was written in Microsoft Visual C++, utilizing object oriented architecture. The simulation normally required less than one minute on a 350 MHz Pentium II processor. As the distortion due to balloon pressure increased, the time required for simulation increased because the minimum cell spacing decreased. Throughout the programming process, standard testing techniques were used to ensure that the algorithm implementation was correct. For example in unperfused tissue planar geometry if the second derivative of the temperature is a constant then the flux integral of all cells should be equal. The burn severity algorithm was also tested, by holding the temperature constant one can check for discrepancies between the calculated and analytically determined damage integral.

Finally program validity was checked against a scenario with a known analytical solution. A semi-infinite, planar tissue, with a constant perfusion rate and no metabolic heat generation, subjected to a step change in temperature at the boundary condition

will be described by the following formula (160):

$$T(x,t) = T(x,0) + \frac{(T(0,t) - T(x,0))}{2}\left(\begin{array}{l} \exp\left[x\sqrt{\frac{\omega_b c_t p_t}{k_t}} \right] erfc\left[\frac{x}{2\sqrt{\frac{k_t}{c_t p_t} t}} + \sqrt{\omega_b t} \right] \\ + \exp\left[-x\sqrt{\frac{\omega_b c_t p_t}{k_t}} \right] erfc\left[\frac{x}{2\sqrt{\frac{k_t}{c_t p_t}}} - \sqrt{\omega_b t} \right] \end{array} \right) \quad (61)$$

In Figure 34 the model predictions, using the same assumptions, are compared at various times during a simulation of the Thermachoice™ 2 treatment protocol (87°C for 8 minutes). The model appears to be in excellent agreement, the only discrepancy occurred late in the simulation, when the further tissues began to become warm. This discrepancy disappears when the spacing between cells is halved. In practice, time increments and spatial discretization were decreased until the solution no longer changed significantly. The final grid size selected was six cells per millimeter and the time interval was 0.03 seconds.

Chapter 5: Meat Trial Methodology And Parameter Calibration

The purposes of the meat-model experiments were to: (1) determine the balloon fluid temperature during treatment, (2) determine the surface temperature of the endometrium during treatment and calibrate a heat-transfer coefficient to allow calculation of this temperature from the balloon fluid temperature, and (3) to verify the model predictions of the temperature distribution through the tissue during treatment (for a non-perfused system). This chapter describes the materials and methods used in these experiments.

The determination of the temperature at the balloon-tissue interface is a difficult task. In many engineering applications an infrared camera would used to determine surface temperatures; however this approach is not possible when the temperature of interest is inside animal tissue. Instead thermocouples were placed within the cavity of a meat model of the uterus, and the interface temperatures were continuously recorded on a computer. A wire thermocouple was found to either press into the balloon or into the meat, introducing uncertainty regarding the location where the temperature was being measured. Because the temperature gradient at the balloon-tissue interface is very large, the temperature recorded is strongly affected by the position of the thermocouple. Using thermocouples constructed of copper disks solved this problem. The location of this type of thermocouple is more easily maintained at the balloon-tissue interface. Multiple thermocouples were used throughout the tissue and at different positions on the inner cavity wall, both to validate

the observed temperature time-series and ensure that the balloon surface is contacted despite some uncertainty regarding the actual balloon position within the cavity.

Apparatus and Materials

The following materials were used in the meat-model experiments:

- meat model of the uterus (~1 kg)
- TRS device
- 2-4 copper disk thermocouples (4 mm diameter disks)
- wire thermocouples if desired
- computer with thermocouple data logger
- needle and thread
- "loctite" glue
- heavy-duty fishing line and extra-large needle
- meat model cavity cutter
- sharpened metal tube (5 mm internal diameter, 1 mm wall thickness)
- standard mercury thermometer
- cavity volume instrument (balloon, pressure sensor and syringe)
- bucket and plastic bag
- razor blade

5.1 Thermocouples

During the meat trials all tissue implanted thermocouples were type 'T', where the positive lead is composed of copper and the negative lead is composed of constantan copper-nickel. The temperature range of this thermocouple is –200°C to 350°C, far in excess of the requirements for the meat trial. The error of this thermocouple is either 1.0°C or 0.75%, whichever is greater. All thermocouples were constructed out of standard thermocouple wire and then flame was use to melt and fuse the wires to create the dissimilar metal junction. Data logging was recorded automatically, either with a specially constructed input device or with an IOTech

Personal Data Acquisition device. The constructed device had a sampling period of two seconds; the sampling rate used with the commercial device was three per second, although far higher rates were possible. In some early trials the balloon thermocouple was of type J, compatible with a manual display device that was available. In this thermocouple device the positive lead is iron, the temperature range is 0°C to 750°C and the error limit is the greater of either 2.2°C or 0.75%. For later trials a TRS cartridge with a T-thermocouple was constructed. To estimate the cavity surface temperature 4 mm diameter copper disks were punched, and two pinholes were punched approximately 1 mm from the outer radius. The leads of a T-type thermocouple were placed through the pinholes, bent and then soldered into place. Both the wire and disc thermocouples were tested in water at various temperatures, as measured independently with a mercury thermometer, to confirm that the recorded temperatures were correctly calibrated and accurate.

5.2 Experimental Protocol

1. The sharpened tube was inserted down the longest axis of the meat, cutting a hole representative of the cervical canal. The cavity cutter was then inserted down the simulated cervical canal. The result is a cavity shaped slot inside of the meat model (Figure 35).
2. With the cavity-cutting device still inserted, wire thermocouples were inserted and secured in the meat at various depths from the cavity. It is very difficult to control the depth of insertion; therefore the depth during insertion is approximate and was more accurately determined after treatment is complete.

In some cases the thermocouple was tied with two lengths of fishing line, securing it against both forward and reverse movement. However this approach did not work on large cavity uteri, where the large amount of distortion during balloon inflation would cause the fishing line to cut into the meat. Therefore, in large cavity meat models only one line was used to secure the wire thermocouple.

3. The disk thermocouples were inserted into the canal and then were pushed outside the meat model via the cavity slot; the thermocouples were guided through the canal by the sharpened tube. Thread was tied around the base of the disk thermocouple (where the wire leads attach to the copper disk). The needle was then inserted on the inside of the cavity posterior to the desired thermocouple location (closer to the canal). The needle was drawn through to the outside of the meat, and the thermocouple was pulled tight to the cavity surface. The thread was then secured and tied to the outside of the meat. Ideally two disk thermocouples were be placed in the top and bottom respectively. Thermocouples must be placed such that they are not in contact, or else interference will occur.
4. All thermocouples were taped together externally to minimize the transfer of stress to the internal thermocouple attachment sites. Thermocouples were individually marked.
5. The slotted end of the cavity was sewn closed. The volume of the cavity was adjusted, if necessary, by changing the closure sewing location relative to the canal entrance to the cavity. Although the cavity at this time was shaped like a flattened 'V', it became spherical/ellipsoidal once inflated by the balloon. The

stitches must be close together or it is possible to press the balloon past the cavity during treatment.

6. The volume of the cavity was measured with a separate syringe and balloon device, with an attached pressure sensor. Air was removed from the tubing, and the balloon checked for leaks and then was emptied and inserted into the cavity. It was then inflated until the pressure is equal to 180 mmHg; at this point the pressure sensor tube was clipped off to eliminate any influence on the measured cavity volume. The volume of liquid in the syringe was noted, and the fluid within the balloon was withdrawn. The difference in volume was recorded as the cavity volume during TRS treatment.
7. The meat model was placed within a plastic bag, with the thermocouple-computer plugs kept outside to prevent wetting. The bag was placed within warm water (39-42°C) to accelerate warming to physiological temperature. The water bath temperature was maintained constant throughout the warming process.
8. The TRS unit was turned on and the glycerine was warmed to treatment temperature. A platform for the meat was constructed such that the simulated cervical canal was level with the balloon.
9. Once the meat cavity temperature has warmed to 37°C the meat model was removed from the water bath and placed on the platform. The thermocouples were attached to the computer and the mapping of the thermocouple label to the data logger label was recorded. The logger program was used to check that thermocouples are performing properly.
10. The TRS device was inserted to the correct depth and the logging program was

started. The treatment was initiated after a final check of the apparatus. Care was taken to avoid applying torque to the shaft, as this may result in hot or cold spots at the cavity surface (see Figure 36). Once treatment was complete, the cavity volume (as reported by the TRS device) is recorded. The device was removed and data logging stopped.

11. The meat model was transferred to a table for dissection. The cavity was opened and the location of the disk thermocouples were noted, both with regard to the coagulated tissue indicative of the balloon contact area and with regard to whether placement was at the top or bottom during treatment. If deep tissue thermocouples were used they were dissected and the depth from the cavity surface was measured.

5.3 Parameter Estimation

For the TRS model, there were three parameters whose values could not be obtained from the literature or from available correlations or measured directly: the heat transfer coefficient, the balloon residual volume and the "excess glycerine" that accounts for heat stored in the TRS device. Originally a silicone model of the uterus was to be used to calibrate the computer model; however concerns arose that the calibrated parameter values would not be well suited to describing the events in animal tissue. For example, the thermal diffusivity of silicone rubber is not very different from tissue, 15×10^{-4} $cm^2 \cdot s^{-1}$ for silicone as compared to 13.8×10^{-4} $cm^2 \cdot s^{-1}$ for animal tissue. Therefore silicone and animal tissue will behave similarly given the same constant temperature boundary condition. However the thermal conductivity and heat

capacity are both less than half the value found in tissue. When a specific flux of heat is utilized as the boundary condition, as is the case for the TRS model, the temperature at the boundary will increase more quickly for silicone than for tissue due to the lower heat capacity. In fact this was observed in the trials; the maximum cavity surface temperature in the silicone model uteri was observed to be above 120°C. In addition to having different thermal properties, the silicone model uterus was also much less flexible than the meat model; because passive deflation is used for most pulsation cycles, the balloon was observed to have a residual volume nearly as large as the cavity volume of the uterus. It is expected that this condition favoured natural convection over forced convection, and would therefore result in an artificially low heat transfer coefficient.

Meat trials were therefore used for both model calibration and validation. A trial using an intermediate cavity volume (16 mL) was selected for experiments to validate the model. The balloon temperature and cavity surface temperatures were used for evaluating the fit of the model predictions to the data collected. Although data was available from two thermocouples implanted within the tissue, these data were not used for fitting. Identifying the correct depth of thermocouples after a treatment was a difficult task. There is no way to be sure that the thermocouple has not moved following the treatment or during dissection; due to the large temperature gradients, small changes in position can have a very large impact on the reported temperature. Analysis of goodness of fit was done visually; the variability was not expected to be constant during treatment and therefore an error minimization routine would be expected to be biased. For example, if positional uncertainty were the only source of

error, then it would be expected that variability would be proportional to the temperature gradient. For parameter estimation, a stochastic approach was used to determine the values that gave the best fit. Finally the parameters were increased or decreased by 20% in all possible combinations in order to demonstrate that the fit is optimised; the results confirm that the parameters chosen represent the closest fit to the observed data. The model predictions using the estimated parameters are presented along with the data in Figure 37. Although it is possible that this parameter set represents only a local optimum, experience during the evolutionary fitting process suggests that the parameters are, with a high degree of probability, the global optimum.

The parameters chosen are presented in Table 5. The heat transfer coefficient, effective glycerine volume and additional residual volume during passive deflation were fitted, while the minimum residual volume was selected to be 0.5 mL based upon the estimated volume of the balloon, shaft and glycerine film in the deflated balloon. The parameter values appear to be physically reasonable, for example the heat transfer coefficient chosen (325 $W \cdot m^{-1} \cdot K^{-1}$) is similar to that found for hot oil (250 – 500 $W \cdot m^{-1} \cdot K^{-1}$ (133)). The heat transfer coefficient and the effective glycerine volume had very large effects on the temperature profile. However the temperature profile was insensitive to the effect of variations in the residual volume, this parameter is expected to have a larger effect in small cavity volumes.

Table 5 – The parameter values selected for the TRS heat balance model.

Parameter	Value
Heat Transfer Coefficient	325 $W \cdot m^{-2} \cdot K^{-1}$
Glycerine Volume	38 mL
Active Deflation Residual Volume	0.5 mL
Added Residual Volume During Passive Deflation	1.5 mL

Chapter 6: Model Validation

In this chapter the model validation is described where data from the literature and from clinical trials were compared with model predictions. Several approaches were used to validate the thermal ablation model developed in this thesis. Data available in the literature were compared to model predictions for the same treatment protocol. In addition, model predictions were compared with temperature data from the meat-model experiments conducted using cavity volumes over the range that may be encountered during clinical use. Finally a limited amount of balloon temperature and burn depth information was available from *in vivo* clinical trials.

6.1 Model Validation Using Published Data

A limited amount of data was available with which to test the model, and often not enough information was given to calculate model parameters. However some useful data was found, and with a few assumptions, were used to determine if the model predictions are at least realistic. In studies where cavity volume is not given, the initial volume was assumed to be 7.8 mL, resulting in an 11 mL cavity volume when 180 mmHg of pressure is applied (as this was the average of uterine cavity volumes reported in the literature).

The first study examined in this section did not involve thermal balloon ablation; rather free saline was infused into the uterus (24). But the data were useful because

the thermal resistance of the thin material during thermal balloon ablation is expected to be small. Data from this study are given in Table 6. No cavity surface temperatures were reported, therefore the cavity surface temperature was assumed to be equal to the bulk saline temperature. The minimum serosal temperature recorded during treatment was 26°C, this is below the normal physiological temperature of 37°C and may result in a burn depth that was lower than predicted; however the mean temperature amongst individuals ranged from 34 to 38°C. Intrauterine pressure varied from 27 to 57 mmHg during treatment, however an average pressure of 41 mmHg was used for model verification purposes. Burn depth was evaluated by a combination of gross histochemical staining, hematoxylin and eosin, and nitroblue tetrazolium staining. The predicted burn depths were in good agreement with the experimental data at temperatures of 80°C or higher. However one of the treatments at 80oC resulted in significantly smaller burn depths (2.0 – 2.4 mm) than the other equivalent treatments (3.5 – 4.2 mm), the reason for this discrepancy is not known.

Table 6 – Comparison of the predicted burn depths with experimental results of Bustoz-Lopez et al. (24). Uterus cavity volumes were not reported, thus all volumes were assumed to be 7.8 mL prior to internal pressurization. The lower alpha and upper beta burn depths are expected to correspond to the depth of histochemical staining.

Trial Number	**1**	**2**	**3**	**4**	**5**	**6**	**7**	**8**	**9**	**10**
Bulk Saline temperature(°C)	70	70	80	80	80	80	85	85	85	85
Treatment time (min)	17	17	15	15	15	15	15	15	15	15
Pressure (mmHg)	36.5	42.5	46	41.5	31	55	31	54.5	53	51
Experimental Burn Depth (mm)										
Gross Examination	4.8	4.8	3.5	4.0	2.0	4.1	4.0	5.3	4.8	6.0
Hematoxylin and Eosin	4.8	5.1	3.7	4.0	2.3	4.1	4.0	4.7	4.7	4.0
Nitroblue Tetrazolium	4.9	5.1	3.7	4.0	2.4	4.2	4.1	4.9	4.7	4.5
Simulated Burn Depth (mm)										
Alpha – Lower	**2.7**	**2.8**	**3.9**	**3.8**	**3.6**	**4.1**	**4.0**	**4.5**	**4.5**	**4.5**
Beta – Upper	**3.3**	**3.4**	**4.5**	**4.4**	**4.1**	**4.7**	**4.6**	**5.1**	**5.1**	**5.1**

Data were also available from a study using the Cavaterm™ device (32). Two patients were treated using different protocols, and the depth of histopathological destruction was measured. Unfortunately the criteria used to define histopathological damage were not explicitly stated, and it is not clear to which burn category these results correspond. The experimental data and simulated results are presented in Table 7. If the beta burn depth corresponds to the depth of histopathological damage, then the agreement with the model predictions with the data are very good.

Table 7 – Comparison of histopathologically determined burn depth from the data of Friberg et al. with the predicted burn depths for the Cavaterm™ device. Cavity volume information was not given, therefore the standard cavity volume was not known. However differences in cavity volume may therefore explain discrepancies between the observed and predicted burn depth. It is expected that the histopathological burn depth corresponds to the beta burn depth; however without elaboration of the burn boundary criteria this presumed correspondence is tentative.

Experiment Number:	1	2
Treatment temperature (°C)	75	61.5
Treatment time (min)	35	34
Balloon pressure (mmHg)	225	175
Measured Burn Depth (mm)	8	6-7
Simulated Burn Depths (mm)		
Alpha – Upper	2.8	0
Alpha – Middle	5.4	2.0
Alpha – Lower	7.4	4.4
Beta – Upper	8.2	5.4
Beta – Middle	**9.7**	**7.0**
Beta – Lower	11.8	9.2

Neuwirth et al. (29) reported the results of two trials with the Thermachoice™ 1 device. The first is the Mexico City Safety and Effectiveness Study (Table 8), and the second is the London Safety and Effectiveness Study (Table 9). In these trials, both the balloon cavity volume and the endometrial temperature were recorded. The Thermachoice™ 1 device does not contain a mixing device, relying on natural convection to prevent thermal stratification within the balloon. Only the maximum balloon surface temperature was reported; it is not known if this temperature was consistently maintained throughout the treatment procedure.

Table 8 – Mexico City trial results reported by Neuwirth et al. (29), as compared to the model predictions. Cavity volume information for these trials was available for all but one trial, in that case the standard cavity volume was assumed. The burn depth described is either the depth of coagulation or visible erythema, a description that may refer to either an alpha or a beta burn. The variability of the experimental burn depths limits the conclusions that can be drawn from this data set regarding the correspondence of the model predictions. It is likely that the 10mm reported burn depth refers to erythema, while the 4mm burn depth refers to the depth of coagulation.

Experiment Number	1	2	3	4	5	6
Balloon Fluid Temperature (°C)	87.7	89.4	89.4	89.4	88.3	97.2
Treatment time (min)	6	8	10	11	12	7
Balloon pressure (mmHg)	75	75	75	75	75	75
Cavity Volume (mL)	Unknown	3	5	10	4	8
Measured Burn Depth (mm)	4	5	10	8	6	5
Simulated Burn Depths (mm)						
Alpha – Upper	2.4	2.0	2.3	2.6	2.2	2.9
Alpha – Middle	3.4	3.1	3.5	4.0	3.4	4.2
Alpha – Lower	4.6	4.2	4.6	5.2	4.5	5.3
Beta – Upper	5.4	4.8	5.3	5.9	5.1	6.0
Beta – Middle	6.4	5.7	6.2	6.9	6.0	7.0
Beta – Lower	7.6	6.9	7.5	8.3	7.4	8.2

Table 9 – London Safety and Effectiveness trial results reported by Neuwirth et al. (29), as compared to the model predictions. Cavity volume information for these trials was available for all but one trial, in that case the standard cavity volume was assumed. Burn depth was determined using diaphorase staining.

Experiment Number:	1	2	3	4
Balloon Fluid temperature (°C)	87.7	89.4	89.4	89.4
Treatment time (min)	6	6	6	6
Balloon pressure (mmHg)	75	75	75	75
Uterine Cavity Volume (mL)	Unknown	3	5	10
Measured Burn Depth (mm)	5.1	3.3	4.2	4.3
Simulated Burn Depths (mm)				
Alpha – Lower	4.6	4.0	4.3	4.8
Beta – Upper	5.4	4.7	5.1	5.6

The Thermachoice™ 1 system was also evaluated, using light and electron microscopy, by Andersen et al. (31). The results are presented in Table 10. Balloon pressure for this trial was 160 mmHg, higher than in the Neuwirth trial. The mean body core temperature was only 35°C, lower than the standard blood temperature. Uterine cavity volumes were not reported.

Table 10 – Comparison of the results of Andersen et al. (31) with model predictions. Cavity volume was not reported, therefore the inflated volume of 11 mL was used. Balloon pressure was 160 mmHg. Macroscopic coagulation depth was determined visually, while microscopic burn depth was determined with light microscopy. Electron microscopy was also used to analyse cell depth, where condensed and ruptured nuclei indicated coagulation, and damaged or destroyed plasma membranes and mitochondria indicate severe cell damage. The depth of the alpha burn is best compared to the depth of widespread coagulation under electron microscopy, while the depth of severe cell damage is believed equivalent to the depth of the beta burn.

Experiment Number	1	2	3	4	5	6	7	8
Temperature (C)	87	87	87	87	87	87	87	87
Time (min)	8	14	14	14	15	16	16	16
Maximum Macroscopic Coagulation Depth (mm)	NR	4	3	2	4	1	4	3
Maximum Microscopic Coagulation Depth (mm)	3.8	5.0	3.2	2.7	2.9	11.5	3.9	3.8
Electron Microscopy Coagulation Depth	**Total coagulation 0-4 mm Widespread coagulation 4-6 mm**							
Electron Microscopy Depth of Severe Cell Damage	**6-9 mm**							
Simulated Burn Depths (mm)								
Alpha – Upper	2.8	3.2	3.2	3.2	3.3	3.3	3.3	3.3
Alpha – Middle	**4.5**	**5.0**	**5.0**	**5.0**	**5.0**	**5.1**	**5.1**	**5.1**
Alpha – Lower	6.0	6.4	6.4	6.4	6.5	6.5	6.5	6.5
Beta – Upper	6.9	7.1	7.1	7.1	7.2	7.2	7.2	7.2
Beta – Middle	**7.8**	**8.1**	**8.1**	**8.1**	**8.2**	**8.2**	**8.2**	**8.2**
Beta – Lower	9.0	9.4	9.4	9.4	9.4	9.5	9.5	9.5

NR – Not recorded

The depth of coagulation observed in the data of Andersen et al. indicates a slight tendency of the model to overestimate burn depth (approximately 1-2 mm). However in one case the coagulation zone extended 11.5 mm from the fundus

and no explanation was offered for the discrepancy. Although this patient had the greatest rise in serosal temperature (38.8°C), one may hypothesize that this uterus had a reduced blood perfusion rate. Electron microscopy was also used in this study to determine the depth of tissue damage. From 0-4 mm total coagulation was observed and collagen fibers were mostly unrecognisable. Widespread coagulation was observed from 4-6 mm, though collagen fibers were only a little disorganized. Note that this is in agreement with the estimate alpha burn depth of approximately 5 mm. Severe damage was evident from 6 – 9 mm, the cells appeared dead or dying, and muscle actin organization was disturbed. This also compares favourably to the estimated beta burn depth of 7.1 to 9.5 mm, assuming that the severe damage noted does result in eventual necrosis of the tissue. From 9-15 mm there was moderate to slight damage (slightly condensed nuclear spaces and coarsening of organelle structure), and past 15 mm no cell damage was observed.

An examination of the published endometrial ablation clinical trials indicates that there is a significant amount of variability for the burn depth, even utilizing the same device and treatment protocol. In the data of Andersen et al. (31), light microscopy of coagulation burn depth following very similar treatments resulted in maximum burn depths ranging from 2.7 to 11.5 mm. In another study the depth of erythema was determined immediately following treatment with the Thermachoice™ 1 device followed by hysterectomy in six patients (163). On gross examination the mean red zone depth was 5.4 mm (range 3-9 mm). In comparison the calculated depth of the beta burn, which is believed to be correlated with the depth of the red zone, for the treatment parameters is 6.6 mm. The depth of the red zone ranged from three to nine

millimeters amongst just six patients in this study. In the Mexico City trial of Neuwirth et al. (29), the reported burn depth ranged from 4 to 10 mm, although this depth could be either coagulation or erythema and therefore this variation probably represents the selection of different damage threshold types by the clinicians (the threshold used was not specified for each trial). The inter-individual variation is a cause for concern; is this uncertainty real or is it an artefact of how burn depths are determined amongst multiple observers? In other cases the cause of the variability may be inter-individual blood perfusion responses to hyperthermia, although differences in balloon pressure or the extent of balloon contact could also be responsible.

The large variability in the burn depths reported in the literature on endometrial thermal ablation limit the conclusions that can be drawn from this data regarding the model's validity for simulation of fixed temperature and volume ablation devices. It would be useful if, during *in vitro* trials, endometrial ablation researchers would use thermocouples at the cavity surface and demonstrate that the maximum bulk fluid temperature really can be acceptably used in place of the cavity surface temperature. During *in vivo* trials magnetic resonance imaging could be used to determine the exact temperature distribution throughout the uterus; this would be an extremely desirable experiment. Further experiments to better characterize the blood perfusion response to hyperthermia, pressure and thermal damage would be very desirable. Finally all parameters important for performing simulations should be included, in particular the volume of the distended cavity.

6.2 Validation Using Meat-Model Experimental Data

The meat-model data were used to validate temperature versus time and distance model predictions. Burn depth was difficult to measure, there was a gradual change in the extent of coagulation instead of a sharp demarcation; thus predicted burn depth could not be compared with meat-model data.

The tissue thermal conductivity was assumed to be 0.528 $W \cdot m^{-1} \cdot K^{-1}$, based on the majority of reported values for bovine muscle tissue (164); however it should be noted that the thermal conductivity range was from 0.197 to 0.545 $W \cdot m^{-1} \cdot K^{-1}$. Both the perfusion rate and the metabolic heat generation rate parameters were set to zero. Graphs of the experimentally determined and simulated temperature-time series are reported in Appendix C. The meat-model experiments were performed in two phases. An initial experiment was used to calibrate model parameters (see section 5.3) and later experiments validated the model predictions.

6.2.1 Balloon Temperature Prediction

The model generally was very successful at predicting the balloon temperature-time series across the full range of cavity volumes tested (5 – 26 mL), despite having the parameters only calibrated from a meat experiment with a 16 mL cavity volume. Although the average temperature over a pulsation cycle was generally correct, the temperature-time series over each pulsation period was qualitatively different. The simulated temperature-time series was much sharper than the observed data, which lacked discontinuities.

This difference is attributed to two of the model simplifications: that the balloon is fully mixed and that fluid exchange occurs immediately. In practice, at the end of a pulsation the balloon fluid will be partially mixed. As deflation occurs the hottest glycerine will be removed, then cooler and cooler glycerine will pass the thermocouple. The reverse will occur upon inflation, since the reservoir is expected to be only partially mixed as well. The worst fit, although still good, occurred at the smallest cavity volume, where the total volume was closest to the residual volume (Trial 12-13-01A) and the model assumptions were under the greatest stress.

Interestingly the fitted glycerine volume parameter value is significantly larger than the actual liquid volume within the reservoir. Only 32.5 g of glycerine are inside the device, this translates into a volume of 25.7 mL – yet the calibrated volume is 38 mL. Two explanations, possibly complementary, are proposed to explain this result.

The first is that the 'volume of glycerine' is not really a measure of liquid volume but of the heat stored in the TRS apparatus prior to treatment. The reservoir is surrounded by a metallic heating device, this device is in thermal equilibrium with the glycerine at the start of treatment (the exterior of the device, although insulated, becomes warm to the touch when sufficient heating has occurred). It is proposed that the reservoir contacting parts of the TRS contribute heat once the glycerine is cooled by contact with the tissue. The second proposed explanation is that incomplete balloon contact may reduce the surface area that is available for heat transfer, causing less total heat to be lost than expected for a given temperature gradient.

6.2.2 Surface Temperature Prediction

The model appears to have accurately predicted the cavity surface temperature, within the limits of the experimental variation. Interpretation was complicated by the lack of quantitative and qualitative agreement among different thermocouples within even the same trial. In some trials, including the calibration trial, one thermocouple would exhibit a distinct "saw tooth" pattern while the other would report a smoothly varying temperature profile. The maximum temperature obtained could also vary significantly. For example, in trial 11-29-01B the maximum temperature difference between thermocouples is almost 20°C.

Perhaps the most important cause of variation is the extremely high temperature gradient at the balloon-tissue interface. Considering that the disc thermocouples were approximately 0.5 mm in thickness, factoring in the solder and wire, there is scope for significant error. Using equation 10 and the calibrated heat transfer coefficient, the thickness of the hypothetical boundary layer is predicted to be only 0.9 mm; this indicates that even a slight protrusion into the balloon will significantly bias the result. If any thermocouples became embedded in the meat or balloon (Figure 38), deviations will be observed.

In some cases it is believed that the thermocouple was only partially contacting the balloon. This appears to have occurred in trial 2-01-02B, where the surface

temperature at the top of the cavity behaves anomalously. In the first 20 seconds of the trial it appears to be asymptotically approaching approximately 100-105°C, as expected from the model. However there is a sudden qualitative change and the temperature converges instead on 80°C. The proposed explanation is that the thermocouple shifted within the cavity at the end of the active pulsation cycles.

Although in some cases reported surface temperatures have deviated from model predictions, in most cases the deviations have been small. Where multiple thermocouples have been used the average value is close to the model predictions. In future experiments an improvement may be obtained by attaching the thermocouple directly to the balloon material.

6.2.3 Deep Tissue Temperature Prediction

The data from thermocouples implanted inside the meat itself appear to support model predictions, although these data have not been as useful as the balloon fluid and surface temperature data due to larger variability. In some cases the fit is excellent, such as the 5 mm depth of 5-25-01 or 12-13-01A. In other data sets the discrepancy is much worse, such as the 4 mm thermocouple in 11-29-01B.

There are two main sources of experimental error: movement of the thermocouple during manual manipulation and the inflation/deflation cycle, and the difficulty of estimating of thermocouple depth during dissection. It is estimated that thermocouple position can't be determined with an uncertainty less than 1 mm.

Where there is a discrepancy between model predictions and experimental data, it is generally less than expected from the positional uncertainty. For example, in trial 11-29-01B, the temperature data at 4 mm depth is compared to the simulation results; although the simulation data appears to be a poor fit, the predicted temperature data 1 to 1.25 mm closer to the cavity surface is a nearly perfect match.

Not all discrepancies may be explained by positional uncertainty. For example in trial 2-01-02B, the data from the 1.5 mm depth thermocouple does not qualitatively match model predictions at any depth; yet the 2.5 mm depth thermocouple is in excellent agreement with the model predictions. It is proposed that in this case the temperature deviation is physically real and is due to incomplete balloon contact or other surface temperature inhomogeneities; this hypothesis is supported by the unusual nature of the recorded surface temperature data.

In the majority of cases, the temperature profile was accurately predicted, within the limits of thermocouple position uncertainty. Greater accuracy may be obtained in future experiments by obtaining X-ray images of the cavity during the inflated phase of the treatment cycle, and by minimizing thermocouple movement during post-treatment meat manipulation and thermocouple dissection.

6.3 Validation using Clinical Trial Data from the TRS Device

The best data with which to compare the model are those obtained from clinical trials. Ten clinical trials were conducted with the TRS device, three in Canada and seven in Mexico. Only seven of these trials were used in this thesis, either due to problems in determining the cavity volume or to a violation of model assumptions (in this case a myomatous growth that would not allow the balloon to conform to the model geometry). During these clinical trials, no data were collected on the balloon surface temperature or temperatures through the uterine wall due to safety concerns (risk of perforation of either the balloon or the uterus).

In the Canadian trials, balloon-fluid temperature measurements were made manually utilizing a 'J' type thermocouple implanted in the balloon and a hand-held digital readout. During the first 30 seconds, data were obtained at the refresh rate of the display (1.21 seconds), and afterwards data were recorded every five seconds. The treatment protocol during the first two trials was only 90 seconds long; the third treatment was conducted for the full 130 seconds. During the first two trials all balloon deflations were performed passively, therefore a passive balloon residual volume was used throughout the cycle. Cavity volumes were measured independently at the treatment pressure; displaced cavity volumes were 5.5, 8.5 and 21 mL for the first, second and third experiments, respectively. Comparisons of the simulated and experimental balloon temperature time-series are presented in Figures 39 - 41. The match between the predicted and observed balloon temperature-time series was

excellent, for example in figure 40 and 41 throughout approximately half of the graph the predicted line is obscured by the data points. The smallest cavity volume (5.5mL) provided the worst fit, although the cavity volume is approaching the residual volume and deviations between the actual and model residual volumes will have an increasingly large effect. A comparison between the predicted and observed maximum burn depth, as determined by nitroblue tetrazolium staining, is presented in Table 11.

Table 11 – The maximum reported burn depth of the TRS Delta hospital trials is compared to the burn depth predicted by the model. Burn depth refers to the depth of NBT staining (believed equivalent to the lower alpha or upper beta burn depth), additionally in CT0011-06 the depth of erythema was also reported (the right hand figure in the measured burn depth column). Balloon fluid temperatures and treatment times are given in Figures 39-41. Burn depth data were recorded at many positions within the cavity, the maximum was recorded due to concerns that low burn depths were due to incomplete balloon contact.

	CT0011-04	CT0011-05	CT0011-06
Uterine Cavity Volume (mL)	5.5	8.5	21
Maximum measured Burn Depth (mm)	2	4	4.5/6.0
Predicted burn Depth (mm)			
Alpha – Upper	1.2	1.8	2.8
Alpha – Middle	2.3	2.9	4.3
Alpha – Lower	**3.3**	**4.0**	**5.7**
Beta – Upper	**4.1**	**4.7**	**6.6**
Beta – Middle	4.7	5.4	7.5
Beta – Lower	5.5	6.2	8.6

The depth of the red zone, which may be associated with the maximum extent of necrosis, was available in one trial (CT0011-06). The model estimated the depth of eventual necrosis (most probable beta burn) as 7.5 mm, which was 1.5 mm greater than the observed depth of the red zone. However, one data point is not enough and clearly more clinical trials are needed in which the red zone is measured.

Four of the seven Mexican clinical trials contained enough data to compare with model predictions. Data for these clinical trials and the model predictions are presented in Table 12.

Table 12 – Comparison of the TRS experimental results of the Mexico trials with the predicted burn depths. TRS cavity volumes have been assumed to be correct, although the estimate is considered only approximate. Burn depth was determined by nitroblue tetrazolium (NBT) and hematoxylin and eosin (H&E) staining. The depth of erythema was not recorded.

Trial Number:	112-01-001	112-01-002	112-01-04	112-01-007
Uterine Cavity Volume	16	19	21	24
Maximum Experimental Burn Depth – NBT (mm)	4.0	3.2	4	5
Maximum Experimental Burn Depth – H&E (mm)	6.6	2.5	6	4.5
Predicted burn Depth (mm)				
Alpha – Upper	2.8	2.8	2.8	2.8
Alpha – Middle	4.3	4.3	4.3	4.3
Alpha – Lower	**5.6**	**5.6**	**5.7**	**5.7**
Beta – Upper	**6.5**	**6.5**	**6.6**	**6.6**
Beta – Middle	7.4	7.4	7.5	7.5
Beta – Lower	8.5	8.6	8.6	8.7

In the Canadian trials the lower alpha and upper beta burn depth was 1-3 mm greater than the depth of staining. The Mexico trials are less useful; the cavity volume was not determined independently (see meat trial protocol) and therefore only the much less accurate TRS volume estimate was available. The model predicted depth of staining was 5.6 - 6.6 mm (upper alpha and lower beta burn), however the observed depths ranged from 2.5 to 6.6 mm. The reported burn depth is the maximum observed from many positions within the cavity. The maximum burn depth, rather than the average over the uterus cavity, was included because in these trials we suspect that

there was insufficient balloon-uterus surface contact since the reported uterine cavities were much larger than expected.

The same stain was not used for all the clinical trials. In the Mexico trials the stains were nitroblue tetrazolium and hematoxylin and eosin. In one case where the two stains were used on the same uterus sample, they gave estimates that were up to 2.6 mm apart. Furthermore this discrepancy was not consistent; in half of the trials NBT staining yielded the greatest burn depth while in the other half the situation was reversed. The disagreement between different stain types suggests that the burn depth is genuinely variable, and that there is a limit to the predictive accuracy that may be achieved with a computer model.

The meat trial data indicate that the model approximately predicts the correct temperature-profile in the meat model uterus. Therefore it appears that the discrepancy appears when a living uterus is substituted for the meat model. Although it is possible that the Arrhenius damage integrals used are incorrect for the human uterus, the parameter limits cover a large range and it seems unlikely that uterine tissue is that different from the other tissues used to calibrate the Arrhenius parameters. Therefore it seems that the explanation is most likely related to either the switch from *in vitro* to *in vivo*, or to the change from bovine muscle uterus analogue to the human uterus. One possible explanation is that balloon contact is more intermittent *in vivo*, for example the balloon may be directed preferentially into one horn of the uterus.

The most likely reason for the discrepancy between the *in vitro* and *in vivo* trials is that the blood perfusion rate is incorrect. Although sufficient information was available regarding the baseline perfusion rate, little was found regarding the response to hyperthermia. All information related to other tissue types, and was often not in quantitative agreement. There is no way of knowing if the uterus responds to hyperthermia in a manner identical to other muscle tissues. In general it is mild hyperthermia that has been studied; it is possible that the high temperature associated with endometrial ablation invokes a different perfusion response. Doppler ultrasound of the uterine artery during *in vivo* treatment would help to quantify the variation of the blood flow to the entire uterus during treatment, although such an approach would not provide the fine-scale perfusion information that would be most desirable for model validation. Basic experiments in other more accessible tissues, aimed at developing an equation of state for the blood perfusion rate during hyperthermia, would be very desirable.

Another possible explanation, one that also relates to the tissue perfusion rate, is that the model of pressure induced perfusion reduction is incorrect. Note that this issue is different from the uncertainty regarding the stress distribution within the uterus wall; there is also uncertainty regarding the effect such stress has on the perfusion rate. The difficulty of determining what calibre of blood vessel is associated with the perfusion term of the Pennes equation has already been discussed. If larger vessels should prove more important, then the critical stress will be higher and the reduction in perfusion rate will be correspondingly smaller. Certainly the model indicates a great deal of sensitivity to the critical pressure factor, as is presented in Table 13. A two-

phase experiment using artificially perfused uteri obtained by hysterectomy would improve the model parameter estimates; the first phase to evaluate the relationship between vessel calibre and stasis pressure in the uterus, and the second phase to use the developed relationship to assess the importance of each vessel size to heat transfer throughout the tissue.

It has been assumed that the stress distribution may be estimated, even if a linear stress-strain is used in place of the approximately exponential relationship experimentally determined. If the actual stress distribution allowed perfusion to occur closer to the cavity surface, then the model would predict lower burn depths. It is recommended that the stress distribution be solved numerically for the non-linear elasticity relationship. Ideally pressure transducers could be implanted at various depths throughout the uterus, however it should be remembered that the effect of muscular contractions on the pressure distribution could limit the usefulness of in vitro experiments.

In this computer model, the compression of the tissues during inflation that allows the burn depth to reach further than would occur if the inflated radius was the natural (uninflated) radius of the cavity. The burn depth has been reported in the undistended state, because that is the condition where the endometrium thickness is measured following hysterectomy. The distension causes a significant increase in the depth of the burn. Tor example at the largest cavity volume in the Mexico TRS trial the lower beta burn depth was 1.2 mm greater if distension was taken into account.

If significant compression of the inner cavity tissues does occur it may explain part of the increased success observed when higher balloon pressures are used in place of lower ones (116). Alternatively if it does not occur significantly one may hypothesize that the increasing volume is obtained during inflation by 'recruiting' noncontacting tissue, rather than by stretching material already in contact with the balloon (see Figure 42). The magnitude of the tissue compression effect could be determined by either ultrasound or magnetic resonance imaging of the endometrium and myometrium junction in the undistended and distended state.

Despite a tendency to overestimate the burn depth of these clinical trials, it should be emphasized that the mean of the upper alpha and lower beta burn only deviated from the reported depth of vital staining by an average of 1.2 mm, which is less than the reported inter-individual differences in reported burn depths for similar cavity volumes.

Chapter 7: Model Analysis And Safety Implications

In this section the model is analysed for safety and efficacy implications. The sensitivity to input parameters, such as cavity volume and the blood perfusion rate, is evaluated. The effect of possible tissue water vaporization, which may potentially be induced by the heated glycerine, is examined and quantified. The model is used to determine the optimal treatment protocol, and determine if the TRS may be improved. Finally the implications of the model predictions for the safety of the peritoneal organs are discussed.

7.1 Parameter Sensitivity Analysis

In this section the sensitivity of the model results to input parameters is assessed. Because the Thermachoice™ 2 device and the TRS may differ in their sensitivity, both were examined. Calculated alpha and beta burn depths (in Table 13) and temperature profiles through the uterine wall are compared for the two devices for various multiples of the original parameter values.

Table 13 – Sensitivity Analysis of model parameter values for both the TRS and Thermachoice™ device. Only the most probable alpha and beta burn depths (in mm) are presented, for the sake of simplifying the presentation. In cases were a null value for the parameter was inappropriate, N/A is displayed (for example if thermal conductivity was zero, there would be no effect of thermal treatment).

	TRS Device				Thermachoice™ 2 Device			
Parameter tested	x0	x1/2	x1	x2	x0	x1/2	x1	x2
Thermal Conductivity k_t	N/A	3.5/5.7	**4.1/7.1**	3.8/7.9	N/A	4.3/7.6	**5.0/8.8**	5.6/10.1
Heat Capacity c_t	N/A	5.4/9.0	**4.1/7.1**	2.7/4.2	N/A	5.3/9.1	**5.0/8.8**	4.3/7.9
Base Perfusion Rate ω_b	4.3/8.5	4.2/7.4	**4.1/7.1**	4.0/6.9	5.9/12.0	5.3/9.6	**5.0/8.8**	4.7/8.1
Perfusion Time - Response θ	N/A	4.1/7.0	**4.1/7.1**	4.1/7.1	N/A	4.9/8.6	**5.0/8.8**	5.1/9.1
Maximum Perfusion Multiplier	N/A	4.1/7.2	**4.1/7.1**	4.1/7.1	N/A	5.1/9.2	**5.0/8.8**	4.8/8.3
Perfusion Temperature Sensitivity ϕ	N/A	4.1/7.1	**4.1/7.1**	4.1/7.1	N/A	5.1/9.1	**5.0/8.8**	4.9/8.5
Vascular Stasis Pressure	N/A	4.1/7.2	**4.1/7.1**	3.9/6.8	N/A	5.6/10.3	**5.0/8.8**	4.1/7.2
Vascular Stasis pre-exponential term	N/A	4.1/7.1	**4.1/7.1**	4.1/7.1	N/A	5.0/8.8	**5.0/8.8**	5.0/8.8
Metabolic Rate q_m	N/A	4.1/7.1	**4.1/7.1**	4.1/7.1	N/A	5.0/8.8	**5.0/8.8**	5.0/8.8

The model was insensitive to the following parameters: perfusion response half time, maximum perfusion multiplier, perfusion temperature sensitivity, vascular stasis A-term, and the metabolic rate.

From this sensitivity analysis it appears that the TRS device is considerably less affected by parameter variables than the Thermachoice™ 2 device. For example, the predicted depth of immediate necrosis (alpha burn) for the TRS only differs by 0.3 mm for a perfusion rate that ranges from null to double; the range of the Thermachoice™ 2 device over identical conditions is 1.2 mm. This is primarily due to the short treatment time for the TRS device(2 min) as opposed to the longer treatment time for the Thermachoice device (8 min). In the TRS device, the temperature profile has not reached steady state after 2 minutes and elevated temperatures are predominantly in the un-perfused zone, as seen in Figure 43. In contrast, in the Thermachoice™ treatment protocol, the temperature profile has reached steady state after 8 minutes, as seen in Figure 44, and blood perfusion becomes an important heat sink to prevent excessive thermal penetration into the uterine wall and surrounding tissues.

The most sensitive parameter is the tissue thermal conductivity, however the expected variation of this parameter is small. A study of 13 different uteri found the coefficient of variation was only 1.5% (136). However it is instructive to discuss why the current thermal conductivity yielded the maximum alpha burn depth in the TRS device. At a half the expected thermal conductivity the penetration of heat is too low to result in a deep coagulation depth, while at twice of expected thermal conductivity the heat is removed too quickly and the temperature isn't raised sufficiently high at the coagulation boundary (see Appendix D).

The qualitative effects of changes in heat capacity are very different in the TRS and Thermachoice™ device. In unperfused tissue treated with the Thermachoice™

device, a change in thermal conductivity may be compensated by a change in the heat capacity; only the thermal diffusivity (the thermal conductivity divided by the product of the heat capacity and tissue density – see equation 5) determines the temperature profile. In perfused tissue this relationship no longer holds, the temperature profile is determined by both the thermal diffusivity and the perfusion term. Therefore in perfused tissue a change in the heat capacity must be accompanied by a change in both the thermal conductivity and perfusion rate, if the same temperature profile is to be maintained.

In contrast, the TRS temperature profile is a function of both the thermal diffusivity and heat capacity even in unperfused tissue. The rate of change of temperature at the cavity surface, for a given tissue temperature gradient at the start of the time step, is a function of the heat transfer coefficient, the surface and balloon temperature, and the heat capacity-density product. Therefore the boundary conditions will be different, even if the thermal conductivity is adjusted to maintain the identical value for thermal diffusivity.

The next most sensitive parameter is the pressure at which we assume blood perfusion stops. The relationship between this factor (used in equation 17), burn injury and temperature-induced changes in blood flow are examined further in Table 14.

Table 14 – The effect of enabling or disabling the three perfusion modification factors are examined. A 'plus' sign indicates that that factor is engaged. Only the most probable alpha and beta burn depth are presented. Pressure factor refers to the perfusion reduction induced by stress in the tissue, burn factor is vascular stasis induced by thermal damage and temperature factor is the increased perfusion response to hyperthermia. When pressure factor is disengaged then the perfusion rate is not reduced in response to mechanical tissue stress. If the burn factor is disengaged then the effect of vascular stasis is neglected, thermal damage does not reduce the perfusion rate. Disengagement of the temperature factor results in a perfusion rate that is not increased in response to local hyperthermia. The important result of this table is that the burn and temperature factor effects are diminished because the balloon pressure eliminates blood perfusion in the zone of tissue where these factors can influence the temperature distribution, these factors are expected to become more important if the balloon pressure is reduced.

Pressure Factor	Burn Factor	Temperature Factor	TRS	Thermachoice™ 2
+	+	+	4.1/7.1	5.0/8.8
+	+		4.1/7.4	5.3/9.8
+		+	4.0/7.1	5.0/8.8
+			4.1/7.4	5.3/9.8
	+	+	3.2/5.7	3.1/5.6
	+		3.7/6.7	4.4/8.1
		+	2.3/4.8	2.2/4.8
			3.1/6.1	3.7/7.5

It is evident that the pressure factor, PF, dominates the determination of burn depth because the perfusion is shut down in much of the region of elevated temperature; this is particularly true for the TRS where other factors had little effect on burn depth. The depth of vascular stasis is effectively irrelevant since it does not extend past the depth of pressure-induced stasis. In the absence of pressure induced stasis, the TRS and the Thermachoice™ device display virtually identical burn depths. While that is almost certainly coincidental, it does underscore the sensitivity of the model to the exact form of the pressure distribution and the response of the perfusion rate to local stresses. The actual depth of non-perfused tissue depends on which blood vessels contribute the most to the heat sink effect, and what the required

pressure is to prevent perfusion of these vessels.

In this computer model, an approximately spherical uterus geometry was assumed. The uterus cavity tends to conform to an approximately ellipsoidal shape when inflated by the balloon. Because only bulk uterus properties were found, and because sufficiently detailed measurements of the internal cavity were not, the use of a more complicated two-dimensional or three-dimensional model was not deemed to be justified. A more complicated model geometry only increases accuracy to the extent that the changes genuinely reflect the actual conditions. Current uncertainties, such as the extent of balloon contact at the entrance to the Fallopian tubes, would undermine the benefit of the increased spatial resolution of three dimensional model. To what extent the assumed geometry affects model predictions was investigated for the following assumed geometries: spherical, cylindrical and planar.

Only the constant temperature boundary condition (i.e. Thermachoice^{TM} 2 device) is investigated, the TRS device, with its volume dependence and inflation/deflation cycling, would require significant modification of the computer code. Although the effect of pressure on the perfusion rate is important in terms of the clinical results, it must be neglected (i.e. pressure distribution has no effect on the perfusion rate) here for two reasons. The first is that this section aims to demonstrate the effect of geometry on heat transfer properties of the tissue, and adding geometry specific elastic effects would prevent the isolation of the heat transfer effects. The second is that a linear solution of the pressure distribution in an infinite plane is not possible where the plane is not restrained from moving away from the applied

pressure.

Table 15 – The most probable alpha and beta burn depths (mm) calculated by assuming spherical, cylindrical or planar geometries, for both a perfused (standard value) and unperfused uterus. The cavity surface temperature was maintained at 87°C for 8 minutes. The effect of balloon pressure on tissue distension and blood perfusion is ignored to allow for valid comparisons. The cavity volume was assumed to be 7.8 mL.

	Spherical	Cylindrical	Planar
Perfused	2.5 / 4.7	2.9 / 5.3	3.5 / 6.0
Unperfused	5.0 / 11.5	6.8 / 16.8	10.2 / 28.0

The assumed uterus geometry is important since calculated burn depths vary greatly, as seen in Table 15; this is particularly true in unperfused tissue, where heat stored near the balloon during the treatment can only be removed by conduction through the outlying tissues. The reason for this is because the tissue surface area increases with distance from the centre in the cases of spherical and cylindrical geometries. This means that the heat is spread over a larger area as it travels through the uterine wall. The use of a linear approximation becomes reasonable if the internal radius is much larger than the depth of heated tissue. Results from the meat experiments and clinical trials indicate that thermal penetration occurs at least 5-10 mm from the cavity surface. Given that the maximum volume of glycerine available is 26.5 mL (a radius of 18.5 mm), then it appears that cavity volume is not large enough relative to the thermal penetration depth to justify the use of planar or cylindrical geometries.

Model simulations were also conducted for different assumed uterine cavity volumes, using spherical geometry. The results for uterine cavities from 3.5 to 26 mL are shown in Figure 45. For a constant temperature device increasing the cavity size increases the burn depth; the additional surface area and spherical geometry improves

thermal penetration. To illustrate this, consider the case of an unperfused cavity maintained at a constant temperature and at thermal equilibrium (steady-state) with the surrounding tissue. For any given treatment time, there is a critical temperature that will result in thermal injury. In the following derivation it is shown that under these assumptions the burn depth will increase in direct proportion to the cavity radius.

$$\alpha \nabla^2 T = \alpha\left(\frac{\partial^2 T}{\partial r^2} + \frac{2}{r}\frac{\partial T}{\partial r}\right) = 0 \quad (62)$$

$$T(r_i) = T_i \quad (63)$$

$$T(\infty) = T_\infty \quad (64)$$

Solution:

$$T_{crit} = T_\infty + (T_i - T_\infty)\frac{r_i}{r} \quad (65)$$

$$\text{Burn depth} = (r - r_i) = r_i\left(\left(\frac{T_i - T_\infty}{T_{crit} - T_\infty}\right) - 1\right) \quad (66)$$

where:

α is the thermal diffusivity
T is the temperature
r is the radius
r_i is the cavity radius
T_{crit} is the temperature causing a burn at the given treatment time

This effect of cavity size on increasing burn depth is also true for the TRS, but only below a threshold volume of approximately 10 mL. Above this threshold volume the TRS is virtually unaffected by increases in cavity volume, this is particularly true for the alpha burn depth. Although the increased heat flux at higher cavity volumes would result in greater thermal penetration in a constant temperature, in the TRS the balloon temperature is lowered faster and thus the surface area effect is mitigated.

The sensitivity of the TRS device to its four internal parameters, heat transfer coefficient, glycerine volume, active residual volume and passive residual volume, was also assessed. The purpose of this study was both to determine the importance of accurate fitting for each parameter and to assess the effect of variations in the treatment process. For example, if more or less glycerine is removed than expected during deflation, it is desirable to know whether there will be a significant effect on burn depth. Calculated balloon and surface temperatures are reported in Figures 46-49, while the predicted burn depths are presented in Table 16. The model predictions indicate that the heat transfer coefficient and glycerine volume are important, while variations in the residual volume had little effect.

Table 16 – Sensitivity Analysis of the TRS device in the perfused uterus. The effect of arbitrary changes in the heat transfer coefficient, effective glycerine volume and additional residual volume during passive deflation are presented. The effect of varying the active deflation volume, while maintaining a constant passive residual volume is presented.

Parameter	Value	Alpha / Beta Burn Depth (mm)
Heat Transfer Coefficient ($W \cdot m^{-2} \cdot K^{-1}$)	225	3.6 / 6.7
	325	4.1 / 7.1
	425	4.4 / 7.4
Glycerine Volume (mL)	26	3.6 / 6.8
	38	4.1 / 7.1
	50	4.4 / 7.3
Active / Passive Residual Volume (mL)	0.25 / 2.0	4.2 / 7.2
	0.5 / 2.0	4.1 / 7.1
	2.0 / 2.0	3.8 / 6.9
Passive Residual Volume (mL)	0.5	4.2 / 7.2
	2.0	4.1 / 7.1
	3.5	4.0 / 7.1

7.2 Treatment Temperatures above the Boiling Point of Water

In this section, the model was used to predict the consequences of using treatment temperatures above the boiling point of water. One of the unique features of the TRS device is a balloon fluid temperature above 100°C. Thus, there is the potential for the temperature to reach the boiling point of water in the uterine tissue causing vapourization. It is hypothesized that there are two qualitatively different forms of vaporization that may occur. The first may be described as localized, where protrusions of tissue receive a greater net heat flux than the rest of the uterine cavity. Vaporization may occur at these locations, but as the steam bubbles are transported away they encounter cooler regions and recondense. Under these conditions the effect of vaporization is to homogenize the surface temperature, in effect reinforcing the assumption of spherical symmetry used in this model. This is the regime that the TRS is believed to operate in under standard operational conditions.

It is not known if any tissue temperatures reached the boiling point with subsequent vapourization in either the meat-model experiments or the clinical trials. The calculated boiling temperature for the tissue, based on the inflation pressure of 180mmHg, is 106°C. During the meat model experiments surface temperatures greater than 100°C were recorded and a "sizzling" sound was heard, suggesting that vapourization may be occurring. The "sizzling" sound noted during meat trials coincided with the maximum measured surface temperatures, yet the disc thermocouple data indicated that the mean temperature was below the boiling point

calculated for the balloon pressure. The sizzling sound may indicate localized vapourization since, in one meat trial the balloon protruded past the cavity stitches and could be observed externally. Small vapour bubbles could be seen at the tissue/balloon interface when sizzling was heard. However, there may be other causes of the sizzling sound like fluid movement during balloon pulsations.

If the tissue becomes sufficiently hot then the entire cavity surface can reach the boiling temperature, a process that will be referred to as complete cavity vapourization. Any additional vapour generated does not immediately condense, and would instead be forced out of the cavity by the balloon pressure. Condensation would occur again once cooler tissues were reached, and here the water would release the heat of vaporization. It is expected then that once total cavity vaporization occurred, there would be an advancing boiling temperature front of tissue that would proceed into the Fallopian tubes or cervical canal.

Total cavity vaporization is not believed to have occurred during sea level trials. The surface temperature measured during the meat trials was not sufficiently high, and there was no evidence of steam being expelled through cavity openings. In the clinical trials the tissue at the entrance to the Fallopian tubes was still viable, indicating that steam had not been forced over this area.

The risk with water vaporization is the concern that heat may be transported from where it is desired (the cavity surface) to where it is not (the Fallopian tubes or vaginal canal). If sufficient heat is transported, the tissue may become warm enough

to thermally damage neighbouring organs such as the rectum or bladder. Although neither the model nor the meat trials indicate that total cavity vaporization occurs under normal conditions, it will inevitably occur if treatment occurs at a high enough altitude, with the associated reduced boiling temperature. From a safety perspective the question is whether the critical altitude may be encountered during normal clinical operation.

To answer this question the mass of water vaporization was determined at several ambient pressures (see Figure 50). Note that a small mass of water vapour will require a large volume, far larger than the cavity volume will permit. For example, 10 milligrams of water will occupy 17 mL at 100°C. Therefore if there is practically any net production of water vapour in the uterus cavity it must either be extruded or condensed.

An ambient pressure of 70 kPa corresponds to an altitude of approximately 3,000 m; the maximum mass of water vapour predicted to be released at this pressure is 0.138 g. Although this forms a large volume (235 mL), it carries relatively little latent heat, only 312 J. At most this is sufficient to heat 10 g of tissue by 8.7 °C. At a pressure of 80 kPa there is even less heat predicted to be transported by vaporization, only enough to elevate 10 g of tissue by 2°C.

Vapour formation was greatest for cavity volumes of intermediate size (~16 mL), for the same reason that surface temperatures tend to be highest. Although in principle perfusion will cause cooling and result in less vapour formation, the

elimination of perfusion in the first several millimeters of tissue by balloon pressure means that the surface temperature is relatively insensitive to this parameter.

It is recommended that further tests be performed to confirm the hypothesized onset altitude of total cavity vaporization. Ideally additional meat trials will be conducted under hypobaric conditions. It is possible to investigate the consequences of total cavity vaporization at sea level, accomplished by increasing the initial temperature of the tissue and placing thermocouples in the canals where steam may be forced out.

7.3 Comparison of Different Thermal Ablation Treatment Protocols

Certainly all of these devices have demonstrated their usefulness in the treatment of menorrhagia. A valid question though is whether any of these provide a more precise form of treatment, in this case burn specificity, defined as maximizing the damage to the target tissue while minimizing the thermal stress that the non-target tissues experience. Ideally one would like to have a perfectly sharp boundary between the thermally destroyed and undamaged tissue; this boundary should occur exactly at the desired burn depth, slightly beyond the endometrium/myometrium interface. In reality there is a gradation of injury, with the depth of damaged tissue extending past the depth of necrosis that is also past the depth of coagulation. The computer model was used to compare different thermal ablation devices.

For our comparison we assumed that a most probable alpha burn depth of 3.8 mm, the predicted value for the TRS, is required for successful treatment. In Figure 51, the predicted burn depth is compared to an idealized constant temperature device that operates at several temperature-time combinations that yield the same depth of the middle alpha burn. For example, both a 1.7 minute treatment at 106°C and a 60 minute treatment at 67°C are predicted to result in a most probable alpha depth burn to a depth of 4.1 mm. However the most probable beta burn depth increased from 7.0 mm to 8.8 mm as the temperature decreased. If we define burn specificity as the difference between the alpha and beta burn depth (i.e. the distance between tissue immediately killed and mortally wounded), then the model indicates that burn specificity improves as the balloon fluid temperature increases.

The TRS appears to have a 0.6 mm improvement in burn specificity when compared to the equivalent treatment (alpha burn depth) at 87°C. Interestingly the model predicts that the Thermachoice™ 2 device would only have to be used for less than half its normal treatment time (3.9 minutes instead of 8 minutes) in order to achieve the same alpha burn depth as the TRS; if used for the full treatment time of eight minutes the most probable alpha burn depth of the Thermachoice™ 2 device is predicted to increase by 0.9 mm. The treatment time discrepancy illustrates that a range of temperature and time combinations will result in a successful treatment. Provided the endometrium is sufficiently cauterised while damage to the myometrium is kept below a certain threshold, patient satisfaction will be achieved.

Maximum burn specificity is achieved by using the highest possible temperature throughout the course of the treatment, however the highest possible temperature that may be used is determined by the boiling temperature of the tissue. The limitation posed by the boiling temperature imposes a strict limit upon the burn specificity that may be achieved by conduction heating devices; further improvements are only possible if radiative heating is used (such that energy penetrates the tissue prior to being transformed into heat). In the early phases of the development of the TRS it was believed that the device would offer improved heat transfer, and shorter treatment times, by the greater temperature difference of the glycerine and the deep tissue (approximately 150°C minus 37°C) than for other devices (87°C or 75°C minus 37°C). However, as a result of this mathematical model one can see that it is the cavity surface temperature, not the bulk fluid temperature, that determines thermal penetration. Therefore the thermal gradient is limited by the boiling temperature of the tissue, and hence the maximum temperature difference is lower (106°C minus 37°C). Although the temperature gradient is not as large as initially believed, the treatment time is nevertheless much shorter than for the other balloon ablation devices due to the large sensitivity of tissue to increases in temperature.

Prior to this study an analysis of the cavity surface temperature had not been performed, meat experiments had instead been aimed at establishing the bulk fluid and deep tissue temperature. Without the cavity surface temperature information it was not possible to determine if further improvements in burn specificity were possible. Figure 51 indicates that the current TRS treatment protocol is nearly optimal; treatment at the boiling temperature would only be predicted to improve the specificity by 0.1

mm, although the treatment time could potentially be reduced by almost thirty seconds if the cavity surface temperature was maintained at the boiling temperature.

Although burn depth continues to increase after treatment ends, the magnitude of this increase appears to be small. The predicted progression of burn depth for the TRS and Thermachoice™ device is presented in Figures 52 and 53 respectively. The post-treatment increase in burn depth is greatly reduced by the return of blood perfusion following balloon deflation; Figure 54 illustrates the predicted progression of burn depth for the TRS device in the unperfused uterus. A more subtle contribution occurs following the return of the uterus to its undistended size. The surface area is reduced as the tissue shrinks to its original radius. Additionally the temperature gradient for heat transfer away from the cavity is reduced as the stretched layers relax (see Figure 55), therefore the heat that is contained in the previously burned layers is transferred to the undamaged layers more slowly, and these layers to not warm to as large an extent. These effects, when combined with the limited increase in burn depth following treatment, suggest that cooling the cavity (by infusion of cool liquid) after treatment will not significantly improve burn specificity because the blood perfusion is already removing this heat effectively.

7.4 Safety Analysis

A primary concern with endometrial thermal ablation is that significant temperature elevation of the uterus serosa and the organs of the peritoneal cavity should not occur. The risk of ancillary damage is at a maximum in the unperfused

uterus, and the burn depth of this worst-case scenario should be investigated in addition to the normally perfused uterus. In Table 17 the maximum depth of eventual necrosis is examined for the TRS and Thermachoice™ 2 device. Additionally the depth of tissue that experienced a maximum of 42°C, the lowest known temperature threshold for thermal damage, is presented.

Table 17 – Indicators of the maximum possible depth of thermal damage in the Thermachoice™ 2 and TRS treatments. The burn depth is always maximal in the unperfused uterus, but the TRS is less affected by the lack of blood perfusion. The depth of tissue that experiences 42°C, the lower limit for thermal stress, is also presented.

Damage Threshold	Thermachoice™ 2: normal perfusion	Thermachoice™ 2: unperfused	TRS: normal perfusion	TRS: unperfused
Maximum Beta Burn Depth (mm)	10.4	16.4	8.2	11.0
Maximum Depth of 42°C Isotherm (mm)	13.0	23.9	11.5	14.6

Thermal damage to tissue in the peritoneal cavity is not expected in the perfused uterus for either device. From the literature review the average thickness of the uterus body was 17 mm, suggesting that even in the unperfused uterus the TRS does not pose a risk. The model does indicate that a constant temperature device, treating at 87°C for 8 minutes, may pose a risk of thermal penetration in the unperfused uterus – particularly if thin walled. The numerical model of endometrial thermal ablation of Persson et al. (34) supports this finding; they suggested that in the unperfused uterus thermal damage (defined as a maximum temperature of 45°C) may extend 18.4 mm. However in the absence of a compromised vascular system both devices present little risk of ancillary damage, unless there is marked thinning of the wall of the uterus.

Chapter 8: Recommendations for Future Research

The model of endometrial thermal ablation that has been developed in this thesis is, subjectively speaking, the most sophisticated model of this procedure that has been created to date. This work has contributed significantly to the understanding of burn modelling and endometrial thermal ablation, and has also suggested many avenues of further research that may prove fruitful. Before discussing recommendations for additional research, this model is compared to another model of endometrial thermal ablation, that of Perrson et al. (34). This model utilized many of the components present in the model developed in this thesis, such as increased blood flow due to hyperthermia, and the effect of balloon pressure on the blood flow rate. However these factors are more fully developed in the present model. In the Persson model, the effect of hyperthermia-induced blood flow increase was modelled by simply tripling the normal blood perfusion rate of the entire uterus throughout the treatment. This contrasts significantly from the approach of this model, where the perfusion increase is determined locally and where there is a time delay between initial temperature elevation and the perfusion response.

The heat transported by the blood perfusion was affected by thermal damage in the Persson model. From 37 to 42°C the heat transported by the blood supply increased in proportion to the temperature difference, as per the Pennes equation. From 42 to 46°C the heat transported was assumed to be constant, as higher temperatures were compensated for by a reduced blood perfusion rate. The heat transported by the blood perfusion then decreased linearly until 60°C, at which

temperature no heat was transported by blood perfusion. In contrast an Arrhenius expression was used in the model developed in this thesis, causing the onset of vascular stasis to be a function of both temperature and time of exposure.

Although a pressure factor was used to determine the effect of balloon pressure on blood perfusion rate, the implementation was slightly different in the Persson model. In comparison to the analytical solution of the spherically symmetrical model used in this thesis, the Von Mise's effective stress formula was used. Another difference is that Persson et al used the arterial pressure (140 mmHg) to determine the pressure factor; in this thesis the significantly lower value of 45 mmHg was used, a value consistent with the arterioles that are believed to determine the heat transfer due to blood perfusion in the Pennes equation.

Another significant difference between the two models is the method used to model thermal damage. Persson et al. assumed that tissue became irreversibly damaged if the maximum temperature exceeded 55°C, in contrast in this thesis Arrhenius functions were used to quantify two different damage thresholds, the alpha and beta burn. The uterus geometry used in the Persson model is more complicated however; they assumed a rotationally symmetrical model of the uterus and calculated the deformation due to the balloon pressure, the result was an approximately ellipsoidal balloon of very high eccentricity. In contrast this thesis assumed a spherically symmetrical model, an assumption that is supported by observations during independent uterus cavity volume determination in clinical trials with the TRS.

One of the primary contributions of this thesis is the development of a generalized approach to burn modelling. While grades of thermal damage at a specific location have been recognized qualitatively, this information has not been collated in a way that can be used quantitatively.

While a significant amount of data was reviewed in order to derive the appropriate Arrhenius parameters for the alpha and beta burn, data generated from a consistent experimental protocol would be desirable. Ideally future experiments would be designed to assess the variation in thermosensitivity across individuals, tissues and species. Direct measurement of the depth of eventual necrosis would be useful, as would be correlation of this information with the depth of the red zone, as evaluated immediately post-burn. Changes in the optical properties (for example, the scattering or absorbance coefficient) of many different tissues could be used to rigorously quantify the Arrhenius parameters of the alpha burn. If future experiments are performed to better calibrate the alpha and beta burn parameters; it is highly recommended that the experiments be performed across the full temperature range of interest in hyperthermia. Specifically alpha burn thresholds need to be established at near-physiological temperatures, to determine if there are critical temperature effects that need to be included in the model. Finally further research is recommended to determine if an Arrhenius parameter may be used to predict the depth of scar tissue formation in a variety of tissues.

Thermal modelling has changed little since Pennes first developed the bio-heat equation. One of the contributions of this thesis is an attempt to develop a realistic

model of the response of the blood perfusion rate to hyperthermia. However there is much work to be done in this field. A high priority for future research should be the quantification of the blood perfusion response, both regarding hyperemia and thermal damage. Furthermore this research needs to be performed across the full temperature range of interest during hyperthermia. Doppler ultrasound of the uterine artery could improve the understanding of the average hyperthermic response of the uterus body during thermal ablation, however local variations may limit the usefulness of this approach. An additional avenue for further research would be to establish experimentally the caliber of blood vessel that best represents the blood perfusion term in the Pennes equation, and consequently the effect of pressure on the temperature distribution in perfused tissue could be better understood. By artificially perfusing the uterus *in vitro* following hysterectomy, one could better understand the relationship between the balloon pressure, the blood perfusion rate and the temperature profile.

This model of endometrial thermal ablation could be improved by removing the assumption of spherical symmetry and solving the bio-heat equation for the full three-dimensional geometry of the uterus. Before this research may be performed, the internal and external dimensions of the uterus need to be quantified in far greater detail (beyond the commonly reported measurements of sounding depth and cavity volume). Such a model would also need to solve the stress distribution throughout the uterus, ideally using the non-linear stress-strain relationship. Although thermocouples have been useful for determining the temperature at specific points, uncertainty regarding the true thermocouple position has limited the usefulness of this approach.

A better approach would use magnetic resonance imaging to determine the temperature at all points of the uterus body during the entire duration of the treatment.

This thesis has identified many areas for future research. At present little progress may be made to improve this model of thermal ablation without a significant amount of fundamental research to quantify both burn pathophysiology and the thermal effect of blood perfusion and its modifying factors.

Chapter 9: Conclusions

A computer model of balloon thermal ablation treatment was developed that was shown to predict the tissue temperature profile and burn depth. A mathematical model of thermal damage to tissue was developed that predicts the depth of immediate cell death and the depth to which tissue death will eventually occur. A model of a heat reservoir device, the TRS, was also developed that utilizes a heat and volume balance between three fully mixed compartments. The model has predicted the temperature-time series observed in meat models of the uterus that were implanted with thermocouples at the cavity surface and at depth, suggesting that computer predictions of *in vivo* treatments are useful. The model was also found to approximately predict the burn depths from clinical trials with the TRS and from clinical trials reported in the literature for other endometrial ablation devices.

In general thermal ablation appears to be a safe and effective treatment for menorrhagia. A sensitivity analysis indicates that in the absence of blood perfusion the depth of eventual tissue necrosis may extend close to the outer wall of the uterus in devices that treat using cavity temperatures at or below a balloon temperature of 87°C, although the treatment is still predicted to be safe if the uterus wall is of normal thickness.

The TRS device is predicted to provide a treatment that is less affected by variations in patient-specific parameters than other available treatments. The short

treatment time of this device minimizes thermal penetration into the tissue past where perfusion ceases due to the balloon pressure, and therefore variations in the perfusion rate have only a minimal effect on treatment outcome. Additionally the TRS device provides a virtually constant burn depth across intermediate to large cavity volumes, although burn depth is quickly reduced if the cavity volume is less than approximately 11 mL. Prior to this thesis, the effect of the use of very hot fluid temperatures (>100°C) in the uterus cavity was poorly understood with regard to tissue-water vaporization. It is now known that the cavity surface temperature does not generally exceed the boiling temperature, and that the model predicts that significant water vaporization is not predicted to occur below 2,000 m.

The model indicates that the specificity of a treatment, the ability to destroy targeted tissues while minimizing undesired damage, improves as the treatment temperature increases. The TRS operates over the majority of the treatment time at just below the boiling temperature of tissue, and therefore has a treatment efficiency that is almost optimal. Although further improvements may be possible, the effect would be to shorten the treatment time by up to twenty-five seconds; specificity will not be significantly improved.

During the course of this thesis, a classification scheme ideally suited to modelling internal burns was developed. Although qualitative and quantitative information was available, the data had not been synthesized into an approach that is readily applicable to modelling internal burns. In place of a single irreversible/reversible damage threshold that has been commonly used, there is now

an approach that recognizes that there are grades of thermal damage and predicts the occurrence of the different damage types.

The use of a computer model for investigating endometrial thermal ablation devices has proven to be very effective. A conceptual understanding of the TRS device, and of the physical and physiological principles behind endometrial thermal ablation, has been significantly advanced by both the numerical model and by the meat experiments that were conducted. The model allows one to conduct "numerical experiments" that would be prohibitively expensive to perform *in vivo*. For example, the model provides an indication of the sensitivity of the burn depth induced by the thermal ablation devices to differences amongst individuals of the treatment parameters. To demonstrate treatment efficacy and safety for all permutations of these parameters using clinical trials would be exceedingly difficult; this is particularly true if these parameters are not measured (i.e. the response time of the perfusion rate); in such a case, previous success is not a guarantee that a set of treatment parameters does not exist that results an unsuccessful treatment. Computer modelling, while not a replacement for clinical trials, greatly complements other investigative approaches for demonstrating the safety and efficacy of both thermal ablation and hyperthermia treatments in general.

Bibliography

1. A. Coulter, J. Bradlow, M. Agass, e. al, *Br. J. Obstet. Gynaecol.* **98**, 789-796 (1991).
2. C. Barrow, *Aorn J* **70**, 80, 83-6, 89-90; quiz 92-6 (1999).
3. I. S. Fraser, G. J. Arachchi, in *Menorrhagia* S. S. Sheth, C. Sutton, Eds. (Isis Medical Media Ltd., Oxford, 1999) pp. 1-10.
4. R. W. Shaw, K. Duckitt, in *Menorrhagia* S. Sheth, C. Sutton, Eds. (Isis Medical Group, Oxford, 1999) pp. 79-98.
5. N. N. Amso, et al., *British Journal of Obstetrics and Gynaecology* **105**, 517-523 (1998).
6. M. H. Goldrath, *Obstet Gynecol Clin North Am* **22**, 559-572 (1995).
7. A. La Londe, *Br. J. Obstet Gynaecol* **101**, 559-572 (1994).
8. B. L. Sheppard, J. Bonnar, in *Menorrhagia* S. Sheth, C. Sutton, Eds. (Isis Medical Media Ltd., Oxford, 1999) pp. 11-22.
9. S. S. Sheth, G. N. Allahbadia, in *Menorrhagia* S. Sheth, C. Sutton, Eds. (Isis Medical Media Ltd., Oxford, 1999) pp. 23-42.
10. H. Gray, *Anatomy, Descriptive and Surgical.* T. Pick, R. Howden, Eds. (Running Press, Philadelphia, 1974).
11. E. Ramsey, in *Biology of the uterus* R. Wynn, Ed. (Plenum Press, New York, 1977) pp. 59-66.
12. M. Ferin, R. Jewelewicz, M. Warren, *The Menstrual Cycle: Physiology, Reproductive Disorders, and Infertility* (Oxford University Press, New York, 1993).
13. M. C. P. Rees, in *Menorrhagia* S. S. Sheth, C. Sutton, Eds. (Isis Medical Media Ltd., Oxford, 1999) pp. 127-132.
14. M. H. Goldrath, T. A. Fuller, S. Segal, *Am J Obstet Gynecol* **140**, 14-9 (1981).
15. E. A. Hellen, S. B. Coghill, E. J. Shaxted, *Histopathology* **22**, 361-365 (1993).
16. A. Pooley, C. J. G. Sutton, in *Menorrhagia* S. S. Sheth, C. Sutton, Eds. (Isis Medical Media Ltd., Oxford, 1999) pp. 155-163.
17. H. O'Connor, A. Magos, *N. Engl. J. Med.* **335**, 151-156 (1996).
18. J. B. Unger, G. R. Meeks, *Am. J. Obstet. Gynecol.* **175**, 1432-1436 (1996).
19. W. S. Alford, M. P. Hopkins, *J. Reprod. Med.* **41**, 251-254 (1996).
20. W. R. Meyer, et al., *Obstet. Gynecol.* **92**, 98-103 (1998).
21. C. J. G. Sutton, in *Menorrhagia* S. S. Sheth, C. J. G. Sutton, Eds. (Isis Medical MediaLtd., Oxford, 1999) pp. 253-264.
22. G. A. Vilos, *J. Soc. Obstet. Gynaecol. Can.* **22**, 668-675 (2000).
23. V. L. Baker, G. D. Adamson, *Fertility & Sterility* **64**, 1066-1069 (1995).
24. H. H. Bustos-Lopez, et al., *Fertility and Sterility* **69**, 155-160 (1998).
25. R. W. Dover, in *Menorrhagia* S. Sheth, C. Sutton, Eds. (Isis Medical Media Ltd., Oxford, 1999) pp. 317-328.
26. G. A. Vilos, *The Journal of the American Association of Gynecologic Laparoscopists* **4**, 559-565 (1997).
27. D. B. Yackel, *J. Soc. Obstet. Gynaecol. Can.* **21**, 1076-1080 (1999).
28. U. Ulmsten, et al., *Acta Obstetricia Et Gynecologica Scandinavica* **80**, 52-60 (2001).

29. R. S. Neuwirth, A. A. Duran, A. Singer, R. MacDonald, L. Bolduc, *Obstet Gynecol* **83**, 792-6 (1994).
30. H. Fernandez, S. Capella, F. Audibert, *Human Reproduction* **12**, 2511-2514 (1997).
31. L. F. Andersen, et al., *Eur J Obstet Gynecol Reprod Biol* **79**, 63-8 (1998).
32. B. Friberg, B. R. R. Persson, R. Willen, M. Ahlgren, *Acta Obstettricia et Gynecologica Scandinavica* , 330-335 (1996).
33. A. A. Shah, et al., *Fertil Steril* **70**, 692-7 (1998).
34. B. R. Persson, B. Friberg, J. Olsrud, J. Rioseco, M. Ahlgren, *Gynaecological Endoscopy* **7**, 203-209 (1998).
35. S. L. Thomsen, in *Thermal Treatment of Tissue with Image Guidance* T. P. Ryan, T. Z. Wong, Eds. (SPIE, Bellingham, WA, 1999).
36. P. R. Morrison, et al., *J Magn Reson Imaging* **8**, 57-63. (1998).
37. E. J. Patterson, C. H. Scudamore, D. A. Owen, A. G. Nagy, A. K. Buczkowski, *Ann Surg* **227**, 559-65 (1998).
38. D. E. Johnson, R. E. Price, D. M. Comreens, *Lasers in Surgery and Medicine* **12**, 254 (1992).
39. E. Orihuela, M. Pow-Sang, M. Motamedi, D. F. Cowan, M. M. Warren, *Urology* **48**, 600-8. (1996).
40. B. Mauroy, et al., *Eur Urol* **32**, 198-208 (1997).
41. S. K. Huang, et al., *Circulation* **78**, 416-27. (1988).
42. R. A. Boni, et al., *Radiology* **202**, 232-6. (1997).
43. A. R. Moritz, *American Journal of Pathology* **13**, 915-941 (1947).
44. M. L. Nozaki, M. M. Guest, T. P. Bond, *Burns* **6**, 213 (1979).
45. D. M. Green, K. R. Diller, *Journal of Biomechanical Engineering* **100**, 153-158 (1978).
46. G. Arturson, *Acta Physiol Scand Suppl* **463**, 111-22 (1979).
47. K. N. Ham, J. V. Hurley, *J Pathol Bacteriol* **95**, 175-83 (1968).
48. K. R. Diller, in *Heat Transfer in Medicine and Biology, Analysis and Applications* A. Shitzer, R. C. Eberhart, Eds. (Plenum Press, New York, 1985), vol. 2, pp. 85-134.
49. D. P. Orgill, M. G. Solari, M. S. Barlow, N. E. O'Connor, *J Burn Care Rehabil* **19**, 203-9 (1998).
50. I. Blomgren, B. R. Johansson, J. Lilja, *Scand J Plast Reconstr Surg* **18**, 277-84 (1984).
51. M. P. Wiedeman, M. P. Brigham, *Microvasc Res* **3**, 154-61 (1971).
52. S. Nath, et al., *Circulation* **89**, 2667-72. (1994).
53. S. F. Badylak, C. F. Babbs, T. M. Skojac, W. D. Voorhees, R. C. Richardson, *Cancer* **56**, 991-1000. (1985).
54. I. Blomgren, U. Bagge, *Scand J Plast Reconstr Surg* **18**, 269-75 (1984).
55. D. C. Ross, K. R. Diller, *ASME Journal Heat Transfer* **98**, 292-295 (1976).
56. D. L. deCamara, T. J. Raine, M. D. London, M. C. Robson, J. P. Heggers, *Plast Reconstr Surg* **69**, 491-9 (1982).
57. S. Thomsen, *Photochem Photobiol* **53**, 825-35. (1991).
58. S. L. Jacques, C. Newman, X. He, Thermal coagulation of tissues: liver studies indicate a distribution of rate parameters, not a single rate parameter, describes the coagulation process, J. J. McGrath, Ed., Advances in Biological Heat and Mass Transfer - 1991 presented at the winter annual meeting of the American Society of Mechanical Engineers, Atlanta, GA. (ASME, 1991).

59. F. C. Henriques, *Archives of Pathology* **43**, 489-502 (1947).
60. R. D. Peters, et al., *Magn Reson Med* **44**, 873-83. (2000).
61. J. A. Moriarty, et al., *J Magn Reson Imaging* **8**, 128-35. (1998).
62. S. Thomsen, J. A. Pearce, W. F. Cheong, *IEEE Trans Biomed Eng* **36**, 1174-9 (1989).
63. H. Barr, et al., *Photochemistry & Photobiology* **46**, 795-800 (1987).
64. S. S. Chen, N. T. Wright, J. D. Humphrey, *Journal of Biomechanical Engineering* **120**, 382-388 (1998).
65. Y. Anzai, R. B. Lufkin, S. Hirschowitz, K. Farahani, D. J. Castro, *J Magn Reson Imaging* **2**, 671-8. (1992).
66. K. Matthewson, P. Coleridge-Smith, J. P. O'Sullivan, T. C. Northfield, S. G. Bown, *Gastroenterology* **93**, 550-7. (1987).
67. M. Pow-Sang, et al., *Urology* **45**, 790-4. (1995).
68. M. Dyson, S. Young, C. L. Pendle, D. F. Webster, S. M. Lang, *J Invest Dermatol* **91**, 434-9. (1988).
69. I. Blomgren, E. Eriksson, U. Bagge, *Burns* **11**, 161-165 (1985).
70. J. Haveman, W. Jansen, J. Wondergem, A. C. Begg, *Int J Radiat Biol* **54**, 105-13. (1988).
71. R. C. Ngim, *Ann Acad Med Singapore* **21**, 597-604. (1992).
72. J. V. Hurley, K. N. Ham, G. B. Ryan, *J Pathol Bacteriol* **94**, 1-12 (1967).
73. T. Suzuki, et al., *J Urol* **151**, 1092-5. (1994).
74. D. F. Cowan, et al., *Mod Pathol* **8**, 716-21. (1995).
75. A. Meshorer, et al., *Arch Pathol Lab Med* **107**, 328-34. (1983).
76. S. D. Prionas, et al., *Cancer Res* **45**, 4791-7. (1985).
77. S. Sporri, B. Bell, E. Dreher, H. Schneider, M. Motamedi, *Contraception* **62**, 141-7. (2000).
78. B. E. Zawacki, *Surg Gynecol Obstet* **139**, 867-72 (1974).
79. J. C. Schenker, W. Z. Polishuk, M. I. Sack, *Journal of Reproductive Medicine* **11**, 43-57 (1973).
80. M. J. Borrelli, L. L. Thompson, C. A. Cain, W. C. Dewey, *Int J Radiat Oncol Biol Phys* **19**, 389-99. (1990).
81. K. Buckshee, K. Banerjee, H. Bhatla, *Int. J. Gynaecol. Obstet.* **63**, 139-143 (1998).
82. N. M. deSouza, et al., *AJR Am. J. Roentgenol.* **167**, 1121-1126 (1996).
83. P. Cameron Reid, W. Thurrell, J. H. F. Smith, A. Kennedy, F. Sharp, *International Journal of Gynecological Pathology* **11**, 174-179 (1992).
84. S. Thomsen, J. A. Pearce, R. Randeri, E. Chan, Determination of Isotherms of Thermal Damage (1995).
85. A. R. Moritz, F. C. Henriques, *American Journal of Pathology* **23**, 695-720 (1947).
86. K. R. Diller, R. D. Klutke, Accuracy analysis of the Henriques model for predicting thermal burn injury, Advances in Bioheat and Mass Transfer: Microscale Analysis of Thermal Injury Processes, Instrumentation, Modeling and Clinical Applications (ASME, 1993).
87. D. A. Torvi, J. D. Dale, *Journal of Biomechanical Engineering* **116**, 250-254 (1994).
88. E. A. Kach, F. P. Incropera, *IEEE Trans Biomed Eng* **21**, 8-12. (1974).
89. K. R. Diller, J. A. Pearce, *Ann N Y Acad Sci* **888**, 153-64 (1999).
90. G. j. Crile, *Cancer Research* **23**, 1963 (1963).

91. K. Breuing, E. Eriksson, P. Liu, D. R. Miller, *J Surg Res* **52**, 50-8 (1992).
92. M. C. Robson, J. O. Kucan, K. I. Paik, E. Eriksson, *Arch Surg* **113**, 621-5. (1978).
93. F. C. Regas, H. P. Ehrlich, *J Trauma* **32**, 557-63 (1992).
94. M. Bloch, *Br J Plast Surg* **19**, 347-60 (1966).
95. D. C. Ross, K. R. Diller, *Journal of Biomechanical Engineering* **100**, 149-152 (1978).
96. K. R. Diller, L. J. Hayes, G. K. Blake, *J Burn Care Rehabil* **12**, 177-89 (1991).
97. T. A. Miller, *Burns* **1**, 207-211 (1975).
98. R. C. Lee, R. D. Astumian, *Burns* **22**, 509-519 (1996).
99. K. R. Diller, *J. Burn Care Rehabil.* **19**, 420-429 (1998).
100. J. A. Pearce, S. Thomsen, *Biomed Sci Instrum* **29**, 355-60 (1993).
101. A. Takata, *Aerospace Medicine* **45**, 634-637 (1974).
102. J. S. Knabl, et al., *Burns* **25**, 229-35. (1999).
103. S. Sevitt, *Journal of pathology and bacteriology* **61** (1949).
104. D. J. Maitland, J. T. j. Walsh, *Lasers in Surgery and Medicine* **20**, 310-318 (1997).
105. K. J. Henle, L. A. Dethlefsen, *Cancer Res* **38**, 1843-51 (1978).
106. S. B. Field, *Int J Hyperthermia* **3**, 291-6. (1987).
107. J. D. Bancroft, *Histochemical Techniques* (Butterworths, London, 1975).
108. H. H. Pennes, *J Appl Physiol* **85**, 5-34. (1948).
109. B. Rivolta, F. Inzoli, S. Mantero, A. Severini, *Journal of Biomechanical Engineering* **121**, 141-147 (1999).
110. R. K. Jain, *Journal of Biomechanical Engineering* **101**, 82-86 (1979).
111. W. R. Johnson, A. H. Abdelmessih, J. Grayson, *Journal of Biomechanical Engineering* **101**, 58-65 (1979).
112. D. T. Tompkins, S. A. Klein, R. A. Steeves, *Journal of Biomechanical Engineering* **119**, 153-158 (1997).
113. M. M. Chen, K. K. Holmes, *Annals of the NY Acad. of Science* **335**, 137-150 (1980).
114. G. T. Anderson, J. W. Valvano, *Journal of Biomechanical Engineering* **116**, 71-78 (1994).
115. J. W. Valvano, S. Nho, G. T. Anderson, *Journal of Biomechanical Engineering* **116**, 201-207 (1994).
116. G. A. Vilos, F. A. Aletebi, M. A. Eskandar, *Journal of the american association of gynecologic laparoscopists* **7**, 325-329 (2000).
117. T. M. Atanackovic, A. Guran, *Theory of Elasticity for Scientists and Engineers* (Birkhauser, Boston, 2000).
118. R. M. Berne, M. N. Levy, *Physiology* (C.V.Mosby Company, St. Louis, Missouri, 1988).
119. K. Olmarker, B. Rydevik, S. Holm, U. Bagge, *J Orthop Res.* **7**, 817-823 (1989).
120. B. Vollmar, S. Westermann, M. D. Menger, *J Trauma* **46**, 91-96 (1999).
121. S. Weinbaum, L. M. Jiji, D. E. Lemons, *ASME Journal of Biomechanical Engineering* **106**, 321-330 (1984).
122. L. X. Xu, L. Zhu, K. R. Holmes, *Ann N Y Acad Sci* **858**, 21-9. (1998).
123. R. B. Roemer, J. R. Oleson, T. C. Cetas, *American journal of physiology* **249**, R153-8 (1985).
124. C. W. Song, *Cancer Research (Suppl.)* **44**, 4721s-4730s (1984).
125. T. e. Dudar, R. K. Jain, *Cancer Research* **44**, 605-612 (1984).

126. P. A. Taheri, et al., *J Clin Invest* **93**, 147-54. (1994).
127. P. Taheri, et al., *Life Sci* **56**, 701-7 (1995).
128. C. R. Davies, G. M. Saidel, H. Harasaki, *Journal of Biomechanical Engineering* **119**, 77-80 (1997).
129. K. M. Sekins, et al., *Arch Phys Med Rehabil* **65**, 1-7. (1984).
130. J. L. Bert, R. K. Reed, *Biorheology* **32**, 17-27 (1995).
131. P. Ateba, G. Mittal, *International Journal of Food Science and Technology* **29**, 429-440 (1994).
132. R. G. Moreira, J. E. Palau, X. Sun, *Food Technology* **April**, 146-150 (1995).
133. B. E. Farkas, R. P. Singh, T. R. Rumsey, *Journal of Food Engineering* **29**, 227-248 (1996).
134. F. Kreith, W. Z. Black, *Basic Heat Transfer* (Harper & Row Publishers, New York,).
135. J. H. Noggle, *Physical chemistry* (Harper Collins, New York, ed. 3, 1996).
136. J. Olsrud, B. Friberg, M. Ahlgren, B. R. Persson, *Phys Med Biol* **43**, 2397-406 (1998).
137. R. Skalak, S. Chien, *Handbook of Bioengineering* (McGraw Hill, New York, 1987).
138. R. M. Wynn, *Biology of the uterus* (Plenun Press, New York, 1977).
139. D. G. Mitchell, et al., *Radiology* **174**, 827-831 (1990).
140. J. Santolaya-Forgas, *Journal of Ultrasound Medicine* **11**, 139-142 (1992).
141. M. F. Delisle, M. Villeneuve, M. Boulvain, *J. Ultrasound Med.* **17**, 481-484 (1998).
142. H. Strohmer, A. Obruca, K. M. Radner, W. Feichtinger, *Fertility and Sterility* **61**, 972-975 (1994).
143. G. W. Bartelmez, *Am. J. Obstet. Gynecol.* **74**, 931-955 (1957).
144. C. T. Fitzgerald, M. W. Seif, S. R. Killick, M. Elstein, *British Journal of Obstetrics and Gynaecology* **101**, 229-233 (1994).
145. T. Douchi, M. Yoshinaga, M. Katanozaka, M. Mitani, Y. Nagata, *Acta Obstet. Gynecol. Scand.* **77**, 905-908 (1998).
146. J. Bornstein, et al., *Am. J. Obstet. Gynecol.* **183**, 583-587 (2000).
147. R. F. Valle, *Int. J. Gynaecol. Obstet.* **41**, 3-15 (1993).
148. V. S. Rai, M. D. G. Gillmer, W. Gray, *Human Reproduction* **15**, 1989-1992 (2000).
149. T. Romer, G. Schwesinger, *Eur. J. Obstet. Gynecol. Reprod. Biol.* **74**, 201-203 (1997).
150. O. Bakos, O. Lundkvist, T. Bergh, *Human Reproduction* **8**, 799-806 (1993).
151. R. Hurskainen, J. Teperi, J. Paavonen, C. B., *Hum. Reprod.* **14**, 186-189 (1999).
152. I. Zalud, C. Conway, H. Schulman, D. Trinca, *J. Ultrasound Med.* **12**, 737-741 (1993).
153. R. S. Neuwirth, A. A. Duran, A. Singer, R. MacDonald, B. E. Lee Bolduc, *Obstet. Gynecol.* **83**, 792-796 (1994).
154. L. Garrido, V. J. Wedeen, K. K. Kwong, U. M. Spenser, H. L. Kantor, *Circulation Research* **74**, 789-793 (1994).
155. I. Jansson, *Acta Obst. et Gynec. Scandinav.* **48**, 302-321 (1969).
156. N. J. Secher, N. Einer-Jensen, B. Juhl, *Am. J. Obstet. Gynecol.* **117**, 386-388 (1973).
157. L. Forssman, *Acta Obstet Gynec Scand* **52**, 327-334 (1973).

158. I. S. Fraser, G. McCarron, B. Hutton, D. Macey, *Am. J. Obstet. Gynecol.* **156**, 158-166 (1987).
159. G. W. Pearsall, V. L. Roberts, *Journal of Biomechanics* **11**, 167-176 (1978).
160. J. Crank, *The Mathematics of Diffusion* (Clarendon Press, Oxford, England, 1975).
161. R. M. Beam, R. F. Warming, *J. Computational Physics* **22**, 87-110 (1976).
162. W. H. Press, B. P. Flannery, S. A. Teukolsky, W. T. Vetterling, *Numerical Recipes: The Art of Scientific Computing* (Cambridge University Press, Cambridge, 1986).
163. K. Banerjee, K. Buckshee, N. Bhatla, S. Gupta, *J. Obstet. Gynaecol. Res.* **25**, 143-146 (1999).
164. H. F. Bowman, E. G. Cravalho, M. Woods, in *Annual Review of Biophysics and Bioengineering* L. J. Mullins, W. A. Hagins, L. Stryer, C. Newton, Eds. (Annual Reviews Inc., Palo Alto, 1975).
165. R. Agah, J. A. Pearce, A. J. Welch, M. Motamedi, *Lasers Surg Med* **15**, 176-84 (1994).
166. G. Arturson, O. P. Jakobsson, *Burns Incl Therm Inj* **12**, 1-7 (1985).
167. S. L. Jacques, S. A. Prahl, *Lasers Surg Med* **6**, 494-503 (1987).
168. C. Linke, A. Elbadawi, V. Netto, A. Roberts, M. Russo, *J Urol* **107**, 599-602. (1972).
169. B. E. Lyons, et al., *Radiat Res* **106**, 234-51 (1986).
170. I. Nissenkorn, A. Meshorer, *J Urol* **149**, 1613-6. (1993).
171. T. Suzuki, K. Kurokawa, K. Suzuki, K. Imai, H. Yamanaka, *Int J Urol* **1**, 162-6. (1994).
172. A. Yerushalmi, Z. Shpirer, I. Hod, F. Gottesfeld, D. D. Bass, *Int J Radiat Oncol Biol Phys* **9**, 77-82. (1983).
173. R. Agah, A. H. Gandjbakhche, M. Motamedi, R. Nossal, R. F. Bonner, *IEEE Trans Biomed Eng* **43**, 839-46. (1996).
174. Y. Okumura, H. S. Reinhold, *Eur J Cancer* **14**, 1161-6 (1978).

Appendix A – Individual Burn Data Points

---

(165)

Description: Sections of human aorta were subjected to hyperthermia *in vitro* by contact with a temperature controlled copper block. Tissue was exposed at constant temperature for various time intervals, and then sections were fixed and submitted for histological examination. In this manner the first noticeable sign of damage could be determined, for this experiment it was a slight separation of the muscle and connective tissue fibers. It is suggested in this paper that the separation is due to the denaturation of the collagenous connective tissue. An additional experiment utilized laser heating of aortic samples with an infrared camera providing real-time monitoring of the tissue surface temperature.

Comments: The use of separation criteria is not a traditional definition of thermal damage. It will be assumed instead that this data may be included in the "immediate coagulation" category. Only the "threshold" damaged data from the laser heating is included.

Thresholds: Contact Heating
65.7°C for 1470 seconds – immediate coagulation
66.1°C for 870 seconds – immediate coagulation
66.9°C for 330 seconds – immediate coagulation
67.5°C for 450 seconds – immediate coagulation
68.1°C for 660 seconds – immediate coagulation
71.1°C for 195 seconds – immediate coagulation
71.4°C for 135 seconds – immediate coagulation
72.8°C for 5 seconds – immediate coagulation
73.1°C for 85 seconds – immediate coagulation
76.1°C for 15 seconds – immediate coagulation

Laser Heating
67°C for 97 seconds – immediate coagulation
68°C for 37 seconds – immediate coagulation
72°C for 46 seconds – immediate coagulation
75°C for 72 seconds – immediate coagulation
75°C for 79 seconds – immediate coagulation

---

(166)

Description: Rat hind paws were scalded in water up to the ankle joint in water for periods of time ranging from 5 to 40 seconds. At 30-minute intervals the extent of edema was measured by the fluid displacement method up to 240 minutes post-burn.

Thresholds: 52.5°C for 20 seconds – edema
55°C for 5 seconds - edema

---

(53)

Description: Normal skeletal muscle in rats was subjected to microwave induced hyperthermia at 43°C and 45°C for twenty minutes. Histopathological analysis was performed 5 minutes, 6 hours, 48 hours and 7 days after exposure to hyperthermia.

Comments: Vascular congestion was observed in 30% of all samples at 5-minutes, and peaked at 78% of the six hour samples, unfortunately the results were not specified for the individual treatment temperatures. Therefore it will be assumed that the significant damage threshold was at 45°C, and that the damage that did occur at 43°C was not critical. The congestion of the blood vessels was not immediate and therefore did not qualify for the vascular stasis category. Heated tissue showed diffuse coagulation necrosis of skeletal muscle fibers and edema.

Thresholds: 45°C for 20 minutes – edema

---

(54)

Description: Mouse ears were subjected to 20 seconds of hyperthermia in a water bath. Vital microscopy determined the presence or absence of blood flow in central and peripheral vessels and allowed for a subjective evaluation of edema development.

Comments: After scalding at 52°C there was a rapid increase in edema, but blood flow could be seen in most cases. After four days approximately 50% of the ear had become necrotic.

Thresholds: 52°C for 20 seconds – eventual necrosis

---

(80)

Description: Cultured baby hamster kidney cells were heated *in vitro*, afterwards the cells were plated for colony formation analysis. Survival curves were then constructed over the temperature range of 43.5 to 57°C.

Comments: There was a significant initial 'shoulder', or reduced mortality rate, until the cumulative mortality fraction exceeded 90%. As the thermal exposure increased further the mortality rate assumed a mono-exponential form. This study is more valuable than other in vitro studies

of cell cultures due to the large temperature range that was analysed.

Thresholds: 43.5°C for 600 seconds – 10% cell culture survival fraction
46.0°C for 1560 seconds – 10% cell culture survival fraction
50.0°C for 130 seconds – 10% cell culture survival fraction
54.0°C for 15 seconds – 10% cell culture survival fraction
57.0°C for 3 seconds – 10% cell culture survival fraction

---

(90)

Description: Data from a subset of a larger investigation into the effect of combined heat and radiation on cancers implanted in the feet of mice was useful for defining thermal tolerance limits for eventual necrosis. Mouse feet were submerged in a temperature controlled water bath and the fraction of mice experiencing the eventual loss of the foot was recorded.

Comments: Data is reported where foot loss occurred, but does not necessarily represent exposures of equivalent risk.

Thresholds: 44°C for 200 minutes – eventual necrosis
45°C for 100 minutes – eventual necrosis
46°C for 60 minutes – eventual necrosis
47°C for 30 minutes – eventual necrosis
48°C for 15 minutes – eventual necrosis
49°C for 10 minutes – eventual necrosis

---

(125)

Description: An observation capsule was implanted in a rabbit ear and allowed to heal. A blood vessel in the surrounding mature granulation tissue was monitored during contact hyperthermia and the time until vascular stasis occurred was recorded.

Comments: Vascular stasis is reported here for individual vessels, not the average of the tissue.

Thresholds: 47.1°C for 50 minutes (1) – vessel stasis
47.1°C for 45 minutes (1) – vessel stasis
47.1°C for 42 minutes (2) – vessel stasis
47.4°C for 33 minutes (1) – vessel stasis
47.4°C for 32 minutes (1) – vessel stasis
49.0°C for 12 minutes (1) – vessel stasis
49.7°C for 22 minutes (1) – vessel stasis
52.4°C for 14 minutes (1) – vessel stasis

---

(45)

Description: This study visualized the increase in vessel permeability following hyperthermia by the release from the vascular system of a normally impermeable macromolecule tagged with a fluorescent dye. The hamster cheek pouch is everted and pinned over a transparent, temperature-controlled chamber on a special microscope stage. Following hyperthermia the macromolecules are admitted to the circulatory system and the extent of transfer to the extravascular tissue is examined.

Thresholds: 49°C for 15 seconds – edema

---

(47)

Description: A heated copper disk was used to apply 20-second burns to either the skin or the abdominal muscle of the rat. Electron microscopic examination of the tissue was performed at various intervals from 25 minutes to 5 weeks after the injury. Changes in vascular permeability were analysed by the injection of ferritin into the vascular system.

Comments: Cellular changes in the endothelial cells 3-4 hours after injury and release of ferritin were signs of mild thermal injury inducing edema in the affected tissue. The number of animals treated was not reported.

Thresholds: 51°C for 20 seconds – no evidence of significant thermal damage
53°C for 20 seconds – edema formation and increased vascular permeability, reversible damage to endothelial cells

---

(70)

Description: The right hind legs of mice were exposed to a temperature-controled water bath for various time intervals. The subcutaneous temperature was observed to stabilize 0.2°C below the water bath temperature one minute after exposure. Treatment for 15 or 30 minutes resulted in immediate dermal edema that resolved 2 days after treatment. After 60 minutes of hyperthermia the edema developed into subepidermal blistering and a considerable area of tissue became necrotic 4 days after the hyperthermic exposure.

Thresholds: 44°C for 15 minutes – edema
44°C for 60 minutes – eventual necrosis

(167)

Description: Bovine liver samples were cut into slices and were placed in a temperature controlled water bath once enclosed in a foil wrapping. At the end of the treatment the sample was placed in a spectrophotometer and the optical scattering coefficient was used to determine the extent of coagulation.

Comments: The spectrophotometric data indicated that coagulation was a continuous process that would require a number of rate parameters for accurate prediction. Threshold times were used that resulted in a 50% change in the scattering coefficient based on their fitted monoexponential approximation rate constant.

Thresholds: 50°C for 9011 seconds – immediate coagulation
62.5°C for 173 seconds – immediate coagulation
70°C for 17 seconds – immediate coagulation

---

(167)

Description: Albino mice were sacrificed and the fur was removed from the back. The full thickness of skin was excised and the fat layer was removed until only the dermis and epidermis remained. The dermis was placed against glass and a 3 x 3 grid of black points 1 cm apart was marked. The skin was then immersed in a water bath for 10-second intervals and the degree of coagulation, as measured by the shrinkage in the lateral direction across the skin, was noted. These kinetics of contraction were first order in time, and a rate constant was fitted to the data. The time threshold for coagulation was assumed to occur when 63.2% of the existing material had been damaged, equivalent to a damage integral value of 1.0.

Thresholds: 60°C for 28 seconds – immediate coagulation
62°C for 9.2 seconds – immediate coagulation
64°C for 8.7 seconds – immediate coagulation

---

(168)

Description: The effect of irrigation with hot water of the canine bladder was examined over a range of temperatures. Thermocouples were implanted at three locations to assess the temperature of the tissue throughout the procedure. Six weeks later the animals were sacrificed and histological analysis of the bladder was performed.

Comments: Tissue temperature was found to be varying among the three points

studied by 3-4°C, therefore the data is taken from the mean temperature. Patchy damage was first noted at 46.5°C, although gross deformity was minimal at this temperature. It is not known what the effect of earlier examination of the bladder would have found.

Thresholds: 46.5°C for 8 minutes – eventual necrosis

---

(169)

Description: Local ultrasonic hyperthermia was induced in the anaesthetized feline brain. Animals were sacrificed at various intervals from 1 to 56 days and the histopathological results were noted. Coagulative necrosis, defined by the homogenization of normal tissue, gray matter nuclear pyknosis, and white matter edema and vacuolation, was the recorded on days 1 to 3 post-treatment. Although information regarding the area of eventual necrosis was recorded only the presence/absence of coagulative necrosis is considered here due to uncertainty in the temperature field away from the central heated area.

Comments: Results from a linear regression analysis of the coagulative necrosis lesion size was used and the x-interecept was used to predict the damage threshold.

Thresholds: 42.2°C for 50 minutes (8) – eventual necrosis

---

(104)

Description: Tail tendon sections from freshly sacrificed rats were examined microscopically on a hot stage with heating plates above and below the sample. Linear birefringence measurements were made throughout the hyperthermic exposure. It was found that a first order Arrhenius expression could be fit to the denaturation rate constant data. The inverse of the rate constant was defined as the time required to reach thermal damage to the tail tendon collagen.

Thresholds: 50°C for 5000 seconds – collagen denaturation
52°C for 2142 seconds – collagen denaturation
54°C for 845 seconds – collagen denaturation
56°C for 937 seconds – collagen denaturation
58°C for 102 seconds – collagen denaturation
60°C for 66 seconds – collagen denaturation

---

(66)

Description: Low-power neodymium:yttrium-aluminum-garnet laser light was applied

intrahepatically in rats at various power settings and exposure times. Thermocouples recorded the temperature-time series and the time at the steady-state temperature was compared with the histological effects on the third or fourth day post-injury.

Comments: Additional information on the observed time-temperature profiles over the range of 44°C to 90°C was available graphically but could not accurately be included in this data set.

Thresholds: 44°C for 30 minutes – eventual necrosis

---

(75)

Description: The alterations produced by radio-frequency induced hyperthermia were studied in the skeletal muscle of the swine. The presence of acute lesions, defined by the presence of edema, vascular damage, necrosis and granulocytic infiltration, were noted for treatment temperatures ranging from 42°C to 48°C for 30 minutes.

Comments: A histologic grading system was used to define the extent of damage. Unfortunately there was insufficient information available to quantify the first appearance of specific conditions, however all of the damage indications are consistent with eventual necrosis. Signs of damage were present at lower temperatures but were uncommon.

Thresholds: 46°C for 30 minutes (15) – eventual necrosis

---

(85)

Description: Porcine and human skin burns were induced using flowing, heated water directed through a small cylindrical chamber applied to the skin for various time and temperature combinations. The physiological reaction was monitored in the following days and wounds were classified according to the extent of hyperemic reaction, the presence of scaling and the complete destruction of the epidermal layer. Irreversible damage to the epidermis was assessed most reliably by the ease with which the epidermis could by displaced by friction on the second and third days and by the development of complete encrustation of the wound within one week.

Comments: The first occurrence of irreversible damage was reported in the dataset; however it should be mentioned that the original data suggested that there was a probabilistic component to the occurrence of trans-epidermal necrosis. In some cases exposure times greater than the indicated threshold did not result in significant damage. Although testing was

conducted at temperatures greater than 60oC, this data is not included in the data set because the temperature profile is still in the transient phase and cannot be considered constant.

Thresholds: 44°C for 420 minutes – eventual necrosis - pig
45°C for 180 minutes – eventual necrosis - pig
46°C for 90 minutes – eventual necrosis - pig
46.5°C for 60 minutes – eventual necrosis - pig
47°C for 45 minutes – eventual necrosis - pig
48°C for 14 minutes – eventual necrosis - pig
49°C for 9 minutes – eventual necrosis - pig
50°C for 5 minutes – eventual necrosis - pig
51°C for 3 minutes – eventual necrosis - pig
52°C for 90 seconds – eventual necrosis - pig
53°C for 60 seconds – eventual necrosis - pig
54°C for 35 seconds – eventual necrosis - pig
55°C for 25 seconds – eventual necrosis - pig
56°C for 15 seconds – eventual necrosis - pig
58°C for 10 seconds – eventual necrosis - pig

44°C for 360 minutes – eventual necrosis -human
45°C for 180 minutes – eventual necrosis - human
47°C for 25 minutes – eventual necrosis - human
48°C for 15 minutes – eventual necrosis - human
49°C for 570 seconds – eventual necrosis - human
51°C for 240 seconds – eventual necrosis - human
53°C for 90 seconds – eventual necrosis - human
55°C for 30 seconds – eventual necrosis - human

---

(170)

Description: A thermal electrode applied intraurethrally was used to cause hyperthermia in the canine prostate. Electrode surface temperature was 44.5°C, applied for 3.5 hours, and thermocouples were used to map the temperature profile at increasing distances from the electrode. Histological sections were taken immediately, one week and one month after hyperthermia and hemorrhagic necrosis was observed to occur to a distance of 5mm from the urethra.

Thresholds: 43°C for 3.5 hours (5) – eventual necrosis

---

(171)

Description: Canine prostates were heated transurethrally by a balloon laser probe for 20 minutes. Animals were sacrificed one week later and the bladder,

prostate gland and urethra were removed and histologically examined. The probability of coagulative necrosis was calculated for a variety of affected tissues, and the temperature inducing a 50% probability of necrosis was reported.

Thresholds: Prostate: 45.5°C for 20min – eventual necrosis
Bladder neck: 49.4°C for 20min – eventual necrosis
Urethral mucosa: 46.5°C for 20min - eventual necrosis
Urethral sphincter: 43.2°C for 20min – eventual necrosis

---

(73)

Description: Transurethral laser-induced hyperthermia was induced to assess the *in vivo* effects of thermal damage to the canine prostate. Coagulative necrosis was observed to occur to a depth of 5mm, and this tissue began to slough off within one week. Thermocouples were used to determine the temperature distribution within the prostate and used to determine the critical temperature for cavity formation.

Thresholds: 46.1°C for 20min – eventual necrosis

---

(51)

Description: The wing membrane of the brown bat *Myotis lucifugus* was used to evaluate the effects of cooling on the microvasculature after thermal injury. The bat is placed in a specially made holder and the wing is extended over a glass plate and observed through a light microscope. A glass covered hollow plastic disk was used to circulate water over the wing and microscopic observations were made hourly for six hours post-burn.

Thresholds: 55°C for 30 seconds – edema formation

---

(172)

Description: The response of the normal tissues of the rectal cavity and prostate to microwave hyperthermia were assessed. Animals were sacrificed at random from 1 day to 3 months after treatment. Damage was assessed microscopically.

Thresholds: 43°C for 30 minutes -eventual necrosis

Appendix B – Published Damage Integrals

---

(173)

Description: Thermal changes in sections of fresh, heated bovine myocardial tissue was assessed from measured changes in total reflection and transmission of light. Sliced sections were encased in fast-curing epoxy and were flushed with heated water at the desired temperature. A photosensor recorded changes in tissue optical property throughout the heating procedure. Time-dependent changes in the scattering coefficient were found to fit an Arrhenius rate expression and are associated with the coagulation of the tissue.

Comments: For temperatures between 56.8 and 51.5°C the Arrhenius function did not fit, in fact the changes at this temperature appeared to be temperature independent. Therefore the use of this Arrhenius expression below ~57°C is known to be incorrect.

Thresholds: The time required for the optical coagulation of tissue is described with an Arrhenius expression.

$$t(\text{sec}) = \left(2.8 \times 10^{23} \exp\left(\frac{-162{,}000}{RT(K)} \right) \right)$$

---

(106)

Description: The tails of young rats were heated by immersion in a temperature-controlled water-bath. The threshold for damage was the necrosis of the tail by six weeks, assessed radiographically.

Thresholds: An equivalent time equation was fitted to the data, valid over the range of 42.5 to 46°C.

$$t(\text{min}) = 100\left(0.5^{T(C)-43}\right)$$

---

(174)

Description: The effect of moderate hyperthermia (42-47°C) on rat skin was studied,

and the intensity of damage was divided into six grades. The hair on the back was removed by clipping and 30mL of air was injected subcutaneously to form an air pouch. This air pouch was immersed in heated water for various times at various temperatures. Following completion of the procedure the air was removed and the treated area was monitored regularly for eight weeks.

Threshold: The time-temperature relationship for maximum effect is presented in this data. The entire skin surface became a non-viable brittle scale, which sloughed off during the healing process resulting in scar tissue. A power relationship was fit to the time-temperature relationship for eventual necrosis.

$$t(\text{min}) = 3.51 \times 10^{14} \left(0.51^{T(C)}\right)$$

---

(100)

Description: Two experiments are summarized in this paper. In one experiment human aorta samples were excised from cadavers and exposed to a heated copper block for various time-temperature combinations. The other experiment utilized rat skin, which was wrapped in foil and submerged in a heated water bath. In both experiments the damage threshold examined was the loss of the native form birefringence of the collagen.

Thresholds: Human Aorta Collagen Birefringence Loss

$$t(\text{sec}) = \left(5.6 \times 10^{63} \exp\left(\frac{-430{,}000}{RT(K)}\right)\right)$$

Rat Skin Collagen Birefringence Loss

$$t(\text{sec}) = \left(1.606 \times 10^{45} \exp\left(\frac{-306{,}000}{RT(K)}\right)\right)$$

---

(60)

Description: Laser-induced hyperthermia was performed on the prostates of four dogs. The temperature field was continuously recorded by magnetic resonance imaging, and this data was used to derive an Arrhenius-like expression for a damage integral. The damage threshold was based on the boundary of the necrotic tissue as sampled 24 hours after treatment.

Comments: There was a three-fold uncertainty regarding the experimental damage

threshold time estimate. Although the data was analysed across a temperature range of 37 to 95°C the estimated temperature of thermal damage was 51°C over a 3 to 5 minute treatment. The temperature range of the lesion area is less than the total temperature range and is assumed to be approximately 46-54°C.

Damage Function: This study utilized an "equivalent time at 43°C" concept, with an assumed halving of time required per degree Celsius increase in temperature.

$$t(\text{min}) = 200\left(0.5^{T(C)-43}\right)$$

---

(55)

Description: The hyperthermic vascular response of the hamster cheek pouch was investigated utilizing a microscope with a temperature-controlled stage capable of burning or freezing living tissue. With this apparatus the microcirculation may be directly observed during the hyperthermic procedure. The development of vascular stasis within 95% of the microcirculation by twenty seconds after the burn was used to fit an exponential function.

Thresholds: The function used to predict vascular stasis is valid over the range of 60 to 85 °C, and approximates an Arrhenius expression over the temperature range of validity.

$$t(\text{sec}) = \exp\left[0.153\left(85^{o}C - T(C)\right)\right]$$

Appendix C - Meat Experiment Results

Trial 5-25-01

Cavity Volume – 11.8 ml
Comments: Wire thermocouples were used at the cavity surface, 0.5 and 5mm deep. Balloon temperature measurements were made manually using a J-type thermocouple.

Trial 11/02/01A

Cavity Volume – 10 ml
Thermocouples Reported: 2 disk thermocouples on cavity upper surface, 1 disk thermocouple on cavity lower surface
Data Sampling Period – 2 seconds
Comments: Balloon thermocouple not included due to technical problems. Wire thermocouple placed too deep to record significant temperature elevation. Small amount of 'loctite' glue placed behind disk thermocouples to resist movement.

Trial 11/29/01A

Cavity Volume – 12 ml
Thermocouples Reported: 2 disk thermocouples on cavity upper surface, 1 disk thermocouple on cavity lower surface, 1 wire thermocouple 4mm deep in the bottom surface.
Comments: Balloon thermocouple not included due to technical problems.

Trial 11/29/01B

Cavity Volume – 12 ml (retest on meat model in 11/29/01A after cooling to 37°C)
Thermocouples Reported: 2 disk thermocouples on cavity upper surface, 1 disk thermocouple on cavity lower surface, 1 wire thermocouple 4mm deep in the bottom surface.
Data Sampling Period – 0.562 seconds

Trial 12/13/01A

Cavity Volume 5ml
Thermocouples – one disc thermocouple in the top surface, one disc thermocouple in the bottom surface, one wire thermocouple 2 mm into the top surface and 1 wire thermocouple 5 mm into the bottom surface

Trial 12/20/01A

Cavity Volume: 26ml
Thermocouples: Two disc thermocouples in the top and bottom cavity surface respectively. One wire thermocouple 2mm deep in the top center.

Trial 2/01/02A

Cavity Volume: 6ml
Thermocouples: Two disc thermocouples in the top and bottom cavity surface respectively. One wire thermocouple 3mm deep in the top center, another in the bottom, 2mm deep.

Trial 2/01/02B

Cavity Volume: 22ml
Thermocouples: Two disc thermocouples in the top and bottom cavity surface respectively. One wire thermocouple 2.5mm deep in the top center, another in the bottom, 1.5mm deep.

Trial 5-25-01

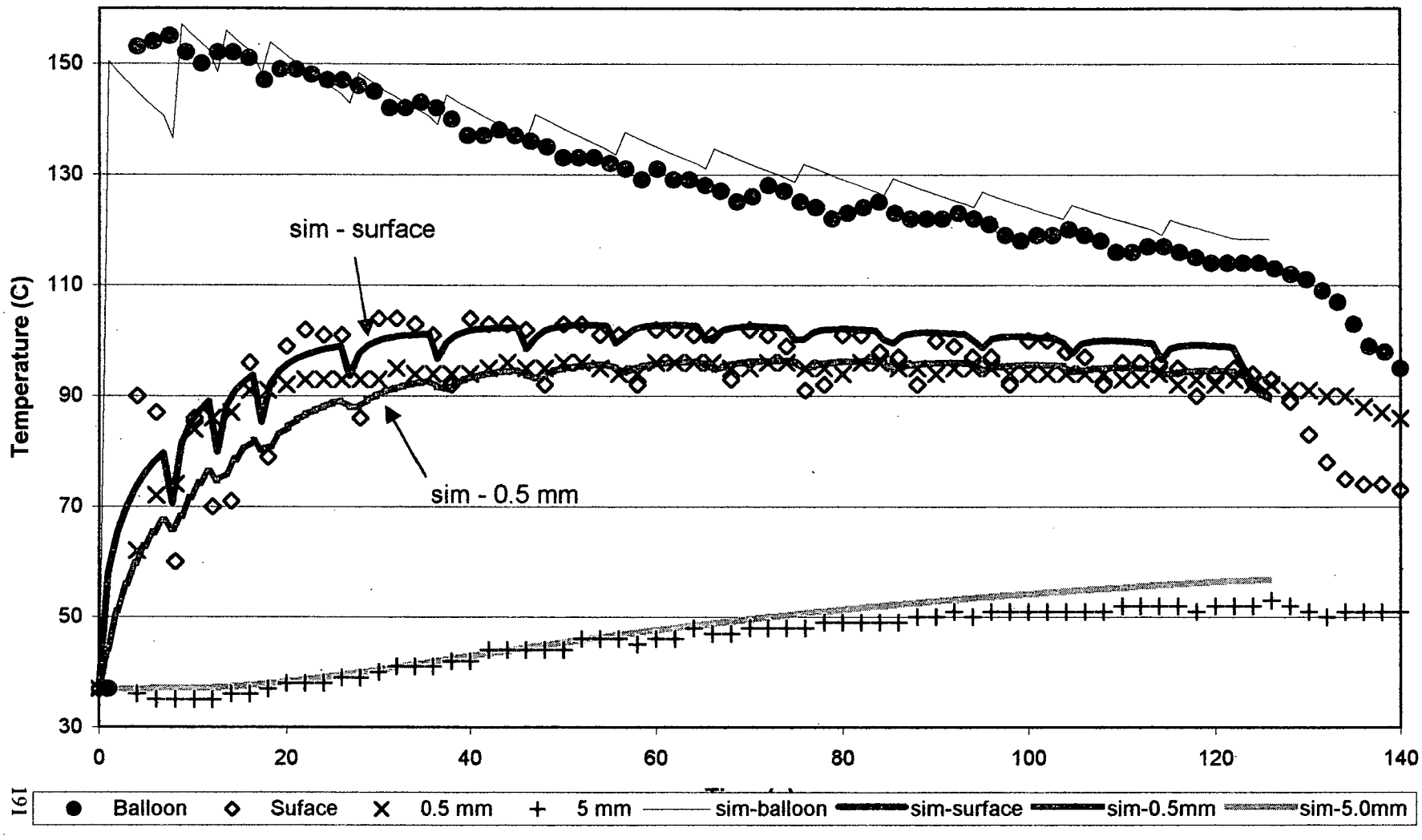
Temperature (C)
150
130
110
90
70
50
30
0
20
40
60
80
100
120
140
sim - surface
sim - 0.5 mm
Balloon
Suface
0.5 mm
5 mm
sim-balloon
sim-surface
sim-0.5mm
sim-5.0mm

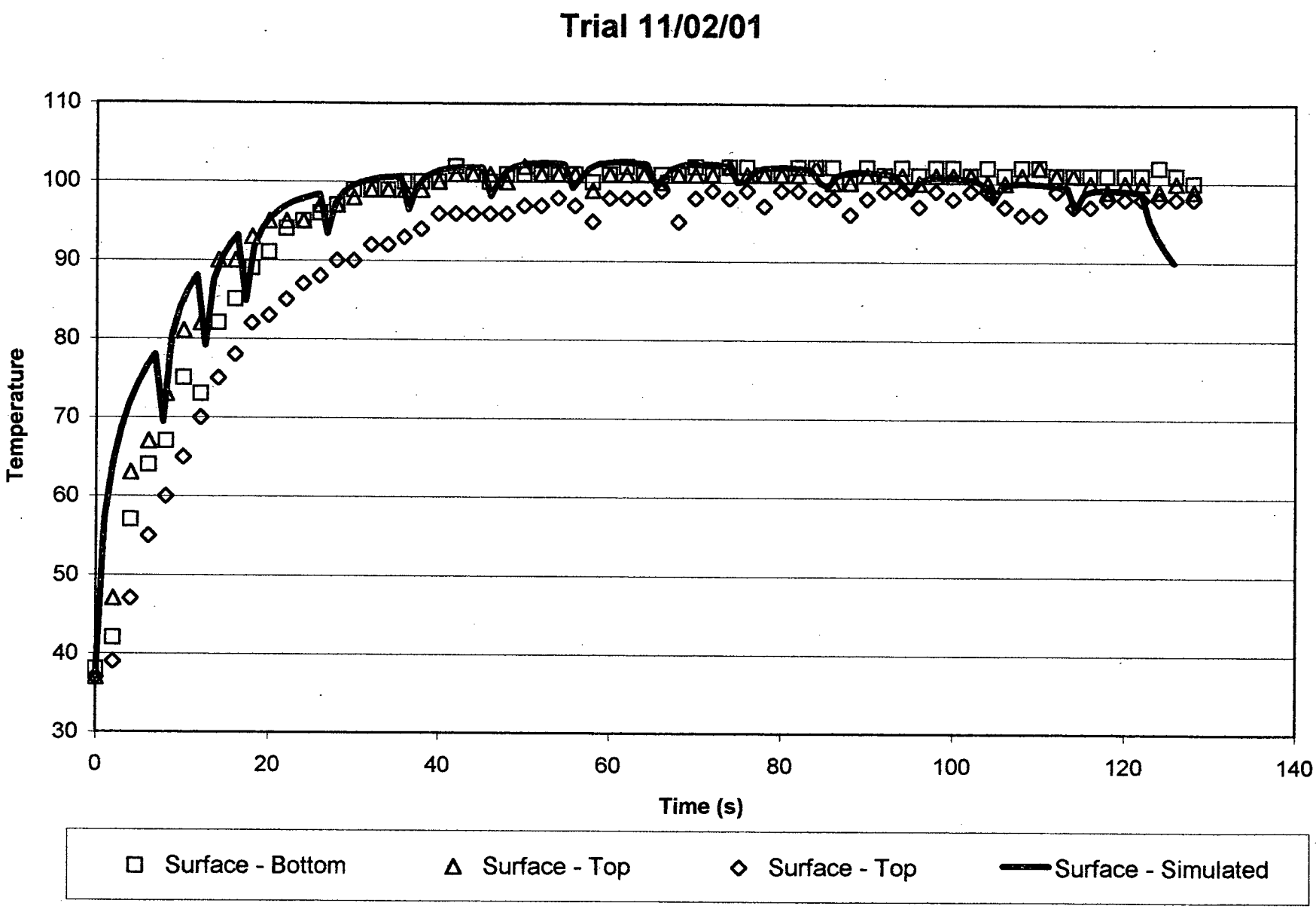
Trial 11/02/01
Temperature
110
100
90
80
70
60
50
40
30
0
20
40
60
80
100
120
140
Time (s)
Surface - Bottom
Surface - Top
Surface - Top
Surface - Simulated

Trial 11-29-01A

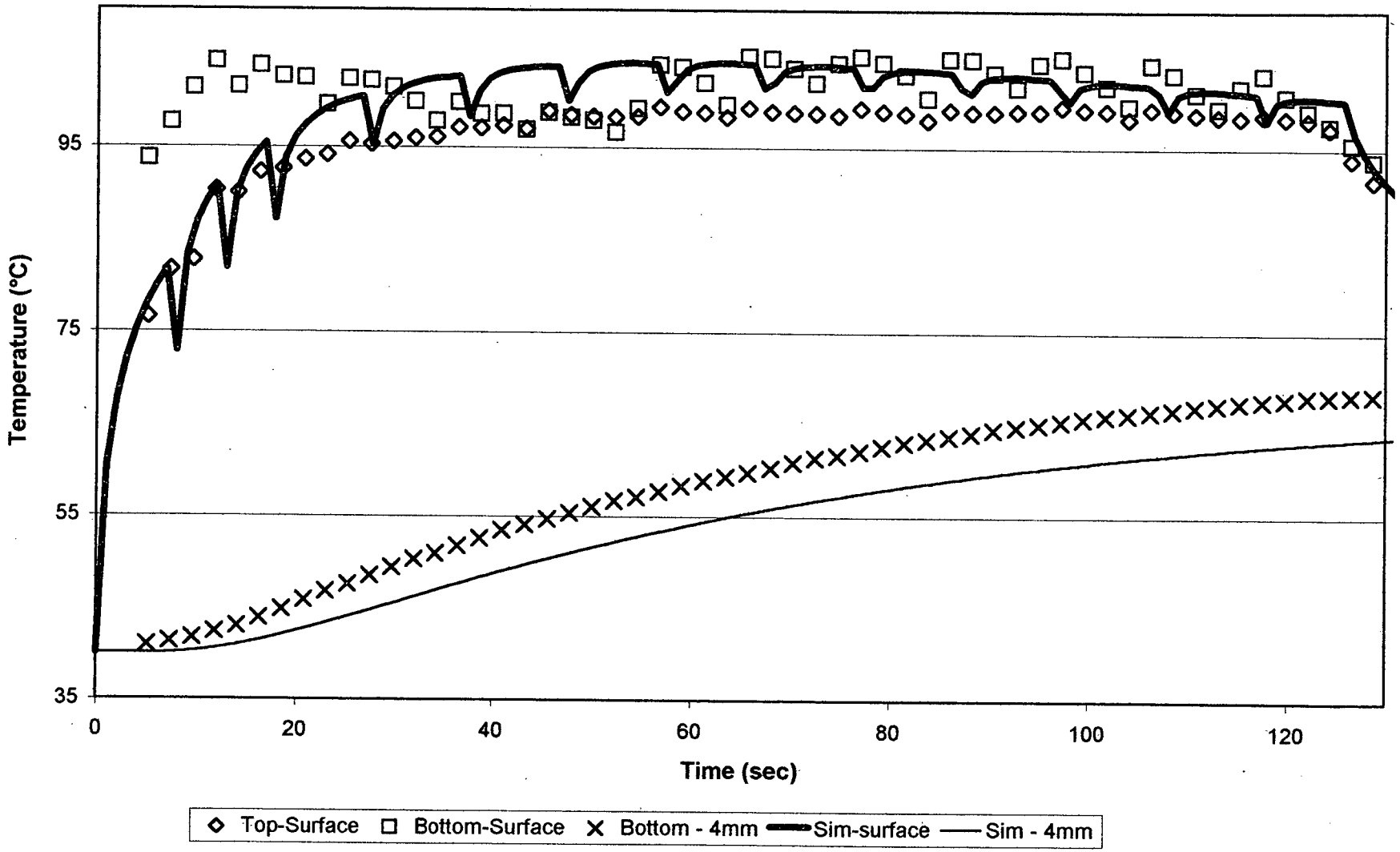

Trial 11-29-01B

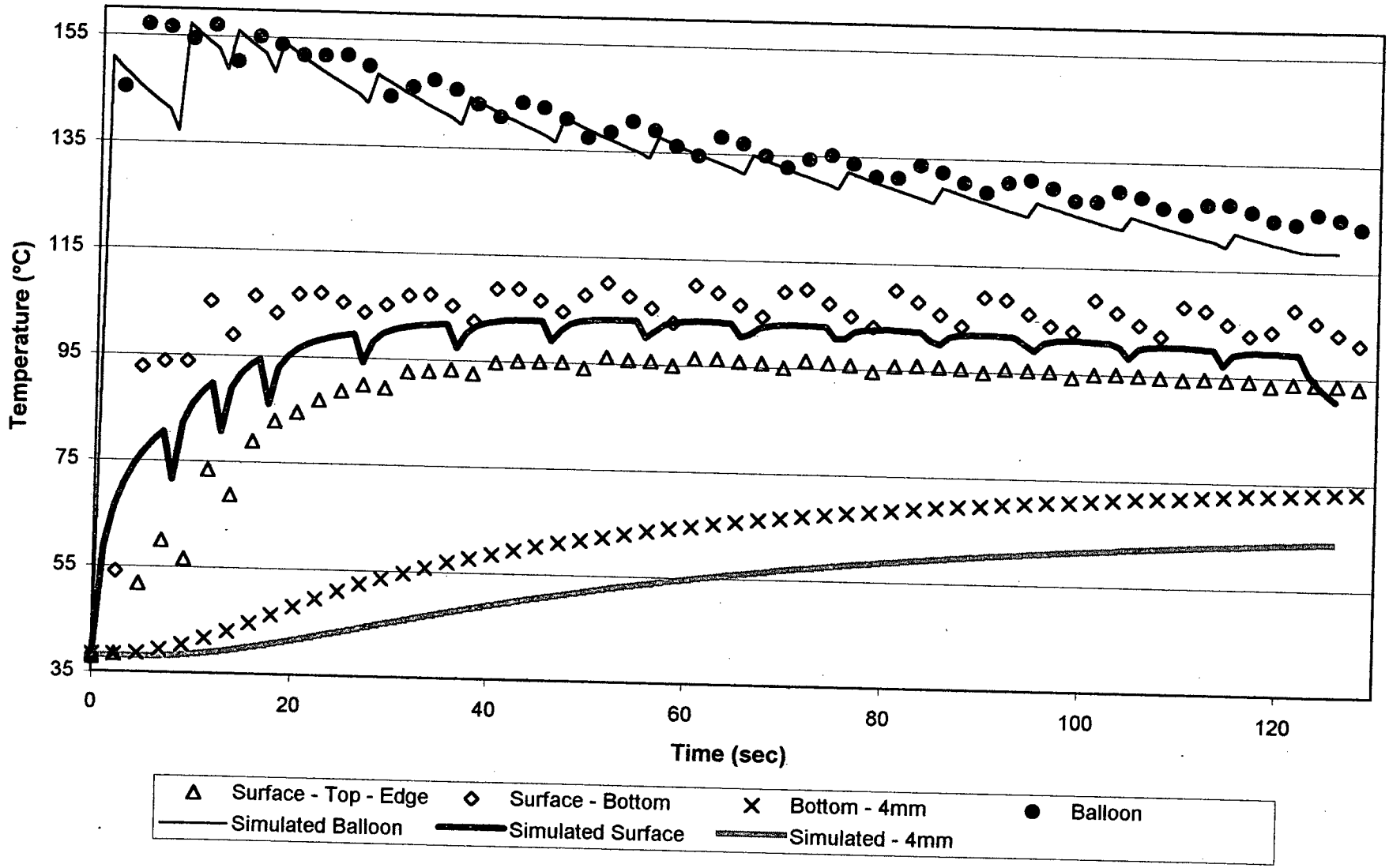

Trial 12-13-01A

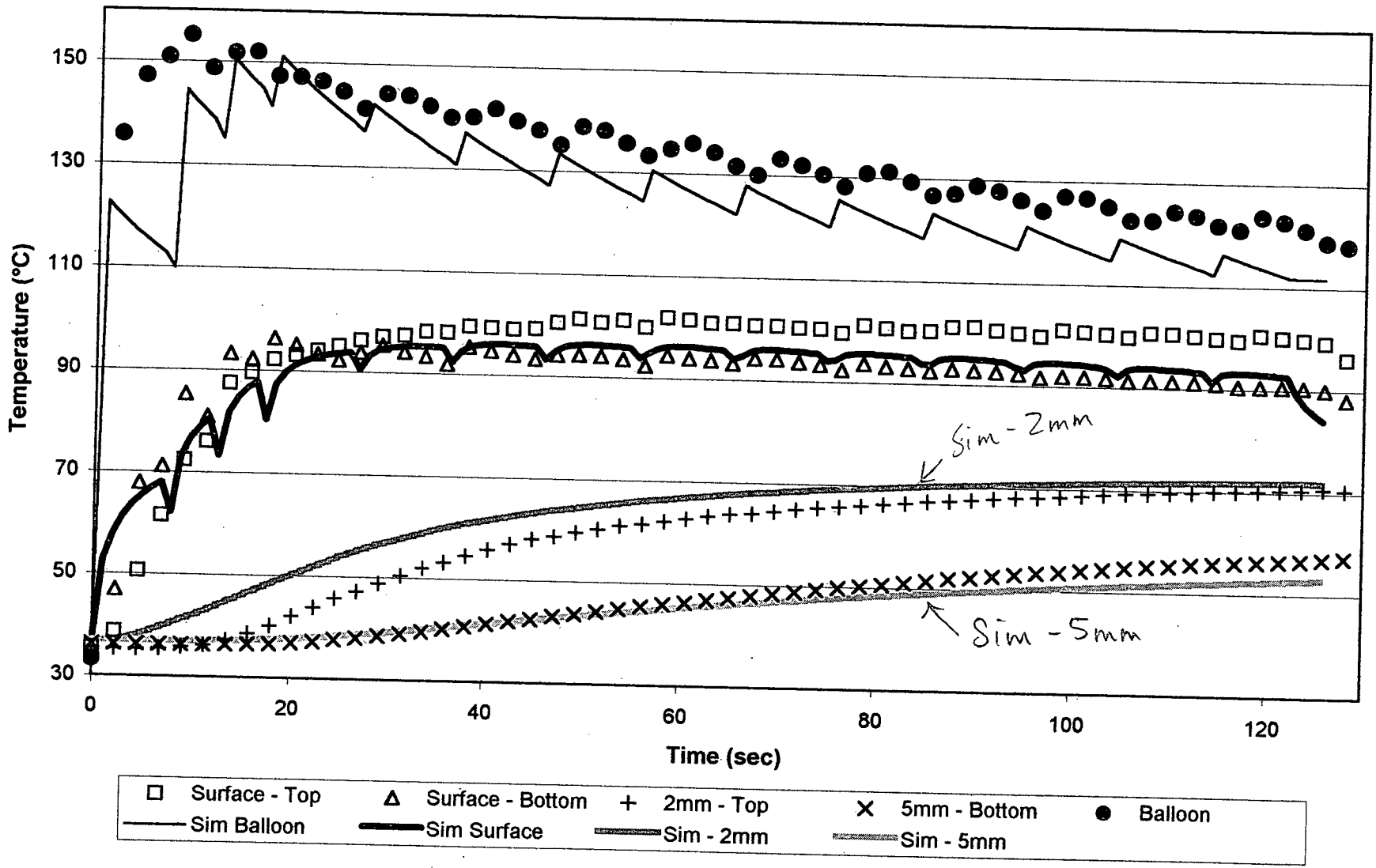

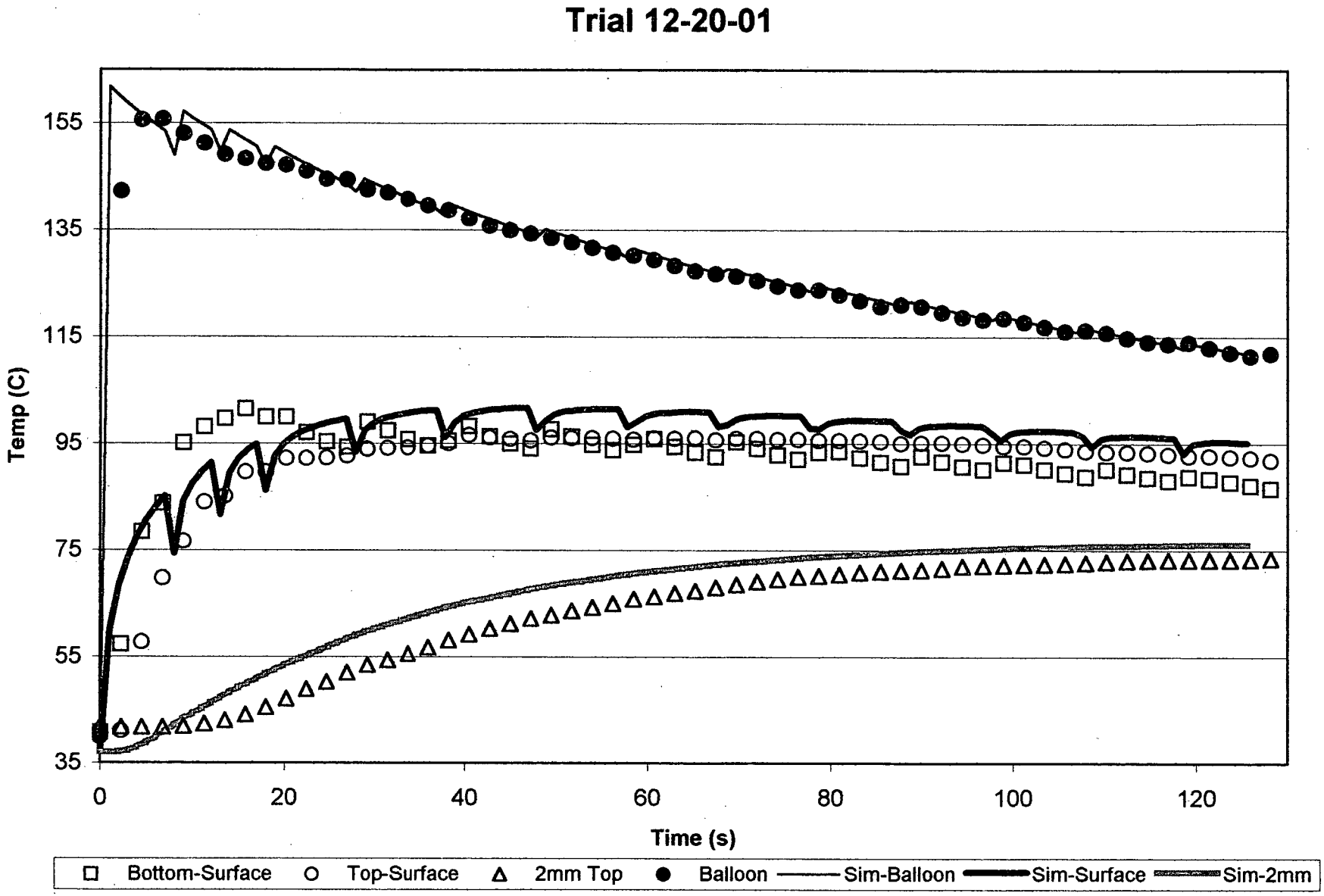
Trial 12-20-01
Temp (C)
155
135
115
95
75
55
35
0
20
40
60
80
100
120
Time (s)
Bottom-Surface
Top-Surface
2mm Top
Balloon
Sim-Balloon
Sim-Surface
Sim-2mm

Trial 2-1-01A

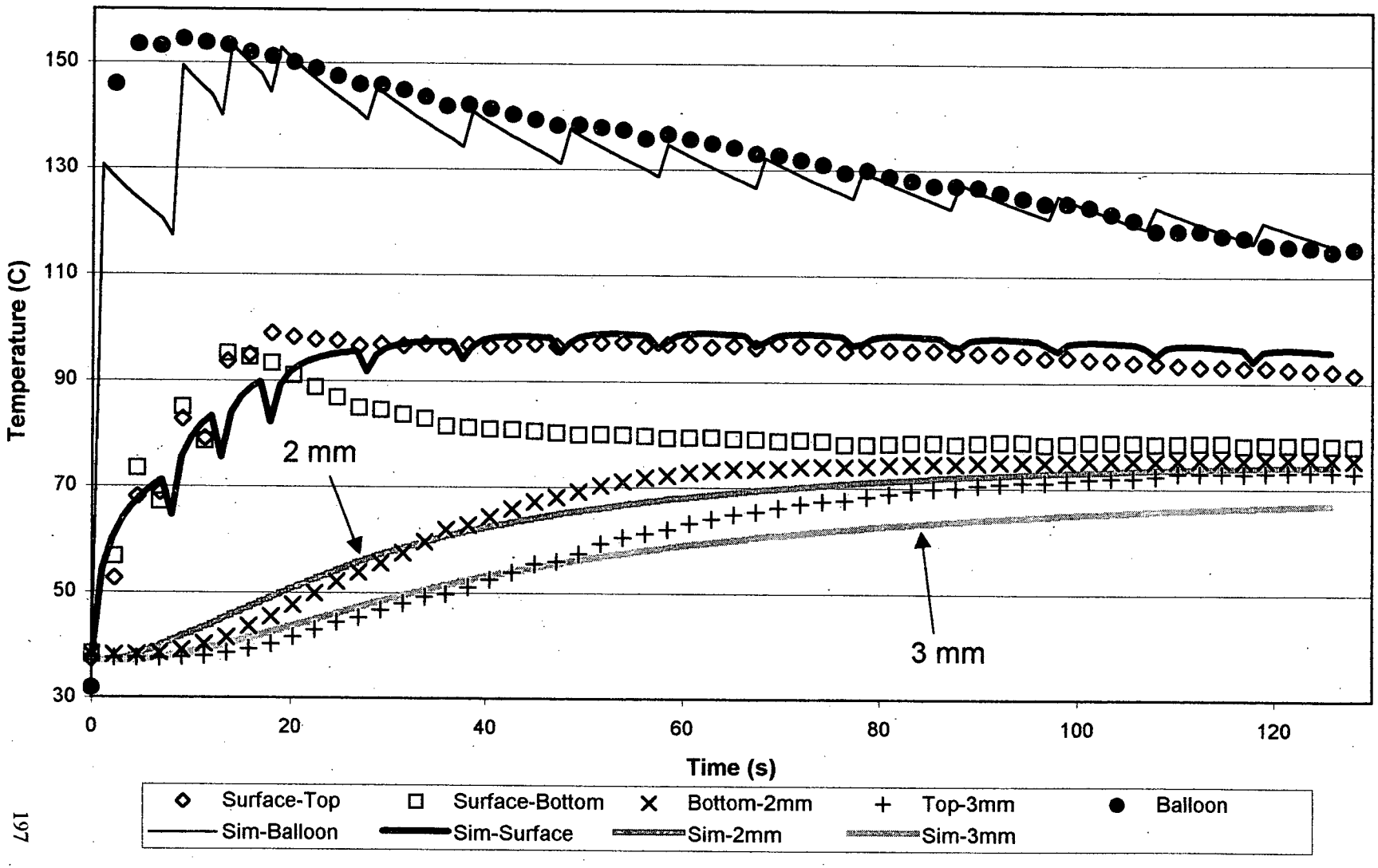
Temperature (C)
150
130
110
90
70
50
30
0
20
40
60
80
100
120
Time (s)
2 mm
3 mm
Surface-Top
Surface-Bottom
Bottom-2mm
Top-3mm
Balloon
Sim-Balloon
Sim-Surface
Sim-2mm
Sim-3mm

Trial 2-1-02B

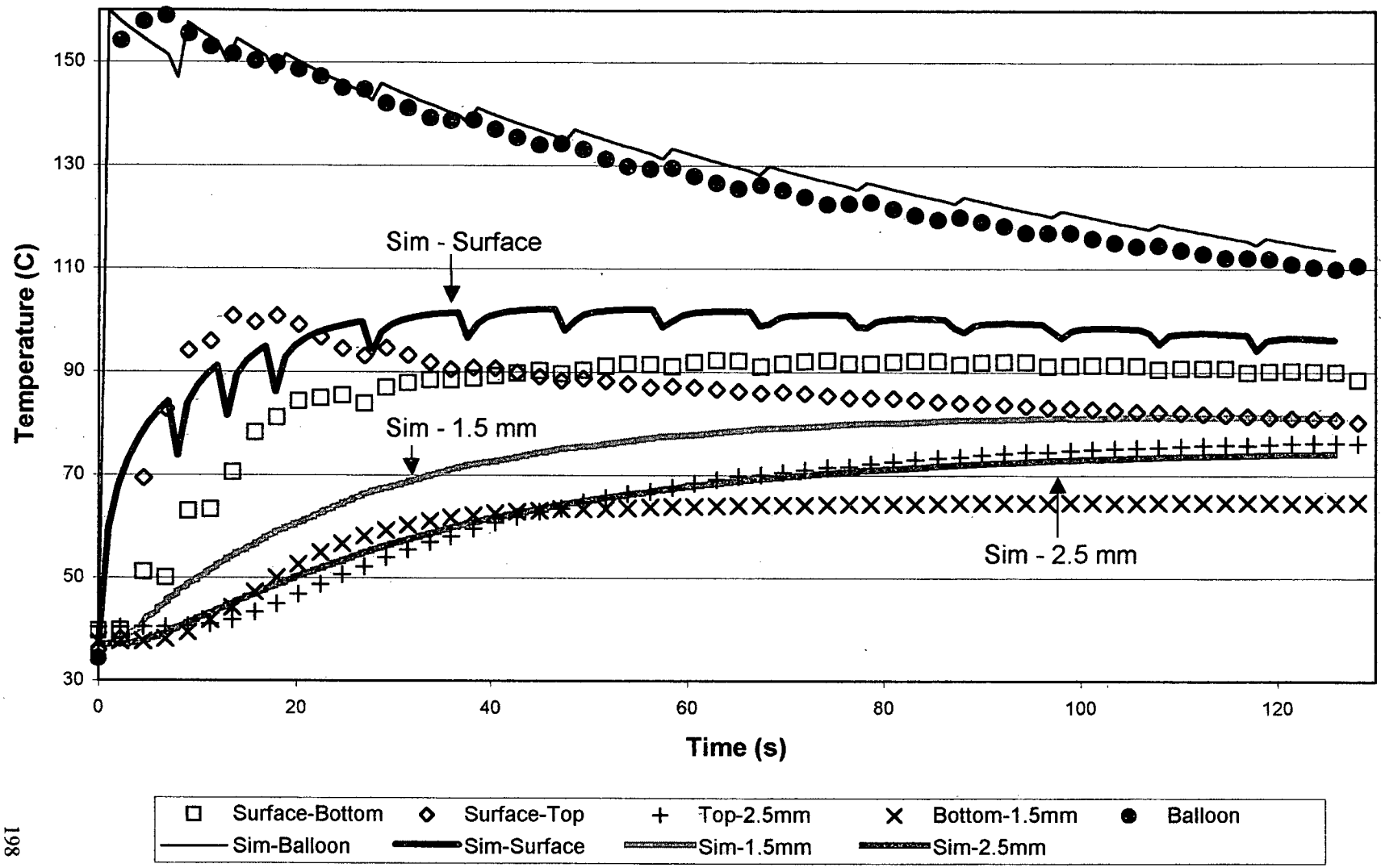
Temperature (C)
150
130
110
90
70
50
30
0
20
40
60
80
100
120
Time (s)
Sim - Surface
Sim - 1.5 mm
Sim - 2.5 mm
Surface-Bottom
Surface-Top
Top-2.5mm
Bottom-1.5mm
Balloon
Sim-Balloon
Sim-Surface
Sim-1.5mm
Sim-2.5mm

Appendix D - Sensitivity Analysis

The temperature profile in the tissue at the end of the treatment is presented in this section for the four parameters that had the largest effect on the temperature distribution in the tissue: thermal conductivity, heat capacity, base blood perfusion rate and the blood perfusion stasis pressure.

Thermal Conductivity Temperature Profile At End Of Treatment- Thermachoice 2 Device

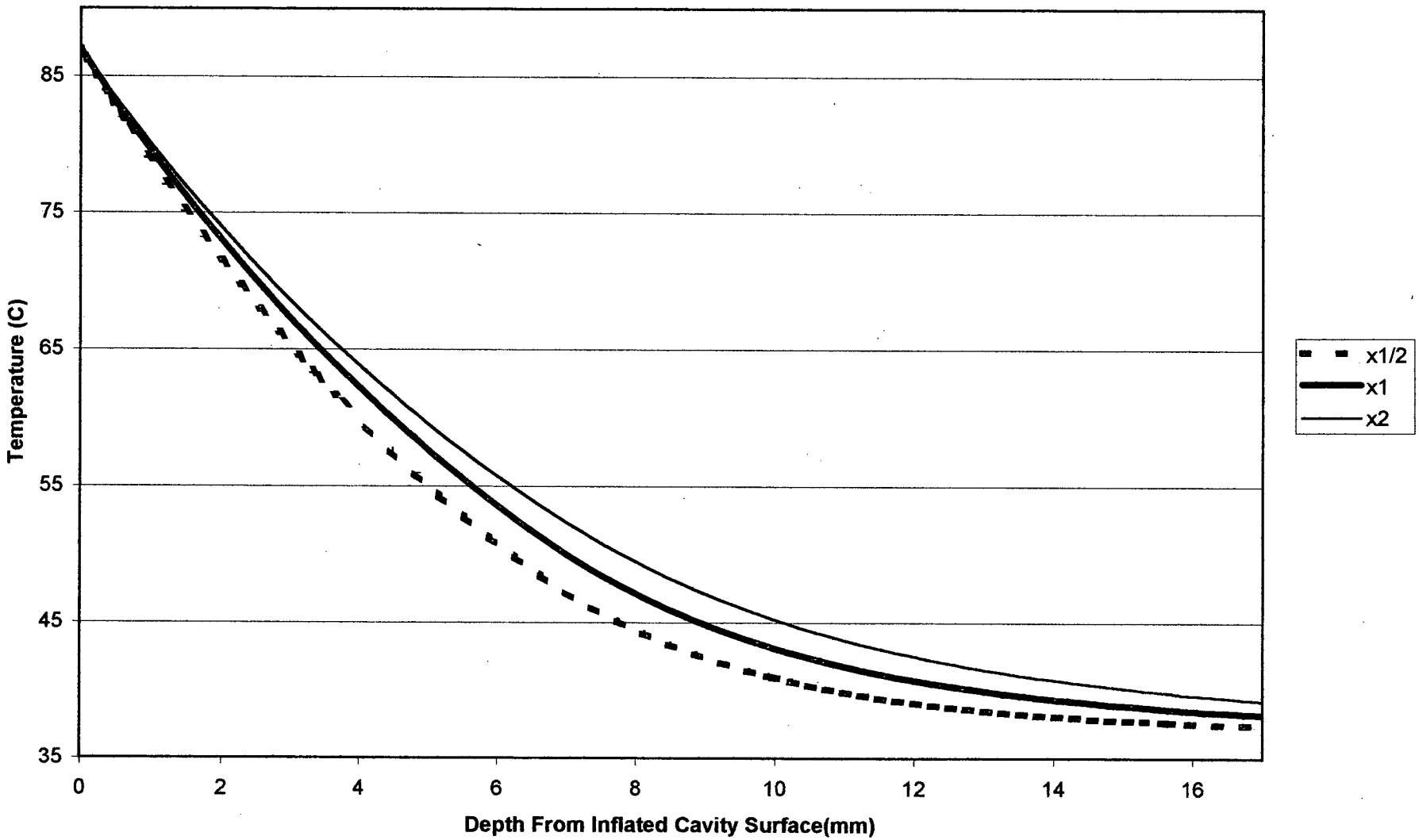

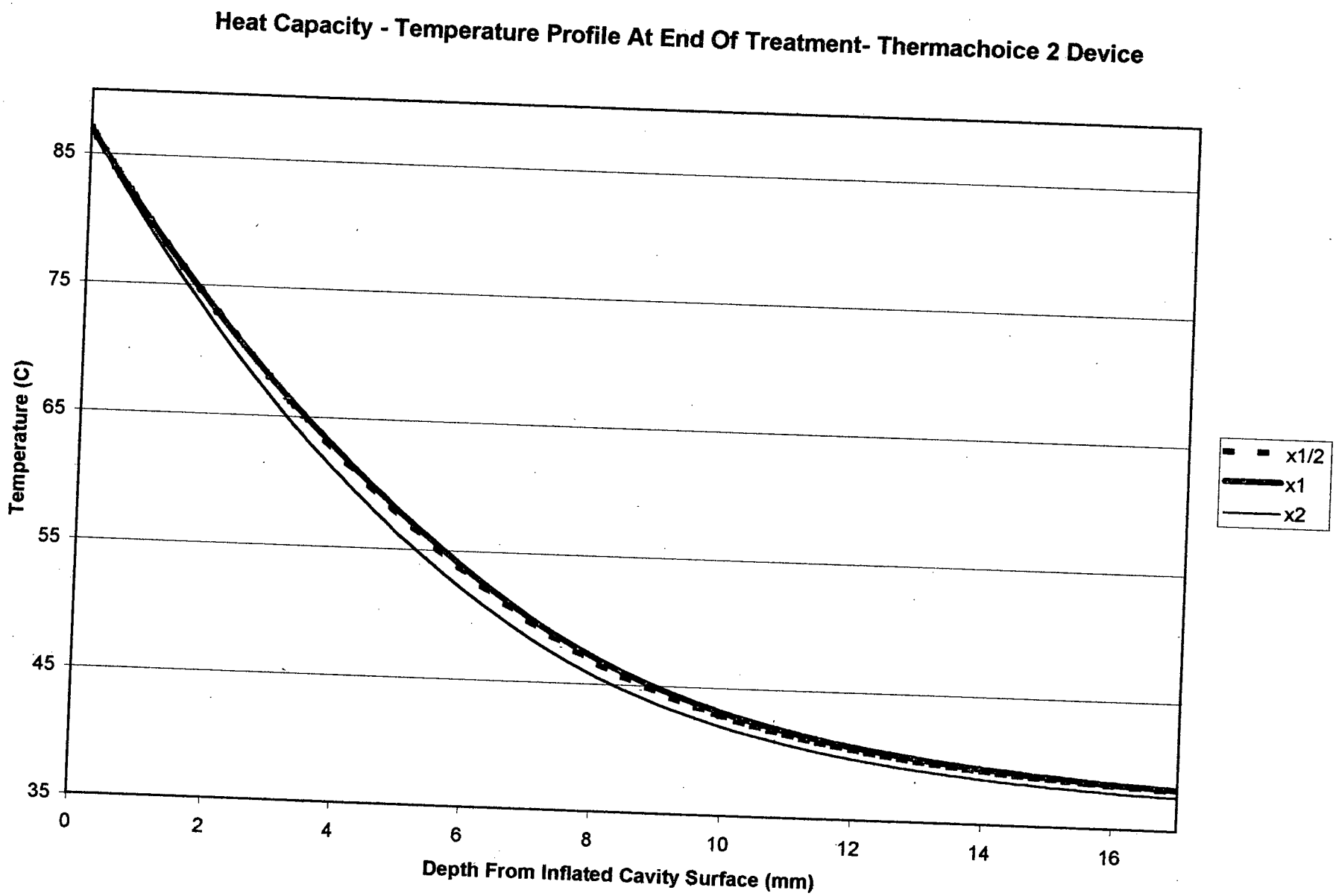
Heat Capacity - Temperature Profile At End Of Treatment- Thermachoice 2 Device
Temperature (C)
85
75
65
55
45
35
0
2
4
6
8
10
12
14
16
Depth From Inflated Cavity Surface (mm)
x1/2
x1
x2

Base Perfusion Rate - Temperature Profile At End Of Treatment- Thermachoice 2 Device

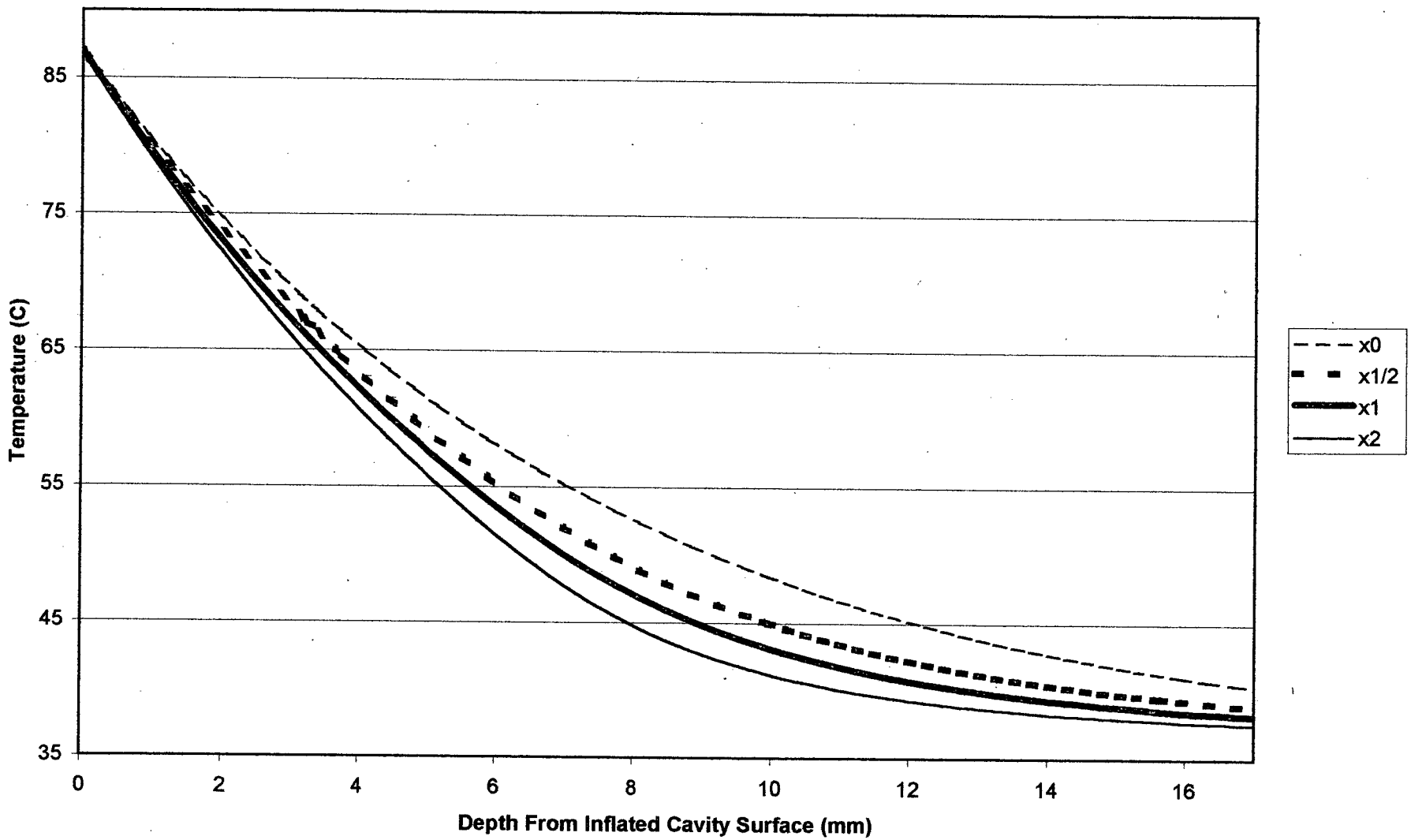

Blood Vessel Stasis Pressure - Temperature Profile At End Of Treatment- Thermachoice Device

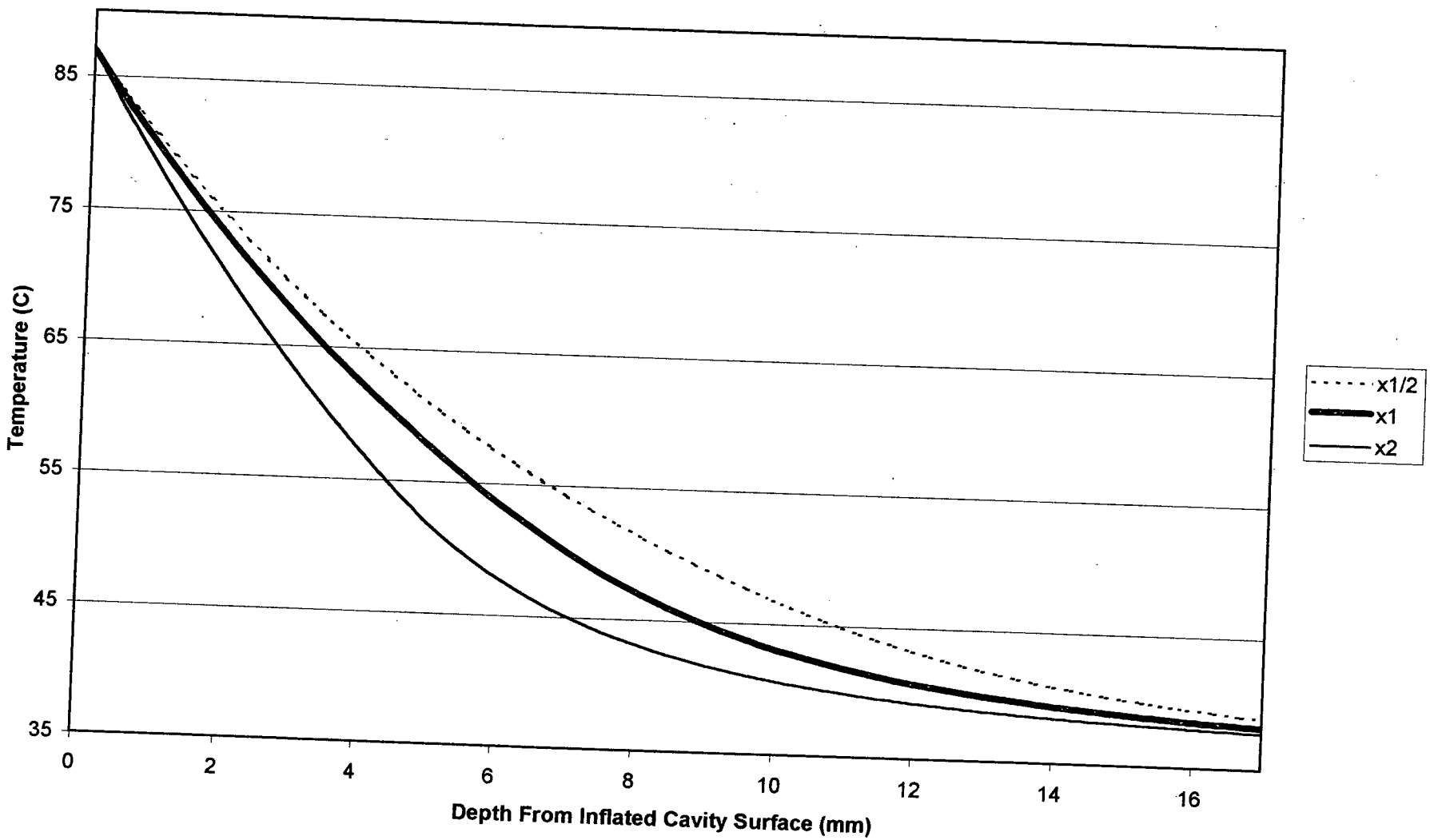

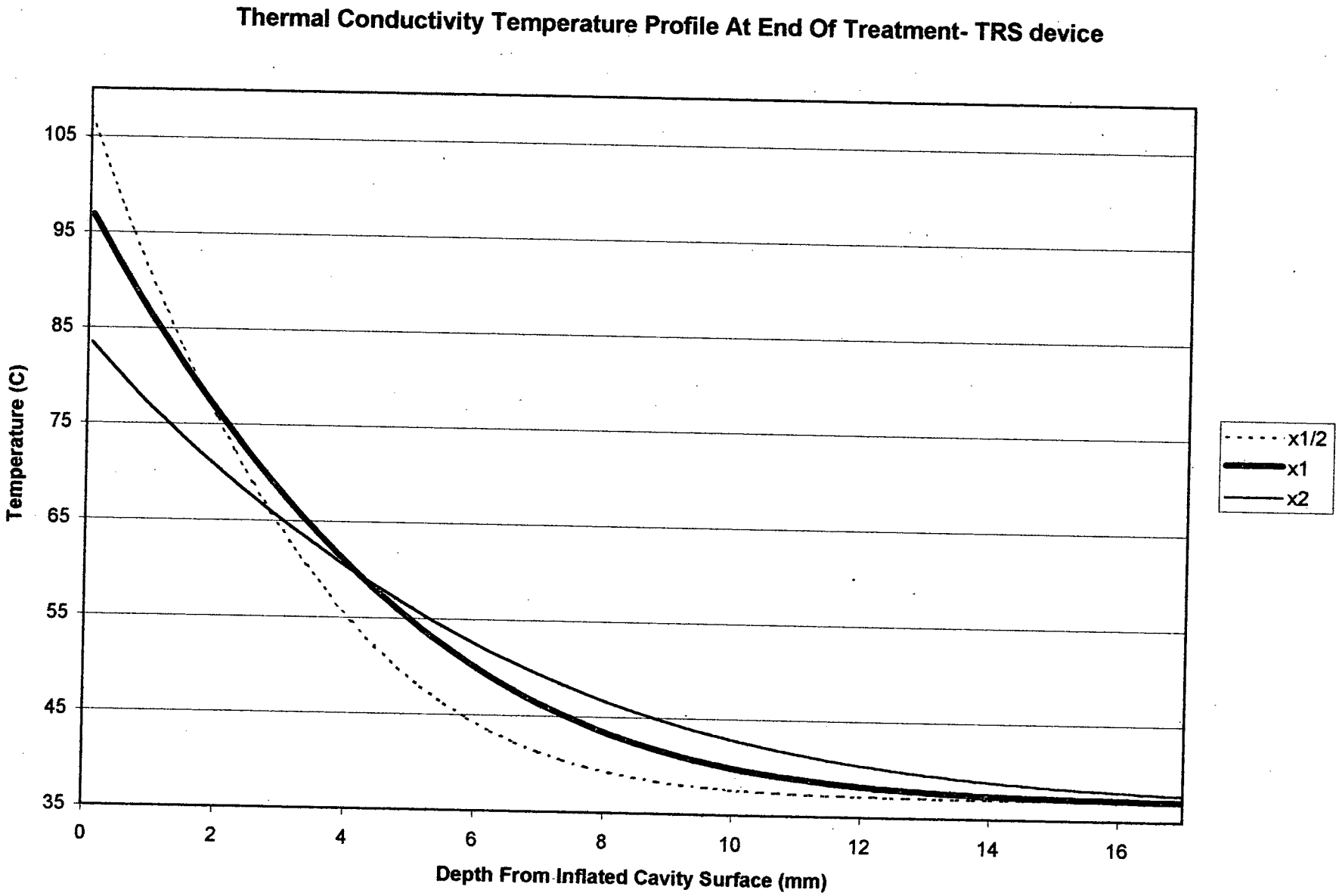
Thermal Conductivity Temperature Profile At End Of Treatment- TRS device
Temperature (C)
105
95
85
75
65
55
45
35
0
2
4
6
8
10
12
14
16
Depth From Inflated Cavity Surface (mm)
x1/2
x1
x2

Heat Capacity - Temperature Profile At End Of Treatment- TRS device

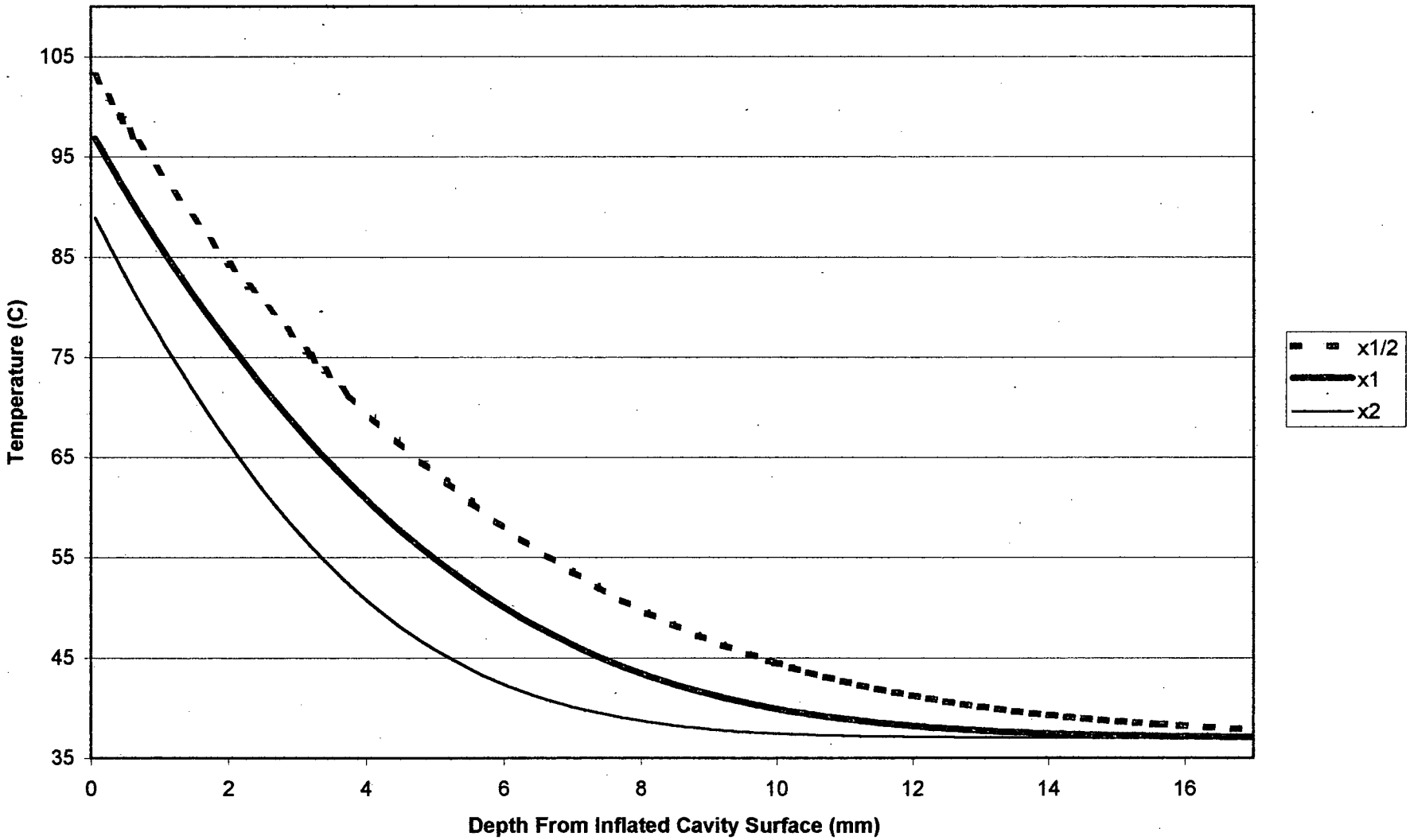

Appendix E

The source code and compiled program are included on CD-ROM. The program was written with Microsoft Visual C++, for Windows NT 4.0. Computers that do not have Visual C++ installed will need the appropriate dynamically linked libraries imported.

Program instructions:

1. Open the top menu and select 'Simulation'. In the drop down box select 'Tissue parameters values'. A new dialog box will open that will allow the desired tissue properties to be entered. The radius of the undistended uterus is adjusted in this dialog box; the displaced volume will be calculated in the simulation dialog box. Depressing the 'Restore Default Values' control may restore the default values. Once the desired parameter values are selected, depress the 'Accept Settings' control.
2. If the Arrhenius parameters determining thermal damage or vascular stasis need to be changed, select 'Arrhenius parameters' from the 'Simulation' menu.
3. Open the treatment protocol dialog box by selecting 'Run'. Select the desired exterior and interior boundary conditions, uterus geometry and perfusion modification factors. In addition to varying the perfusion modification parameter values, the modifying effects of pressure, hyperthermia and thermal damage may be prevented by using the check boxes. Ensure that the displaced cavity volume is correct before performing the simulation.
4. If the TRS is to be simulated, select the 'Thermablate' option for the interior

boundary condition. A new dialog box will open allowing the heat transfer parameters of the TRS to be modified.

5. If a constant temperature device is to be simulated, simply select 'Start simulation'. A progress bar will appear that will display the status of the simulation. At the end of the simulation a new dialog box will appear that provides information regarding the burn depth and the amount of water vaporized. Burn depths on the left are reported in the undistended uterus, while burn depths on the right are for the distended uterus.
6. Data may be viewed within the program by selecting 'Temperature-time series graph', 'Animate temperature profile' and 'Burn depth time series'. Raw data may be viewed directly by opening the notepad program and selecting the desired file to view.
7. Further data analysis may be performed using the output files and a spreadsheet program, such as Microsoft Excel. All files are of text type and are tab-delimited. 'Tempdata.txt' provides the temperature history of the tissue at various selected points. "Burndepth.txt" provides the final Arrhenius values at the end of the treatment throughout the tissue. "Arrout.txt" details the progression of burn depth through the tissue during treatment.

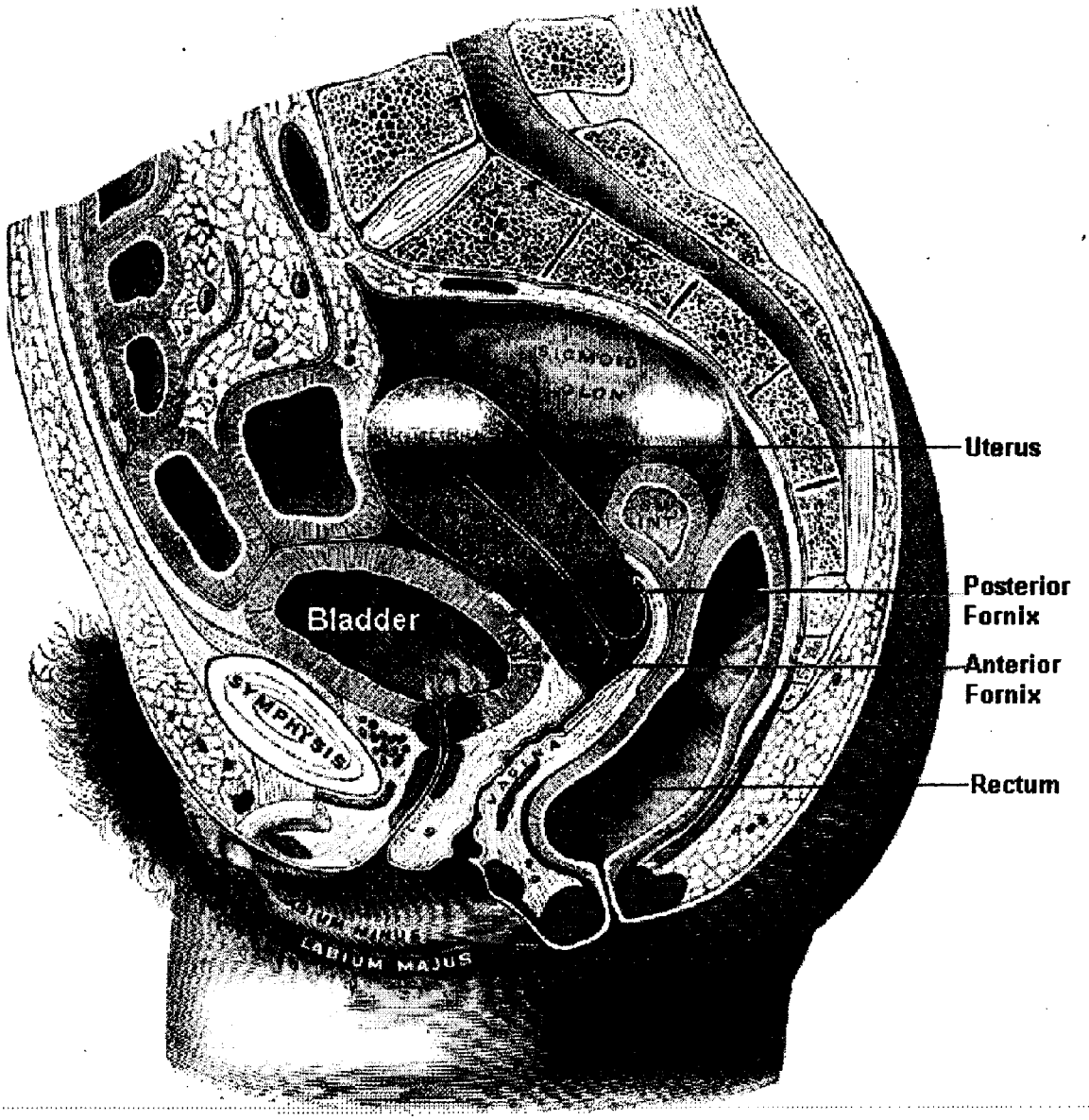

Figure 1 – Side view of the uterus and surrounding internal organs. In the undisplaced position the uterus normally tilts forward relative to the cervical canal. The rectum, colon, and the bladder are the two closest organs, and are the ones at risk should the exterior of the uterus become excessively heated (10).

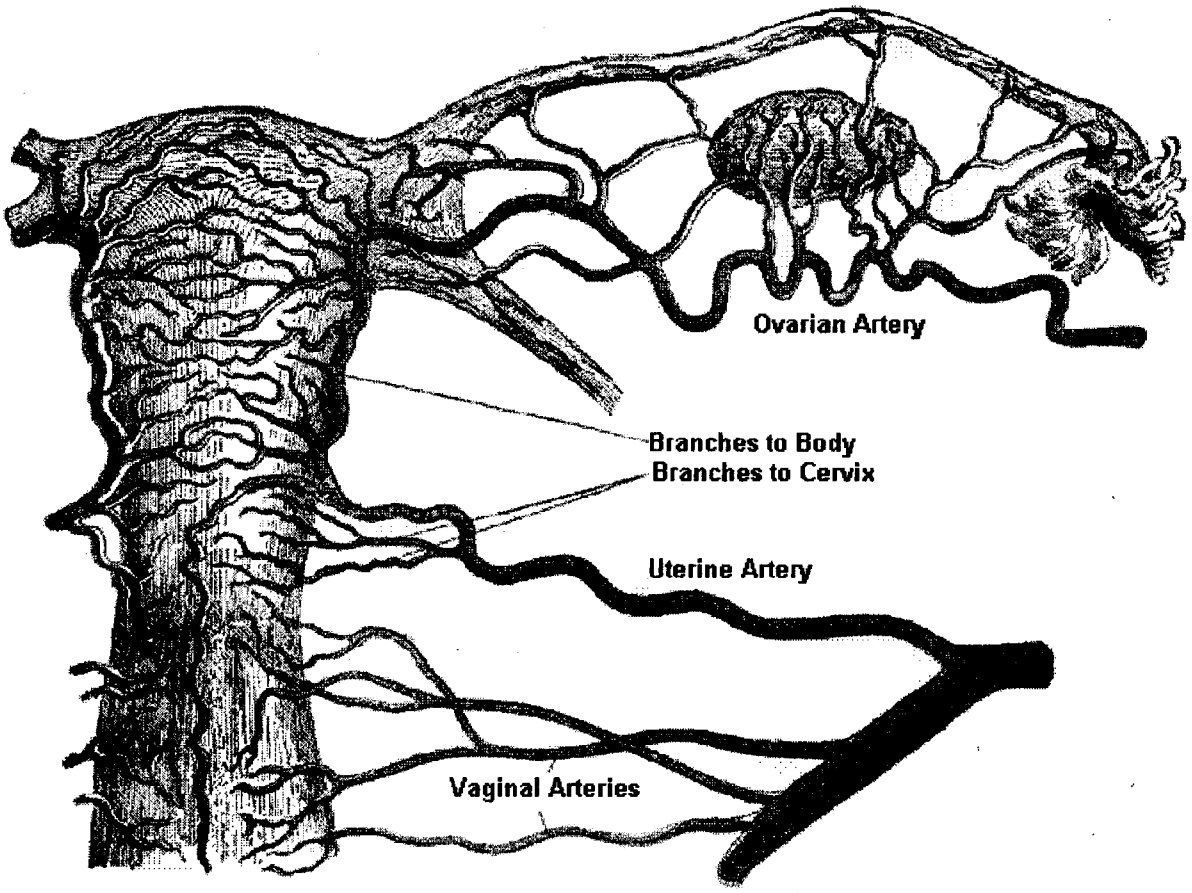

Figure 2 – Exterior view of the uterus and it's vasculature. The fallopian tubes exit near the fundus, and on the outer ends lie the ovaries. During ovulation an ova is released from the ovaries and is drawn into the uterus cavity through the hollow fallopian tubes (10).

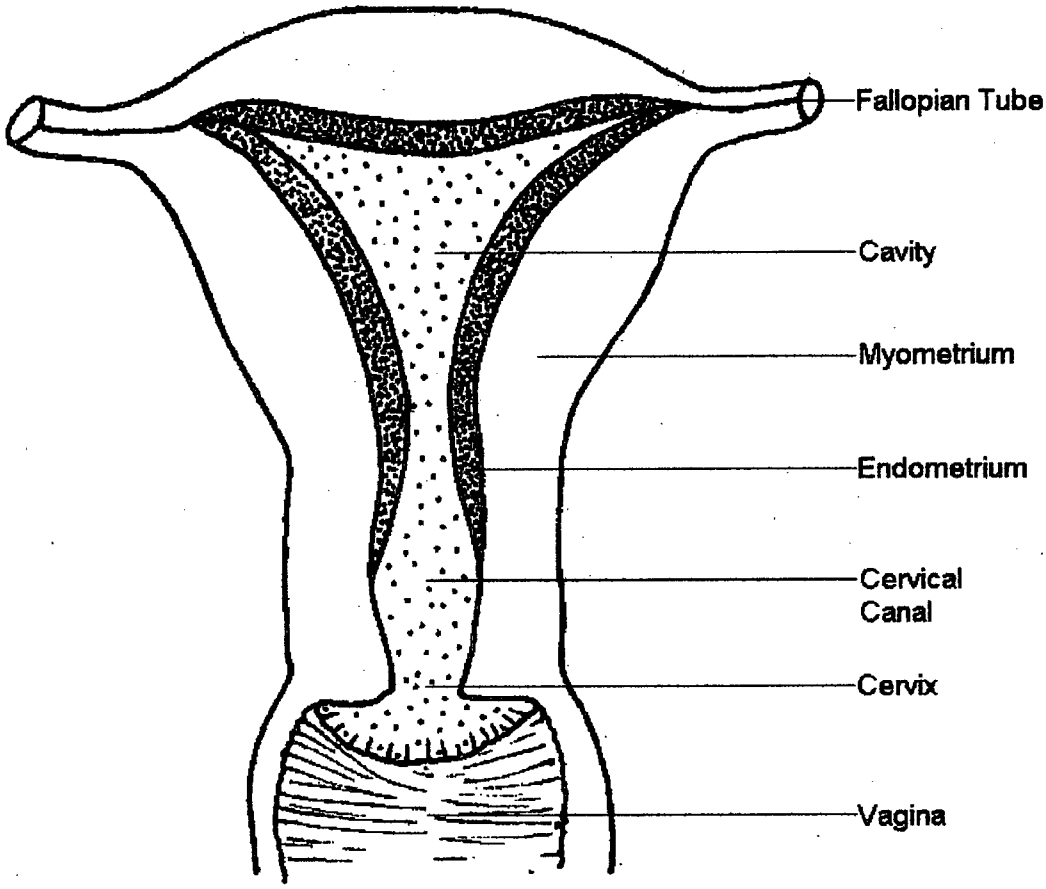

Figure 3 – Frontal view of the uterus in cross-section. The external orifice is the known as the cervix. The line indicating the internal orifice is also the isthmus. Near the fundus are the horns of the uterus, from which the fallopian, or uterine, tubes emerge. The interior is lined with the endometrium layer; this is surrounded by the thick and muscular myometrium layer. Modified from reference 10.

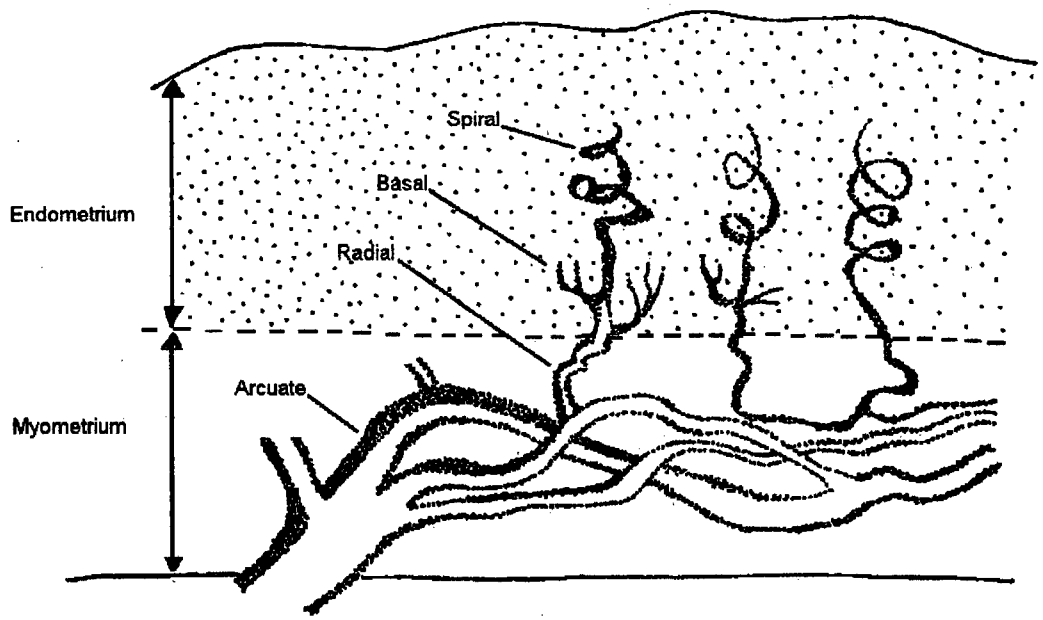

Figure 4 – Schematic representation of the uterine arteries Note that the spiral, basal and radial arteries form a continuous vessel extending from the arcuate wreath (11).

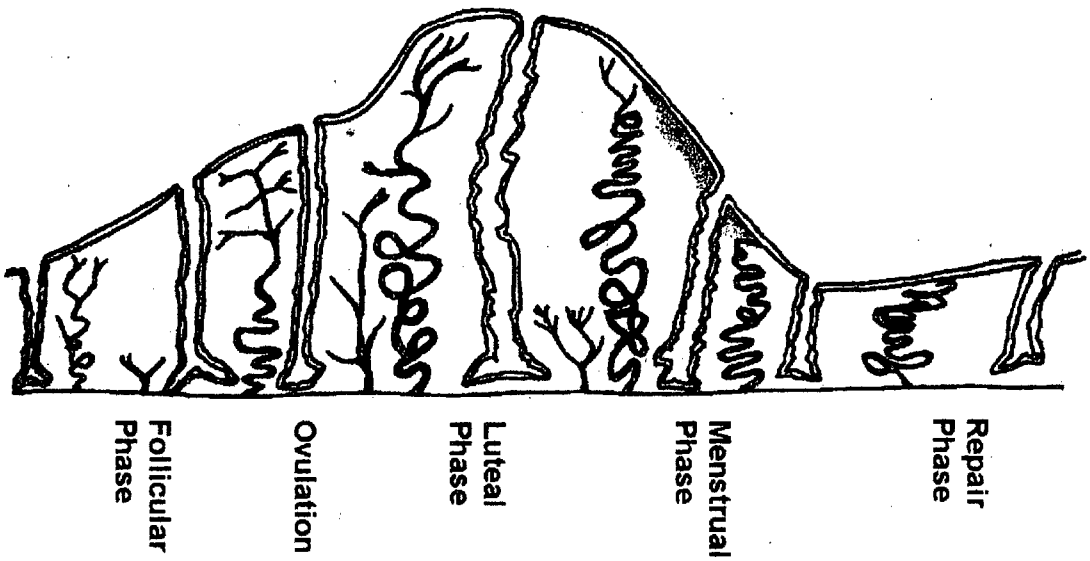

Figure 5 – Diagram of the anatomical changes that occur in the endometrium during the menstrual cycle. The endometrium is thinnest following menstruation, and then rebuilds during the follicular phase. The spiral arteries grow into the thickened tissue throughout the ovulatory and luteal phase. At the ischemic phase tissue necrosis begins to occur, and the menstruation begins again. Also visible are the endometrial glands (the cavities) (11).

Figure 6 – Photograph of the TRS ablation device, with handheld display attached to the balloon temperature thermocouple (not standard).

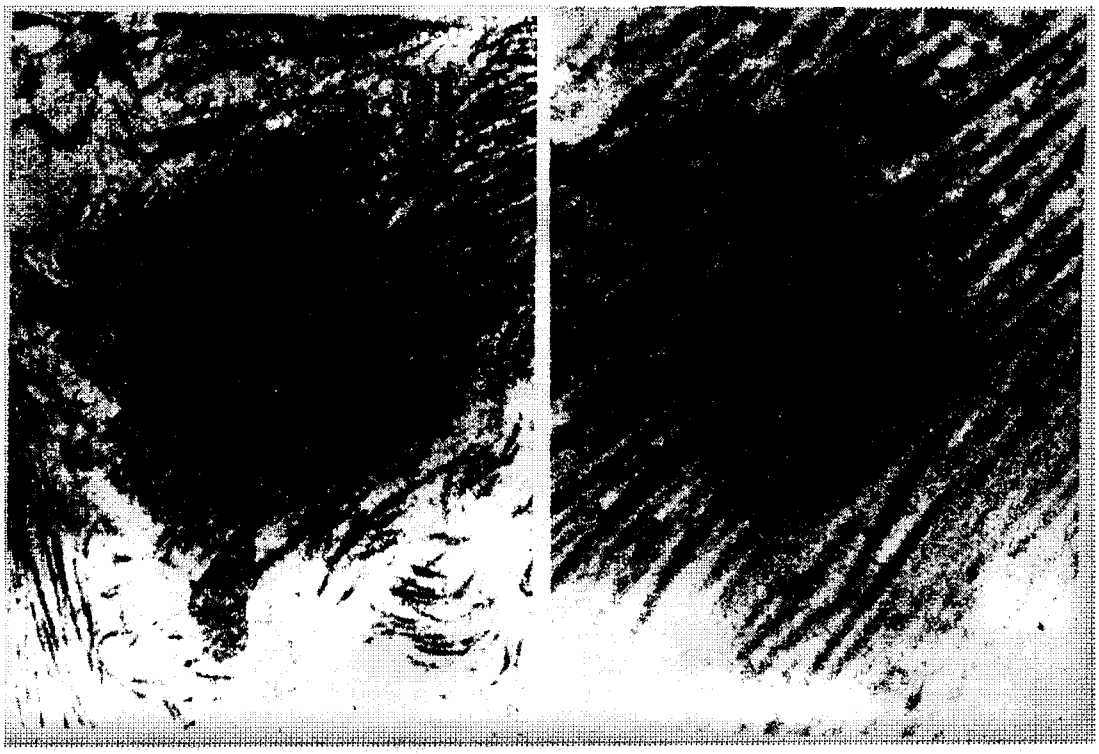

Normal Collagen Fibers Thermally Damaged Collagen Fibers

Figure 7 – Swelling of thermally damaged collagen fibers. In the left image are normal sub-mucosal fibers of the rodent colon (63), on the right are damaged fibrils 72 hours after injury. The tissue was laser heated at 500mW for 100 seconds, resulting at a temperature of 66°C, 1mm from the laser tip. Note the significant increase of thickness for thermally damaged collagen fibrils. Magnification is 60,000 times.

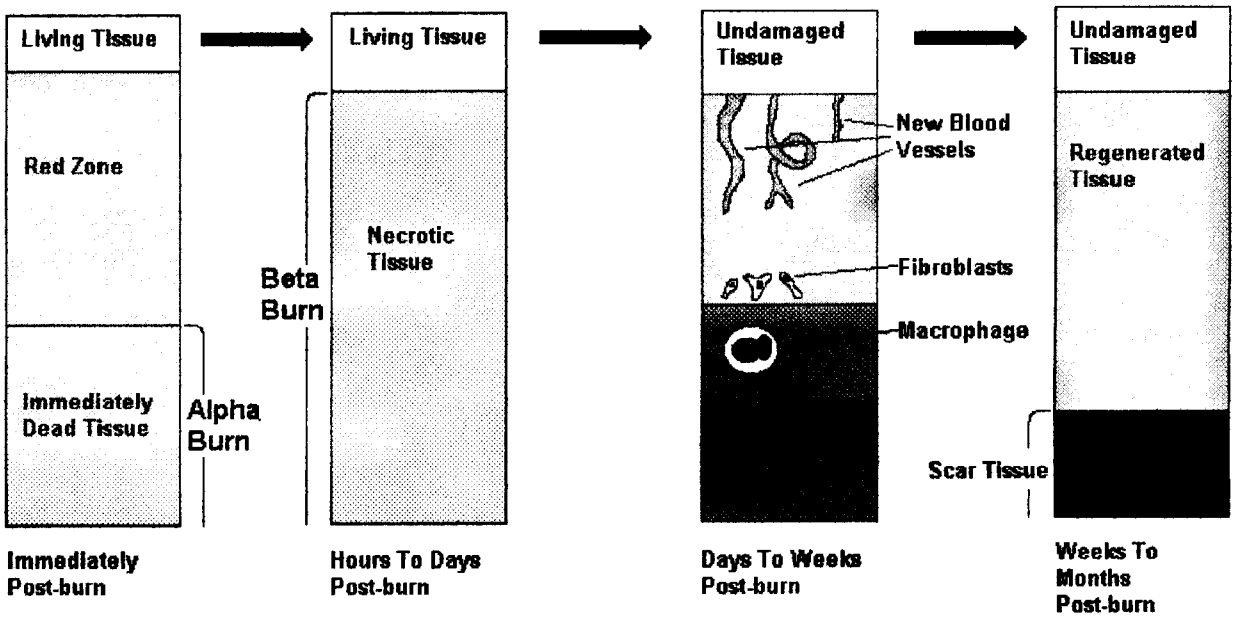

Figure 8 – Diagram illustrating our proposed model of the progression of burn healing and the cells typically seen in the healing zone. Immediately after the injury there is a zone of immediately killed tissue (the 'alpha burn' threshold) surrounded by the hyperemic red zone. Over the period of hours to days the zone of dead tissue expands to its maximum extent, which we define as the 'beta burn'. After several days macrophages digest and remove the necrotic debris, while fibroblasts and blood vessels enter from the edge to form new tissue. Eventually the necrotic tissue is replaced by either regenerated tissue or scar tissue.

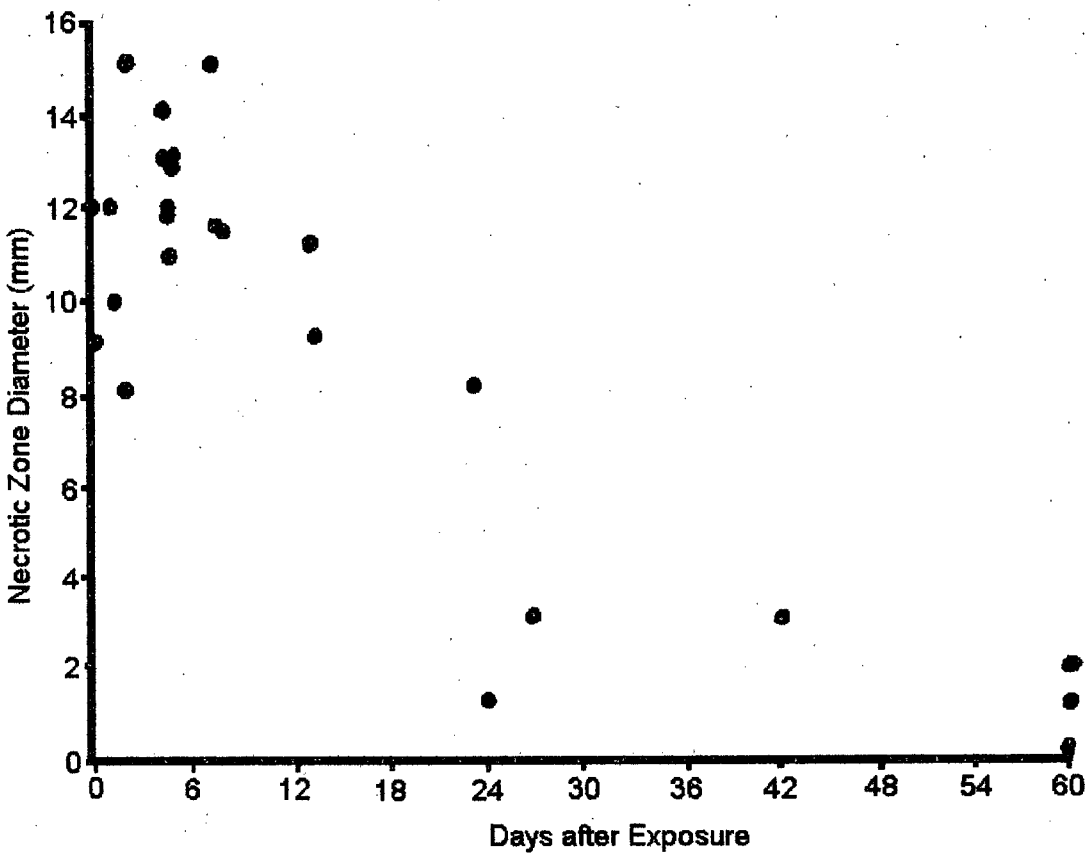

Figure 9 - Progression of burn depth with time (66), following Nd:Yag laser treatment with 1 W for 1000s to the rate liver. Maximum burn depth was reported on day seven, following which tissue regeneration decreased the depth of necrosis.

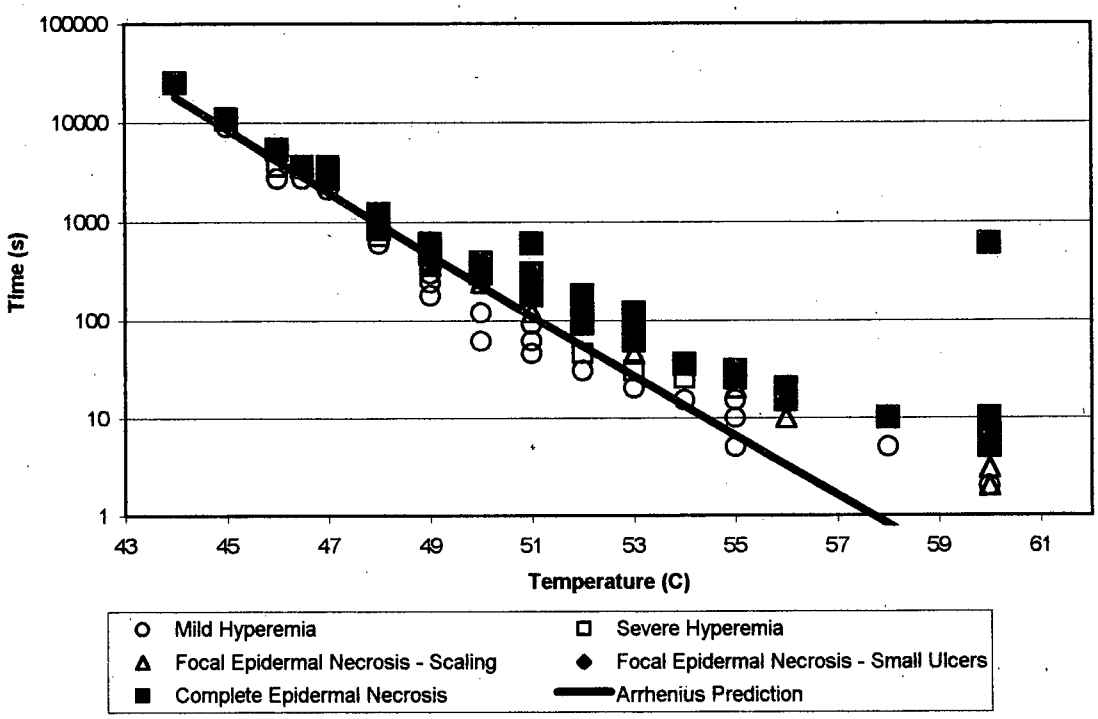

Figure 10 – Chart illustrating the fit of the Henrique's damage integral to the Moritz data (85). Several damage end-points were recorded, ranging from mild hyperemia to complete epidermal necrosis. Open symbols represent 1st degree injuries, while closed symbols are used for 2nd degree burns. The damage integral of Henrique's fits the data quite well for temperatures below ~52°C, the lack of fit at higher temperatures is partially explained by the growing importance of temperature transients as the burn time is shortened.

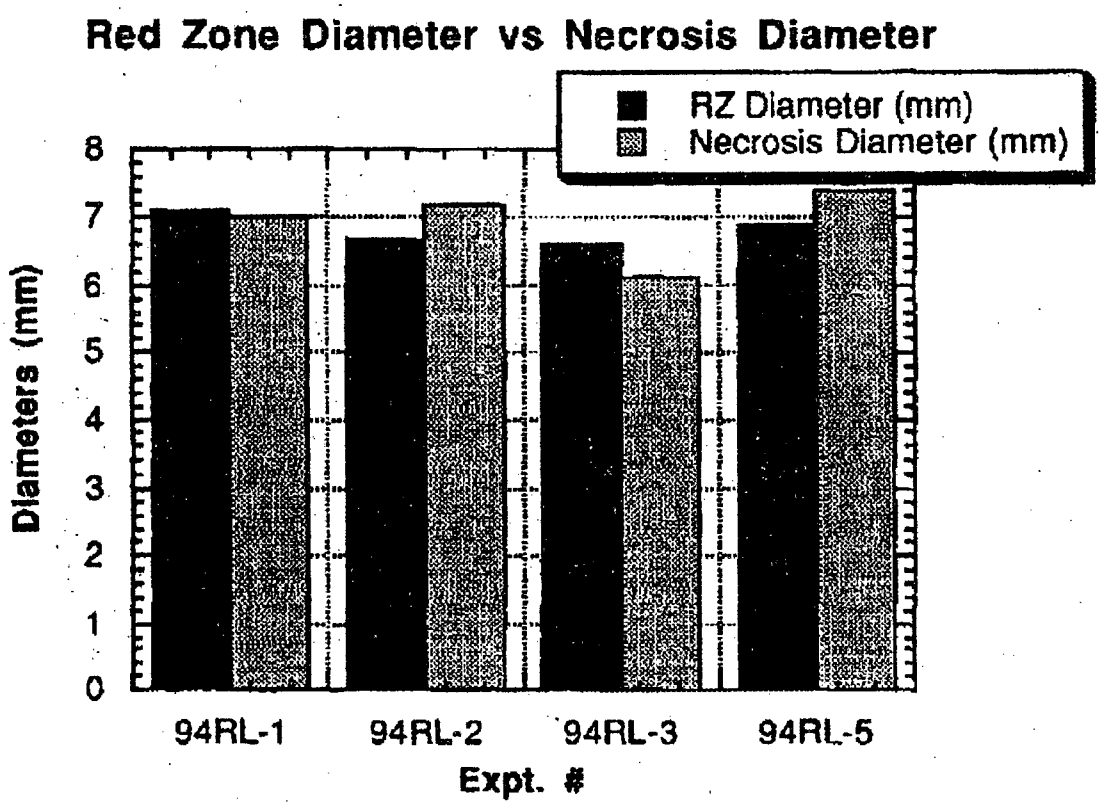

Figure 11 – Illustration of experimental results of laser heating of rat liver tissue (84). The diameter of the red zone (RZ) was strongly correlated with the diameter of eventual necrosis for these four trials, although it is unknown whether this relationship holds for other time-temperature combinations. The red zone and eventual necrosis threshold was associated with a maximum temperature of 55°C over the 9.9 second treatment period.

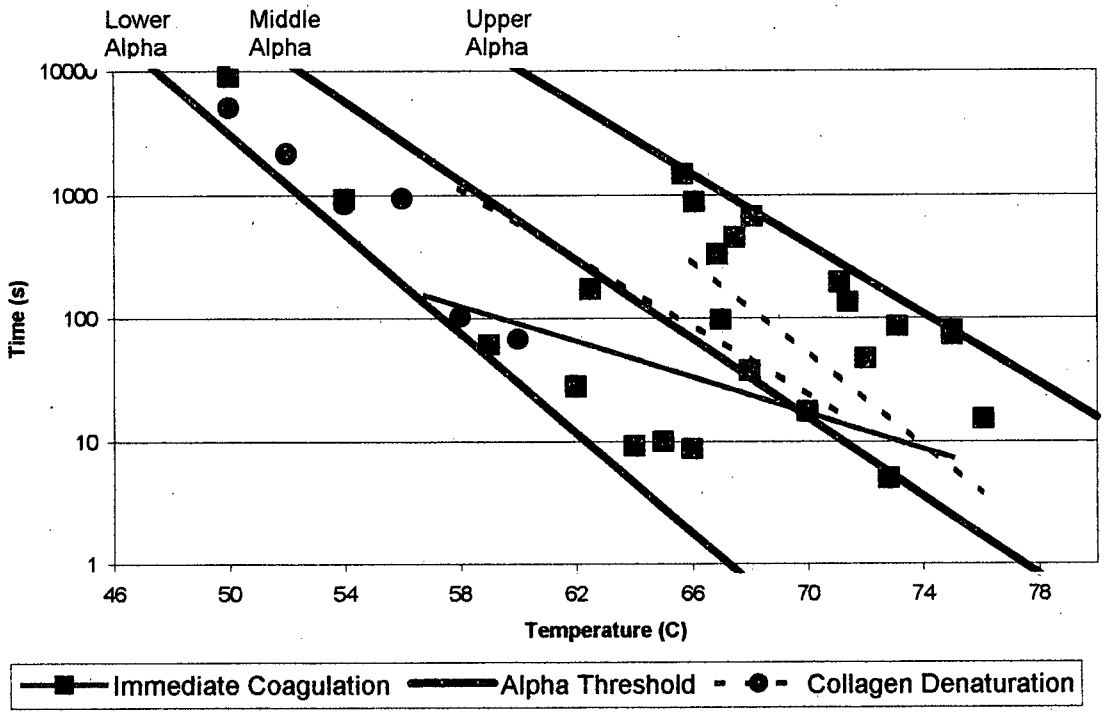

Figure 12 – Graph presenting the alpha burn exposure thresholds (lower, most probable and upper) and the calibration data and functions. Calibration data was based upon visible coagulation and the denaturation of collagen, two damage thresholds that are associated with the immediate death of the tissue.

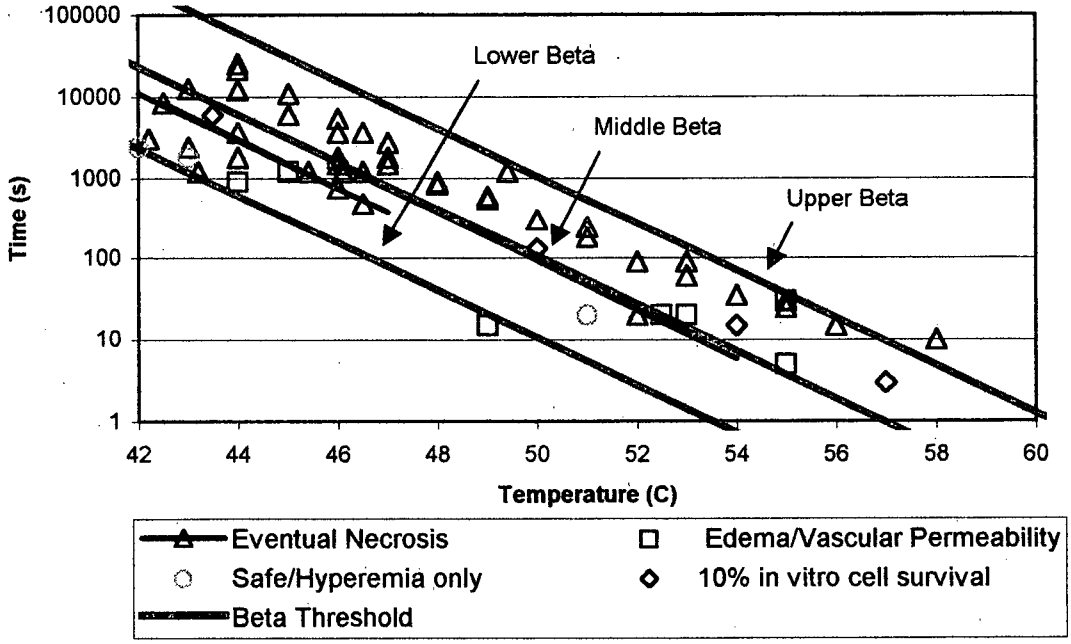

Figure 13 – Graph presenting the beta burn exposure thresholds (lower, most probable and upper) indicative of eventual necrosis of the tissue, and the calibration data and functions. Triangles represent data points that resulted in eventual necrosis, while the black lines represent functions that predict eventual necrosis. Also included are data points that represent mild damage, including edema formation and increases in vascular permeability. The exposure required to induce death in 90% of baby hamster kidney cells *in vitro* was included in the graph, as were exposures that did not result in irreversible damage.

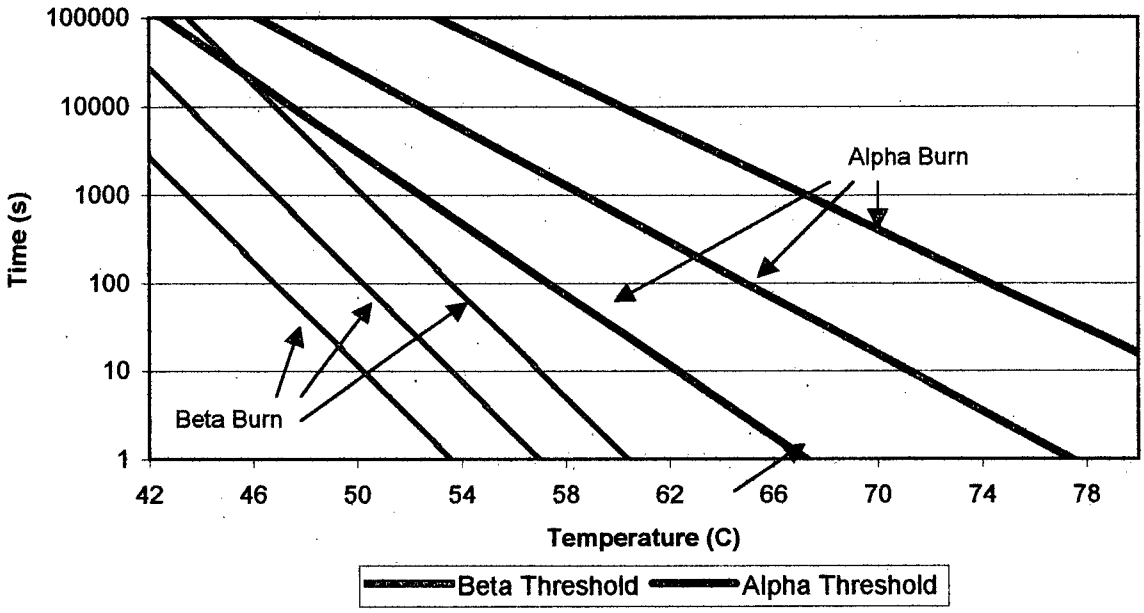

Figure 14 – Graph comparing the thresholds for the Alpha and Beta burn. Far greater exposures are required to induce an alpha burn, for example at 54°C a 10 second exposure will result in the eventual death of the tissue, but over 10,000 seconds are required at the temperature to cause the immediate death of the cell.

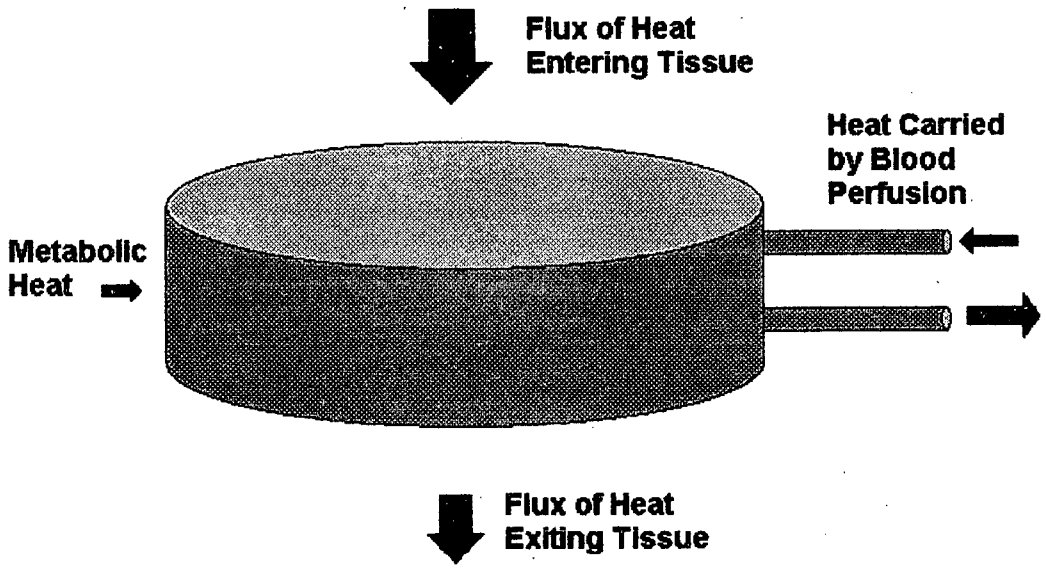

Figure 15 – Conceptual illustration of the Pennes equation as applied to a one-dimensional control volume. Blood is assumed to enter, equilibrate with the tissue temperature and then exit. The rate of heat accumulation is therefore equal to the difference between the flux of heat entering and leaving the volume, plus the net transport of heat by the blood and any contribution from the metabolic heat source term.

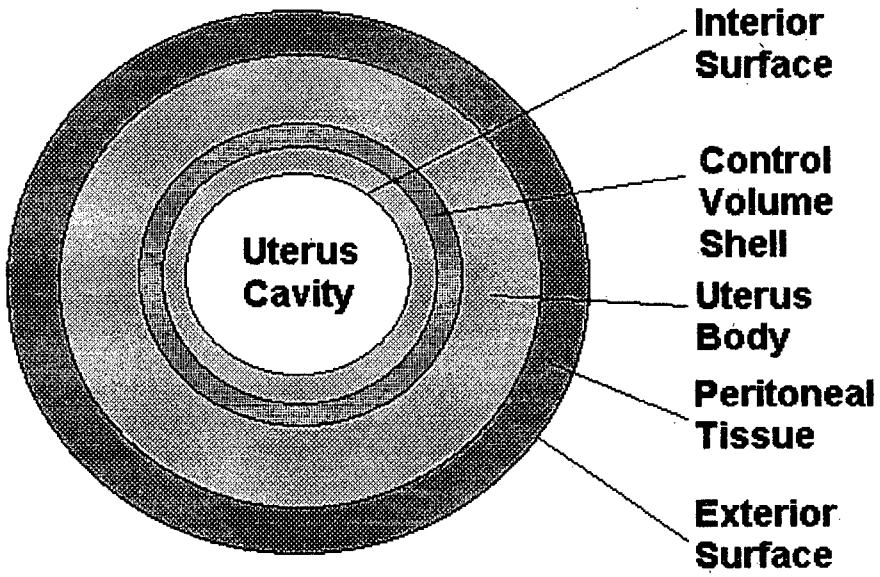

Figure 16 – Illustration of the geometry of the computer model of the uterus. This is a two-dimensional representation of a spherical model. The interior boundary is the uterus cavity. An example of the control volume is shown (not to scale), it is a thick walled spherical shell. Peritoneal tissue is assumed to surround the uterus, and enough tissue is modelled that the uterus may be considered semi-infinite in nature.

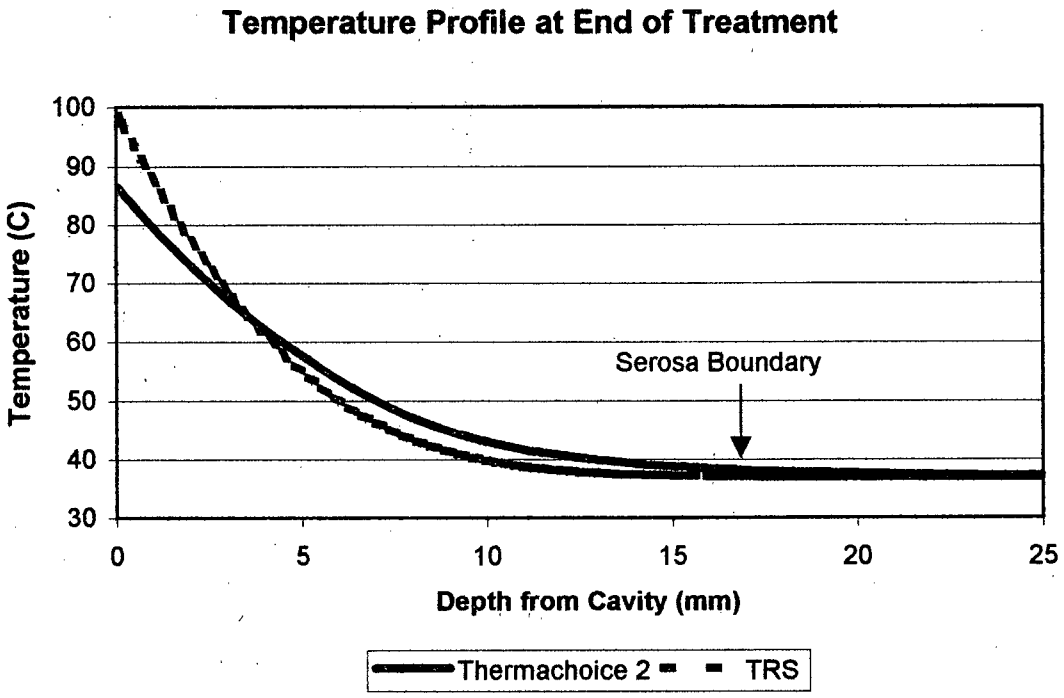

Figure 17 – Predicted Temperature profile at the end of the treatment for the Thermachoice™ 2 device and the TRS. The serosal boundary is at 17mm, and beyond this point there is minimal temperature elevation, suggesting that it is unnecessary here to model tissue beyond 25mm; the temperature profile approximates that which would be observed in a semi-infinite tissue.

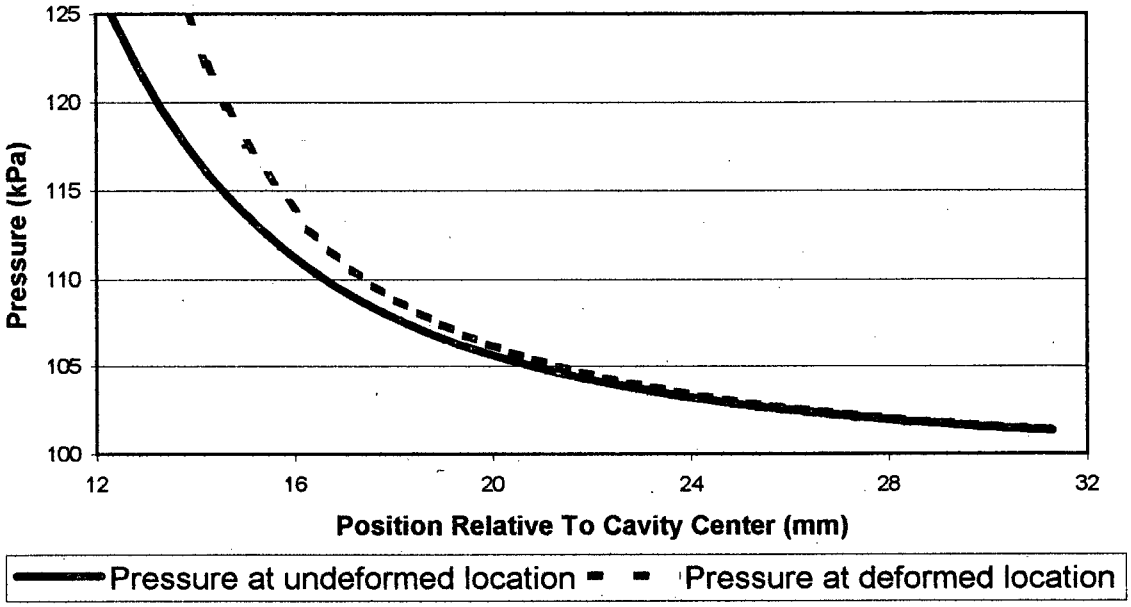

Figure 18 – Chart of the predicted pressure distribution and displacement exhibited by the average uterus upon distension at the standard balloon pressure of 180 mmHg (equal to 125 kPa absolute pressure). In contrast the blood vessel collapse pressure is 45 mmHt (equal to 107 kPa absolute). The pressure is bounded at the interior by the balloon pressure and at the exterior by the atmospheric pressure.

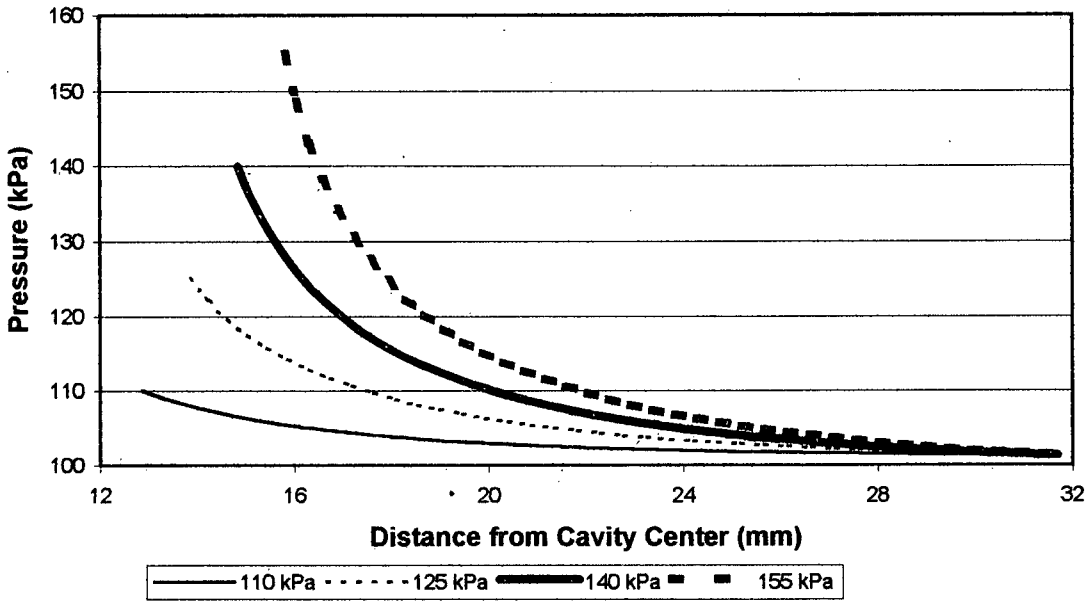

Figure 19 – Predicted effect of increasing absolute balloon pressure on tissue displacement. Note that compression of the interior tissue becomes increasingly severe as the interior pressure increases. Ambient pressure is 101.325 kPa.

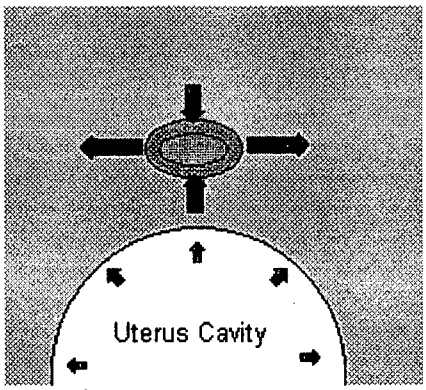

Figure 20 – Illustration of the effect of cavity pressure on a tangentially orientated blood vessel. The radial stress will tend to collapse the vessel, and this collapse is aided by the tangential tension. This process will result in the complete collapse of the vessel if the internal pressure is insufficient to prevent collapse, unless local elastic effects (due to the strength of the capillary wall and local distortion of the surrounding tissue) counteract the stresses inducing vessel collapse. The collapse pressure of the blood vessels was not modelled, instead an empirically derived pressure for the cessation of blood flow was used in the model.

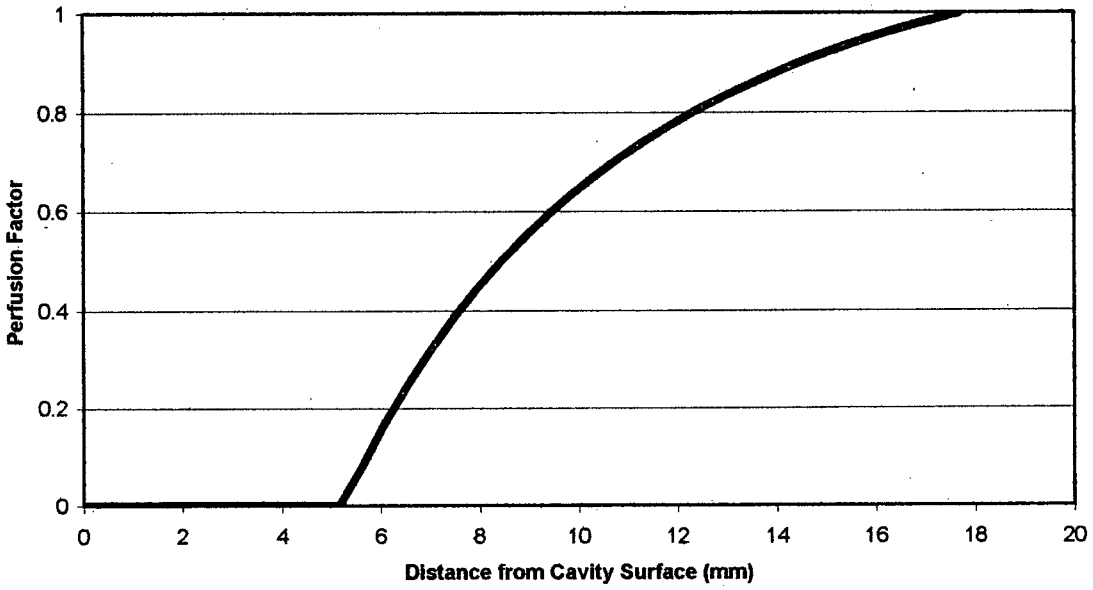

Figure 21 – The predicted variation of the pressure perfusion factor with distance from the distended cavity surface of a typical uterus at a balloon pressure of 180 mmHg. Perfusion is eliminated in the first five millimeters of tissue, and does not reach half of its normal value for three additional millimeters.

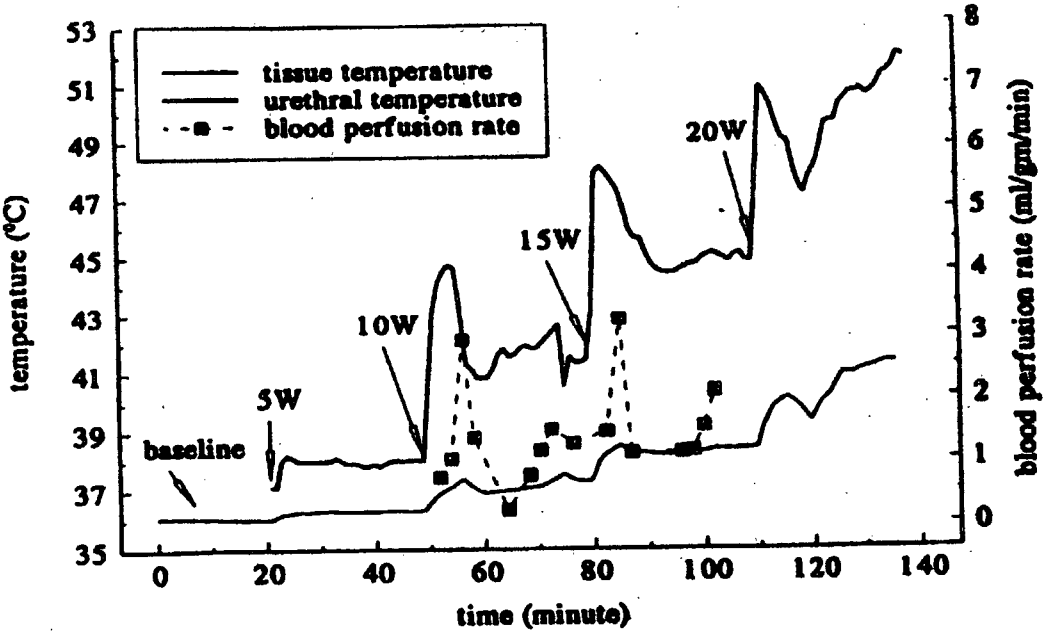

Figure 22 – Canine prostate blood perfusion response to staged radiofrequency hyperthermia (122). There was no significant increase in perfusion at 5 watts. Thermocouples were used to record the temperature, and a thermal pulse technique was used to determine the perfusion rate. Maximum temperature with this device occurs at the urethral wall inside the prostate, the tissue (measured 1 mm radially from the urethral wall) temperature was significantly lower.

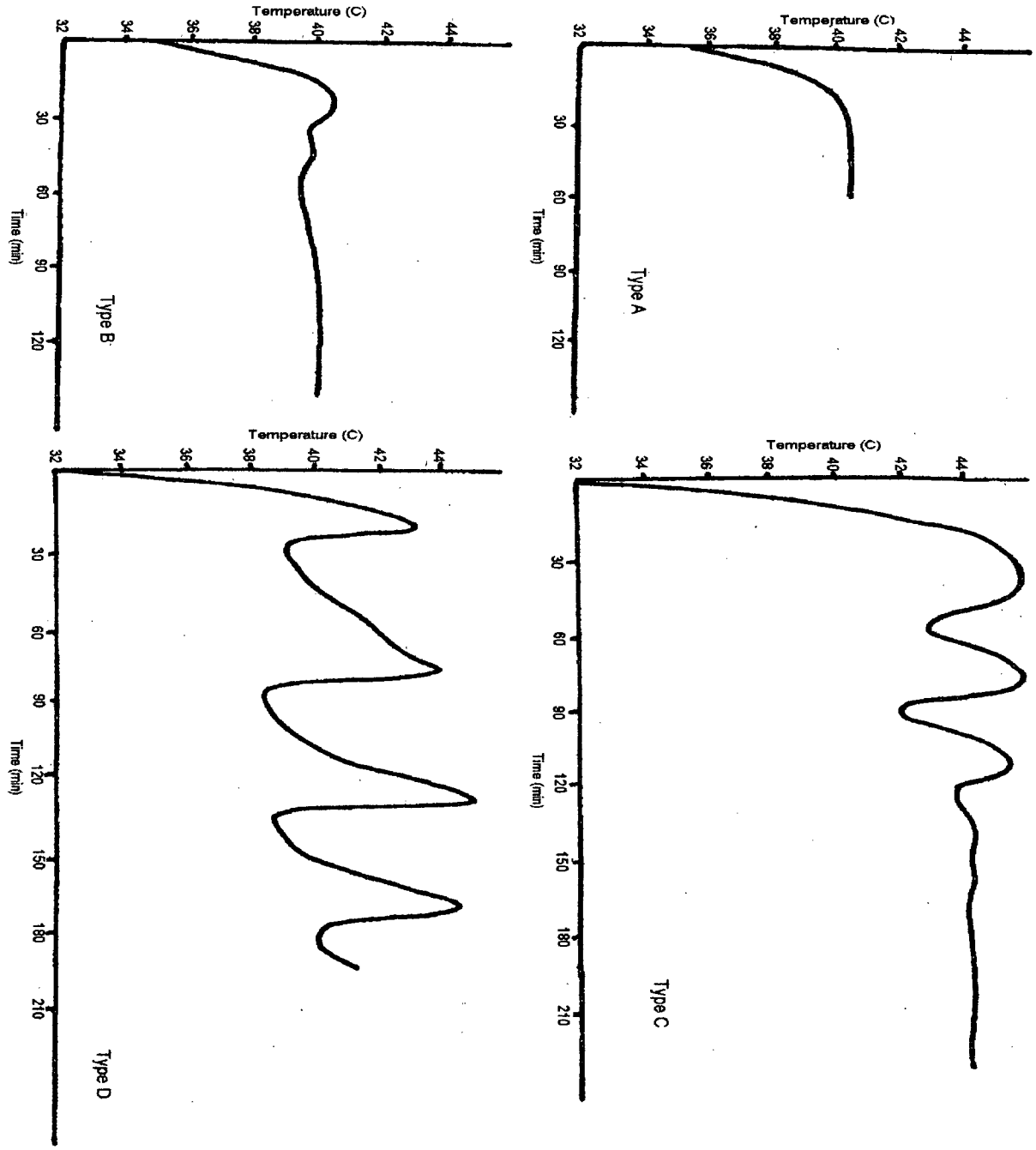

Figure 23 – Temperature Response at 1.5 cm deep probes in canine thigh muscle during four microwave hyperthermia experiments at different power settings (123). Responses A, B, C and D are produced by a specific energy absorption rate of 34.2, 34.2, 52.2 and 79.9 W/kg. As the applied power is increased the perfusion response starts to oscillate, inducing similar changes in the temperature-time series. Note that the graphs depict temperature during a hyperthermia induced by a constant rate of energy deposition. In the absence of blood perfusion the tissue would approach an equilibrium temperature, however the variation in the perfusion rate induces variations in the temperature.

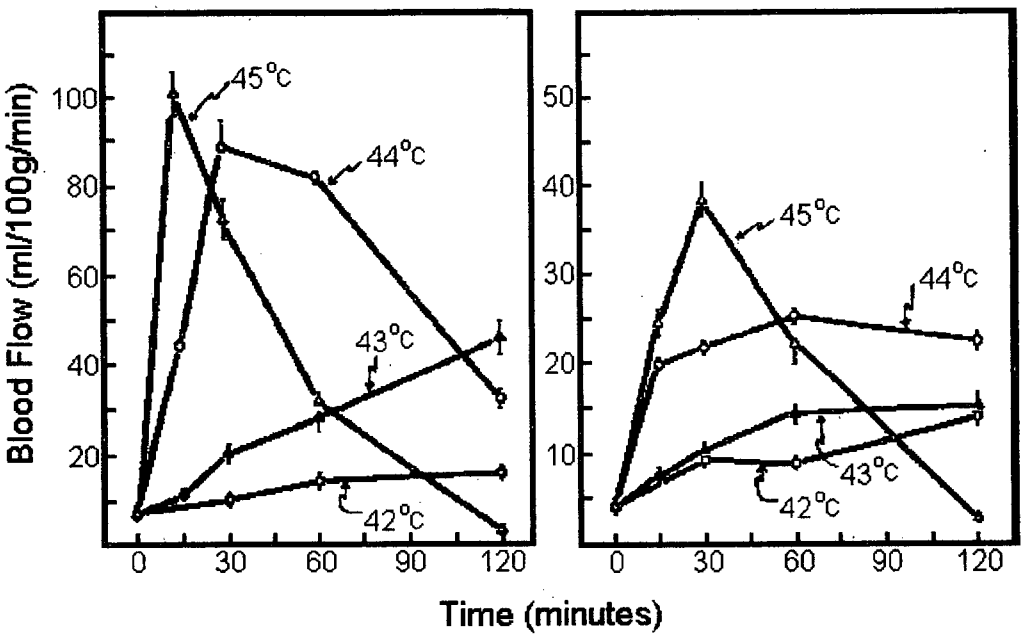

Figure 24 – Response of the skin and muscle perfusion rate to different applied temperatures in the rat leg (124). Perfusion rates were measured by a radioactive microsphere method, and the temperature was maintained by immersion in a water bath. Note that the peak blood flow rate occurs more quickly the higher the applied temperature.

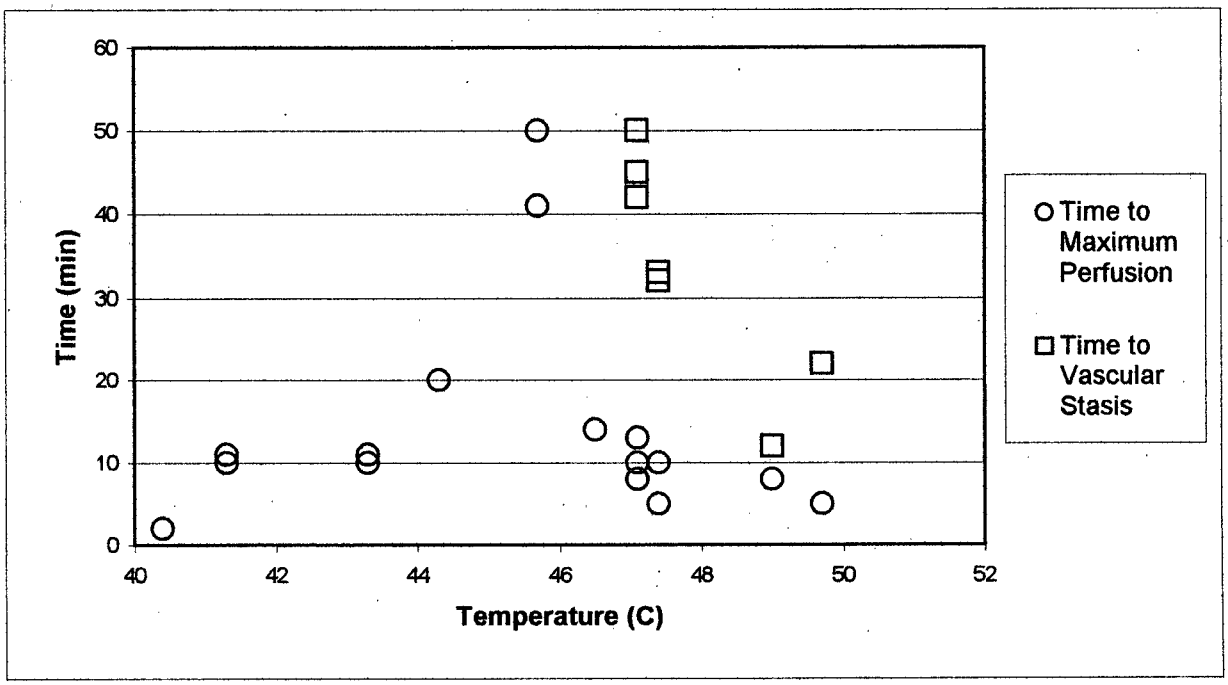

Figure 25 – Illustration of the time to maximum perfusion rate and until vascular stasis occurs, as found in individual vessels in the granulation tissue in the rabbit ear (125). Note that there is a bimodal response of the perfusion response time to temperature, although if the data between 44 and 46°C is neglected the response time is approximately constant.

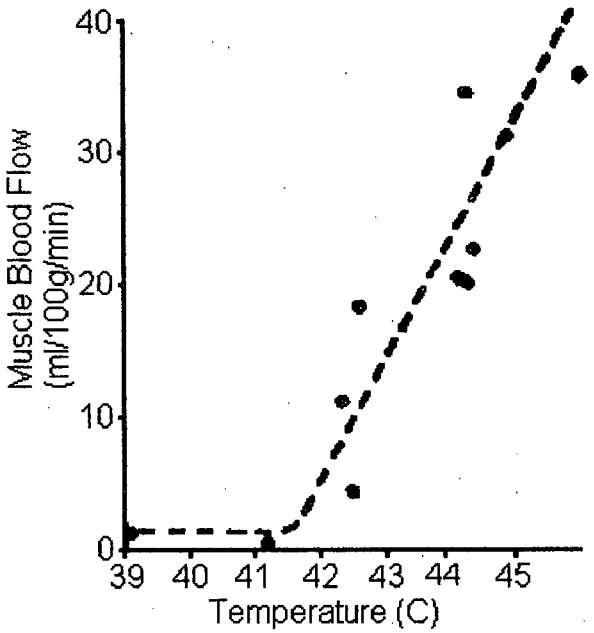

Figure 26 – Illustration of "critical temperature" concept, from Sekins et al (129). Data obtained from microwave diathermy of the human thigh muscle. Perfusion was measured by Xenon^{133} clearance and represents the maximum or the temporary maximum value.

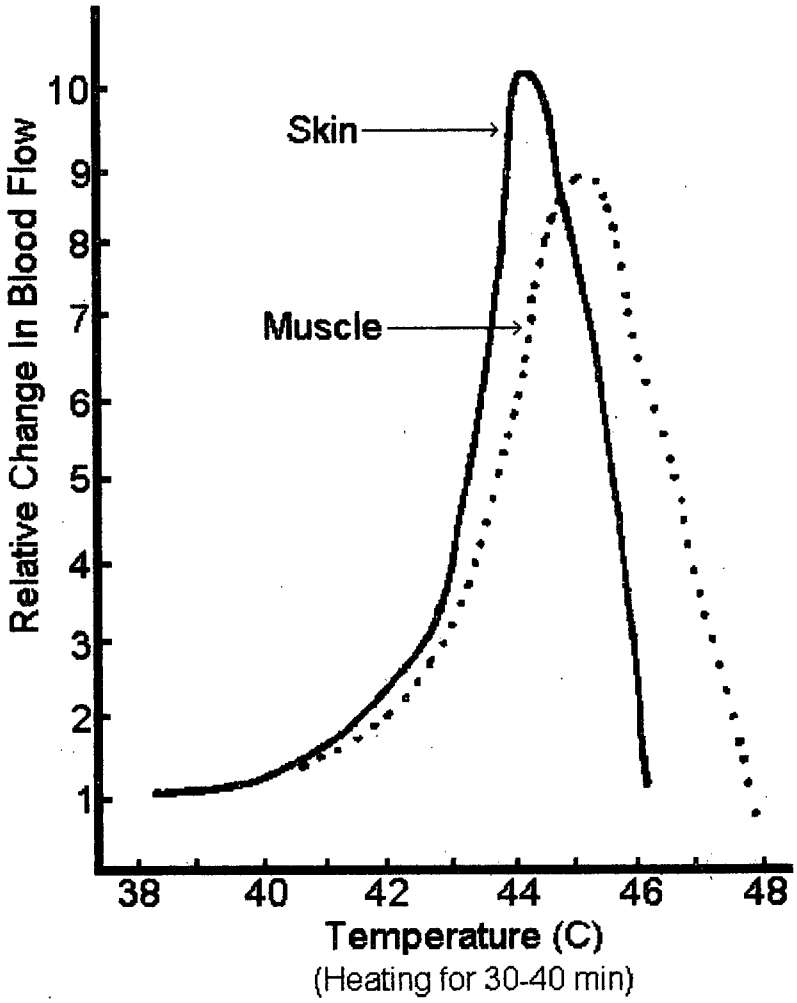

Figure 27 – The elevation in the perfusion rate in the skin and muscle of the rat leg (124). The relationships below are based on the data presented in Figure 24 following thirty minutes of hyperthermia. In this diagram there is little predicted perfusion elevation below 41°C, consistent with a critical temperature hypothesis. Notice that tumor tissue has a much lower perfusion response to hyperthermia, and is correspondingly more vulnerable than normal tissue to thermal injury. At temperatures above 44°C there is less of a perfusion increase due to concurrent vascular stasis onset.

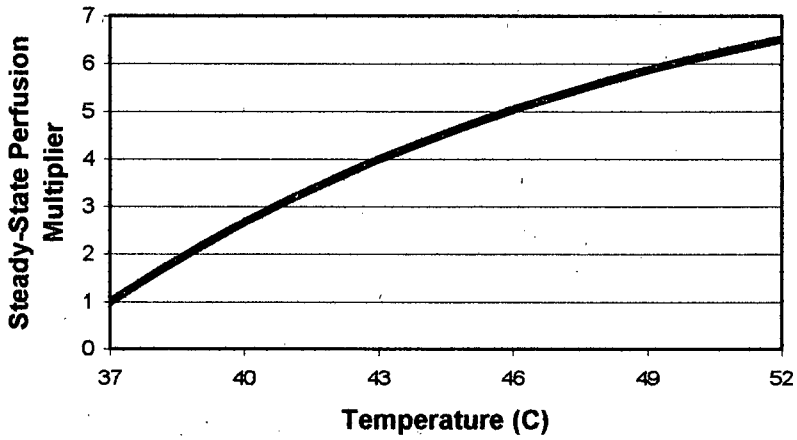

Figure 28 – Predicted increase in steady-state perfusion rate with temperature, based on an exponential approach to the asymptotic maximum perfusion rate of nine times, and assuming a temperature sensitivity value of 0.078 $^{o}C^{-1}$.

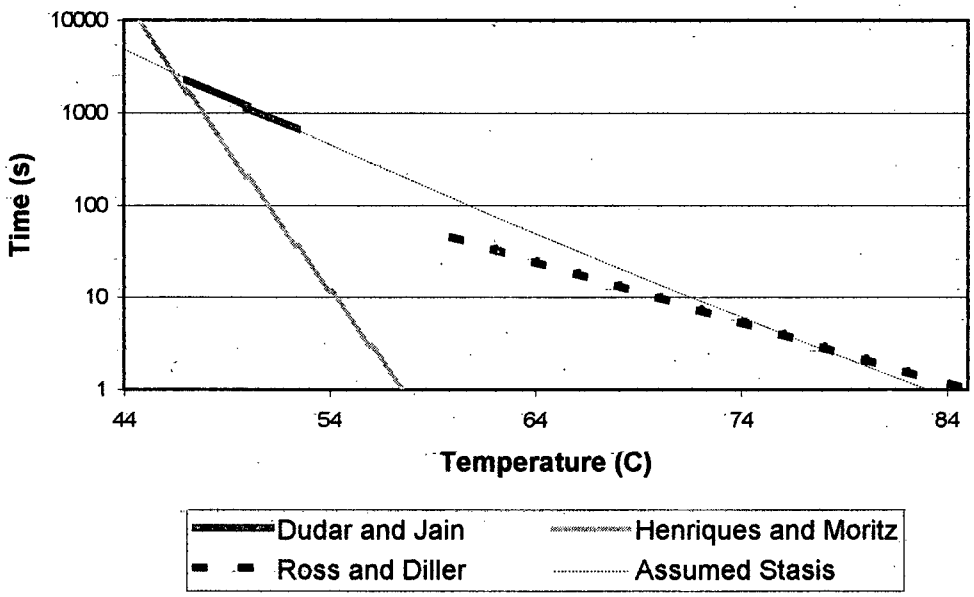

Figure 29 – The correspondence between the vascular stasis fitted curves of Dudar and Jain (125), and Ross and Diller (55). The Arrhenius expression used for calculating the cessation of blood flow is included and is simply an extension of the curve fit to the data of Dudar and Jain. The expression derived by Henriques (59) for the prediction of skin blister formation is also included for comparison purposes, it is clear that the threshold for tissue damage occurs at lower temperatures than immediate vascular stasis and therefore immediate vascular stasis represents a more severe form of thermal injury expression.

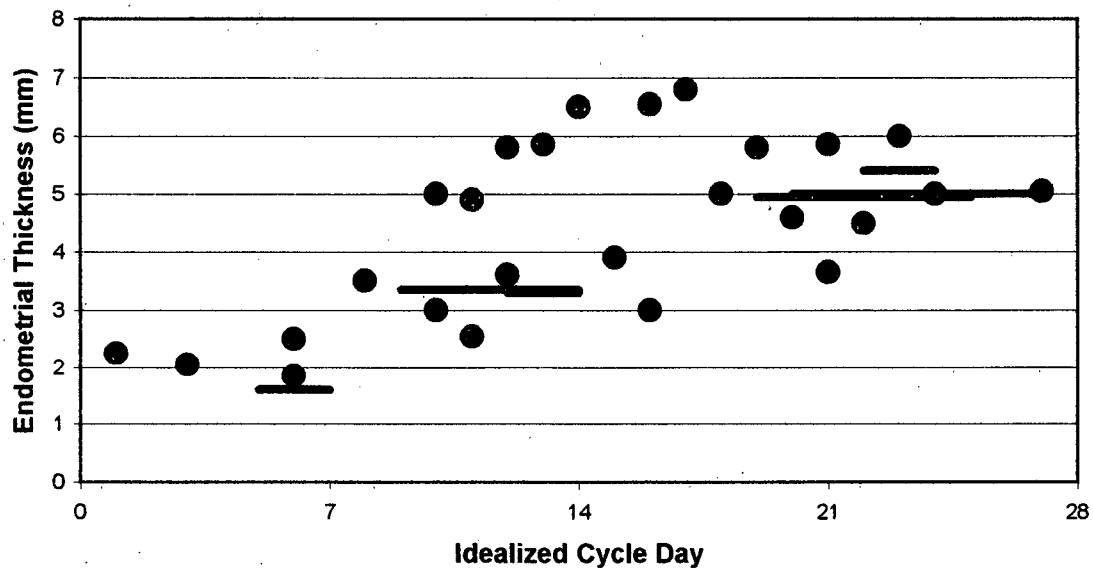

Figure 30 – Compilation of reported endometrial thickness at various stages of the menstrual cycle. A thick line is used where data was obtained over a range of days, while isolated data points represent specific days. Note that this chart has not been weighted for number of samples, and therefore cannot be used for curve fitting purposes. However it is apparent that there is a trend towards increasing endometrial thickness from the end of menstruation to the luteal phase (139, 140, 141, 142, 143, 145, 150).

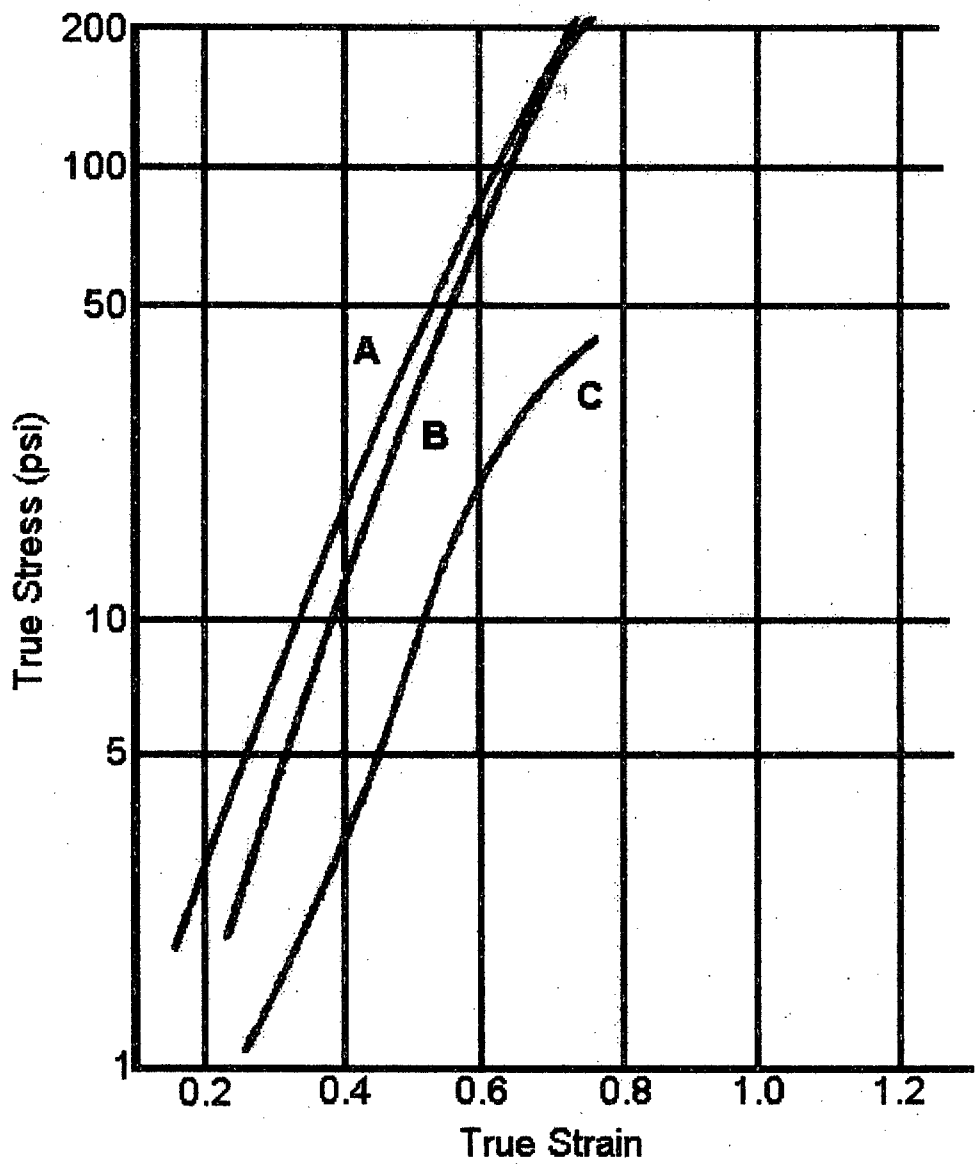

Figure 31 – Diagram of the stress-strain relationship of human myometrium tissue used to estimate Young's modulus in uterine tissue (159). Note that the stress axis is a logarithmic scale; the straight line therefore indicates that stress increases exponentially with strain. Data is from three samples of the same uterus; lines A and B were tested in tension, line C was tested in compression.

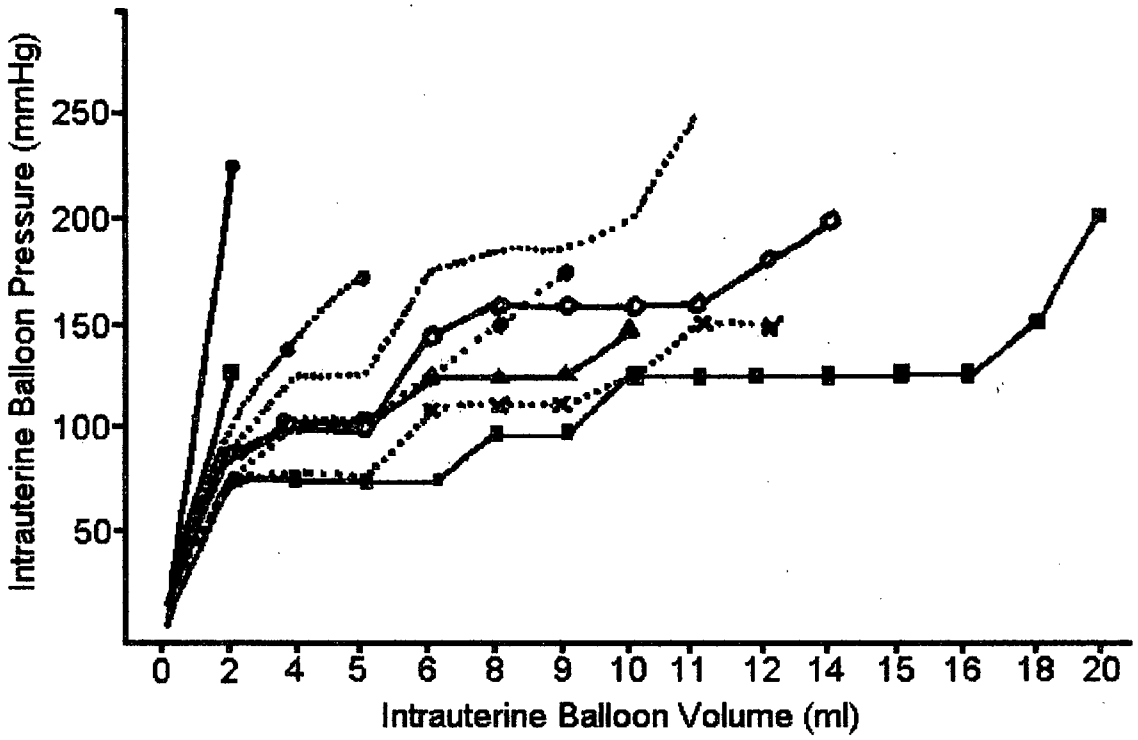

Figure 32 – Pressure-balloon volume relationship for nine patients treated for menorrhagia. Balloon was inflated by incremental infusion of 1 ml of fluid and then the resulting intrauterine pressure was recorded (116). The variability is due to difference in the elasticity modulus, muscular contractions, and the initial cavity volume prior to inflation. Large initial cavities will experience less pressure increase with each additional infusion of fluid. Note that the intrauterine balloon volume refers to the total fluid instilled, not the additional fluid above the initial cavity volume. Note that as the pressure approaches 150mmHg, significantly greater inflation pressures are required to further increase the volume of fluid in the uterus cavity, indicating that the natural cavity volume volume had been filled.

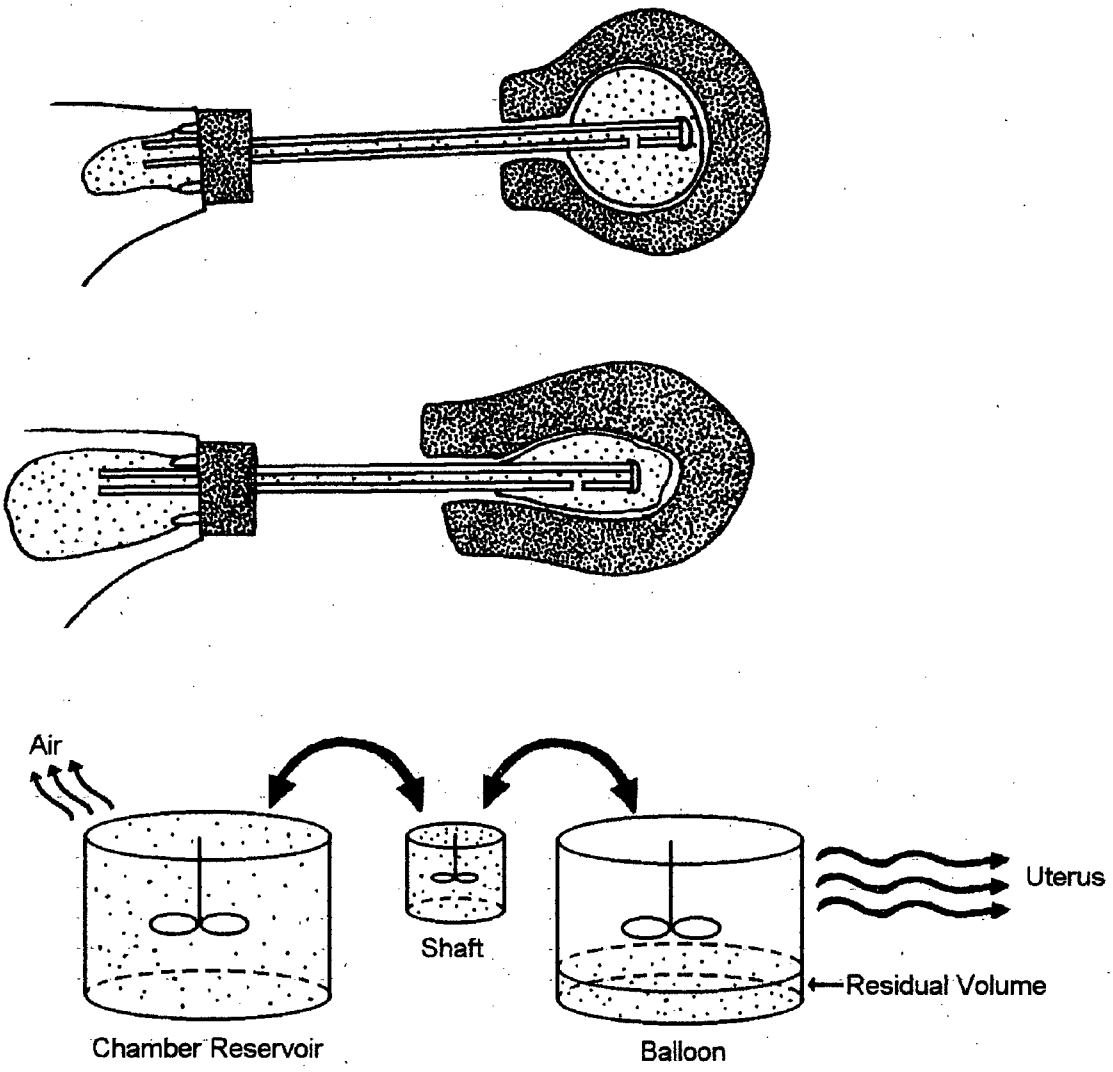

Figure 33 – Illustration of the TRS pulsation method, and the conceptual approximation used in the model. There are three compartments that are considered fully mixed: the reservoir, the shaft and the balloon. During each pulse cycle the required volume of glycerine is transferred from each compartment instantly.

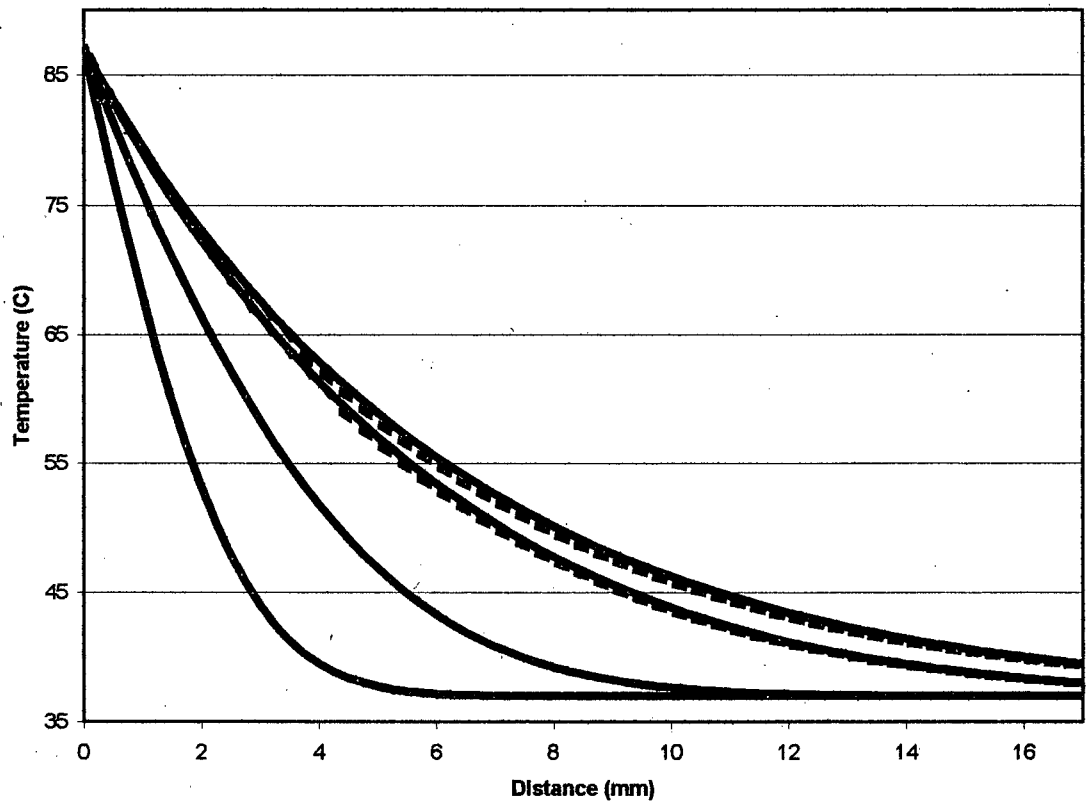

Figure 34 – An analytical solution to heat transfer in a perfused, semi-infinite, planar tissue is presented at 0.25, 1, 4 and 8 minute intervals. The time increment was 0.002min and 6 cells were used per millimeter. Solid line represents the exact solution, while the simulated result is shown with the dashed line. If the length of each cell is decreased further it becomes impossible to distinguish differences between the analytical and numerical solution.

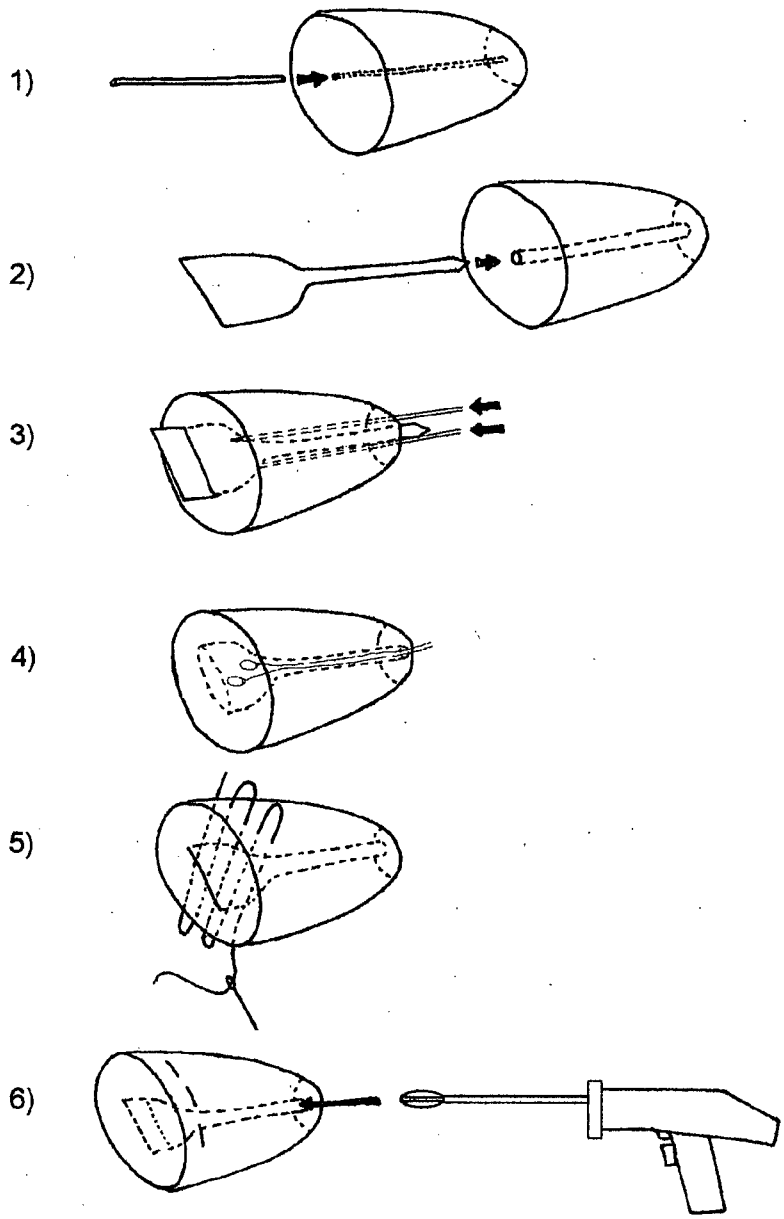

Figure 35 – Illustration of cavity cutting technique for the meat model uterus analogue. First a canal is cut with a sharpened metal tube (1), and then the cavity is cut using a specially designed cutting blade (2). The wire thermocouples are inserted at depth with the blade still in the tissue (3). Finally the disk thermocouples are inserted and secured (4), and the cavity is sewn closed (5). After warming to physiological temperatures the EAS catheter is inserted and treatment commences (6)

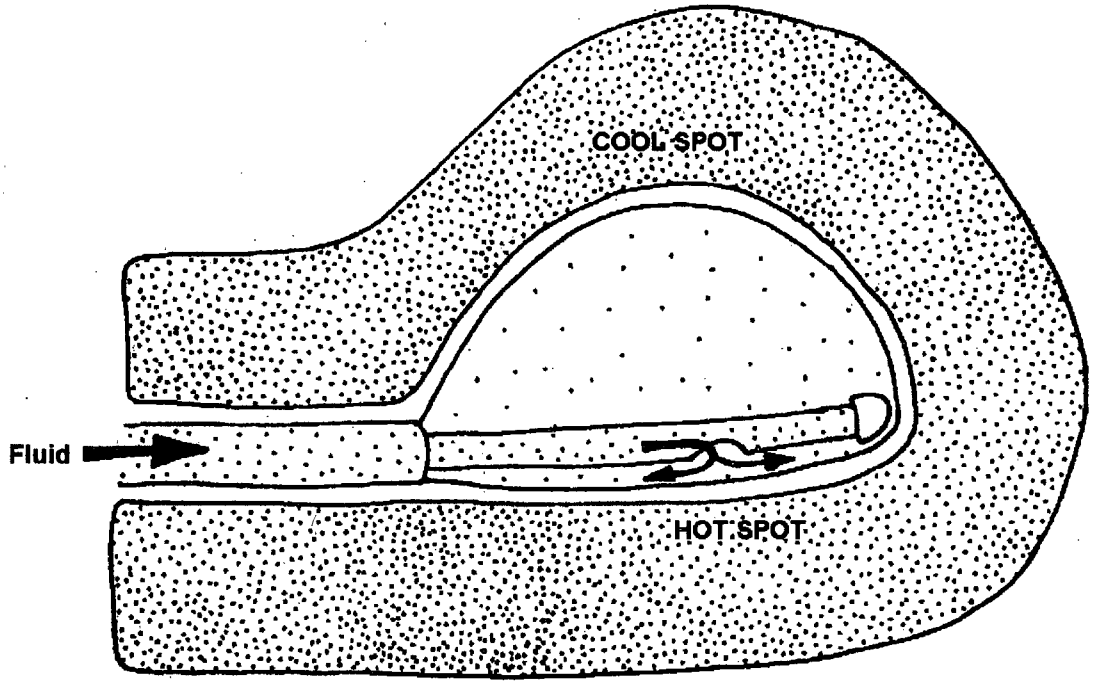

Figure 36 – Illustration of how localized hot spots may be created by applying torque to the catheter. Glycerine exits from a hole in the middle of the balloon catheter, and if this is pressed against tissue a local hotspot may result.

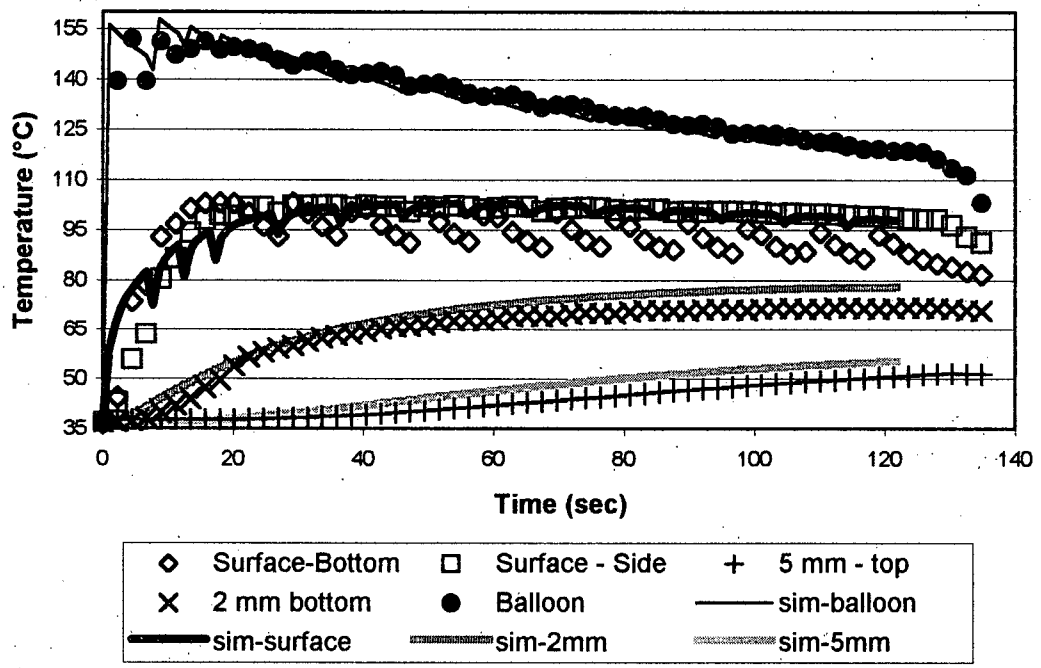

Figure 37 – TRS model calibration dataset compared to the calibrated model predictions (data from meat trial 12-13-01B). Model calibration was only based on balloon and surface temperature; the deep thermocouple data (2mm and 5mm) is included for the sake of completeness. The two surface thermocouples present qualitatively different forms, we hypothesize that the more variable data is due to loss of contact with the balloon, and therefore have selected the less variable thermocouple data for calibration purposes. The 2mm thermocouple exhibits a discontinuity at approximately 20 seconds; it is thought that there was a slight movement of the thermocouple during the initial portion of the treatment. The form of the 5mm thermocouple data is in agreement with model predictions, a slight change in position would result in an excellent data fit at this depth.

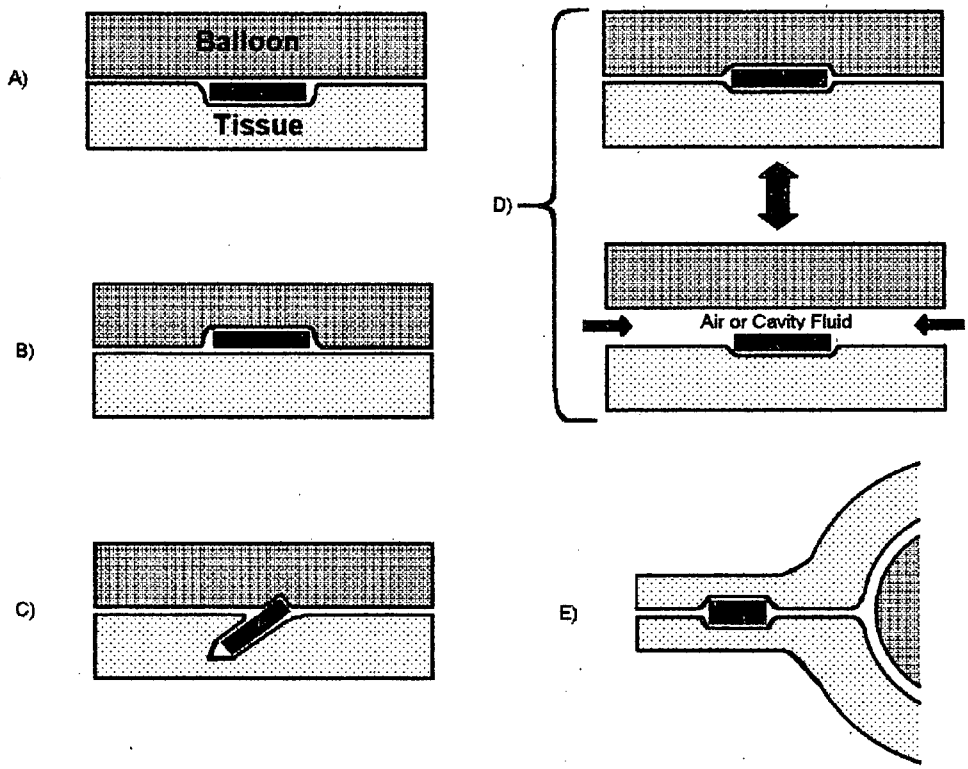

Figure 38 – Diagram of possible ways that surface thermocouples may provide inaccurate temperature data. The thermocouple may protrude into the meat (A) or the meat (B), slice sideways into the meat (C), and may make periodic contact with the balloon (D), or may not even make contact at all (E).

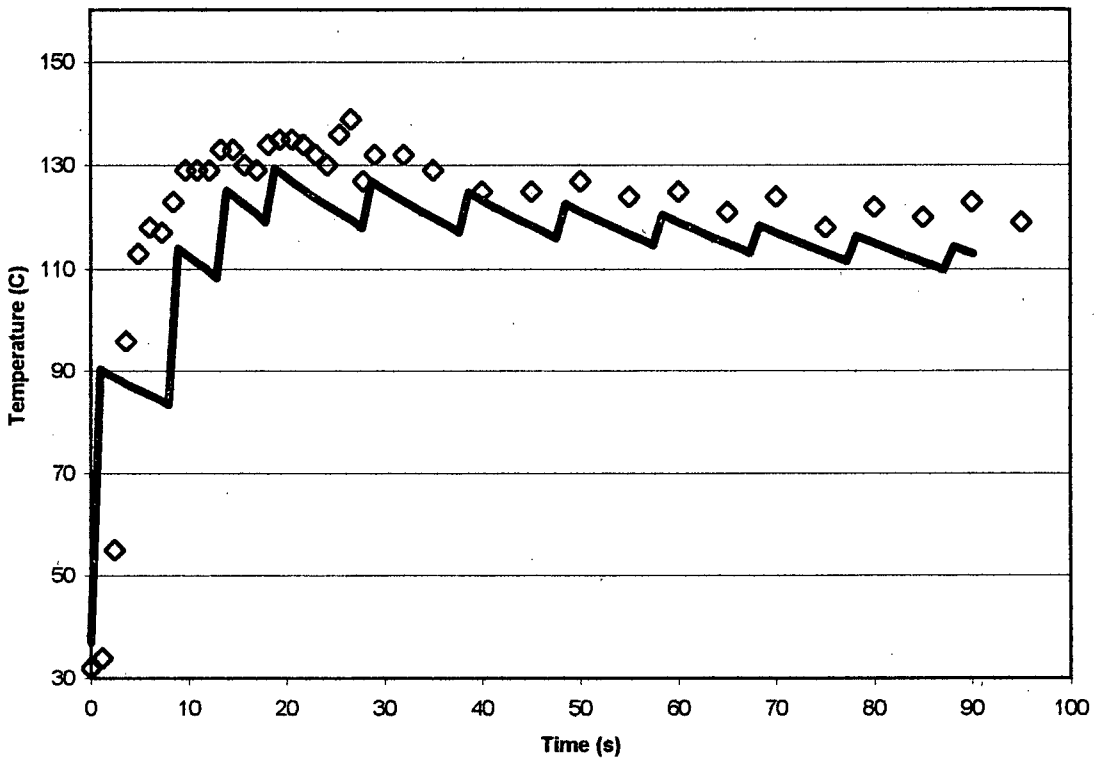

Figure 39 – Manually recorded balloon temperature-time series data from trial CT0011-04, compared to model predictions for the 5.5ml cavity volume. Note that this treatment did not use active deflation, and treatment time was only 90 seconds. Open diamonds represent experimental data, and the solid black line represents the model simulation result.

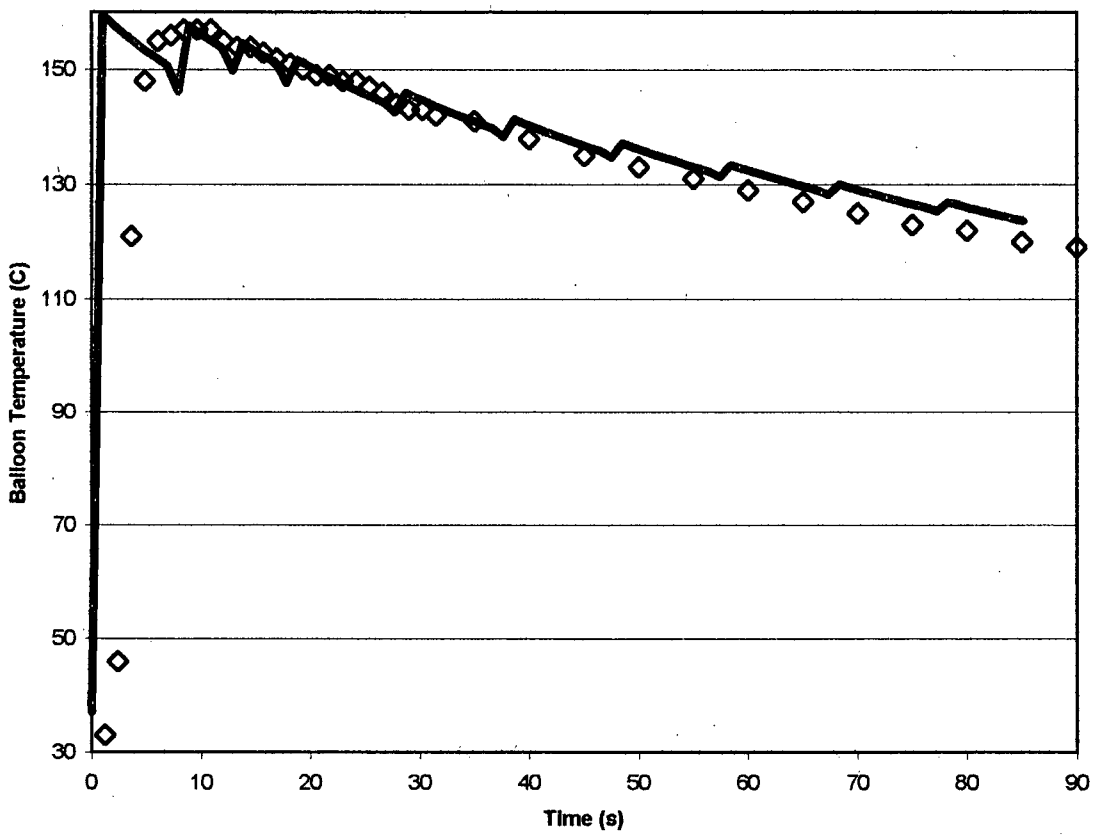

Figure 40 – Manually recorded balloon temperature-time series data from trial CT0011-05, compared to model predictions for the 8.5ml cavity volume. Note that this treatment did not use active deflation, and treatment time was only 90 seconds. One consequence of assuming instantaneous fluid exchange is that the balloon temperature is predicted to adjust instantaneously during each pulsation. This explains the initial discrepancy during the first seven seconds of treatment. Open diamonds represent experimental data, and the solid black line represents the model simulation result.

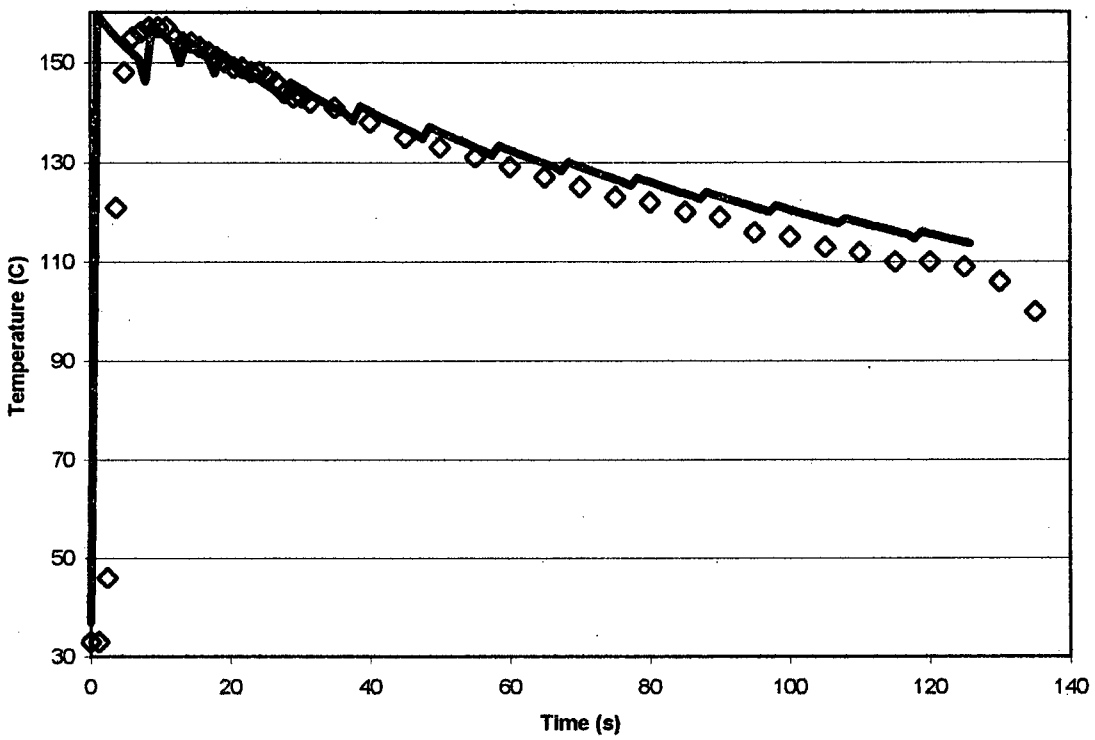

Figure 41 – Comparison of observed and predicted results of trial CT-0011-06, based on a 21ml cavity volume. Active deflation was used for the initial cycles, and the treatment time was the full 2.1 minutes. Open diamonds represent experimental data, and the solid black line represents the model simulation result.

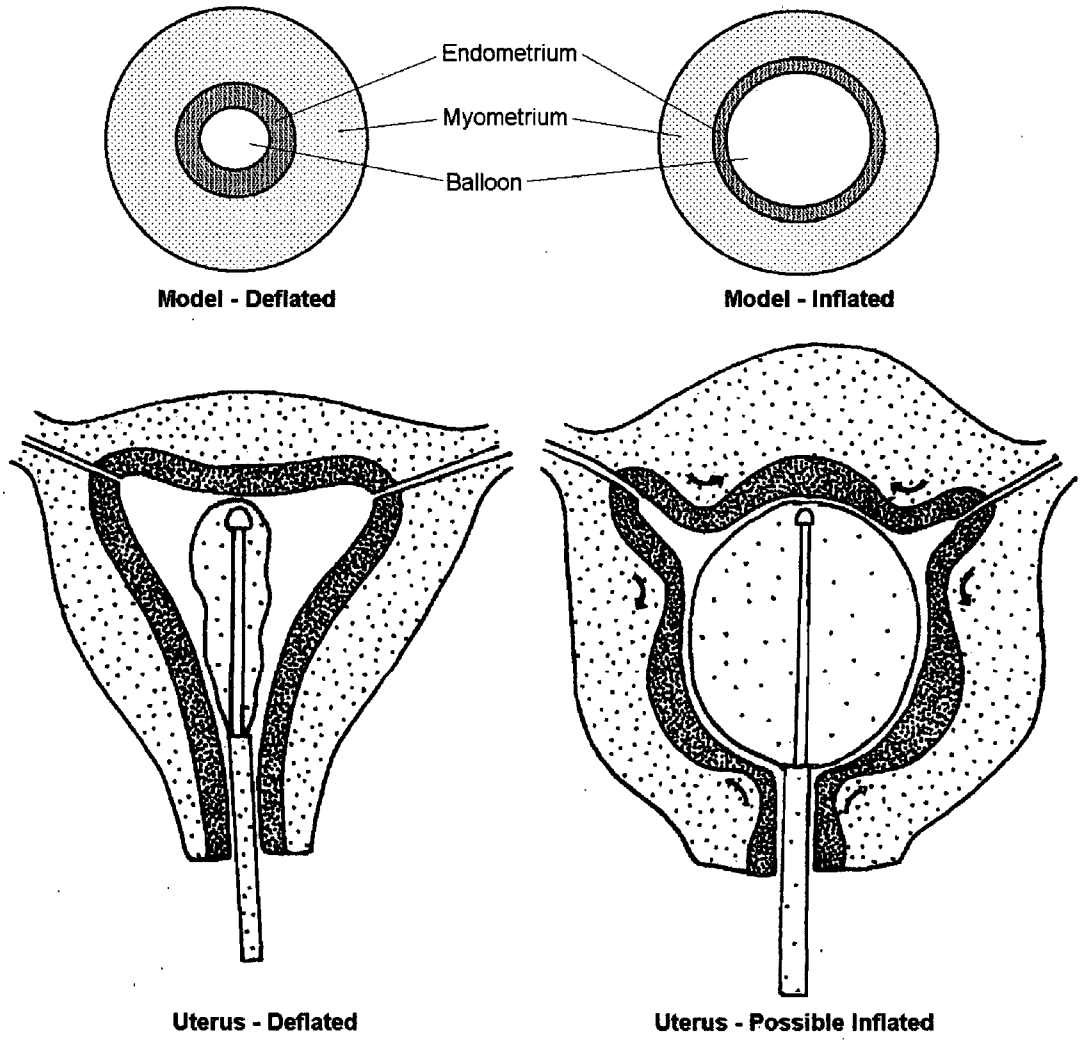

Figure 42 – Illustration of a proposed mechanism that may invalidate some of implications of the spherical elasticity model. Rather than stretching uniformly around the balloon (top), it is hypothesized that tissue may become stretched around holes in the medium (exaggerated on bottom), effectively increasing cavity volume by recruiting new surface rather than completely by stretching the existing surface.

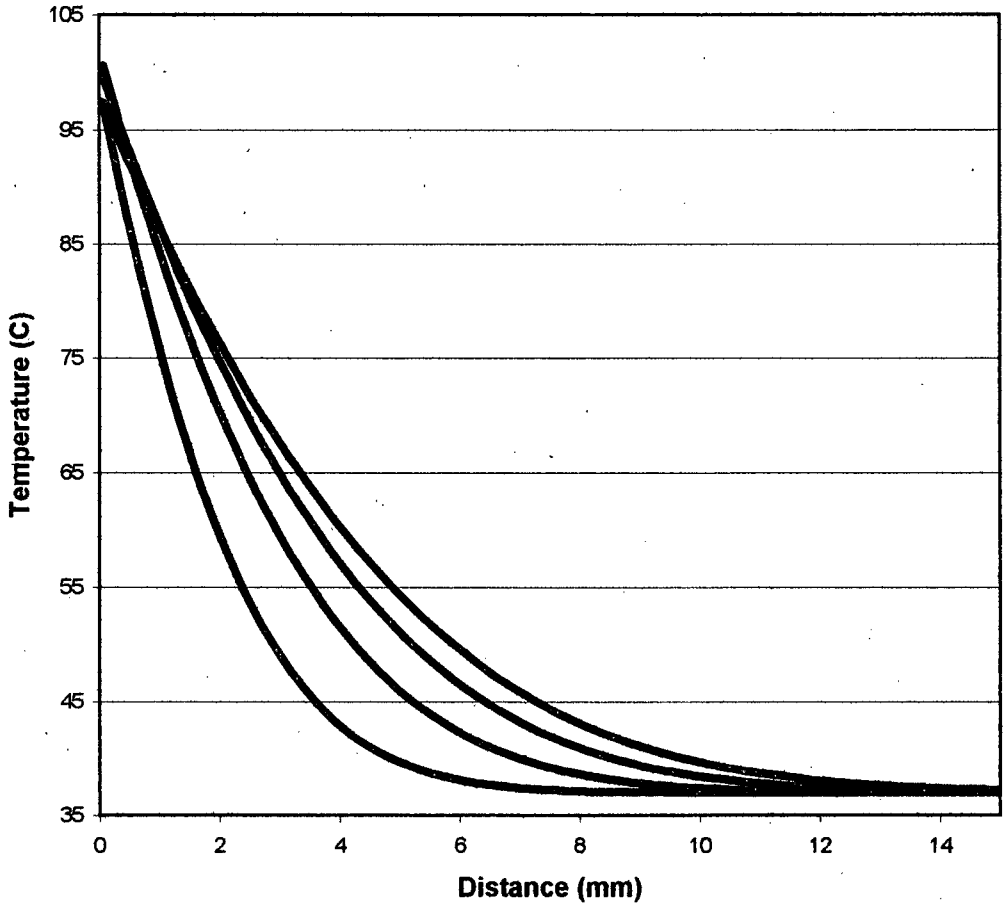

Figure 43 – Examples of the temperature profile throughout the tissue during treatment with the TRS device, as calculated at 30 second intervals. The distance is measured from the cavity surface of the distended uterus.

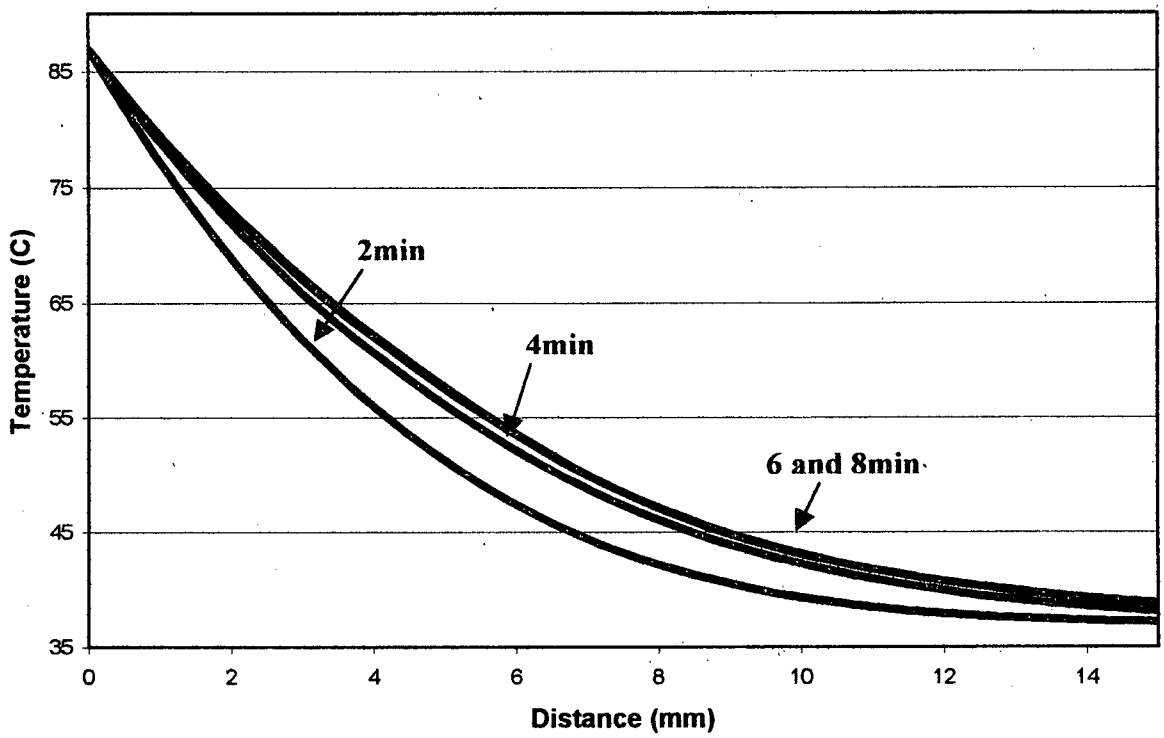

Figure 44 – Temperature profiles extracted every two minutes from a simulation of the Thermachoice 2 treatment protocol (87°C for 8 minutes) applied to the average uterus. Initial temperature was 37°C. Note that by four minutes the temperature is approaching it's steady-state value, and that the six and eight minute profiles cannot be distinguished.

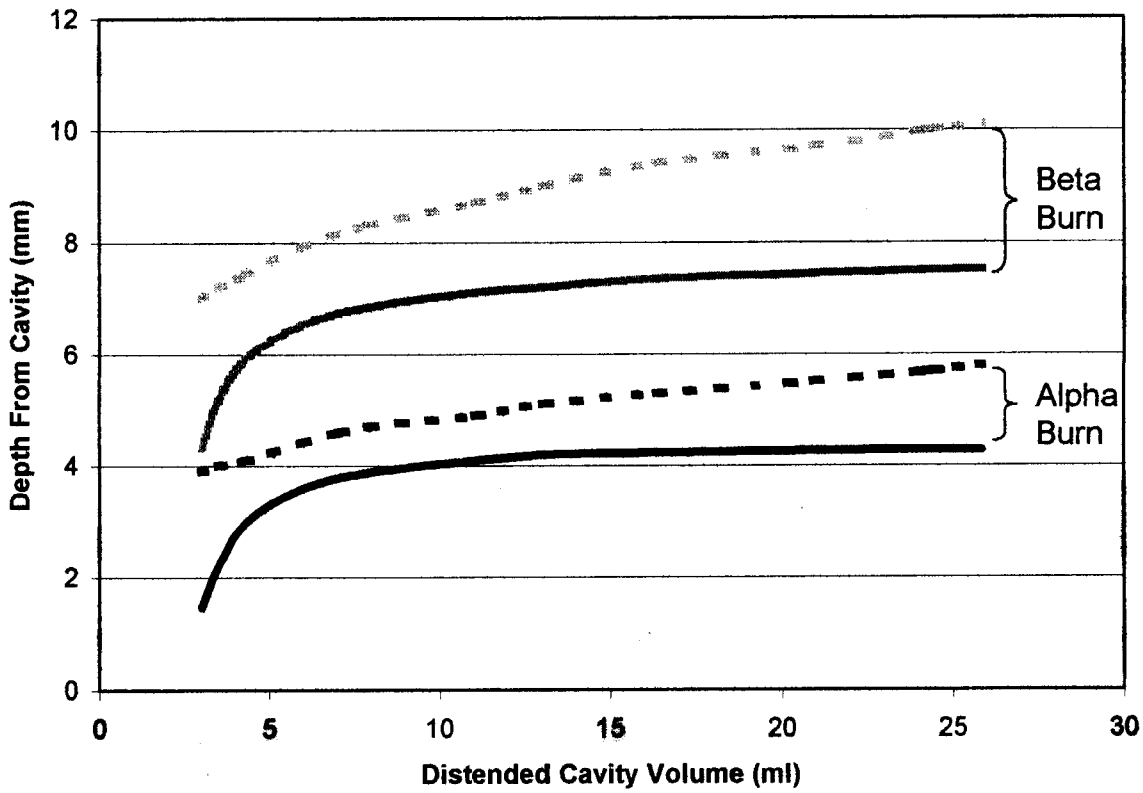

Figure 45 – The effect of the distended cavity volume of the uterus for the TRS (solid) and Thermachoice™ 2 (dashed) is presented. The black lines represents the middle alpha burn depth (coagulation), while the gray lines is used for the middle beta burn depth (eventual necrosis).

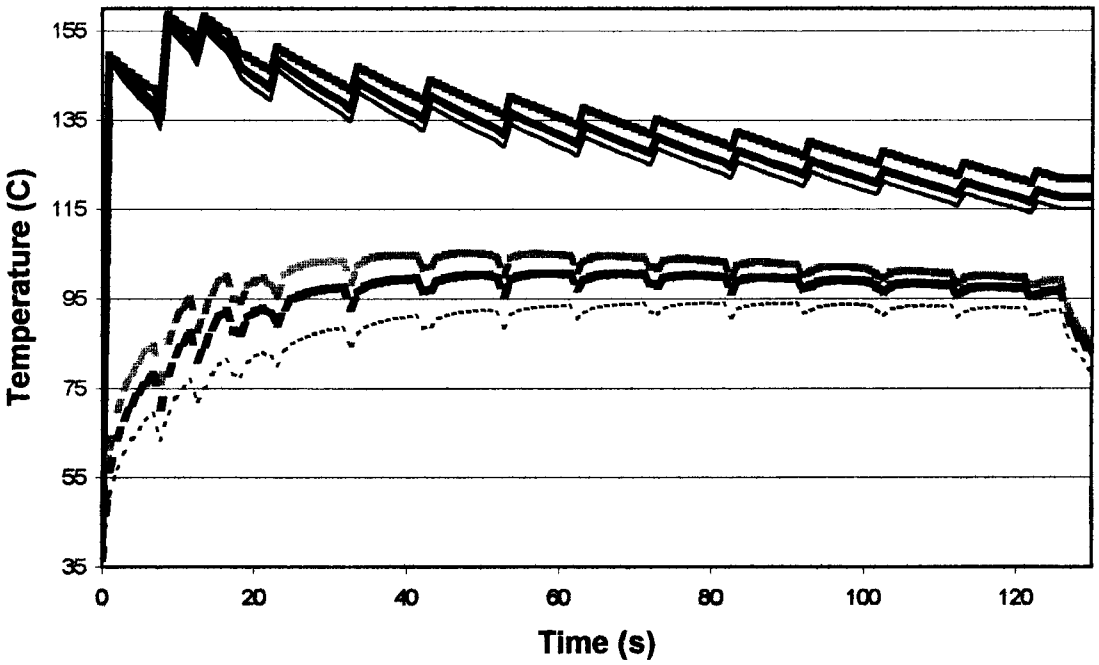

Figure 46 – Effect of changes in the heat transfer coefficient on the balloon (solid) and cavity surface (dashed) temperature-time series. Values tested for the heat transfer coefficient are 225 (thin line), 325 (thick, black line) and 425 (thick gray line).

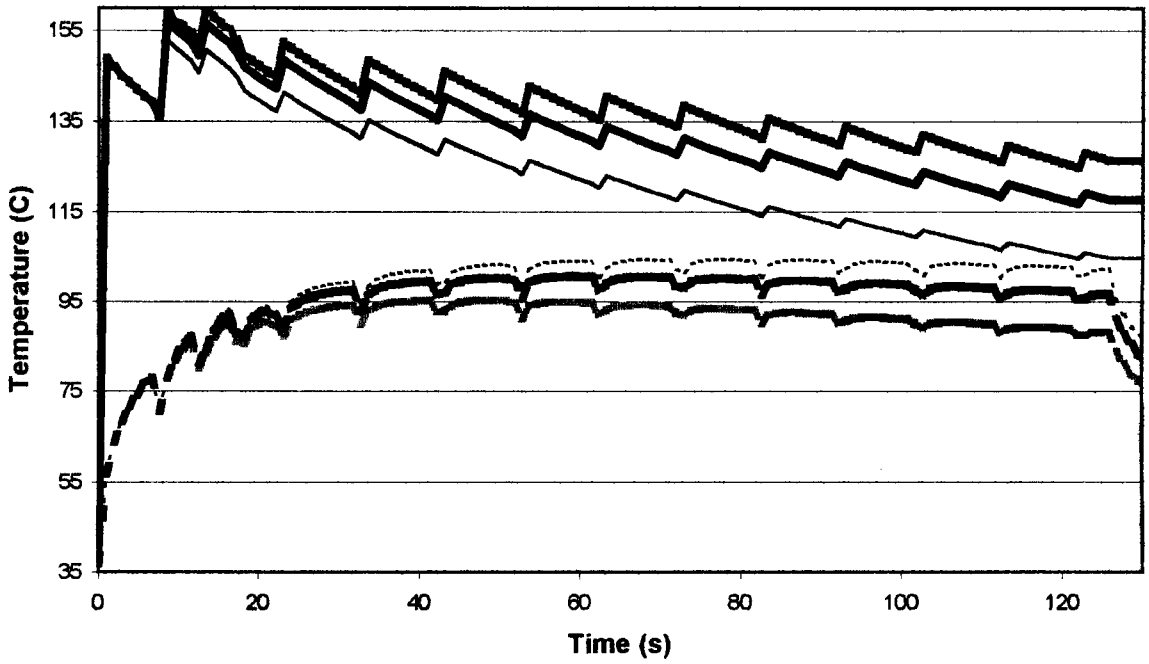

Figure 47 – Effect of changes in the effective glycerine volume on the balloon (solid) and cavity surface (dashed) temperature-time series. Values tested for the glycerine volume are 26 (thin line), 38 (thick, black line) and 50ml (thick gray line).

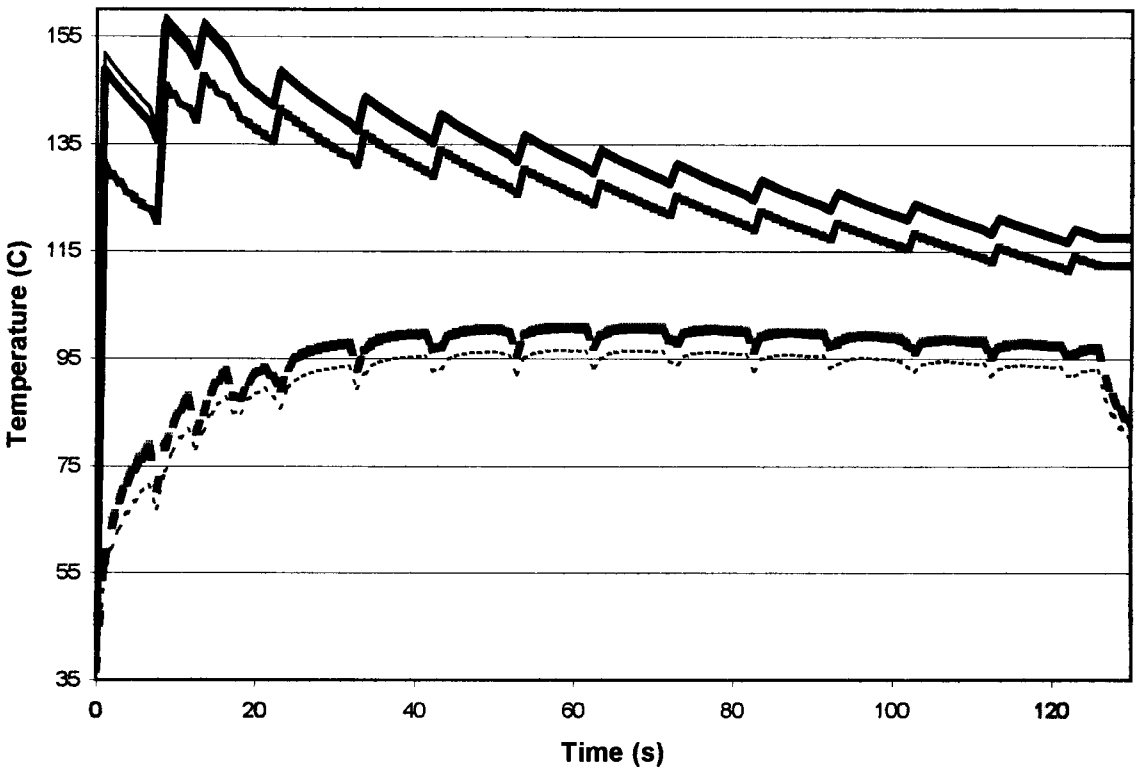

Figure 48 – Effect of changes in the distribution of the active and passive residual volume components of the balloon residual volume on the balloon (solid) and cavity surface (dashed) temperature-time series. Values tested for the glycerine volume, in terms of active/passive are 0/2.0 (thin line), 0.5/1.5 (thick, black line) and 0.25/1.75 ml (thick gray line).

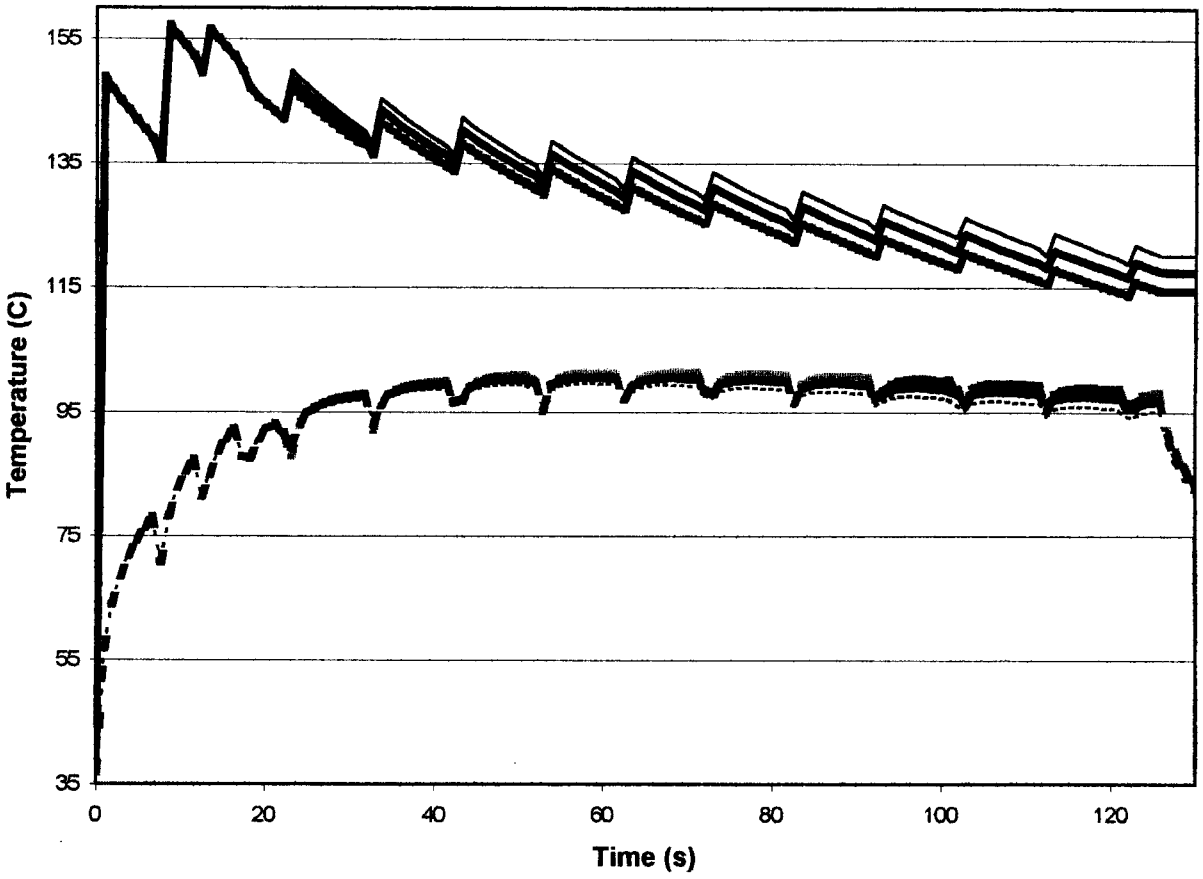

Figure 49 - Effect of changes in the additional residual volume during passive deflation on the balloon (solid) and cavity surface (dashed) temperature-time series. Values tested for the glycerine volume are zero (thin line), 1.5 (thick, black line) and 3.0 ml (thick gray line).

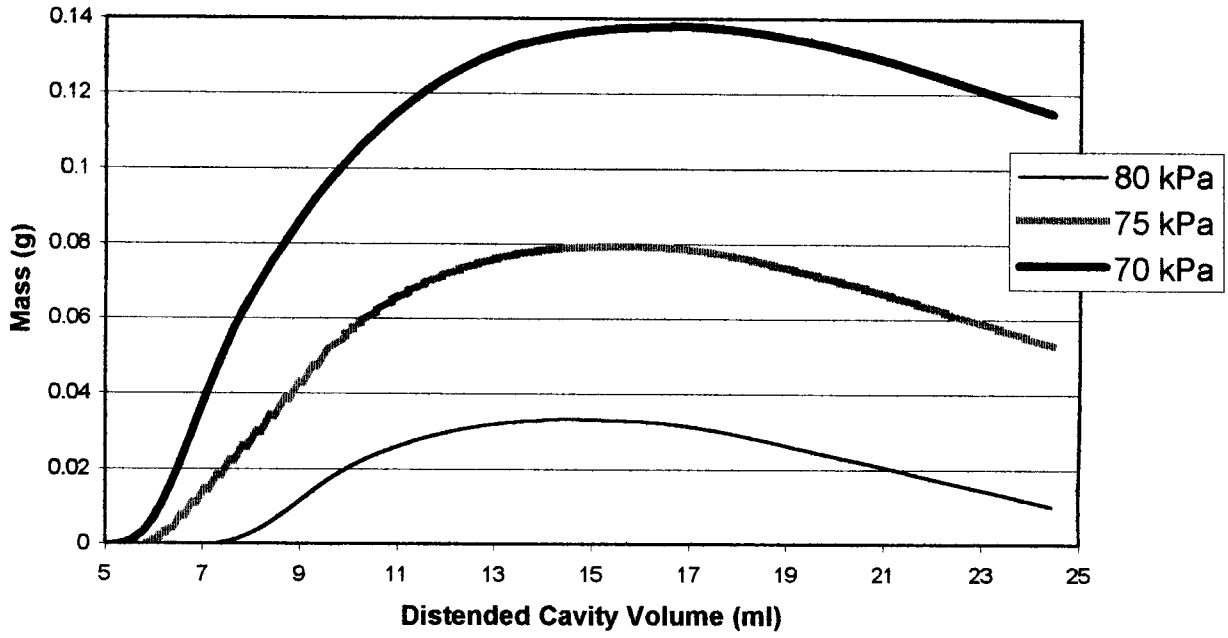

Figure 50 – Variation in the predicted net mass of water vaporized with ambient pressure and the distended cavity volume. No vaporization was observed at 85 kPa or higher, and so these curves were not included. Note that the mass of vaporized water is greatest at intermediate cavity volumes.

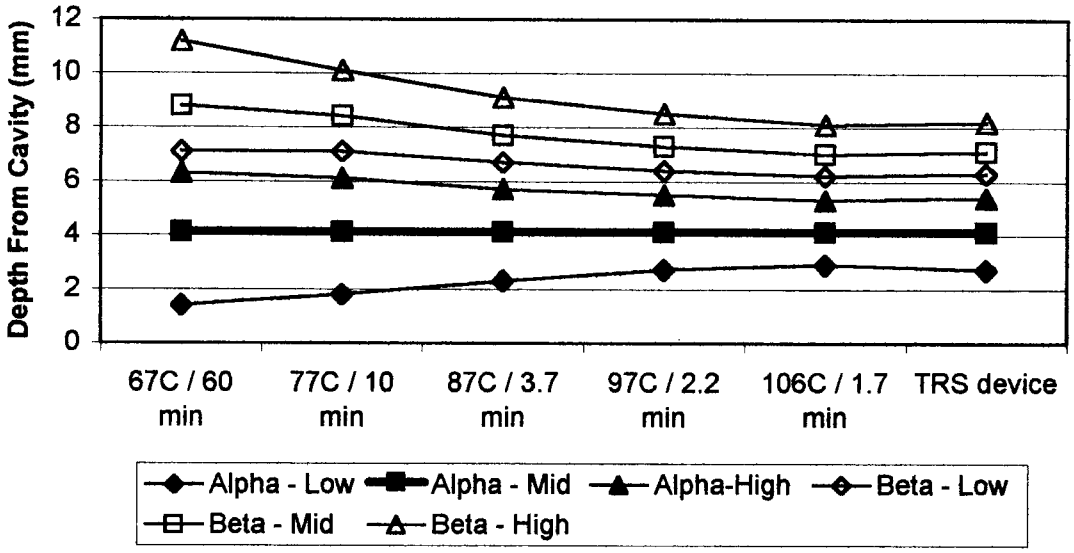

Figure 51 – Variation of burn specificity with cavity surface temperature for the standard uterus parameters. All treatment times have been adjusted to yield the same middle alpha (coagulation) burn depth as the TRS device. The predicted beta burn depth decreases significantly as the applied temperature increases, resulting in greater burn specificity. The performance of the TRS is only marginally worse than a treatment at the boiling temperature of water for 1.7 minutes.

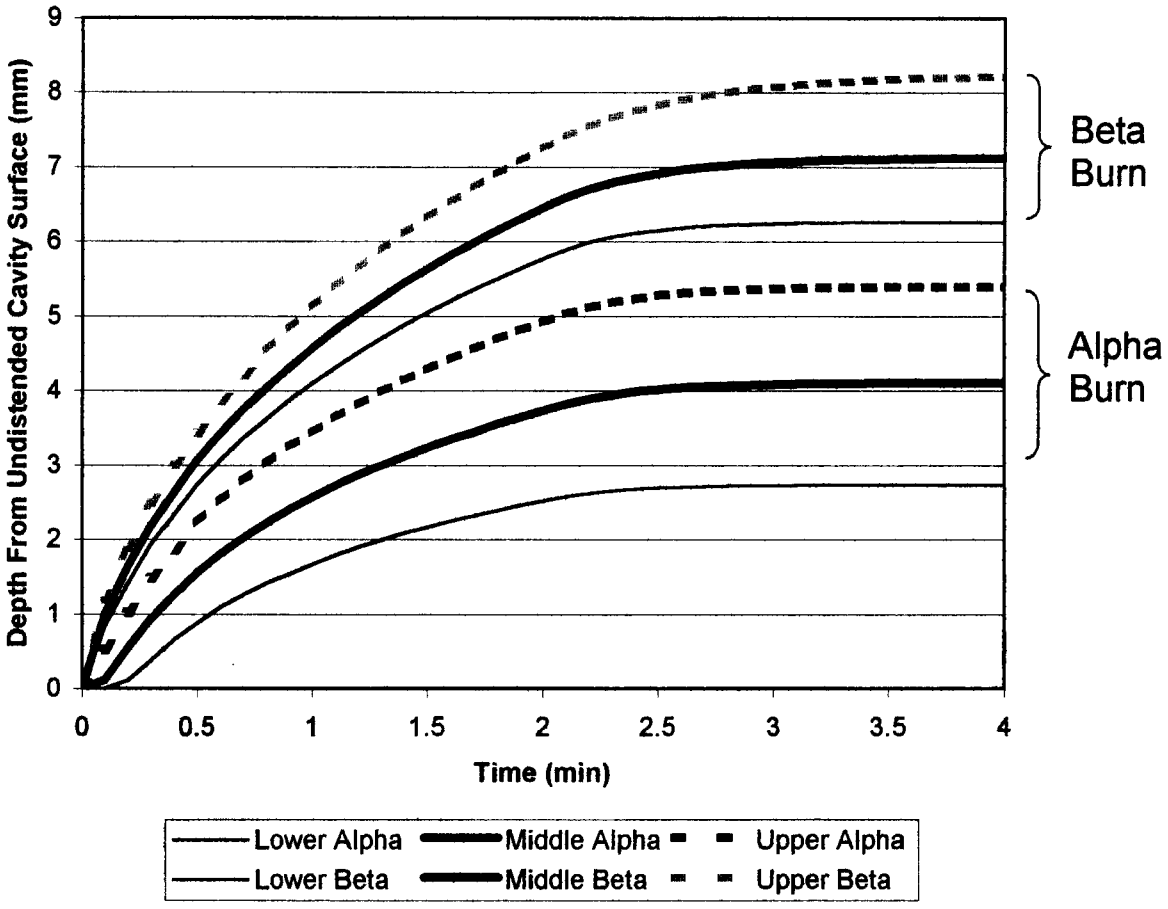

Figure 52 – Progression of burn depth throughout treatment with the TRS device using standard uterus parameters. Burn depth increases following the end of treatment (2.1 minutes), but has ceased increasing two minutes after the end of treatment.

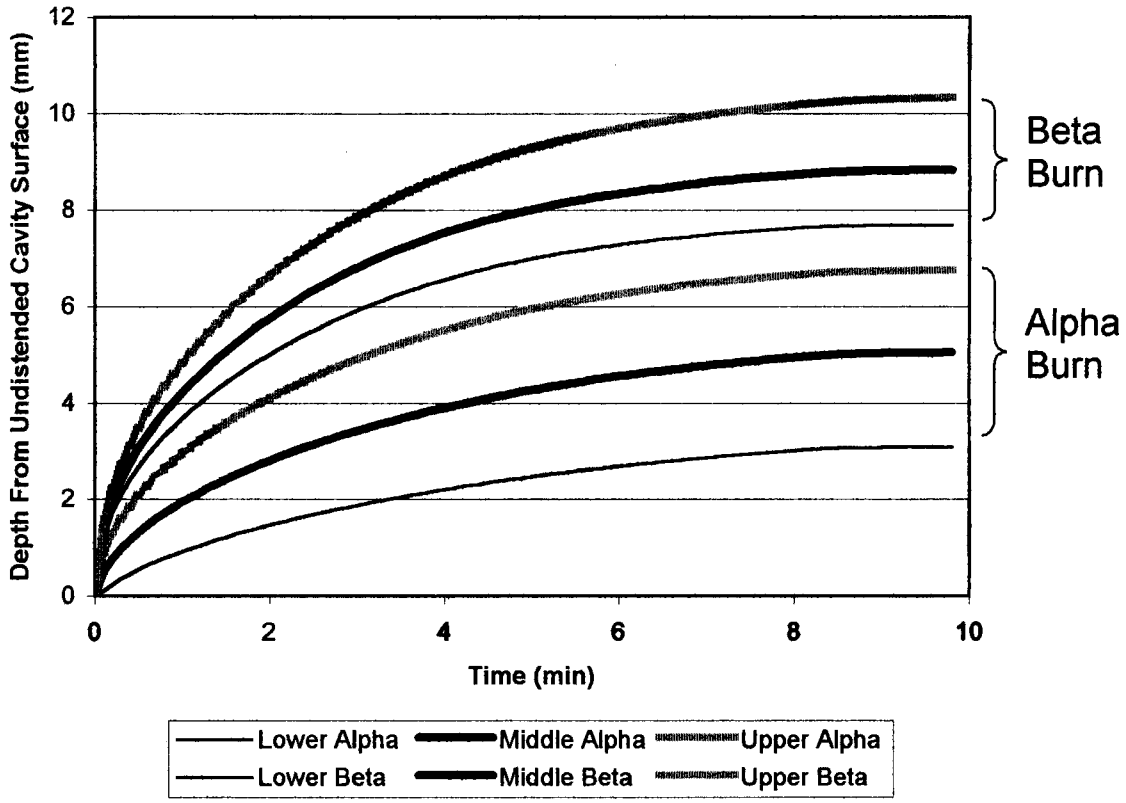

Figure 53 - Progression of burn depth throughout treatment with the Thermachoice 2 device using standard uterus parameters. Burn depth increases following the end of treatment (8 minutes), but has ceased increasing two minutes after the end of treatment. Notice that the rate of burn depth increase falls consistently as the treatment time increases.

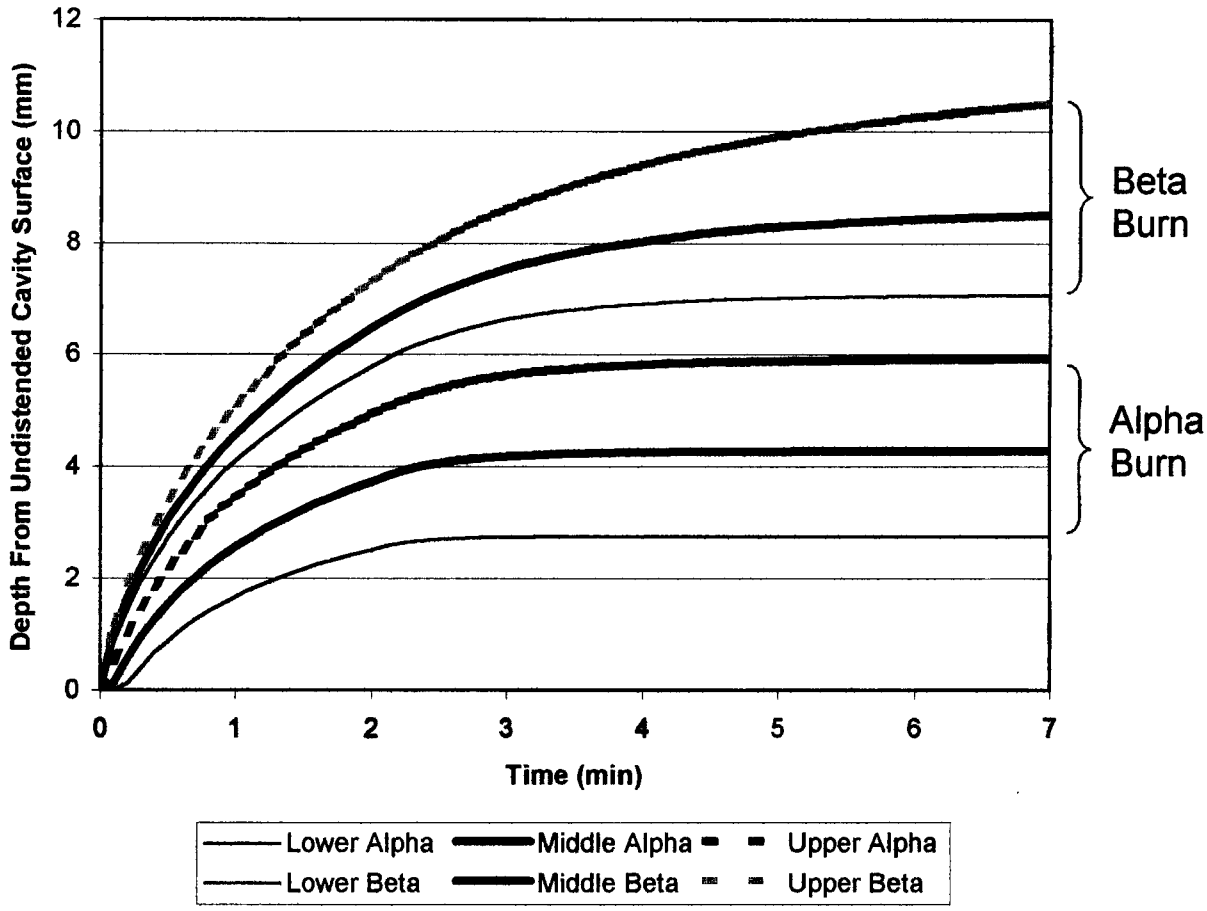

Figure 54 – Progression of burn depth with the TRS device in unperfused tissue. One key feature is that burn depth continues to increase for a longer time following the end of treatment (at 2.1 minutes), because heat cannot be removed by perfusion it may only be eliminated by conduction through the outlying tissues.

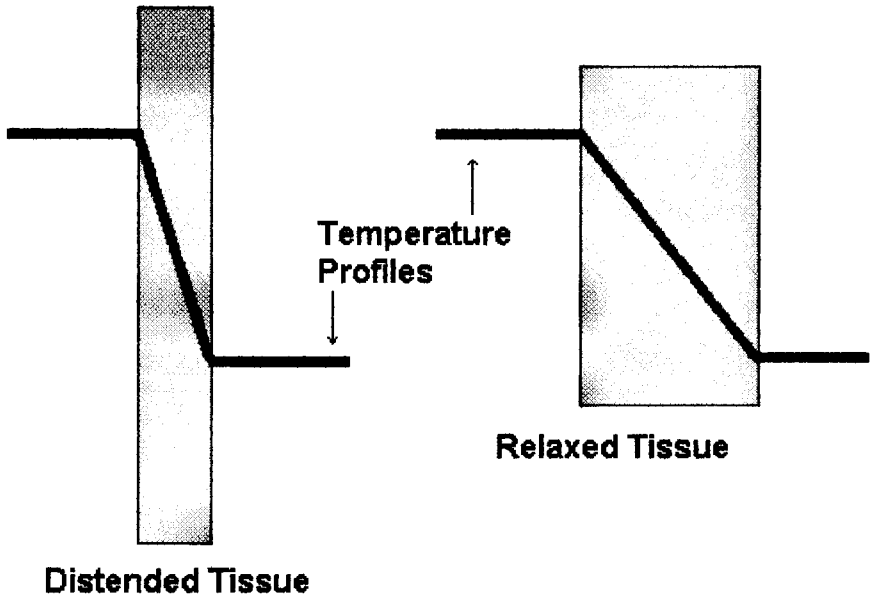

Figure 55 – Illustration of the effect that the relaxation of distended tissue has on the temperature gradient. On the left is a slab of tissue stretched thin with a temperature gradient through the width of the tissue. On the right is the tissue following relaxation. The resulting thickening of the tissue reduces the temperature gradient ($\Delta T/\Delta x$), and therefore reduces the heat flux through the slab.